Observing and quantifying Earth's radiation budget from UVSQ-SAT satellite

Adrien Finance

To cite this version:

Adrien Finance. Observing and quantifying Earth's radiation budget from UVSQ-SAT satellite. Atmospheric and Oceanic Physics [physics.ao-ph]. Université Paris-Saclay, 2023. English. NNT : 2023UPASP026 . tel-04112065

HAL Id: tel-04112065

https://theses.hal.science/tel-04112065

Submitted on 31 May 2023

Observing and quantifying Earth's radiation budget from UVSQ-SAT satellite

Observation et quantification du bilan radiatif terrestre à partir du satellite UVSQ-SAT

Thèse de doctorat de l'Université Paris-Saclay

École doctorale n° 127 Astronomie et Astrophysique d'Ile-de-France (AAIF)
Spécialité de doctorat : Astronomie et Astrophysique
Graduate School : Physique. Référent : Université de Versailles-Saint-Quentin-en-Yvelines

Thèse préparée dans l'unité de recherche **LATMOS (Université Paris-Saclay, UVSQ, CNRS)**, sous la direction de **Mustapha MEFTAH**, docteur en Astronomie et Astrophysique, CNRS, et la co-supervision de, **Antoine MANGIN**, directeur scientifique de l'entreprise ACRI-ST.

Thèse soutenue à Guyancourt, le 31 mars 2023, par

Adrien FINANCE

Composition du jury

Membres du jury avec voix délibérative

Pierre-Richard DAHOO Professeur, LATMOS, Université Versailles Saint-Quentin-en-Yvelines	Président
Steven DEWITTE Directeur de Recherche, ROB	Rapporteur et Examinateur
Karina VON SCHUCKMANN Cadre scientifique, Mercator Ocean	Rapporteur et Examinatrice
Thierry DUDOK DE WIT Professeur, Université d'Orléans	Examinateur
Didier FUSSEN Professeur, Institut royal d'Aéronomie spatiale de Belgique	Examinateur
Nathalie HURET Professeure, LaMP, Université Clermont Auvergne	Examinatrice
Benoît MEYSSIGNAC Docteur en géosciences, CNES, LEGOS	Examinateur

THESE DE DOCTORAT

NNT : 2023UPASP026

université
PARIS-SACLAY

ÉCOLE DOCTORALE
Astronomie
et Astrophysique
d'Île-de-France (AAIF)

Titre : Observation et quantification du bilan radiatif terrestre à partir du satellite UVSQ-SAT.

Mots clés: observation et suivi du climat ; bilan radiatif terrestre ; nanosatellite ; télédétection ; détermination de l'attitude ; méthode d'apprentissage profond

Résumé : Cette thèse a pour objectif d'apporter un regard nouveau sur l'observation depuis l'espace des composants du bilan radiatif de la Terre (ERB). Le climat est contrôlé par la quantité de flux solaire absorbé par la Terre et la quantité de flux infrarouge émis vers l'espace. Ces quantités, ainsi que leur différence, définissent l'ERB. Différentes techniques existent pour quantifier cette variable telles que l'observation par satellite, les mesures in situ, les réanalyses ou les modèles. Le projet UVSQ-SAT fournit des observations par satellite de l'ERB. Les produits UVSQ-SAT comprennent le rayonnement solaire réfléchi et le rayonnement émis par la Terre depuis le sommet de l'atmosphère (TOA). Le CubeSat UVSQ-SAT a été lancé en Janvier 2021. Cette thèse traite de la détermination des flux terrestres émis à courtes et longues longueurs d'ondes, en se basant sur deux ans d'observation d'UVSQ-SAT. L'objectif principal de cette thèse est de déterminer précisément l'attitude du satellite pour obtenir l'ERB. Les méthodes de reconstruction des cartes de flux et les résultats de la mission sont présentés et expliqués. Les résultats de cette première approche fournissent des indications précieuses qui peuvent éclairer la conception et la mise en œuvre de futures missions spatiales. L'observation de l'ERB au TOA avec une précision inégalée ($1.00\,\mathrm{Wm}^{-2}$), en temps quasi réel ($3\,\mathrm{h}$) et en tout point du globe (quelques kms), requiert la mise en oeuvre d'une mégaconstellation de satellites. Les résultats obtenus lors de cette thèse montre l'intérêt d'avoir une constellation d'un minimum de 512 satellites pour atteindre des performances inégalées présentant d'excellentes périodes de revisite et résolution spatio-temporelle.

Title: Observing and quantifying Earth's radiation budget from UVSQ-SAT satellite.

Keywords: climate observation and monitoring; earth radiation budget; nanosatellite; remote sensors; attitude determination; deep learning method

Abstract: The objective of this thesis is to highlight a new vision of the observation from space of the components of the Earth's radiation budget (ERB). Climate is controlled by the amount of sunlight absorbed by Earth and the amount of infrared energy emitted to space. These quantities together with their difference define the ERB. Different techniques exist to quantify this variable such as satellite observation, in-situ measurements, reanalysis, or models. UVSQ-SAT project provides satellite-based observations of the ERB. UVSQ-SAT products include both solar-reflected and Earth-emitted radiation from the top of the atmosphere (TOA). The UVSQ-SAT CubeSat was launched in January 2021. This thesis deals with the determination of the Earth's outgoing shortwave and longwave radiation, based on two years of UVSQ-SAT observation. The main goal of this thesis is to determine accurately the in-orbit attitude determination of the satellite for obtaining the ERB. The methods to reconstruct flux maps and results from the mission are shown and explained. The results from this initial approach provide valuable insights that can inform the design and implementation of future satellite missions. Observation of the ERB at the TOA with a unique accuracy ($1.00\,\mathrm{Wm}^{-2}$), in near-real time ($3\,\mathrm{h}$) and at any point on the globe (few kms), requires the implementation of a mega-constellation of satellites. The results obtained during this thesis demonstrate the advantage to have a constellation of a minimum of 512 satellites for having unequaled performances presenting an excellent revisit, and spatiotemporal resolution.

Acknowledgments

Je remercie chaleureusement toutes les personnes qui ont été impliquées directement et indirectement dans la mise en oeuvre de cette thèse dédiée à la mesure du bilan radiatif de la Terre. Je tiens particulièrement à remercier mon Directeur de thèse Monsieur Mustapha Meftah. Il a insufflé son savoir-faire scientifique, sa passion et ses conseils dans la direction de mes travaux de recherche.

Je remercie Monsieur Antoine Mangin, Directeur scientifique de l'entreprise ACRI-ST. En tant que référent en entreprise dans le cadre de cette thèse en bourse CIFRE (Convention Industrielle de Formation par la Recherche), il a été en permanence à mon écoute. Il m'a apporté des conseils et des suggestions pour approfondir mes analyses.
Je remercie Monsieur Steven Dewitte et Madame Karina von Schuckmann d'avoir accepté d'être rapporteurs de cette thèse. Mes remerciements vont également à Monsieur Pierre-Richard Dahoo, Madame Nathalie Huret, Monsieur Benoit Meyssignac, Monsieur Thierry Dudok de Wit, Monsieur Didier Fussen et Monsieur Philippe Ciais d'avoir accepté d'être examinateurs et de participer à mon jury de thèse.
Je remercie Monsieur Thierry Corbard, astronome adjoint à l'Observatoire de la Côte d'Azur (Laboratoire LAGRANGE) et Madame Cécile Mallet, Professeure à l'Université de Versailles Saint-Quentin-en-Yvelines (LATMOS) de m'avoir suivi à travers les comités de suivi.

Je remercie Monsieur Thierry Fouchet Directeur de l'ED127 (Astronomie et Astrophysique d'Ile de France) pour sa bienveillance et sa disponibilité tout au long de cette thèse. Je remercie aussi Monsieur François Ravetta, Directeur du LATMOS.

Il m'a accueilli au sein de ce laboratoire de recherche dédié notamment à l'étude des processus physiques et chimiques de l'atmosphère terrestre.

Je tiens à remercier toute l'équipe de la mission UVSQ-SAT au sein du LATMOS pour m'avoir permis une intégration chaleureuse, pour leurs conseils et discussions, Christophe Dufour, Thomas Boutéraon, Emmanuel Bertran, André-Jean Vieau, Nicolas Caignard, Cannelle Clavier, Sadok Abbaki, Luc Damé, Philippe Keckhut, Slimane Bekki, Alain Sarkissian, Alain Hauchecorne, Pierre Gilbert, Laurent Lapauw, Jean-Luc Englert et je remercie Pierre Lepetit pour son aide précieuse en intelligence artificielle.

Je remercie de-même les stagiaires Angèle Minet et Hiro Claisse avec qui j'ai pu travailler pendant ma thèse.
Je remercie un grand nombre de doctorants, avec qui j'ai passé d'excellents moments. Je pense notamment à Antonin Zabukovec, Audrey Lecouffe, Marie Bouillon, Thomas Lesigne, Florent Tencé, Julia Maillard, Valentin Steichen, Lilian Loyer, Sebastien Verkercke, Nicolas Streel, Natalie Brett, Elisabeth Werner, Yuki Nakamura.

Mes remerciements vont également à Francois Leblanc, Jacques Lefrère, Cristelle Caileau-Fischbach, Pascal Genau, Yann Delcambre pour leurs conseils et discussions.

Je remercie mes professeurs du LFIDuras pour la qualité de leur enseignement. Je tiens aussi à remercier Madame Comte de m'avoir transmis sa passion et son enthousiasme pour la physique.

Un grand merci à toute ma famille, mes parents Mathilde et Jean-François qui m'ont soutenu et qui ont toujours cru en moi, Alicia et Honza (qui m'ont bien aidé tout au long de ma thèse avec ces relectures), Jana pour ces super séjours, Armand mon coach sportif et Luana pour ces super voyages. Mes grand parents Madeleine, François, Pascale, Philippe pour m'avoir continuellement soutenu. Jérome, Laurence, Pénélope, Angèle, Huguette pour avoir vécu les premiers mois de thèse en super colloc. Eric, Fatna et Sandra pour vous être bien occupés de moi.

Je remercie tous mes amis qui ont partagé ces années avec moi, Kev, Michael, Jakub, Loïk et Martin (qui a passé beaucoup de temps sur la relecture merci encore !). Mais aussi Thomas, Adèle, Flavien, Gaspard, William, Alexandre, Michael W., Jean, Jean Pierre, Mathieu, Servane, Bjorn (thank you very much again for your corrections) et Léa, Rija, Julie, Bastien. Je remercie aussi le groupe d'amis de Boulogne.

Je remercie la famille Fouilloux Renevier Montagnon notamment Jean-Michel, Pascale, Hugo, Clémentine, France, Jean-Jacques, Chloé, Bernard pour leur soutien ainsi que tous ces moments passés. Et je remercie de tout mon coeur bien sûr Julie Fouilloux de m'avoir accompagné, conseillé et soutenu toutes ces années y compris pendant cette thèse, merci pour ces superbes années passées à tes cotés et celles à venir !

Les travaux présentés dans cette thèse ont fait l'objet d'une Convention Industrielle de Formation par la Recherche (CIFRE) gérée par l'Association Nationale de la Recherche Technique (ANRT), entre la société ACRI-ST et l'Université de Versailles Saint-Quentin-en-Yvelines (UVSQ).

Contents

General Introduction

Climate change is a major concern of the 21^{st} century. Global warming poses a threat to humanity and its consequences can be seen all around the world. To understand and address this phenomenon at a regional and global scale, it is important to quantify the warming through various variables. One variable that accounts for global warming is the terrestrial radiation balance. This variable quantifies the energy exchanges at the top of the atmosphere and is directly linked to the temperature on Earth. Estimating this variable is necessary for the scientific community to inform policymakers on climate change, its implications, risks, and to propose adaptation and mitigation options.

Satellite observations are one way to measure the terrestrial radiation balance. Many missions have been developed for this purpose, and the rise of the newspace industry, particularly in France, has also led to new technologies and approaches to spacecraft design. These include the use of CubeSats which concept was suggested by Jordi Puig-Suari of California Polytechnic State University and Bob Twiggs of Stanford University in the late 1990s [Puig-Suari et al., 2000]. CubeSats are a low-cost way of displaying intriguing new technology, and they also promote system miniaturization and urge a fresh approach to spacecraft design.

These novel technologies are jointly developed in a rapidly evolving context with important changes in terms of objectives, actors involved, and training. This has opened up new opportunities for companies and institutions but also introduces challenges. To fully take advantage of these opportunities and address the challenges, it is important to understand the current state of the industry and its potential for addressing climate change. Those changes revolutionize the industry and transform the conquest of space.

In this manuscript, we deal with the terrestrial radiation balance and how a Cube-

Sat can measure the components of that variable at the top of the atmosphere, focusing especially on the attitude determination of this satellite.

The first chapter presents an introduction to the main context of the observation and the importance of measuring the essential climate variables and specifically the Earth's energy imbalance. Specifications are defined to measure the variables of interest. We compare different methods implemented to monitor the radiative budget and describe innovative methods that could be employed for this study. Different datasets from reanalysis or measurements are studied to highlight the advantages and drawbacks of the measurement techniques.

The second chapter details the need for a constellation for Earth observation and how the configuration should be defined. Different architectures are studied to stress major parameters such as the field of view and the number of satellites. Those parameters are crucial to reach the expected spatiotemporal resolution to fit specifications. We show how a megaconstellation of satellites appears to be required to reach the expected resolutions.

The third chapter deals with the UVSQ-SAT mission and the attitude determination challenge. The mission is presented along with instrumental equations and the need for determining the satellite's attitude to compute the Earth's radiative components. An attitude determination method is described and validated on-ground based on a neural network. Two deterministic methods are described as they could help compute the in-orbit satellite's attitude. The neural network-based method is applied to the data in-orbit using the other methods as reference.

The last chapter highlights the UVSQ-SAT outcomes and how data were processed based on the knowledge of the satellite's attitude. The flux is computed in this chapter. UVSQ-SAT products are presented as they include solar-reflected and Earth-emitted radiation at the top of the atmosphere. Maps of the Earth's radiative components appear along with monthly average analysis compared to reference datasets.

In the conclusion, we discuss the approach of measuring and understanding global warming using satellite measurements and the development of a constellation of satellites with high spatiotemporal resolution. We address the perspectives on the INSPIRE-SAT 7 mission where the mission aims to build on the technologies and lessons learned from the UVSQ-SAT mission, with a focus on improving technologies for measuring the Earth's radiation budget.

Chapter 1

Importance of The Earth Energy Imbalance Measurements

In this chapter, we first see how the climate is changing quickly and that it is a threat to humankind. Secondly, we expose quantitative indicators called essential climate variables to measure climate evolution. Then we deal with a state of the art of computation of the Earth's energy imbalance. In the third place, we discuss different quantities of interest considering applications with current datasets. In the fourth part, we present novel techniques to measure this variable from space. Finally, we conclude that section and expose the advantages of measuring such quantities at the top of the atmosphere.

1.1 Introduction and Scientific Background

Since 1880, the global annual temperature has risen at an average rate of 0.08 °C every decade, and by more than double that pace (+0.18 °C per decade) since 1981 (Figure 1.1).

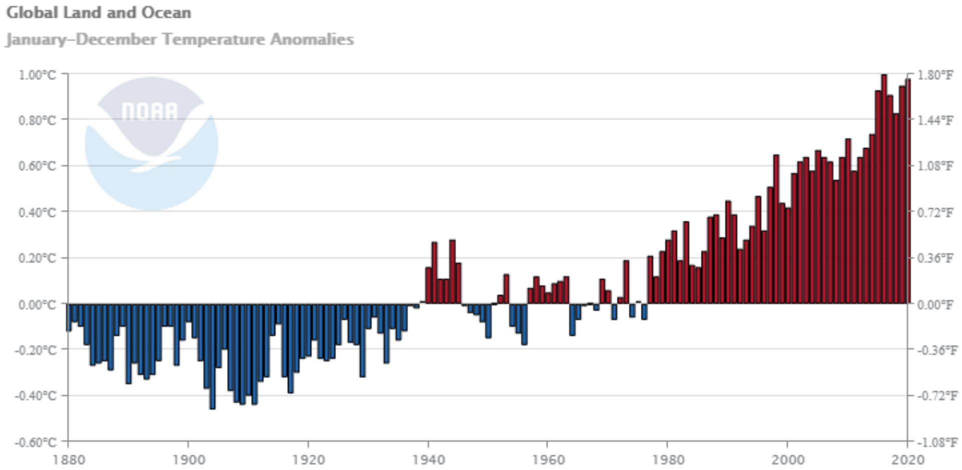

Figure 1.1: Global land and ocean surface average temperature anomaly [NOAA 2021].

The Intergovernmental Panel on Climate Change (IPCC) was created in 1988 to give periodical scientific evaluations of climate change, its implications, and potential future risks to policymakers. It also aims to propose adaptation and mitigation solutions. The IPCC published assessment reports in 1990, 1995, 2001, 2007, 2014 and its sixth assessment in 2022. According to the IPCC's 2022 report [Rama et al., 2022], global warming will surpass the 1.5 °C barrier above pre-industrial levels within the next two decades, and only the most extreme reductions in carbon emissions will prevent environmental disaster. It is important to know that the Earth has not seen a temperature increase of more than 2.5 °C in such a short period of time in over 3 million years. This phenomenon is critical due to its speed of evolution and great magnitude. The scientific consensus is that human activity is the primary cause why the Earth's temperature has been increasing at an unprecedented rate [Masson-Delmotte et al., 2021, Cook et al., 2016]. The oceans have been absorbing much of this excess heat. Recent studies show that they have been warming at an alarming rate [Cheng et al., 2019b]. There are several consequences of this warming which include sea-level rise, ocean acidification, and more intense and frequent extreme weather events [on Climate Change, 2007].

The IPCC has created five scenarios, called "shared socioeconomic pathways", in which it stresses the repercussions of taking drastic actions now, in comparison to what would happen if no action was taken. The worst high-carbon scenario would result in an increase in global temperature of more than 4 °C by the end of the century. This change would cause environmental hazards like drought, wildfires, tropical storms, and other extreme weather events.

To counter this warming, several events took place. In 1987, an international agreement, the Montreal Protocol was signed to ensure the protection of the ozone layer by phasing out ozone-depleting substances on a global scale. In 1992, the United Nations Framework Convention on Climate Change (UNFCCC) established an international environmental treaty to combat "dangerous human interference with the climate system". Since then, a Conference of the Parties (COP) is scheduled every year to verify the proper implementation of the objectives of the international convention adopted. In 2015, the COP met in Paris, where 184 nations ratified the eponymous Paris agreements with the objective to keep the global temperature increase below 2 °C by 2100 and aiming to limit it to 1.5 °C.

Climate change appears to be a menace to mankind. To understand the evolution of Earth temperatures and climate variability, an indicator needs to be computed to quantify this development. von Schuckmann et al. [2020] describes the perfect indicator as the finest single statistic we have for assessing the effect of actions of mitigating climate change. It is, therefore, necessary to study the Earth's Energy Imbalance (EEI) and to quantify each of the input/output fluxes of the Earth system that we must know to compute the EEI. For example, a higher resolution of a few kilometers at a local scale allows us to explore diurnal cycles that can be decisive for the observation of clouds, and aerosols formed from photo-chemistry. Better resolution entails better monitoring of variables such as the albedo or geomorphologic flows. This would improve the atmospheric models, by measuring radiative fluxes, for different surfaces and conditions. It allows us to observe and understand the impact it has on the fluxes at the top of the atmosphere (TOA). The absolute measurement of EEI and its evolution over time is fundamental to climate change and represents a critical quantity. It defines the current state and prospects for further global warming. The variable is highly impacted by greenhouse gases and aerosols that come from human activities [Hartmann et al., 2013]. As we will see later in the manuscript, combining various types of measurements can improve quantification, but this requires globally coordinated efforts. Developing and combining these factors offers a foundation for understanding and anticipating climate change at an unprecedented level, as explained in Schuckmann et al. [2016]. The measurement of the EEI was pushed by Hansen (and Lindzen) [Hansen et al., 1981, 1997] in order to constrain the two variables the diffusion coefficient at the base of the mixing layer and the climate feedback parameter which will be detailed later with the use of ARGO floats. Moreover, one reason for measuring the EEI is societal, as the EEI is an immediate variable that characterizes warming (an increase in EEI is visible in a shorter time than an increase in temperature). It is a way to know the impact of actions and to predict the evolution of climate.

1.2 Historical Context and Difficulty of Measurement

Climate change is a crucial issue because of its abrupt and rapid change. In order to understand and identify the causes and consequences of every phenomenon related to this change, it is important to be able to quantify this warming. This quantification must give information on a local scale in order to be able to adapt and act. One way to quantify these climate changes is through the study of certain parameters called essential climate variables. Understanding climate system phenomena and their distribution, as emphasized in [Trenberth and Fasullo, 2010], is crucial for determining causes and predicting future occurrences. It is essential knowledge for living with and preparing for adaptation to climate change.

1.2.1 Essential Climate Variables

The Global Climate Observing System (GCOS) is co-sponsored by the World Meteorological Organization (WMO), the Intergovernmental Oceanographic Commission of the United Nations Educational, Scientific and Cultural Organization (IOC-UNESCO), the United Nations Environment Programme (UN Environment), and the International Science Council (ISC). The group regularly evaluates the status of global climate observations of the atmosphere, the land, and the ocean and provides recommendations for how to improve these observations. Its objective is to ensure that comprehensive information on the global climate system is provided to users such as national and international organizations, institutions, and agencies. GCOS specifies 54 variables as Essential Climate Variables (ECVs) defined in Table 1.1. Each ECV is either a physical, chemical or biological parameter, or a group of related variables that are critical to the characterization of Earth's climate. Datasets describing these variables are useful for understanding and predicting the evolution of climate, guiding mitigation and adaptation measures, assessing risks, and enabling the attribution of climate events to their underlying causes.

Copernicus is the European Union's Earth observation program coordinated and managed for the European Commission by the European Union Agency for the Space Programme in partnership with the European Space Agency (ESA), and the EU Member States. Copernicus is supported by a constellation of specific satellites (the Sentinel satellites) as well as contributing missions (public and commercial satellites). Since the launch of Sentinel-1A in 2014, the European Union has begun the process of launching a constellation of over 20 more satellites by 2030. Copernicus is also tasked with gathering data from sensors on the ground, in the sea, or in the air [Cop, 2022].

The Earth's radiation budget is the metric that quantifies the energy accumulated in the atmosphere. It indicates climate change trends. This radiation budget represents the balance between incoming and outgoing radiation based on the physics principle of conservation of energy. The Earth's radiation budget is computed based on the downward and upward flux from the Earth's atmosphere. It results from the difference between the incoming solar radiation and the outgoing radiation defined as Outgoing Shortwave Radiation (OSR) radiation and Outgoing Longwave Radiation (OLR).

Atmosphere	**Land**	**Ocean**
Precipitation	Groundwater	Ocean surface heat flux
Surface pressure	Lakes	Sea ice
Surface radiation budget	River discharge	Sea level
Surface temperature	Glaciers	Sea state
Surface water vapour	Ice sheets and ice shelves	Sea surface currents
Upper-air wind speed and direction	Permafrost	Sea surface salinity
Earth radiation budget	Snow	Sea surface stress
Lightning	Above-ground biomass	Sea surface temperature
Upper-air temperature	Albedo	Subsurface currents
Aerosols	Evaporation from land	Subsurface salinity
Lightning	Fire	Subsurface temperature
Upper-air temperature	Fraction of absorbed photosynthetically active radiation	Inorganic carbon
Carbon dioxide, methane and other greenhouse gases	Land cover	Nitrous oxide
Clouds	Land surface temperature	Nutrients
Ozone	Leaf area index	Ocean colour
Precursors for aerosols and ozone	Soil carbon	Oxygen
	Soil moisture	Transient tracers
	Anthropogenic greenhouse gas fluxes	Marine habitats
	Anthropogenic water use	Plankton

Table 1.1: 54 Essential climate variables grouped by domain of observation [CEOS and member agencies, 2022].

The units of measurement of incoming and outgoing radiation are watts per square meter (Wm^{-2}). Requirements for each component are listed in terms of frequency, resolution, uncertainty, and stability in Table 1.2 to resolve spatio-temporal fluctuations at high resolutions. This ECV can be measured at the TOA by quantifying the input and output flux outside the Earth system. Although there are various missions to measure this budget at TOA, there is a significant need to improve observations for expected resolutions, as discussed in [Liang et al., 2019]. Nevertheless, in case there are no estimates of the fluxes, they can also be estimated from in situ data in the system. Indeed, the ocean absorbs the great part of extra energy (93%, [Trenberth et al., 2016]), with considerably lesser quantities going to land/atmosphere (3%), and ice cover heating (4%). Since more than 90% of the energy accumulated on Earth belongs in the ocean [Schuckmann et al., 2016], the Ocean Heat Content (OHC) seems to represent a good proxy of the EEI. The ocean, with a large volume and higher thermal inertia than the atmosphere or land, acts as a buffer and stores the energy accumulated as heat. Measurements in the ocean at both regional and global trends show sustained and considerable warming of the oceans since the late 1950s. Natural variability and variations in ocean circulation play major roles locally, but the most significant shifts are due to human-caused changes in atmospheric composition. As the seas warm, the water expands, and the sea level rises, which represents a concern for coastal areas [Cheng et al., 2022]. As a result, having extensive temperature and heat content data throughout our vast seas is critical to study the growth in Earth system energy content through time. Measuring ocean heat content contributes to a thorough understanding of the climate system by offering important insights into the Earth's energy imbalance.

Product	**Frequency**	**Resolution**	**Uncertainty**	**Stability**
TOA ERB longwave	Monthly (resolving diurnal cycle)	100 km/NA	1 Wm^{-2}	0.2 Wm^{-2}/decade
TOA ERB shortwave (reflected)	Monthly (resolving diurnal cycle)	100 km/NA	1.0 Wm^{-2}	0.3 Wm^{-2}/decade
Total solar irradiance	Daily	NA/NA	0.04%	0.01%/decade

Table 1.2: Current Earth Radiation Budget (ERB) requirements according to the GCOS 2016 Implementation Plan.

As analyzed in [Meyssignac, 2021], utilizing accurate estimations of ocean heat content is the solution to two observational challenges that make it difficult to determine climate evolution. To go further and detail this problem we have to present two variables having a direct role in this determination. They also play a significant role in understanding the impacts of different phenomena such as aerosol injections. These two parameters are λ and κ. λ is the climate feedback parameter and, κ is the diffusion coefficient at the base of the mixing layer. The sensitivity λ characterizes the amplitude, the level of heating while κ characterizes the speed at which we will reach this equilibrium.

The variables λ and κ are detailed in Equations 1.1 and 1.2 as explained by [Meyssignac, 2021].

$$\lambda = \left(1 - \sum_n f_n\right) P = \sum_n \lambda_n \delta T \tag{1.1}$$

where λ_n is the climate feedback parameter associated with the environment parameter n. f_n is the climate feedback on the parameter F_n (a measure of water vapor in the atmosphere, ice cover, cloud cover etc. ...) induced by the increase δT generated by the black body response of the climate system. $P\delta T$ is the black body radiative response of the climate system.

$$\kappa = \frac{\Delta OHU}{\Delta T_s} \tag{1.2}$$

where ΔOHU is the global-mean ocean heat uptake change and ΔT_s the global-mean surface temperature change as detailed in [Liu et al., 2023].

Those parameters describe how the climate system reacts to variations in radiative forcing. Furthermore, it is crucial to project future climate changes and assess the effects of external forcing factors by making accurate estimates of λ.

The first challenge is that without the measurement of the EEI, we only had the surface temperature and we could not separate the two equations linking κ and λ (ambiguity of the determination of these variables). According to [Lindzen, 1994, Lindzen and Giannitsis, 1998], the characteristic response time of surface temperature is not determined solely by λ and the heat capacity of the mixed layer of the ocean but also from κ which is very poorly known. The deep ocean and the oceanic mixing layer play a crucial role in the temporal response of surface temperature. To estimate λ accurately, an additional independent observation is required. Knowing the EEI and the temperature allows us to separate these two equations and determine these two parameters. Measurements of ocean heat content are essential for understanding the climate feedback parameter and κ.

The second challenge is the uncertainty in historical estimates of radiative forcing, specifically from aerosols, which offsets some of the radiative forcings from CO_2. κ and λ cannot be properly estimated. To overcome those challenges [Hansen et al., 2005, 2011] proposes to make use of the accurate estimation of ocean heat content to provide a solution to the problems of uncertainty in estimating historical radiative forcing and vertical heat diffusion in the ocean over the historical period. Actually, with classical measurements, there are several limitations of the radiation balance measurement. There is a linear approximation of the radiative response that seems inconsistent [Andrews and Webb, 2018]. Moreover, there is an insufficient consideration of the geographical structure (temperature and heat penetration in the ocean) [Caballero and Huber, 2013]. Finally, the assumption of a reference equilibrium state is invalid (the equilibrium equation does not correspond to the real state of the Earth). However, by improving the measurement of heat content in the oceans, it becomes possible to overcome these limitations and obtain a more accurate assessment of the Earth's radiation budget, considering the geographical distribution of heat and providing a complete perspective on the Earth's energy evolution.

1.2.2 Earth Radiation Budget

The Earth radiation budget is detailed in this section. The EEI results from the imbalance of several radiative flux. It is important to detail the model we consider for the distribution of the flux and how they are represented. The EEI will be detailed along with the incoming and outgoing radiation.

Different Fluxes

There are three main components to the Earth's radiation budget. They are known as Incoming Solar Radiation (ISR), reflected solar radiation, and the outgoing terrestrial radiation.

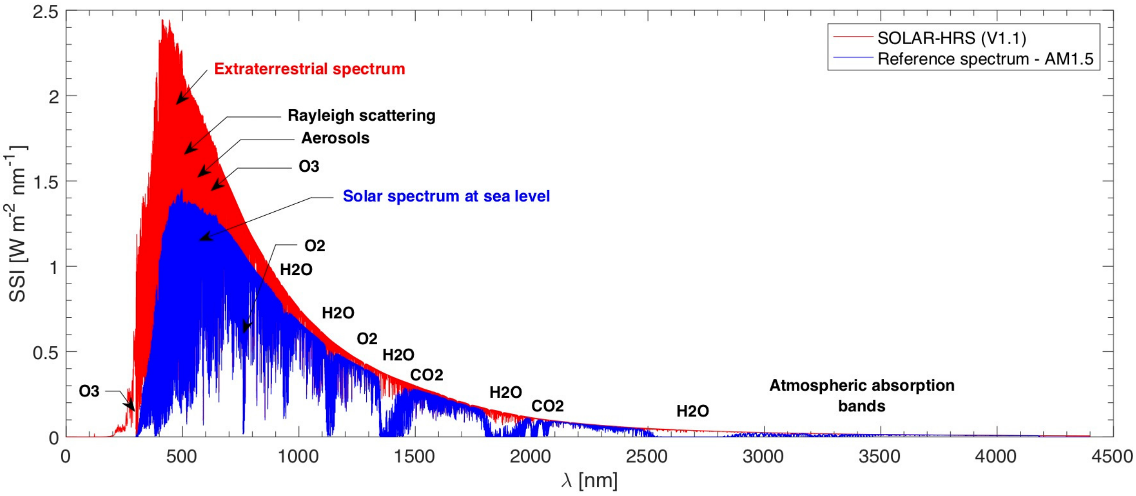

Figure 1.2: SOLAR-HRS spectrum (v1.1). Meftah M. et al., 2022.

The total solar irradiance (TSI) is a measure of solar power per unit area incident on the Earth's upper atmosphere at all wavelengths. It is calculated by taking measurements perpendicular to the Sun's rays. The solar constant is a standard measure of mean TSI at one astronomical unit distance (AU). The solar radiation spectrum is represented in Figure 1.2. The ISR on Earth is defined as (Equation 1.3):

$$ISR = \frac{TSI}{4d^2_{\text{Sun/Earth}}}, \tag{1.3}$$

where $d_{\text{Sun/Earth}}$ is the Sun-Earth distance in AU.
The reflected solar radiation is the shortwave radiation from the Sun that is reflected by the atmosphere or the surface of the Earth, and is defined as follows (Equation 1.4):

$$OSR = \frac{TSI}{4d^2_{\text{Sun/Earth}}} \times \alpha_{\text{TOA}}, \tag{1.4}$$

where α_{TOA} is the planetary albedo. It is the percentage of solar energy reflected back to space. Its value ranges from 0 to 1. The greater the albedo of a surface, the more reflecting it is. Clouds, snow, ice surfaces, and aerosols are the main contributors to the Earth's albedo. The albedo is defined as in Equation 1.5:

$$\alpha = \frac{\text{reflected solar}}{\text{incident solar}} \tag{1.5}$$

Different values of albedo are listed in Table 1.3.

Surface	Albedo (α)
Trees	0.15 - 0.18
Asphalt	0.05 - 0.2
Concrete	0.25 - 0.7
Grass	0.25 - 0.3
Ice	0.3 - 0.5
Oceans	0.05 - 0.1
Fresh Snow	0.81 - 0.88

Table 1.3: Examples of albedo values for different surfaces [Kotak et al., 2015].

The OLR, also called thermal radiation, is emitted by the Earth and its atmosphere. Stefan's or Stefan-Boltzmann's law (named after the physicists Jožef Stefan and Ludwig Boltzmann) defines the relationship between thermal radiation and the temperature of an object considered as a black body. It establishes that the energetic emittance of a body in watts per square meter (total power radiated per unit area in the free half-space of a black body) is related to its temperature T expressed in Kelvin by the Equation 1.6 (where $\sigma = 5.67 \times 10^{-8}\,\mathrm{Wm^{-2}K^{-4}}$ is the Stefan-Boltzmann's constant):

$$M = \sigma T^4 \tag{1.6}$$

The Earth's black body temperature is 250 K, although the surface temperature is around 288 K. The difference (38 K) is the amount by which the planet is warmed by the natural greenhouse effect.
The Earth's outgoing radiation spectrum appears in Figure 1.3.

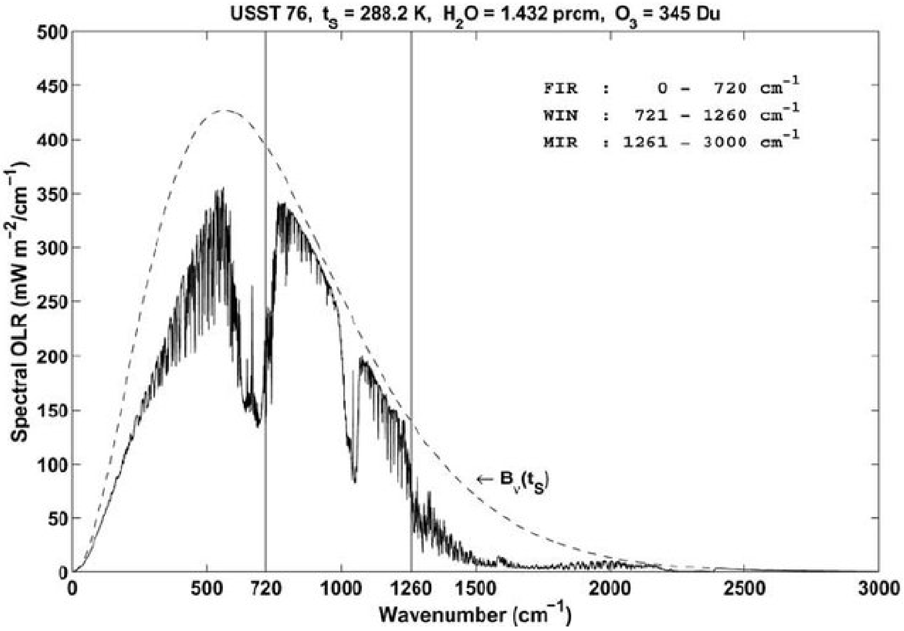

Figure 1.3: Earth outgoing radiation spectrum [Miskolczi and Mlynczak, 2022].

It is the goal of the FORUM mission (Far-infrared Outgoing Radiation Understanding and Monitoring) that will measure radiation emitted by Earth into space. This mission will be presented later on.

Greenhouse Effect

The greenhouse effect is described as the phenomenon where the atmosphere blocks part of the outbound radiation. First, the ISR reaches the Earth and its atmosphere. Part of that flux is reflected, while some are absorbed. The energy is then accumulated on Earth. The surface getting warmer transmits its energy as heat through convection from the surface to the atmosphere and as far infrared radiation. The greenhouse effect is only caused by this radiation, which is absorbed in part by greenhouse gases and hence contributes to atmospheric warming. An increase in gases like CO2 causes the atmosphere to become more opaque to infrared radiation Hansen et al. [2011], Ledley et al. [1999]. The Earth's climate system is no longer in equilibrium as a result of anthropogenic amplification of the atmospheric greenhouse effect in recent decades, with considerable warming occurring in the lower atmosphere and at the surface.

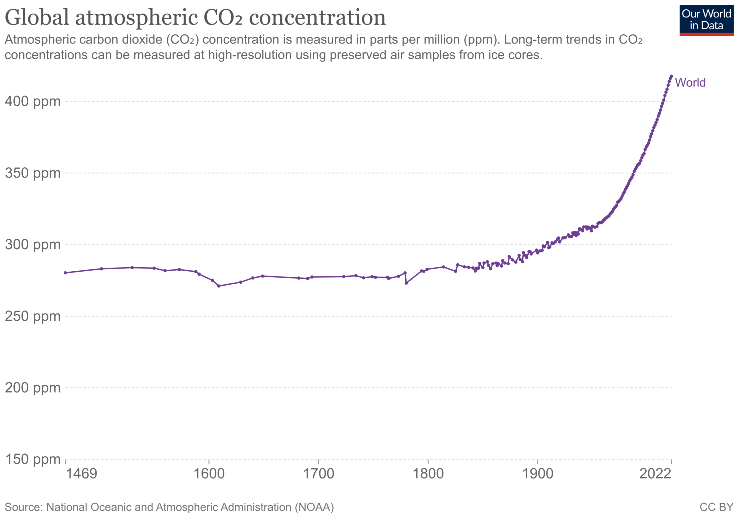

Figure 1.4: Global atmospheric CO_2 concentration [NOAA, 2022].

Those atmospheric gaseous components known as greenhouse gases are mainly water vapor, carbon dioxide (CO_2 in Figure 1.4), methane (CH_4), nitrous oxide (N_2O), and ozone (O_3). Figure 1.4 describes the sharp increase in CO_2 concentration. This is mainly due to anthropogenic actions, increasing atmospheric warming. Global warming, ocean acidification, desertification, and shifting weather patterns might all be made worse by the existing level of industrial pollution and the indiscriminate production of greenhouse gases into the atmosphere [Yoro and Daramola, 2020]. Since 1950, human-caused global CO2 emissions have grown by more than 400% [Maximillian et al., 2019].

Earth Energy Imbalance

From the TOA, the EEI can be explained as in Figure 1.5. The measurement of the radiation balance at the TOA can be decomposed according to the different incoming and outgoing fluxes that were mentioned previously. Measuring the flux from outside the system allows us to make abstractions of the inner processes. The ISR (Φ_{in}) reaches the Earth, approximately one-third of incident flux is absorbed or scattered by the Earth's atmosphere, with the remaining one-sixth scattered back into space from the Earth's surface. The part of radiation reflected by clouds, aerosols, and the atmosphere is noted $\Phi_{\text{out/SW}}$ and is given on the figure with a planetary albedo averaging 0.3. As a consequence, the Earth and the atmosphere emit longwave radiation to space ($\Phi_{\text{out/LW}}$). The energy is emitted as latent heat due to phase change in the atmosphere, as well as sensible heat due to a change of temperature of a substance with no phase change.

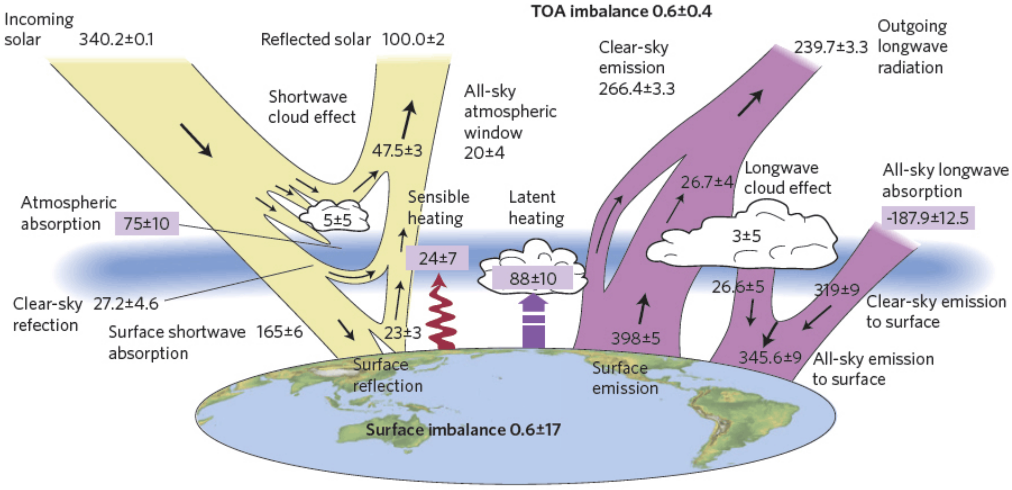

Figure 1.5: Earth Radiation Budget [Stephens et al., 2012].

In equilibrium, the absorbed energy is emitted at longer wavelengths that correspond to the temperature of the source. Because the lower atmosphere is opaque to these longer wavelengths, the radiation directly sent to space originates at higher altitudes. The gas is forced to the 250 K temperatures, required to establish radiative balance by slightly higher surface temperatures. According to the Figure 1.5 the EEI can be computed as in Equation 1.7:

$$EEI = \Phi_{\text{in}} - \Phi_{\text{out}} = \Phi_{\text{in}} - (\Phi_{\text{out/LW}} + \Phi_{\text{out/SW}}) = 340.2 - (239.7 + 100) = 0.5\,\text{Wm}^{-2} \tag{1.7}$$

At equilibrium, the amount of energy from the Sun arriving on Earth is equal to the amount returning from Earth to space. In the case where this value is positive (Equation 1.7), there is an accumulation of energy in the system, and heating is observed. Energy is accumulating in the climate system due to the EEI at the top of the atmosphere [Marti et al., 2022]. Since EEI is a globally integrated variable, measuring it is challenging since its magnitude and changes are minor

([Schuckmann et al., 2016, Loeb et al., 2018b]) in comparison to the quantity of energy entering and leaving the climate system.

1.2.3 Current and Future Missions to Measure the Earth Energy Imbalance at the TOA

Dines supplied the first such budget in 1917 [Dines, 1917]. Kiehl and Trenberth provided the first moderately complete balance of the Earth's energy exchanges and atmosphere in 1997 [Kiehl and Trenberth, 1997]. Stephens et al. improved the Earth's energy budget figure in 2012. Between 2000 and 2010, the EEI was calculated at the TOA to be $0.60 \pm 0.40\,\mathrm{Wm^{-2}}$ [Stephens et al., 2012]. According to Von Schuckmann et al., the EEI is now expected to be $0.87 \pm 0.12\,\mathrm{Wm^{-2}}$ for the 2010-2018 period, compared to $0.47 \pm 0.10\,\mathrm{Wm^{-2}}$ for the 1971-2018 period. Different missions aimed and will still aim to monitor the EEI. Here are examples of such missions.

- Earth Radiation Budget Experiment (ERBE), the NASA Earth Radiation Budget Satellite (ERBS), and two NOAA satellites, implemented to provide Earth Radiation Budget (ERB) monthly measurements, seasonal energy exchanges, and daily imbalance at a local scale [Barkstrom, 1989].

- Scanner for Radiation Budget (ScaRaB), is on-board the Megha-Tropiques satellite to study water cycle and energy exchanges. Payloads are MADRAS, SAPHIR, ScaRaB, and ROSA. The ScaRaB instrument is a broad-band radiometer for radiative budget measurements. Launched in October 2011 to an 866 km orbit and 20° inclination, it achieved 14 orbits per day [Roca et al., 2015] studying Earth between 23° North and 23° South with a Field Of View (FOV) of 40 km at nadir. Longwave (LW) radiation and shortwave (SW) radiations were measured with an accuracy of 1% for the LW and 2% for the SW. It was compared to CERES FM1 instruments as it is reported in [Viollier et al., 2009], and for the LW, a bias of 0.31%, and a standard deviation of 2.75% were found, as for the SW a bias of 3.86% and a standard deviation of 9.80%.

- Clouds and the Earth's Radiant Energy System (CERES) targets to monitor SW and LW radiation. The CERES instruments are located on the Terra, Aqua, Suomi National Polar-Orbiting Partnership (SNPP), and NOAA-20 satellites and are narrow FOV scanning radiometers with at nadir 10 km (TRMM), 20 km (Terra, Aqua), and 24 km (S-NPP, NOAA-20). The Terra is in a descending sun-synchronous orbit with an ECT of 10:30 local time, while Aqua, SNPP, and NOAA-20 are in ascending sun-synchronous orbits with a 13:30 local time equator-crossing time [Loeb et al., 2018a]. The knowledge of local time is important as it properly characterizes the observation location. Additionally, it uses geostationary imagers to obtain hourly diurnal information between 60° South and 60° North [Loeb et al., 2018c, Wielicki et al., 1996]. The instruments cover the whole globe with a 20 km FOV for Terra-Aqua drawing a monthly map of the radiations. SW and LW Radiation have a $2.5\,\mathrm{Wm}^{-2}$ estimated accuracy for regional monthly TOA flux ($3.5\,\mathrm{Wm}^{-2}$ for net) (CERES Energy Balanced and Filled (EBAF) Ed4.1, Data Quality Summary (March 3, 2020)).

- Geostationary Earth Radiation Budget (GERB), [Harries et al., 2005, Parfitt et al., 2016], implementing 4 instruments located on EUMETSAT's Meteosat satellites. The instruments were launched in 2002, 2005, 2012, and 2015 targeting the Indian Ocean and Africa from geostationary orbits. The instruments measure radiations over the total spectrum and over the SW part. It allows us to get data every 15 min of $9 \times 9\,\mathrm{km}^2$ for the example of the High Resolution dataset, with 44.6 km (North-South) × 39.3 km (East-West) resolution at nadir for the regular dataset.

- RAVAN is a 3U CubeSat that aimed to measure EEI using vertically aligned carbon nanotubes (VACNTS) to measure the TSI and the outgoing terrestrial radiation. It is also designed with a pair of gallium black bodies to monitor the degradation of the instruments [Swartz et al., 2019].

- The broadband Bolometric Oscillation Sensor (BOS) operated as a part of the payload of PICARD between June 2010 and March 2014 [Zhu et al., 2015]. The sensor was not originally intended for this measure. By using adapted instrumental functions, observations with a wide field of view can be obtained.

- The SIMBA 3U (Sun-earth IMBAlance) CubeSat was launched as a passenger payload on 3 September 2020 [Dewitte et al., 2015]. The objective of the mission is to measure the Sun-Earth radiation imbalance.

- EarthCare is a mission developed by ESA and JAXA, one of the objectives is to obtain profiles of atmospheric heating and cooling through the combination of the retrieved aerosol and cloud properties. The instrument is a broadband radiometer that will be launched in 2024 to a 393 km altitude orbit with a 14:00 local ECT (descending node). It will achieve 140 orbits in 9 days. It is composed of three fixed single telescopes for forward, nadir, and backward measuring SW and total radiation observing 10 km FOV at nadir for the absolute accuracy of $1.5\,\mathrm{Wm^{-2}sr^{-1}}$ in the LW and $2.5\,\mathrm{Wm^{-2}sr^{-1}}$ in the SW [Illingworth et al., 2015].

- Libera is a NASA mission developed in the LASP to measure solar radiation, infrared radiation, and total radiation leaving Earth. It takes part in the Earth Venture Continuity [Pilewskie and Hakuba, 2020].

- FORUM stands for Far-infrared Outgoing Radiation Understanding and Monitoring and is the 9^{th} Earth Explorer mission to launch in 2026 developed by Imperial College London. It aims to obtain the full spectrum for outgoing radiation as half of the outgoing LW energy is far-infrared and has not been measured [Palchetti et al., 2020].

Different estimates of the EEI from TOA measurements and measurements in the ocean are listed Table 1.4 and summarized in Figure 1.6. The OHC can be measured in different ways. The first approach would be to compute the OHC based on in-situ temperatures-salinity profiles thanks to the Argo floats [von Schuckmann et al., 2020]. Another approach would be to combine the previous approach with sea-level measurements from space observation [Stammer et al., 2016]. Moreover, radiation satellites' measurements can be of use to compute surface net flux [L'Ecuyer et al., 2015].

EEI ($\mathrm{Wm^{-2}}$)	**Period**	**Method**	**Reference**
0.83±0.11	1991 to 2016	Atmospheric oxygen (O2) and carbon dioxide (CO2) measurements	Resplandy et al. (2018)
0.61±0.08	1993 to 2018	Global OHC estimation (0-2000 m)	Ishii et al. (2017)
0.71±0.11	2006 to 2015	Ocean heat uptake at 0.68± 0.10 $\mathrm{Wm^{-2}}$ + other forms of heat uptake over	Johnson et al. (2016)
0.4 to 0.6	2006 to 2013	Argo OHC observations (0-2000 m)	Roemmich et al. (2015)
0.54±0.02	2005 to 2017	OHC observations (0-2000 m)	Cheng et al. (2019a)
0.1 to 0.9	2006 to 2012	OHC rates	Schuckmann et al. (2016)
0.50±0.43	07/2005 to 06/2010	CERES TOA net radiation adjusted ocean measurements (0-1800 m)	Loeb et al. (2012)
0.71±0.10	2005 to 2015	0.61 ± 0.09 $\mathrm{Wm^{-2}}$ for the ocean (0–1800 m); 0.07 ± 0.04 $\mathrm{Wm^{-2}}$ for deeper ocean; and 0.03 ± 0.01 $\mathrm{Wm^{-2}}$ for melting ice, warming land, and an increasingly warmer and moister atmosphere	Johnson et al. (2016)
0.9±0.3	2005 to 2014	CERES product TOA, modeling and OHC data	Trenberth et al. (2016)
0.74±0.22	2002 to 2016	Space geodetic estimation of the OHC changes	Marti et al. (2022)
0.67±0.13	2000 to 2019	ARANN OHC reconstruction	Bagnell and DeVries (2021)
0.50±0.47	2005 to 2019	CERES EBAF Ed4.1 and OHC in situ data	Loeb et al. (2021)

Table 1.4: EEI computed for different periods, from different sources.

The proportion of energy entering the ocean is around 0.9. The EEI can then be calculated by dividing the global ocean heat uptake which is the temporal derivative of the global ocean heat content, by the proportion of energy entering the ocean [von Schuckmann et al., 2020]. Finally, [Marti et al., 2022] described the MOHeaCAN product from "altimetry-gravimetry", a new space geodetic approach to estimate OHC changes from steric level changes based on satellite altimetry and satellite gravimetry measurements.

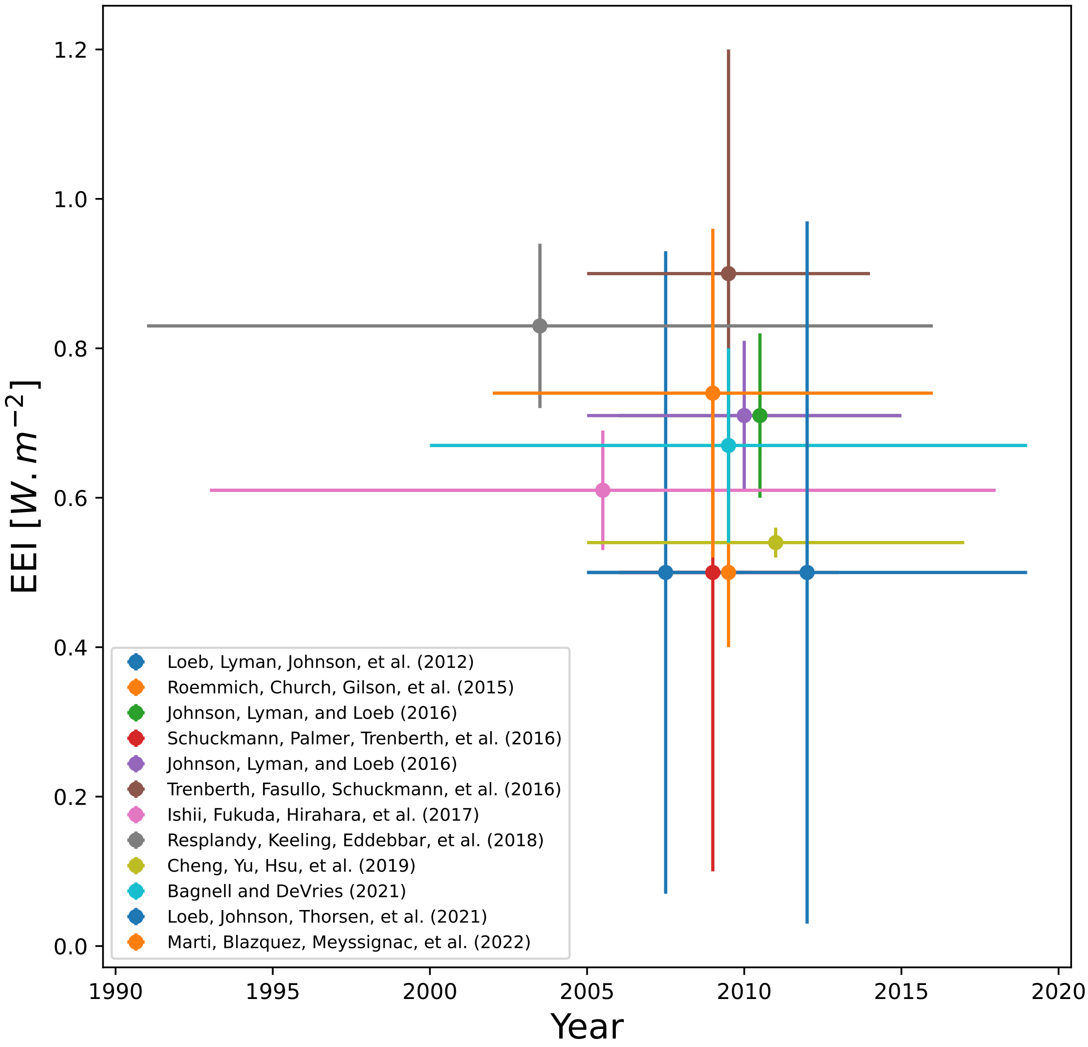

Figure 1.6: EEI computed for different periods, from different sources.

It is based on the physical principle for which the total sea level change results from an increase in ocean mass and in ocean steric sea change. The ocean steric sea level change is equal to the sum of the ocean thermal expansion and the ocean halosteric change. The halosteric change refers to a change in the salinity whereas the thermal expansion is due to variations of temperature of the ocean. Hence, considering the halosteric effect negligible [Gregory and Lowe, 2000], the thermosteric sea level change is equal to the difference between the global mean sea level change and the global mean ocean mass. As it can be seen in Table 1.4, most of the EEI measurements are made from data in the oceans due to the desire to measure this quantity over the long term. Nevertheless, these can be combined with measurements at the TOA. [Smith et al., 2015] examined the relationship between ocean heat content and net incoming radiation at the top of the atmosphere from satellite observations and climate models over the period 1960 to 2014. The study discovered a significant correlation between the two variables from 1960 to 1999. However, inconsistencies were observed between ocean reanalyses of ocean heat content in the early 2000s and observation-based estimates of net incoming radiation. It is important to exercise caution when interpreting estimates of ocean heat content during this particular period. Regardless of the measurement methods used, the values are such that the imbalance is given positive. According to these studies as summarized in Figure 1.6, the EEI values range from 0.5 to $0.9\,\mathrm{Wm^{-2}}$. The Earth's energy imbalance was estimated at $0.6 \pm 0.4\,\mathrm{Wm^{-2}}$ between 2000 and 2010 (Figure 8). A study published in 2020 shows that the Earth's energy imbalance continues to grow unabated ([von Schuckmann et al., 2020]). Estimated at $0.87 \pm 0.12\,\mathrm{Wm^{-2}}$ over the period 2010-2018, it has doubled compared to the period 1971-2018 as explained in [Meftah, 2023]. Phenomena like eruptions or ENSO cycles have a significant impact on the radiation budget, as noted in [Trenberth et al., 2014]. The necessity of combining observation methods for reaching expected accuracy is emphasized in [Hakuba et al., 2019], [Trenberth et al., 2016], and [Dewitte and Clerbaux, 2017]. It is important to consider that the best estimate relies on the accumulation of energy in the oceans. However, current measurements and fundamental analysis fail to adequately explain energy fluctuations, as they indicate error bars that are unreasonably large, as explained in [Trenberth and Fasullo, 2012].

In [Allan et al., 2014] the authors reconstruct and analyze changes in the net downward radiative flux imbalance at the top of Earth's atmosphere from 1985 to 2012. There is a slower surface warming but a higher radiative heating from 1985–1999 to 2000s. This is called the "surface-warming hiatus". Also studied in [Hedemann et al., 2017], the article explores various factors that could have contributed to this hiatus, such as natural climate variability, changes in ocean heat uptake, and volcanic and anthropogenic aerosols [Kaufmann et al., 2011]. A combination of these factors likely contributed to the hiatus [Trenberth and Fasullo, 2013, Solomon et al., 2011]. As mentioned, phenomena such as El Niño oscillations and volcanic eruptions can highly influence the net radiative imbalance. [Allan et al., 2014] find discrepancies between different data sets that highlight the need for better quantification. A better understanding of these factors is necessary to improve climate models and predict future climate change. There is a lack of measurement and further investigation is needed.

1.3 Datasets and Exploitation

We analyze several datasets from various acquisition strategies to obtain quantitative information on these radiation fluxes. We start by describing those datasets and how they differ.

ERA5

The ERA5 reanalysis is a dataset implemented by the European Centre for Medium-Range Weather Forecasts (ECMWF), an independent intergovernmental organization via Copernicus Climate Change Service (C3S). It is the fifth generation reanalysis for the global climate and weather [Hersbach et al., 2020]. The purpose of that new dataset was to replace the ERA-Interim, which was released in 2006 and ended in August 2019. The different objectives of that new implementation were to improve the spatio-temporal resolution, to allow uncertainty estimate, and to add new inputs to the large list. It now reaches a $0.25° \times 0.25°$ spatial resolution (atmosphere) with hourly maps around the whole globe from January 1979 to the present (the preliminary version is set from 1950 to 1978). It is based on the assimilation via IFS Cycle 41r2 4D-Var. This new model launched in 2016 considers three times more prediction points, reaching 904 million points spread around the globe, and allowing a higher resolution. It contains 240 parameters at a spatial resolution of 31 km globally, 62 km for the Ensemble of Data Assimilation, 137 levels to 0.01 hPa.

EBAF Ed 4.1

The EBAF dataset is created based on values retrieved from the CERES instruments. The CERES instruments were described in Section 1.2.3. The EBAF dataset is actually completed with data measured from geostationary satellites measuring radiative fluxes and cloud properties such as the GMS 5, Met 5,7, GOES 8-15, MTSAT 1-2, used to fill in any gaps using hourly diurnal information between 60° South and 60° North [Loeb et al., 2018a] and polar orbiting imagers. The CERES mission aims to monitor long-term Climate Data Record (CDR) from the surface to the TOA along with the cloud and aerosol properties. It aspires to a better understanding of the Earth radiative budget dynamics and how they are linked to the clouds and aerosols. Finally, those datasets can be used to improve or to assess models. The CERES instruments except for the one on NOAA-20 (Window (WN) becomes LW) measure SW between 0.3 and 5 mm, total (TOT) between 0.3 and 200 mm, and WN between 8 and 12 mm. The outputs are monthly maps of 360 × 180 at 1° × 1° spatial resolution around the globe from March 2000 to present.

HIRS

The High Resolution Infrared Radiation Sounder Instrument, HIRS/2/2I/3/4, are located on NOAA TIROS-N Series: 7:30 and 2:30 equator crossing time, NOAA-17 10:30 AM and Eumetsat MetOp-A/B polar orbiters. They cover 0.3-5 µm/8-12 µm/0.3-200 µm with 2.5° × 2.5° from 20 km to 10 km for HIRS/4 spatial resolution at nadir allowing global monthly maps from January 1979 to the present (CDR, 2017). The retrieving algorithm uses inter-satellite calibration and OLR regression models (Schreck et al., 2018).

ARGO

The Argo Program was first implemented in 1999 to monitor the temperature and salinity of the ocean from 0 to 2000 m depths (2000 dbar). It takes a major role in the Global Ocean Observing System (GOOS) and the GCOS, delivering global coverage of the ocean since 2006. The program uses float measurements, the idea is to distribute floats all over the ocean. Those floats will start measurements during their descents down to 2000 m ocean depth, as well as when they ascend back to the surface. Data such as location, pressure, temperature, and salinity will be retrieved thanks to satellite communication. Currently, there are about 3500-4000 profiling floats in the ocean, and the number of floats will keep rising as different sensors will be added to the existing ones in order to measure other variables such as O_2 concentration [Roemmich et al., 2015].

To complete the Argo floats data and estimate the ocean temperature before 2006 we can refer to the estimates for previous years while being aware of the related uncertainty.

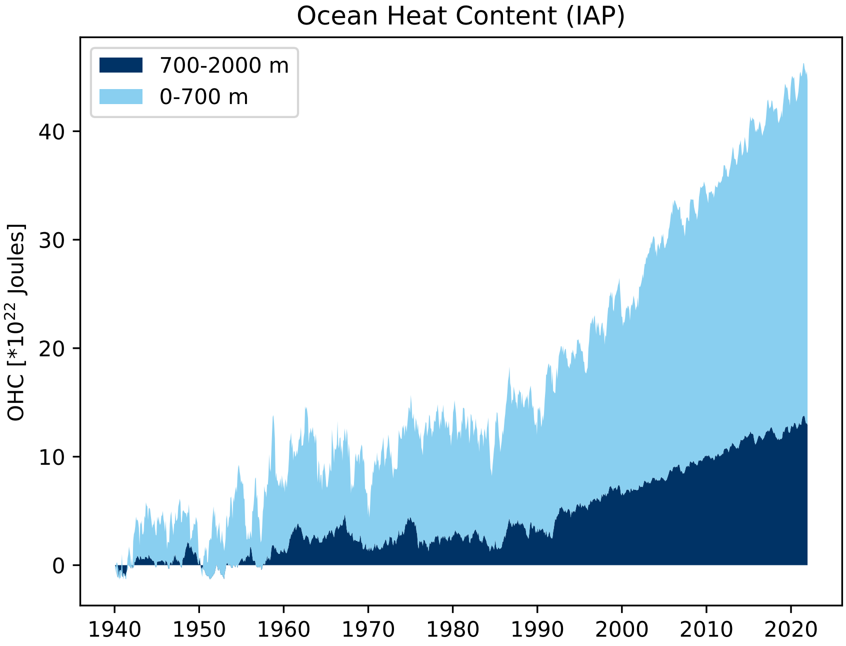

Figure 1.7: Ocean heat content at different depths.

Instruments used prior to the current Argo floats were mechanical (less than

300 m deep) or expendable (400 m, 800 m, or 1500 m deep) bathythermographs [Talley et al., 2011], Nansen/Nisken bottles, and Conductivity-Temperature-Depth (CTD) instruments. Their development stopped because of many issues related to the monitoring methods. These issues were entirely mitigated with the Argo [Meyssignac et al., 2019]. Nevertheless, their use may still be helpful to uncover trends. Therefore, we will investigate OHC from Cheng at the Institute of Atmospheric Physics (IAP) dataset for the upper 2000 m who studied measurements from the previous instruments. It is based on an objective analysis method of ensemble optimum interpolation, and on the Coupled Model Intercomparison Project (CMIP5) model simulations for error covariance and first guess [Trenberth et al., 2016]. The OHC can be decomposed for different layers corresponding to different depths as shown in Figure 1.7.

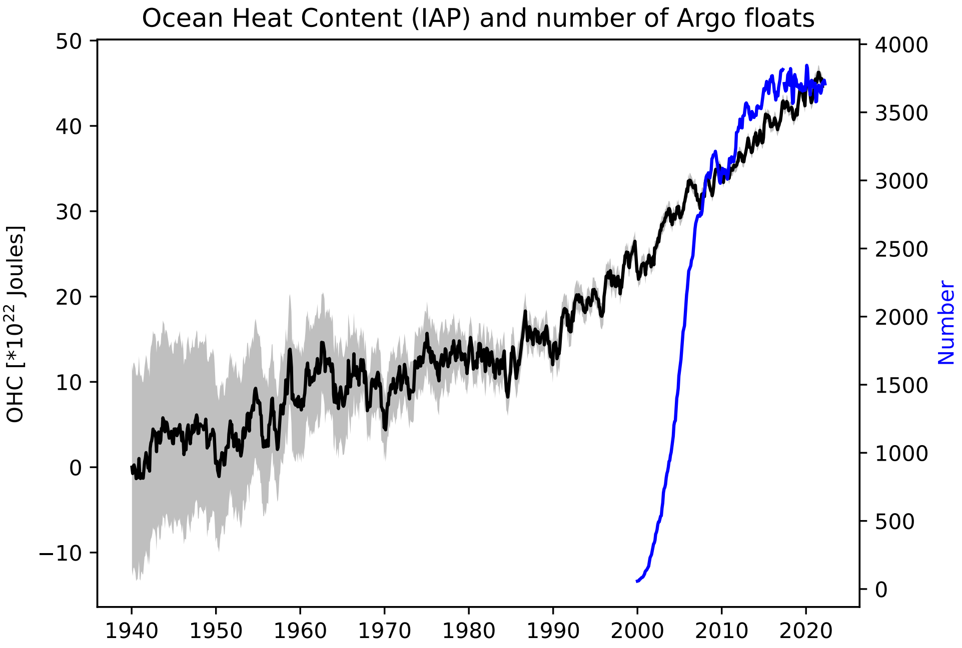

Figure 1.8: Ocean heat content and number of Argo floats (0-2000 m).

Those layers are related to different time scales in terms of frequency change. For example, the 0-300 m layer warms the fastest, although it is significantly influenced by inter-annual variability [Liang et al., 2021]. Figure 1.8 shows the OHC from the overall 0 to 2000 m deep for the previous dataset with respect to the number of Argo floats. The 95 % confidence bounds are convenient as they give a relevant uncertainty on the values used here due to the lack of coverage and measurement. As the Argo floats are deployed, and as their number increases, the uncertainty drops considerably. It is clearly essential to highlight the increase in energy in time, but this will be discussed in the following sections.

1.3.1 Radiation Flux

Method

We choose to focus on the ERA5 case so that we can explain a method to retrieve and compare the datasets. We first download the file (NetCDF format) using the Climate Data Store (CDS) Application Program Interface (API) available on `https://cds.climate.copernicus.eu/`, low-level functions for memory optimization are then implemented to recover each of the radiations at TOA for SW and LW. As the data obtained are given in $\mathrm{Jm^{-2}}$, we convert those values to $\mathrm{Wm^{-2}}$ dividing by the associated time interval which is 86 400 s for monthly mean, as the effective processing period lasts a day. To simplify the computations, flipping the matrix on the longitude can be relevant to obtain a CERES-like matrix (EBAF datasets) in terms of distribution (longitude distribution differs from 0 to 359.75° to -179.75 to 180°). This is just a question of formatting. We can now weigh the gridded values with their associated pixel size given in Equation 1.8, to compute the global mean of each flux over the whole globe. The EEI is computed by subtracting the OSR and OLR from the ISR. Then, integrating the EEI over time allows us to recover the energy accumulation over time:

$$S_{ij} = R_{\text{Earth}}^2 \times \cos(\phi_j) \Delta\lambda_i \Delta\phi_j \tag{1.8}$$

where, R_{Earth} is the Earth radius, ϕ_j the element latitude, $\Delta\lambda_i$ the element size along the longitude axis, and $\Delta\phi_j$ the element size along the latitude axis.

Analysis

The radiative flux can be plotted separately to observe different aspects and correlations for the CERES instruments, the ERA5 reanalysis, and the HIRS data in

Figure 1.9.

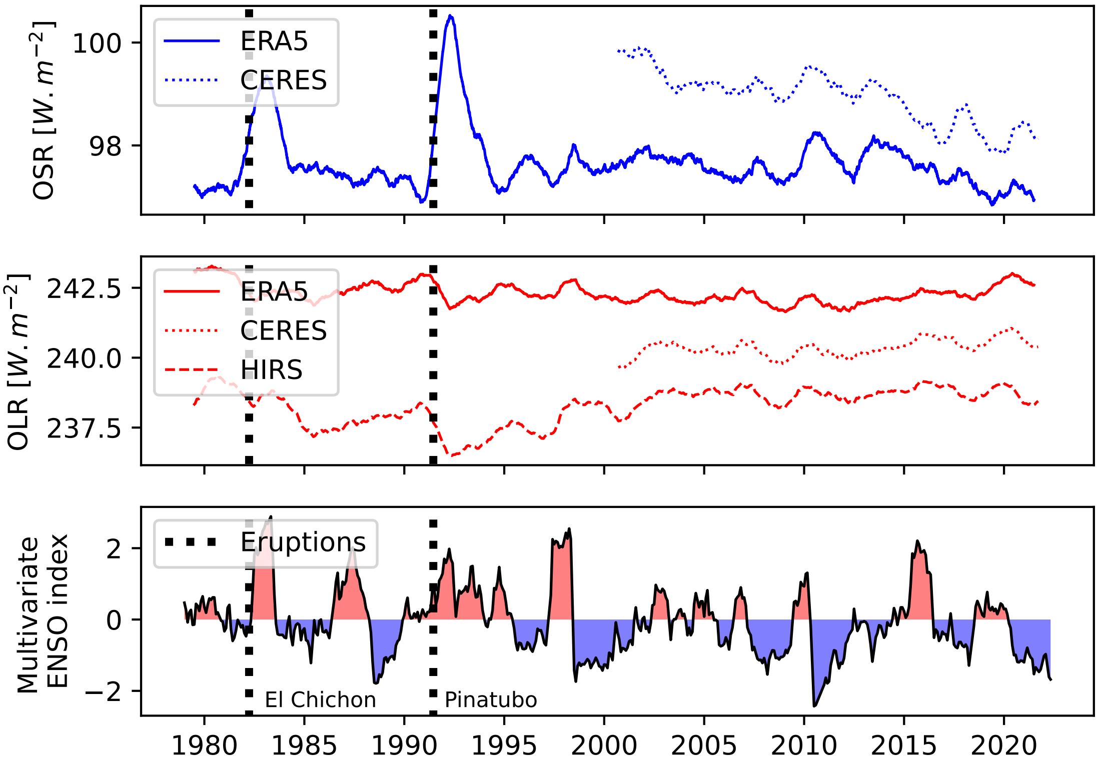

Figure 1.9: OLR and OSR from CERES instruments, HIRS instruments, and ERA5 reanalysis and multivariate El Nino Southern Oscillation (ENSO) index.

The Multivariate ENSO Index Version 2 indicator is also presented, which includes oceanic and atmospheric factors. It allows for an assessment of ENSO in a single index. It offers real-time indications of ENSO severity. Warm periods appear in red and cold in blue. Actually, those datasets allow us to report phenomena that affect the amount of energy getting to the surface or leaving the Earth's atmosphere. [Trenberth, 2020] explains that ENSO cycles have major impacts on the climate system. According to [Palmer et al., 2017], the Mount Pinatubo eruption had a great influence of decreasing the EEI of about $3\,\mathrm{Wm}^{-2}$ whereas El Nino phenomena can increase the EEI of about 1 to $1.5\,\mathrm{Wm}^{-2}$. There is a visible and bigger change on the OLR in 1991 due to the eruption. It achieves a peak-to-peak value of roughly $-3.5\,\mathrm{Wm}^{-2}$ for the ISR in ERA5 and about $2\,\mathrm{Wm}^{-2}$ for the HIRS dataset in Figure 1.9. Another eruption from El Chichón in 1982 is characterized by a sharp increase in the OSR of about $2\,\mathrm{Wm}^{-2}$ and a decrease in OLR. This is explained by the fact that volcanic eruptions release large volumes of dust and gases into the lower stratosphere and high troposphere. The volcanic aerosols will deflect ISR into space, increasing planetary albedo and lowering the incoming solar flux reaching the troposphere and the Earth's surface. Major El Nino phenomena occurred in 1982–1983, 1997-1998, and 2014-2016. This is characterized by an increase in outgoing SW radiation of about $1\,\mathrm{Wm}^{-2}$ for each event. It is interesting to note the gaps appearing between the different datasets (CERES, ERA5, HIRS). And this is why HIRS dataset is used here. As the EBAF dataset did not monitor the radiation before 2000, HIRS is here a relevant element for comparison with the ERA5 reanalysis. The three datasets fluctuate synchronously with the phenomena mentioned before but important biases can be noted. For the LW radiation, we note a bias of about $4\,\mathrm{Wm}^{-2}$ between ERA5 and HIRS. There is a similar bias existing between the LW and SW radiations of the ERA5 reanalysis and EBAF, the bias counts for about $2\,\mathrm{Wm}^{-2}$.

Those gaps can be explained and justified by the different methods used to obtain those results. Different assumptions were made to create the EBAF dataset, those are reported in [Loeb et al., 2007], major biases are justified by the spherical assumption, measurements of albedo at the poles and instruments calibrations leading to uncertainties that can reach 2-3 Wm^{-2} for certain datasets.

1.3.2 Earth Energy Imbalance

The EEI is the resulting budget from the two monthly averaged variables, the absorbed SW radiation, and the OLR. We plot the 12 months moving averages of the EEI computed thanks to the ERA5 reanalysis, the CERES instruments, and the MoHeaCan dataset described in Section 1.2.3. The impact of the different phenomena as mentioned earlier and from [Palmer et al., 2017] have a great influence on the EEI, considering the eruption and the ENSO phenomena. In Figure 1.10, there are several drops of about $1.5\,\mathrm{Wm}^{-2}$ at the El Chichón eruption period, $2.5\,\mathrm{Wm}^{-2}$ at Mount Pinatubos's and about $1\,\mathrm{Wm}^{-2}$ for ENSO cycles.

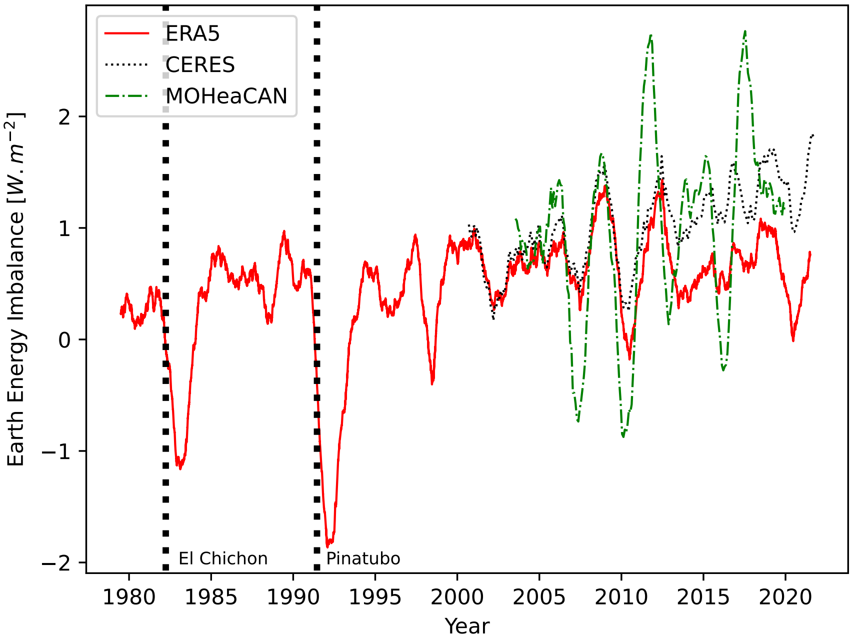

Figure 1.10: 12 months moving averages of the EEI computed from EBAF dataset, ERA5, IAP, and MOHeaCAN.

Those results show how difficult it is to measure the EEI, for example forcing due to an eruption can be 2 to 5 times more important than the imbalance measured. Radiative forcing by a climate variable is a change in Earth's energy balance. Mount Pinatubo aerosols also have impacts (delayed rebound impact) on longer timescale on the ocean heat absorption according to [Hansen et al., 2011].

1.3.3 Earth Energy Accumulation

The EEI is a relevant metric to monitor the amount of energy per unit of surface that will reside on Earth per unit of time. As mentioned earlier some of that energy is melting ice, warming land and atmosphere but the biggest part (93%) is stored in the ocean. And therefore measuring that part of the energy can be a consistent way to monitor the EEI. Figure 1.11 presents the energy accumulated, computed from ocean measurements compared to TOA values.

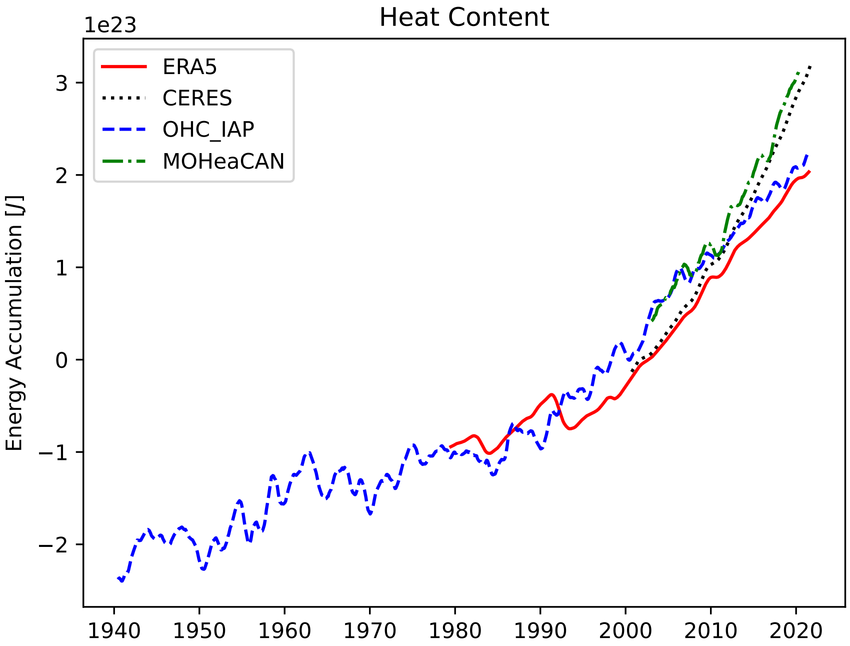

Figure 1.11: Comparison between Argo Floats measurements, ERA5 reanalysis, MOHeaCAN, CERES EBAF Ed 4.1 (at TOA) 12 months moving averages for global monthly mean.

In Figure 1.11, the accumulated energy is shifted (offset) to get equal means for ERA5 and Argo floats energy between 1979 and 1989. The trend retrieved from the ERA5 reanalysis seems to be closer to the trend recovered from the Argo-IAP dataset. The ocean stores the energy, but the inertia of that storage is really important compared to the inertia of the atmosphere. The specific heat of air is about $1158\,\mathrm{J\,kg^{-1}\,K^{-1}}$ and the specific heat of seawater is about $3850\,\mathrm{J\,kg^{-1}\,K^{-1}}$. Therefore, and according to the previous analysis, we suppose that the OHC is a perfect metric to monitor long-term variability whereas the observations at TOA are suitable for high-frequency dynamics. A relevant approach is to adapt the measurements at TOA to long-term trends from Argo data. This is what has been done for the EBAF dataset, adapting the long-term trend to the OHC [Loeb et al., 2009].

The variability of the components of the EEI is directly linked to the specifications of the measurements that should be made. [Meftah et al., 2022] shows the specifications for such measurements below in Table 1.5. Those specifications respond

Variable	Absolute accuracy	Stability per decade	Spatial resolution	Temporal resolution
TSI	$\pm 0.54\,\mathrm{Wm^{-2}}$	$\pm 0.14\,\mathrm{Wm^{-2}}$	-	24 h
OSR	$\pm 1.00\,\mathrm{Wm^{-2}}$	$\pm 0.10\,\mathrm{Wm^{-2}}$	10-100 km	Diurnal cycle (3 h)
OLR	$\pm 1.00\,\mathrm{Wm^{-2}}$	$\pm 0.10\,\mathrm{Wm^{-2}}$	10-100 km	Diurnal cycle (3 h)
EEI	$\pm 1.00\,\mathrm{Wm^{-2}}$	$\pm 0.10\,\mathrm{Wm^{-2}}$	-	-

Table 1.5: Scientific requirements [Meftah et al., 2022].

to a scientific need. However, we can separate the variables to have two different systems. The processes being resolved are different. We mention the objective of accurately measuring the long term trends over decades and the objective of monitoring the high variability at high spatio-temporal resolution.

1.4 Innovative Methods to Measure the EEI from Space

We have seen existing methods to estimate the EEI. Other configurations could be implemented to measure the EEI. Some of the configurations are presented in this section.

1.4.1 Moon-based Observations

Moon-based observations of the Earth have generated considerable interest in a wide range of large-scale phenomena. The Moon is the Earth's only natural satellite. This choice allows having a stable lunar surface with a specific orbit. Moon-based measurements of the Earth allow it to be viewed as a single point. In addition, the changing tilt of Moon-based observations can be adapted to specific Earth observation locations. It is a unique point of view to observe the full Earth disk. Ye et al., Shang et al., Guo et al. discussed the measurements of terrestrial outgoing radiation from a moon-based platform in [Ye et al., 2021, Shang et al., 2021, Guo et al., 2018]. Additionally, Duan et al. contributes to the study by quantifying the effect of spatial resolution and temporal sampling in [Duan et al., 2021].

1.4.2 Earth Observations from Lagrangian Points

Lagrange points are places in space where items tend to remain stationary according to the two celestial bodies of interest. The gravitational attraction of two masses perfectly equals the centripetal force necessary for a small item to move with them at Lagrange points. The L1 point, discovered by mathematician Joseph Louis Lagrange, is 1.5 million kilometers inside Earth's orbit, halfway between the Sun and the planet. L2 is located 1.5 million kilometers behind the Earth as viewed from the Sun. As a result, L1, L2, the Earth orbit, and the Sun are aligned along the same radial line. A satellite has a continuous view of the whole sunlit face of the spinning Earth from L1. L2 stays in eclipse, a satellite at this location would be focused on the unilluminated opposing disc of the Earth. A satellite would not have to perform regular orbits around the Earth and would avoid frequent temperature changes associated with traversing Earth's shadow. L2 gives a far more stable sight.

An adequate example of an instrument at L1 is the National Institute of Standards and Technology Advanced Radiometer (NISTAR) on-board the Deep Space Climate Observatory (DSCOVR) which was specifically designed to estimate the worldwide daylight radiation budget for a whole hemisphere utilizing active cavity radiometers in three channels: total (0.2-100 µm), SW (0.2-4.0 µm), and near-infrared (0.7-4.0 µm). [Yang et al., 2018] and [Tian et al., 2020] developed the study of terrestrial radiation from the DSCVR instruments.

1.4.3 Earth Observations from a Constellation

A constellation of satellites allows us to make use of multi-point observations. Different satellites can observe the same location at consecutive times to reach a higher temporal resolution. Moreover, even with a reduced FOV, it could still be possible to cover the whole world from several satellite observations. Different satellite constellations could be implemented. Geostationary satellite constellations would observe the same zone constantly. Many satellites would be required to observe the whole globe. Fewer satellites would be needed in low Earth orbit (LEO) to monitor the whole Earth. A strict architecture of the constellation should be determined to combine satellites to observe the different localization with adapted parameters. Locations with high variability rates should often be monitored by the satellite for example. This challenge has been described in [Gristey et al., 2017], it explores the possibility of an innovative constellation idea to monitor the EEI. The work demonstrates that, when compared to existing observational products, the baseline constellation is capable of providing stable recovery of hourly outgoing irradiance fields.

1.5 Conclusions, Perspectives and Scientific Project

Climate change appears to be a major issue of our time, insofar as its evolution is unprecedented. Human emissions and activities are responsible for global warming and the risks are very high and increasingly present today. In order to understand this climate change, and its stakes and to develop mitigation and adaptation strategies, it is necessary to quantify its rate of change. Many indicators and metrics are developed to better understand those phenomena. A major metric is the essential climate variable which quantifies the rate of climate change on a global scale by calculating the accumulation of energy in the earth-atmosphere-ocean system.

The radiation imbalance of the Earth includes three main components at the TOA. The first one is the TSI, measured at about $1362\,\mathrm{Wm^{-2}}$. It must be determined with an absolute accuracy of less than $0.54\,\mathrm{Wm^{-2}}$ and a stability of $0.14\,\mathrm{Wm^{-2}}$ per decade. The second component is the reflected solar flux which has an average value of $100\,\mathrm{Wm^{-2}}$. The third component is the outgoing infrared flux averaged at $240\,\mathrm{Wm^{-2}}$. These last two fluxes must be known with an absolute accuracy of $1\,\mathrm{Wm^{-2}}$ and a stability of $0.1\,\mathrm{Wm^{-2}}$ per decade. The EEI results from the budget of those fluxes. It should be measured with $1\,\mathrm{Wm^{-2}}$ absolute accuracy and $0.1\,\mathrm{Wm^{-2}}$ per decade. In view of the specifications mentioned, measuring this balance does not seem trivial and constitutes a real challenge.

Different methods and measuring devices exist to quantify the EEI. The best estimate of the EEI comes from the measurements of the change in heat stored in the ocean (uncertainty of less than $0.1\,\mathrm{Wm^{-2}}$ per decade) using Argo floats. The heat from the atmosphere is absorbed in the ocean and serves as a "buffer" due to the ocean's thermal inertia. While the Argo automated floats give good OHC data, they provide little information on short-term dynamics. However, Earth observation satellites allow us to reach near real-time monitoring. It enables us to observe phenomena with high temporal variability.

Therefore, to monitor high-frequency dynamic and long-term trends it seems unavoidable to use both methods. Nevertheless, a constellation of satellites that provide both narrow and wide fields of view is necessary to reach high spatio-temporal resolution with 10-100 km at 3 h. It would enable a better understanding of climate change as radiative imbalance is substantially impacted by aerosols and clouds, which are geographically and temporally moving and yet relatively little characterized. It would permit to retrieve high-frequency data to resolve the diurnal cycle that has a significant impact on climate evolution (humidity, CO_2). In light of the space enthusiasm and the Newspace approach, it is now conceivable to create new sensors onboard new platforms to enable the most cost-effective constellation deployment.

This manuscript will elaborate on the missions that meet this need. The architecture of the constellation must be optimal. The constellation of satellites should allow us to fit the specifications to monitor the EEI. However, the number of satellites to launch should be in light of the situation of the debris and the numerous satellites present in orbit. It increases the risk of collision.

Chapter 2

Towards a Constellation of Satellites to Monitor the Earth Energy Imbalance

2.1 The Radiation Balance Is Not the Only Concern of the Observation from Space

2.1.1 Improving the Resolution of the Earth Radiative Budget Measurements with a Constellation

The measurements of the ERB could be enhanced from multi-point observation to cover the whole globe at a short revisit time. Many satellites observing the Earth could ameliorate the spatio-temporal resolution of the measurements as presented in [Gristey et al., 2017]. As explained in [Yang, 2019], a hundred satellites per orbital plane and a hundred orbital planes are required to obtain a sufficient mesh and observations with unequaled performances presenting an excellent revisit, temporal resolution, and spatial resolution. [Buzzi et al., 2019] evaluates different constellation designs for the TROPICS mission, which aims to improve tropical storm forecasting. A simulation model compares constellations with different numbers of satellites and orbital configurations. The study finds that a constellation of satellites can provide high-quality observations of tropical storms and improve forecasting. The Swarm mission [Friis-Christensen et al., 2008], a 2013 European Space Agency (ESA) project comprising three identical satellites launched to research the Earth's magnetic field and its interaction with the solar wind, is another example of a constellation. The mission gathers information through various tools and technologies to enhance our comprehension of geophysical processes. [Wu et al., 2021] proposes a three CubeSats mission launched in 2015 for integrated earth observation and marine/air traffic monitoring.

Low resolution is used for global analysis, medium resolution for regional variations, and high resolution for analysis and understanding of CO_2 coupling, CO_2 and methane sinks. A satellite constellation provides unprecedented sampling, in almost real-time which has the potential to improve Earth outgoing radiation observations. Moreover, it may be less vulnerable to individual satellite failures.

As explained in [Sandau, 2010] small satellite constellations are becoming increasingly popular for Earth observation. They offer several advantages over larger satellites such as the cost of deployment. They can achieve global coverage with high temporal resolution. Additionally, constellations allow for easy replacement of a malfunctioning satellite and provide a soft degradation of the system performance if one of the satellites fails. Data are used to feed, constrain and verify the performance of the models. Indeed, their uncertainty is a crucial parameter, so being able to oppose the models to direct observations seems fundamental. But this problem is not only a concern for the ERB measurement, as constellations can be used in different domains.

2.1.2 Examples of Fields

Earth observation from satellites allows monitoring the total surface of the globe from above. The applications are multiple. Many companies are founded with the aim of enabling a global and precise observation of the Earth's surface. Examples of applications are oil spills and gas leaks [Tysiąc et al., 2022], precision agriculture [Mulla, 2013], observing beetles, coastal erosion [Amaro et al., 2015], and infrastructure. Remote sensing for Earth observation is beneficial for different fields. In agriculture, remote sensing is crucial to providing better knowledge of the weather forecast to optimize and protect the crops. It is made to improve the monitoring of fields and to detect anomalies using deep learning for the classification of lands [Debella-Gilo and Gjertsen, 2021, Malerba et al., 2021]. Using satellites allows agricultural workers to check the health of the soil, the hygrometry, the precision farming, watch the health of the plants and foresee automatic actions. Real-time assistance to farmers is provided. For insurance, it helps to predict and prepare for disasters or to assess the impact and prepare to meet the claims. This is directly linked to disaster risk reduction such as with the global wildfire information system, wildfire detection, and monitoring as in [Barmpoutis et al., 2020]. Remote sensing is applied to monitor floods as explained in [Schumann et al., 2018] or perspectives in that field with nanosatellite constellations as in [Kameche et al., 2014]. Satellite observations are also fundamental in infrastructure and energy assessment such as to locate regions of interest for energy converter installations and to precisely locate new places with promising possibilities in [Nezhad et al., 2021]. Earth observation is also of considerable interest in defense and commercial fields.

2.1.3 Methodologies for Instrumental Observations

As we have seen, Earth observation plays a major role in different fields. The satellite images should be adapted to the location, the phenomenon observed, and the spatio-temporal resolutions [Jeon et al., 2016]. Different scanning techniques exist and some of them are represented in Figure 2.1 [Airbus, 2012].

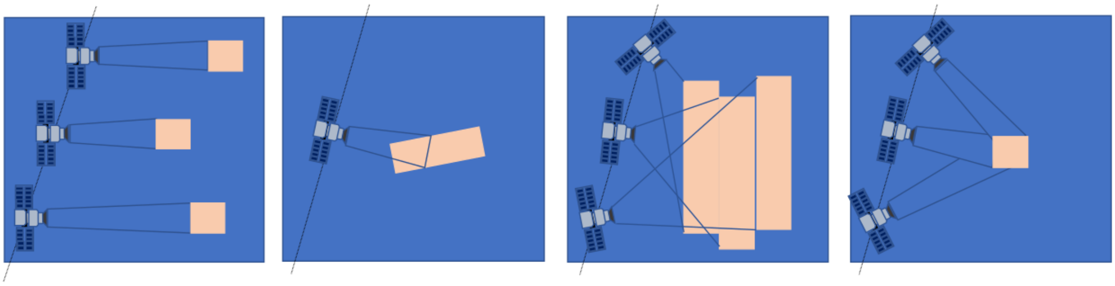

Figure 2.1: Pleiades imagery techniques. Respectively, target collection, corridor acquisition, single-pass strip mapping, and stereo and tri-stereo.

Strip imaging is a scanning method, where a satellite scans the Earth in the direction of motion of the spacecraft. The Earth rotation effect is compensated by a yaw steering maneuver of the satellite. Single-pass stereo imaging is another scanning method that can be utilized to create 3D images. The satellite scans the Earth through one image of the location taken with a positive pitch tilt angle, and the second image is taken at a negative tilt angle. Multi-point imaging is a different scanning method that targets taking several images of the Earth at different locations by quickly rotating the satellite. Wide arbitrary imaging is a scanning method that aims to free the satellite images from its ground track. The scan direction is not the satellite motion direction.

For small satellites, techniques are under development for ground target tracking [Robic et al., 2022] by precisely controlling the satellite attitude thanks to a visual servoing scheme in LEO.

2.2 Simulation-based Optimization of Satellite Configurations

2.2.1 Presentation of the Method

We aim to answer the scientific need using a constellation of satellites. We carry out a non-exhaustive study of the possibilities in order to carry out this measurement. In our case, we consider a constellation in low orbit with satellites in sun-synchronous equispaced orbits. Different solutions are, in fact, exploitable, especially in terms of geostationary satellites. Only 3 would be necessary to cover the globe, however, the coverage at the poles is altered by the effects of the Earth's curvature. Precession orbits could be considered to follow the diurnal cycle over a long period. However, these satellites do not allow to follow a desired area over a few hours [Leroy, 2021]. Ideally, we consider hereafter a constellation almost self-sufficient to reach the mentioned specifications. In reality, this constellation is to be put in parallel with the measurement of the energy accumulation in the oceans in order to reach the requested specifications in the long term. In addition, many space missions could be combined with this constellation to understand these issues. In the same way that the CERES instruments on Terra and Aqua are combined with geostationary imagers [Loeb et al., 2018]. A constellation of satellites would improve the spatial and temporal resolution of the radiation maps obtained from observations. In order to configure a constellation and quantify the improvements in resolution, it is necessary to simulate several constellations to converge toward optimal architecture. It is nevertheless non-trivial to simulate the reconstruction of information measured by one or more satellites in orbit. Indeed, the observation and reconstruction will depend on satellite orbit, attitude, and instrument characteristics. For this purpose, a tool has been developed. The main objective of the code is to model the data retrieved from satellite observations. Given a precise configuration, the code should simulate the signal observed by one or several satellites in orbit and reconstruct the flux maps. It provides the opportunity to quantify the performance of a given constellation.

Input Data to be Observed

The input data are used to simulate the terrestrial flux. Those fluxes are respectively the OLR and OSR (examples in Figures 2.2 and 2.3). The ERA5 dataset was detailed in Section 1.3. It is one of the suitable reference datasets to fit the algorithm expectations as the maps are available hourly. The top net thermal radiation, top net solar radiation, and TOA incident solar radiation will be the variables used.

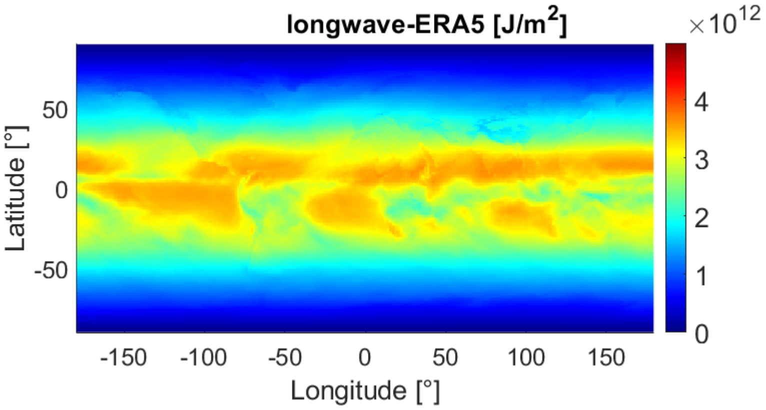

Figure 2.2: Example of net longwave radiation from ERA5.

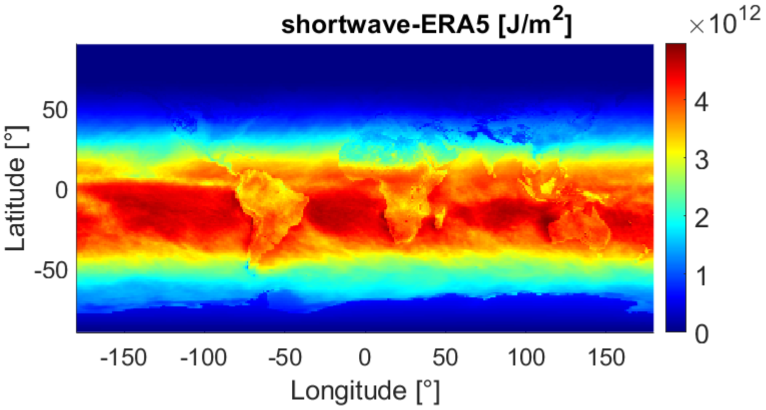

Figure 2.3: Example of net shortwave radiation from ERA5.

The OSR is computed from top net solar radiation and TOA incident solar radiation. The data are available over the whole globe at 0.25° × 0.25° spatial resolution (28 km × 28 km at the equator). The user can determine on what date the observation will take place and for how long. The corresponding data are recovered given those inputs. To perfectly match the measurements, the data set is temporally interpolated in order to fit the sampling to the instrument.

Trajectory

The observer does not monitor the whole globe at each time. It is necessary to retrieve the observer's location to determine the observable part of the globe. There may be one or more satellites, and each can be on a different orbit. This tool must be able to evaluate the location of each satellite at each time step. Given the satellite's Two-Line Element (TLE) orbital components, this program computes the location and velocity of an Earth-orbiting satellite.

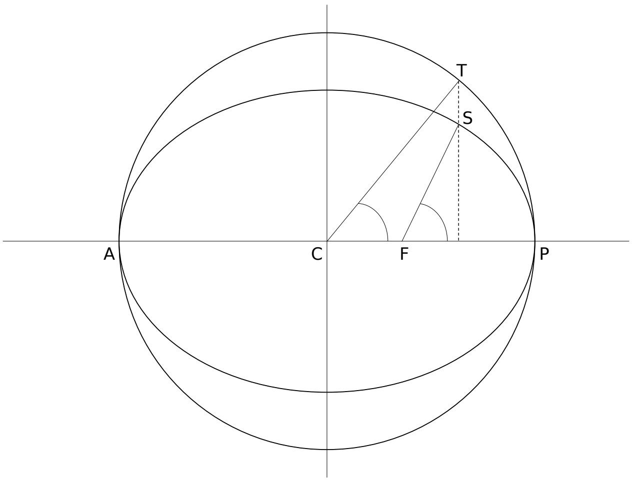

Figure 2.4: Orbital mechanics diagram where S is the satellite, F is the center of the Earth, P the perihelion, A the aphelion, C the center of the ellipse. T the point located at the intersection between the circle of diameter AP and the perpendicular to AP passing through the satellite.

To do so, it uses the most recent version of Simplified General Perturbations 4 (SGP4). It is possible to choose directly the altitude, eccentricity, ascending node, periapsis argument, true anomaly, and inclination corresponding to an epoch instead of using the TLE as input. Thus, the program is able to propagate the satellite's orbit and recover its ground path at each specified time. An example of the characteristic points is given in Figure 2.4. The satellite can then be located from three coordinates as λ_{sat}, ϕ_{sat}, and z_{sat} respectively, its longitude, latitude, and altitude. The ground track is represented in Figure 2.5.

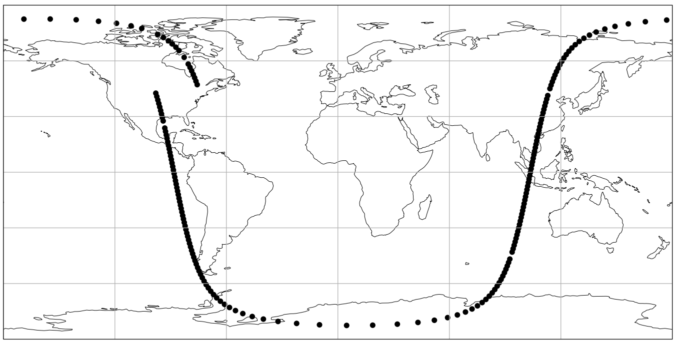

Figure 2.5: Example of ground track of a satellite.

Spacecraft

The spacecraft also called the platform, is orbiting around the Earth following a certain trajectory. Its attitude must be acknowledged as the instrument is directly located on the platform. For ease of use, it is considered that the platform is facing nadir at all times. It represents a simple case where the observable is located along the satellite's ground track.

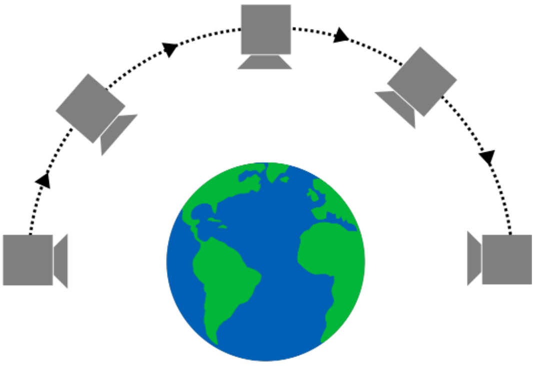

Figure 2.6: Nadir pointing satellite.

This corresponds to the case when the satellite is perfectly pointing toward the

Earth all along its orbit, as shown in Figure 2.6. As an example, the instrument pointing accuracy reaches about 0.2° for CERES FM-3 total channel [Priestley et al., 2010]. The Sentinel-1 platform delivers very accurate pointing knowledge of better than 0.004° on each axis, and high pointing precision of about 0.01° on each axis [Torres et al., 2012].

Instrument

The instrument is considered perfectly facing nadir. Its response depends in that case on the incident angle from the point observed on-ground.

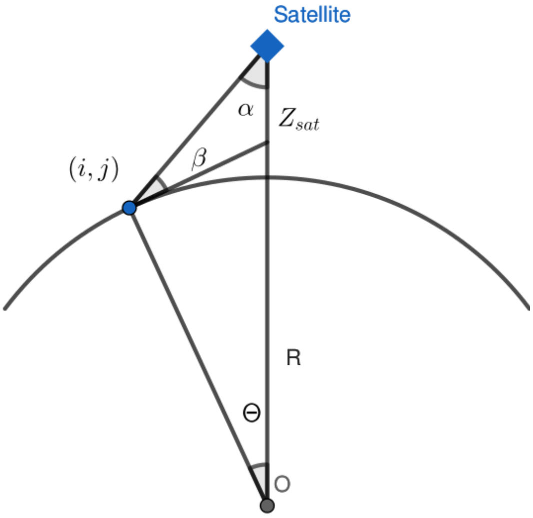

Figure 2.7: Visualization of the satellite in orbit, characteristic angles, and pixel seen by the satellite based on [Meftah et al., 2021].

Figure 2.7 represents the different angles between the satellite, the nadir, and the observation location. The signal received by the modeled instrument results from the integration of the signal received on the sensor surface with respect to the angle of incidence. We use a function to model the observations. Initially, we use a Gaussian function as it can model the general reception of data as a function of this angle. Most sensors have a more Gaussian-shaped responsivity where the FOV is defined as the full width at half maximum (FWHM) of the Gaussian curve [Nguyen et al., 2018]. But this function can be modified to fit the sensor specifications. The satellite has a location λ_{sat}, ϕ_{sat} and an altitude z_{sat}. As explained in [Meftah et al., 2021], the angle $\theta_{i,j}$ at the center of the Earth (nadir) between the satellite and the pixel (i, j) is given by Equation 2.1. The angle $\alpha_{i,j}$ between the nadir of the satellite and the pixel (i, j) is given by Equation 2.2. The satellite elevation $\beta_{i,j}$ (complement of zenith angle) seen by the pixel (i, j) is given by Equation 2.3.

$$\theta_{i,j} = \arccos\left[\cos(\phi_j)\cos(\lambda_i - \lambda_{\text{sat}}) + \sin(\phi_j)\sin(\phi_{\text{sat}})\right] \tag{2.1}$$

$$\alpha_{i,j} = \arctan\left(\frac{R\sin(\theta_{i,j})}{z_{\text{sat}} + R(1 - \arccos(\theta_{i,j}))}\right) \tag{2.2}$$

$$\beta_{i,j} = \frac{\pi}{2} - \alpha_{i,j} - \theta_{i,j} \tag{2.3}$$

The view angle $\Omega_{i,j}$ under which the pixel (i, j) is seen by the satellite is given by Equation 2.4.

$$\Omega_{i,j} = \begin{cases} S_{i,j} z^2 \cos(\alpha_{i,j}) \sin(\beta_{i,j}) & \text{if} \quad \beta_{i,j} \geq 0 \\ 0 & \text{if} \quad \beta_{i,j} < 0 \end{cases} \tag{2.4}$$

Therefore the incident terrestrial flux is seen by the satellite according to the Gaussian distribution $G(\theta_{i,j})$, which is defined by Equation 2.5:

$$G(\theta_{i,j}) = \exp\left(-\frac{\alpha^2}{2\sigma^2}\right) \tag{2.5}$$

with σ, the variance of the Gaussian. σ is related to the FOV via $\sigma = \text{FOV}/2$ which is to be specified by the user.

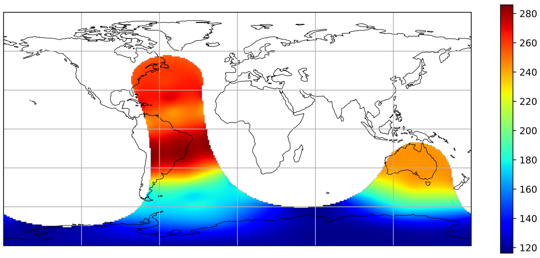

Figure 2.8: Map of the first samples of the reconstructions using a Gaussian distribution function in Wm^{-2}.

For example, for an average altitude of 540 km and a FOV of 135° the diameter of the ground track is about 5000 km (considering the Earth curvature for large FOV).
At each time step the data is recovered as the result of a convolution between the Gaussian function and the input data. An example appears in Figure 2.8.

Output data

The output data from the simulation can be an averaged map of the outgoing terrestrial radiation over the whole globe such as in Figure 2.9. This figure represents an example of global reconstruction in the form of a map. This map is created in 360×180 and shows the OLR from 64 satellites observations in equispaced Sun-synchronous orbits. This map is based on ERA5 data. It is coherent and we can distinguish the different areas such as areas with high OLR like in the tropics (high clouds) and areas with low OLR at the South Pole.

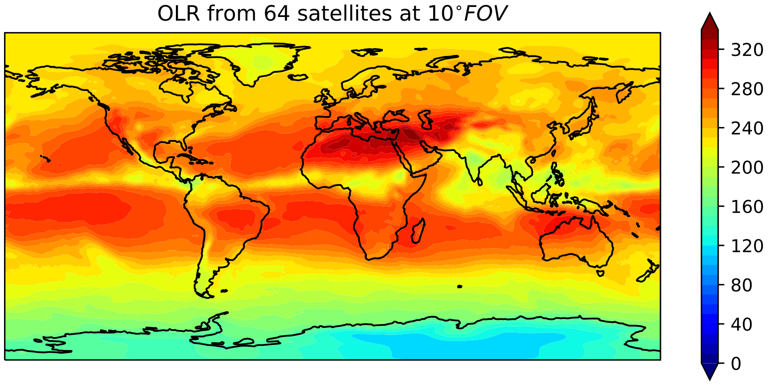

Figure 2.9: Reconstructed monthly terrestrial flux map (example of OLR) in Wm^{-2} for 64 satellites at 10° for the month of July 2022.

2.2.2 Analysis of Simulations for Different Configurations of Satellites and Impacts on the Accuracy

Different configurations of satellites imply different resolutions and revisit times. The architecture must be adapted to the specifications in the short and long term. This section describes the impacts of different configurations on the accuracy reached in the short and long term. We recall that the targeted accuracy is of $\pm 1.00\,\mathrm{Wm^{-2}}$ in absolute and $\pm 0.10\,\mathrm{Wm^{-2}}$ stability per decade in terrestrial flux measurements.

Short Term

The measurement of the terrestrial flux at the TOA is simulated in this section at a short time scale. The objective is to show the impact of the number of satellites and FOV to observe the OSR and OLR. The duration is chosen to be one month. It is long enough to plot a single map of the whole globe with one satellite. This means that the satellite has covered the entire globe and has been able to take readings at every point on the globe during this period. We consider a satellite in low Sun-synchronous orbit. We choose to take data from ERA5 as a reference for the observation during the month of July 2022 with the objective to compare the map of the terrestrial flux retrieved from different configurations of satellites.
An example is to set an orbit of reference with the parameters in Table 2.1:

Parameter	Value
Altitude	533×10^3 m
Eccentricity	0.0012933
Ascending node	153.7201°
Periapsis argument	12.6002°
True anomaly	15.129 648 14°
Inclination	97.4960°
Sampling period	30 s
Field of view	135°
Epoch	2021/04/01 03:18:00 UTC

Table 2.1: Satellite configuration for the simulation.

We consider several satellites in orbit, the satellites are equally distributed over the entire surface of the globe. The orbits are similar, only the ascending node changes for each satellite. The indicators that will help quantify the performance of the configurations are the mean absolute error (MAE defined in Equation 2.6) and the bias (Equation 2.7) computed between the observation model and the input reference data which are monthly maps of the whole globe.

$$\mathrm{MAE} = \frac{\sum_{i=1}^{n} |y_i - x_i|}{n}, \tag{2.6}$$

$$\mathrm{Bias} = \frac{\sum_{i=1}^{n} y_i - x_i}{n}, \tag{2.7}$$

where y_i are the simulated values, x_i the reference values, and n the number of values.

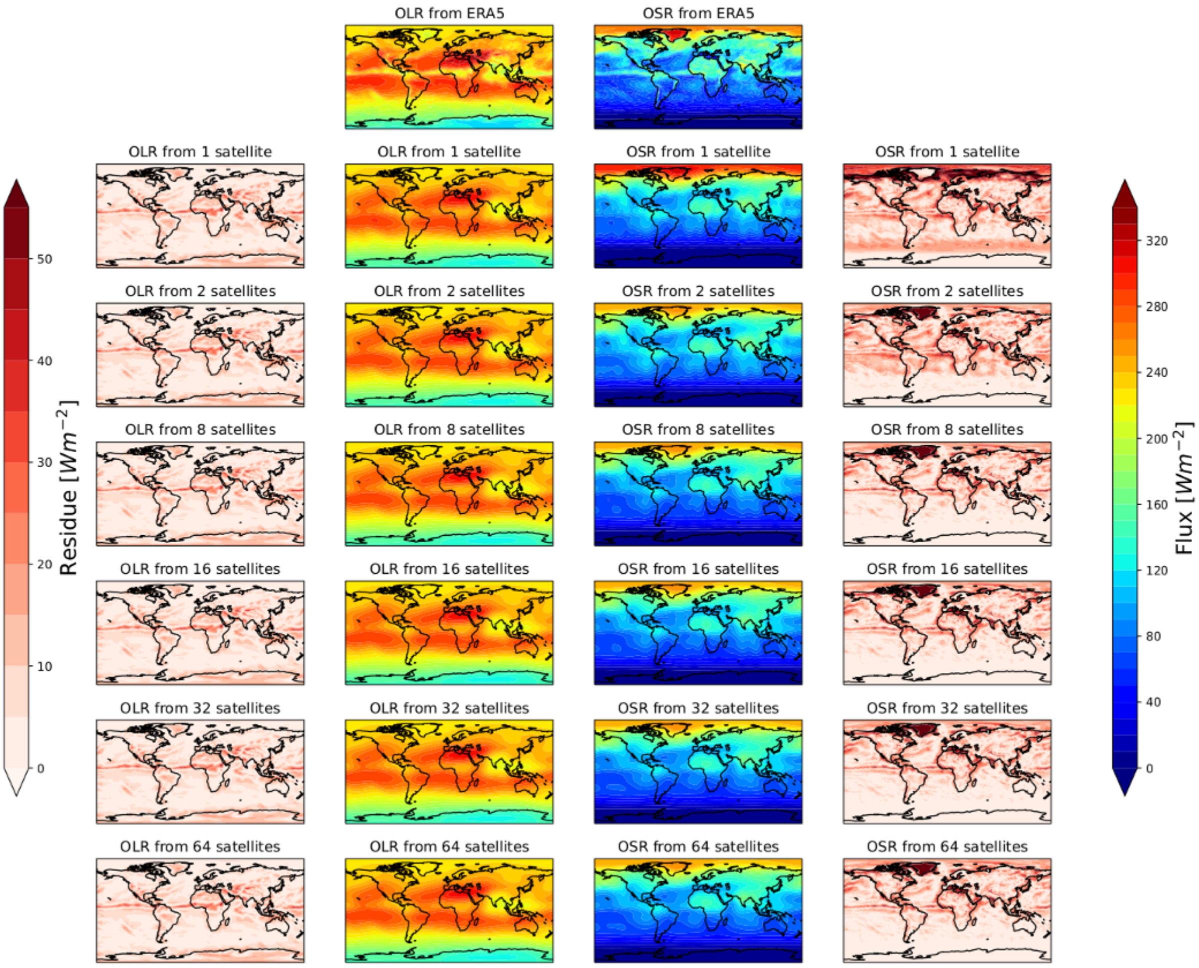

Figure 2.10: Observation from different satellites configuration. OLR and OSR for July 2022 in Wm^{-2}.

The MAE characterizes the average absolute difference between the map created from the simulation and the actual map used as a reference. In comparison with the mean squared error, the MAE does not penalize greater errors more severely. For the MAE the score grows linearly as the magnitude of the error increases. The lower the MAE, the more the configuration allows a precise measurement of the selected variables. The bias characterizes the systematic error or deviation that results in an erroneous estimation of the variables. The lower the bias, the more the configuration allows an accurate measurement of the selected variables.

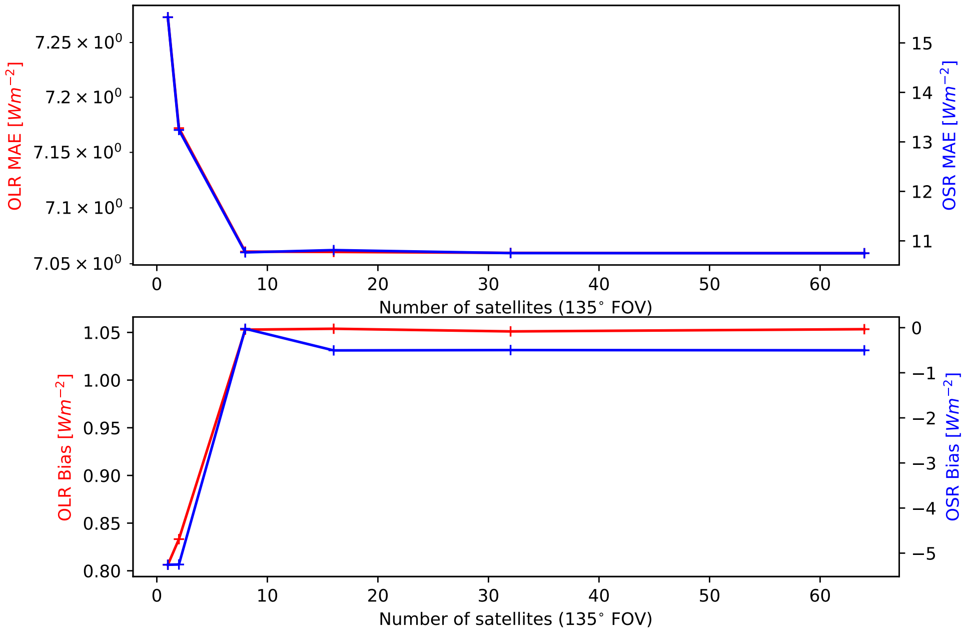

Figure 2.11: MAE and bias from different satellites configuration. OLR and OSR for July 2022 in Wm^{-2} with 135° FOV.

The results obtained from the simulations are shown in Figure 2.10. Both OLR and OSR are simulated. One important parameter to consider is the FOV. This is clearly visible in Figure 2.11 showing the MAE and bias versus the number of satellites in the constellation. Although the number of satellites increases, the FOV of the satellites remains constant. This way, the best result can be reached quickly and is limited by the FOV. It is visible that the best compromise would be to use

8 satellites. The increase in the number of satellites would not allow a significant performance improvement (e.g. in terms of MAE). Nevertheless, increasing the number of satellites has an important impact in the very short term. Indeed, the revisit time will be shorter, proportionally to the number of satellites. Going from a wide FOV to a narrow FOV can then improve the reconstructed map. Therefore, we now simulate the reconstruction for the same configurations but with a much smaller FOV. The FOV is chosen to be 10°.

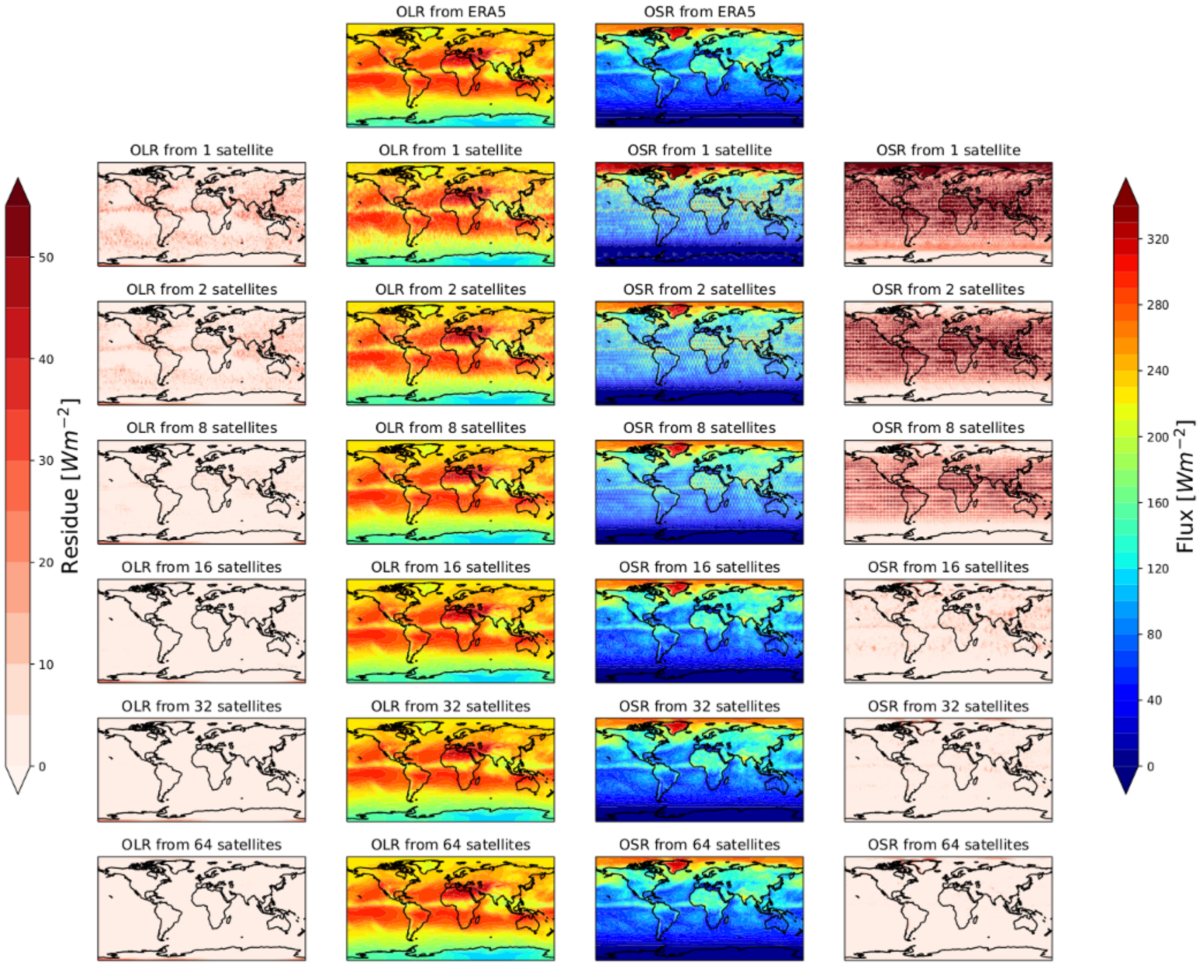

Figure 2.12: Observation from different satellites configuration. OLR and OSR for July 2022 in Wm^{-2} with 10° FOV.

The results from the simulation are different as the FOV of the instrument changes. For the example of a smaller FOV such as 10° in Figure 2.12, mapping the terrestrial radiation is getting more and more accurate as the number of satellites increases. This is due to a small FOV that allows us to depict small phenomena without any complex reconstruction. This is highlighted in Figure 2.13 where we have the MAE and bias versus the number of satellites. The limit reached previously for a wider FOV is not reached even for 64 satellites. The indicators are much better than for a wide FOV. However, many more satellites are needed to cover the whole globe in a small amount of time. This is explained as the observable locations are narrowed. Therefore, many passes are necessary to collect data all around the planet.

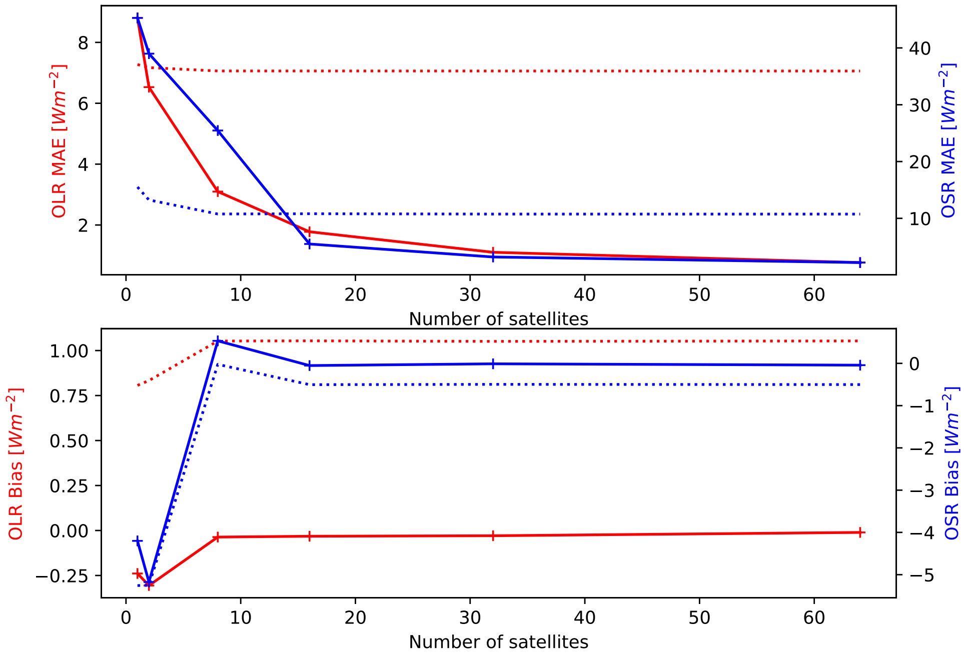

Figure 2.13: MAE and bias from different satellites configuration. OLR and OSR for July 2022 in Wm^{-2} with 10° FOV. The previous configuration for 135° FOV appears in a dotted line for comparison purposes.

The smaller the resolution the better the accuracy will be with a large number of satellites. This explains visually how the FOV has an important role in the observation and can be the limiting variable. For each architecture, the optimal FOV should be determined to optimize the performance such as in Figures 2.14 and 2.15. Figures 2.14 and 2.15 show the simulation for 1 satellite with different

FOV. A small FOV will achieve better accuracy than a wide FOV for the same configuration but the global coverage of the whole globe will be reached much faster with a wide FOV than for narrow FOV instruments. This explained how 40° FOV seems to better optimize the performance. The FOV is narrow enough to reach a high spatial resolution but wide enough to cover the globe.

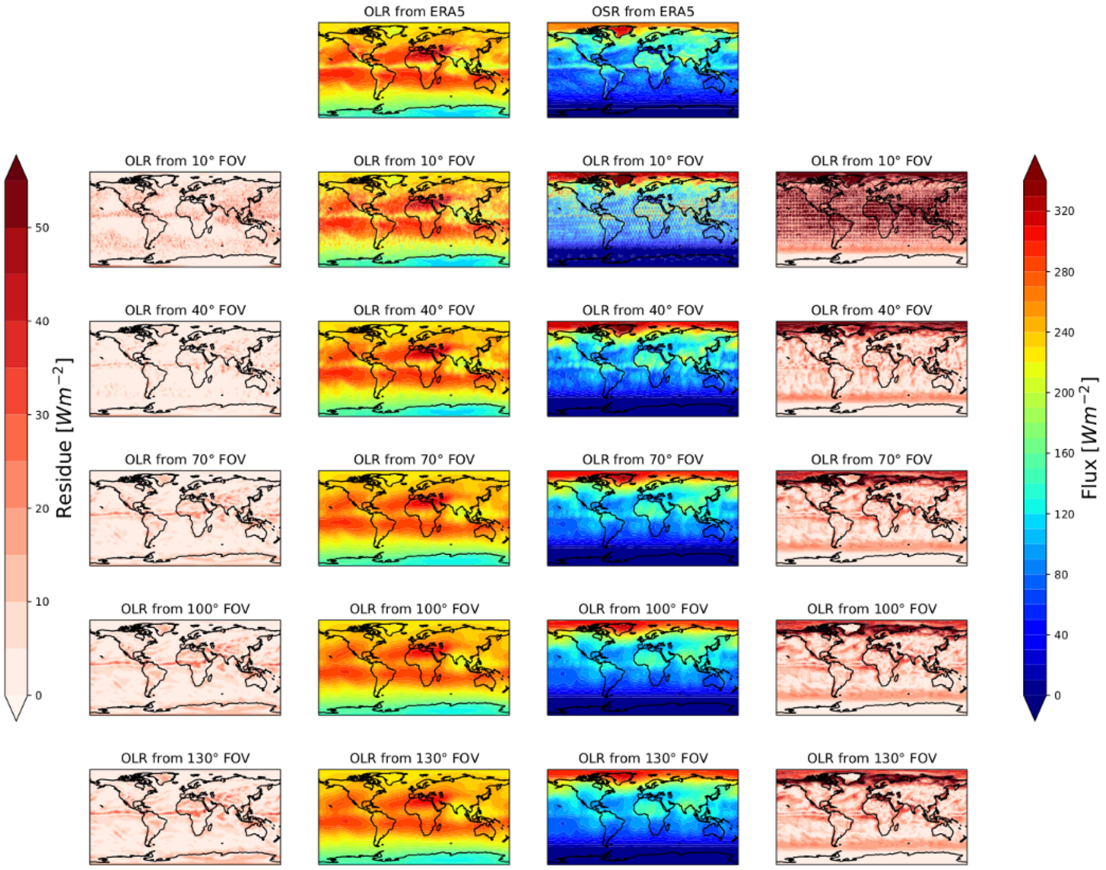

Figure 2.14: Observation from different satellite FOV. OLR and OSR for July 2022 in Wm^{-2}.

We have seen that for a selected orbit, the number of satellites and FOV of the instruments on-board are key parameters to configure a constellation. Those parameters depend on the targeted specifications.

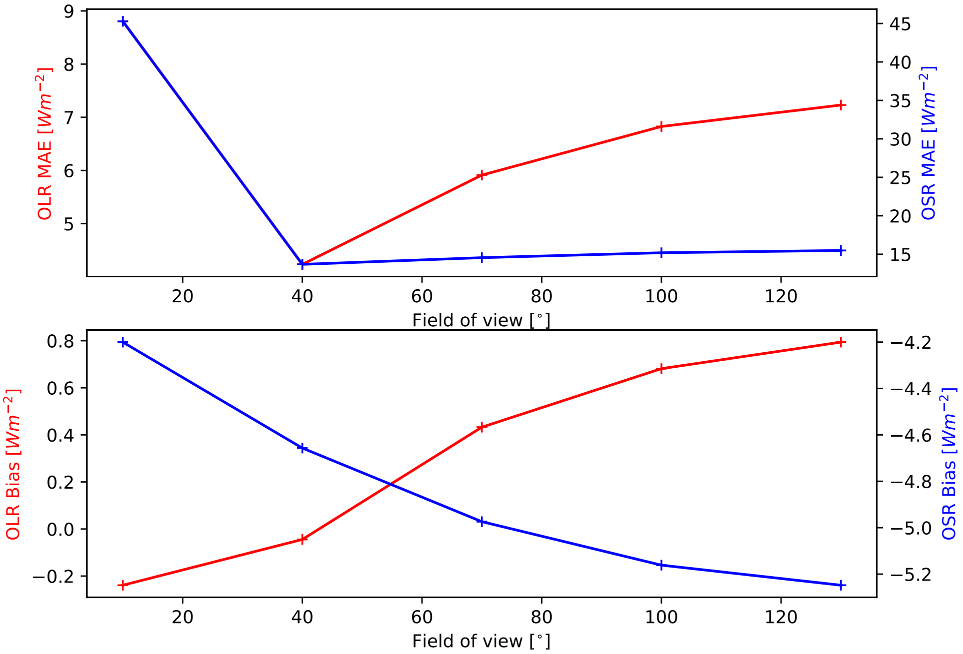

Figure 2.15: MAE and bias from different satellites configuration. OLR and OSR for July 2022 in Wm^{-2} with different FOV.

Long Term

It is interesting to model the measurement of the components of the EEI to simulate long-term Earth observation. The aging of the instruments is not taken into account here. For one satellite observing the Earth's radiation on a Sun-synchronous orbit at LEO, the information is biased as the satellite is not visualizing the whole globe. It is sensing radiation at a certain local time. A constellation of CubeSats could improve spatio-temporal resolution and entail a better representation of the phenomena. This is clearly visible on Figure 2.16.
UVSQ-SAT and INSPIRE-SAT 7 are satellites that will be presented in the manuscript. They are both LEO satellites. Figure 2.16 shows the results from different configurations in the long term (10 years period). It is visible that the observation of the EEI with a satellite implies a bias in the measurement and it is similar for the 2 satellites configuration. The 2 satellites are not equally spaced therefore it could explain the important bias. The measurement would thus not be representative of the value of the EEI.

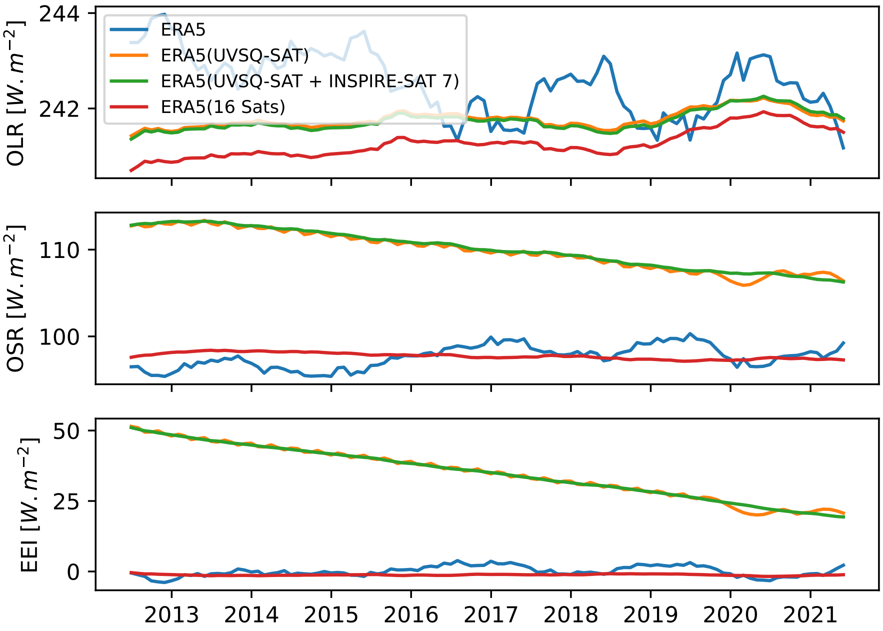

Figure 2.16: 12 Months rolling mean of the TOA outgoing radiation and EEI from ERA5, UVSQ-SAT (simulation), INSPIRE-SAT 7 (simulation), and 16 satellites constellation simulation.

We note that for 16 satellites in orbit, the value of the EEI perceived is consistent with the values of ERA5 data used as a reference. The 16 satellites are equally spaced in LEO Sun-synchronous orbit. We conclude that the number of satellites also plays a role in long-term measurements of the EEI. The aging of the instrument is also major to reach the targeted specifications in the long term.

2.2.3 Spatial Resolution Criterion

According to the specifications from Chapter 1, the spatial resolution of the outgoing terrestrial flux should be around 10 to 100 km to monitor local phenomena such as for example clouds, and aerosols formed from photo-chemistry.

The spatial resolution is defined as the physical dimension that represents a pixel of the maps. It is the size of the surface covered by the instrument at each acquisition. The instrument FOV can be computed from the spatial resolution (Δ_X)

from Equation 2.8:

$$\mathrm{FOV} = 2\arctan\left(\frac{\Delta_X}{z_{\mathrm{sat}}}\right) \tag{2.8}$$

The curvature of the Earth has no significant impact at high resolution (given a very small FOV), simplifications can be made to compute an order of magnitude. To respect the strictest specifications, we must reach 10 km (5 km radius) spatial resolution. The FOV of the instrument must be such that $\tan\left(\frac{\mathrm{FOV}}{2}\right) = \frac{5}{540}$ considering an average altitude of 540 km. The FOV is estimated to be of 1.06°. It corresponds to the characteristics of the instrument on-board the satellite. Instantaneous measurements, meaning corresponding to single pixel instruments covering the whole globe at each time could be done with $\frac{510.1\times10^6}{100} = 510.1 \times 10^4$ satellites where $510.1 \times 10^6\,\mathrm{km}^2$ is the Earth total area. Obviously, this is an unrealistic scenario, the real number of satellites needed is reduced by the will to have a lower temporal resolution and the possibility to realize the measurement with a multi-point instrument.

In order to scan a large part of the ground at each orbit, we can imagine a system composed of several sensors in the form of a strip, or linear sensor and an optical system. The use of the thinnest possible sensors allows to reduce the size of the optical system. We can estimate a field of view of 10° with such a sensor allowing a resolution of 10 km per sub-pixel. The focal length of the lens can be determined by $F = s/FOV$ where s is the sensor's length to get an order of magnitude of about $10\,\mathrm{mm}/0.0185\,\mathrm{rad} = 21.10 \times 10^2\,\mathrm{mm}$. It gives an idea of the overall size of the instrument. The 10° FOV is chosen as it is narrow enough to minimize optical aberrations.

This assumption is purely hypothetical and is provided to illustrate how the measurement may be made without the need to mechanically alter the instrument's tilt to scan the surface.

2.2.4 Temporal Resolution Criterion

Now that the FOV is defined, the configuration must be determined with respect to the temporal resolution criterion. Both of the criteria are directly linked. According to the specifications from Chapter 1, the temporal resolution of the outgoing terrestrial flux should be about 3 hours.

The temporal resolution is, in our case, the revisit period. The satellite revisit period is the time elapsed between observations of the same point on Earth by a satellite. The FOV determined previously plays an important role in the computation.

The larger the FOV, the larger the area visible to the satellite, and the larger the area of the globe scanned. We consider the revisit period as the maximum duration elapsed between observations of the same point on the ground. For two similar orbits, the revisit time will be shorter for a large FOV but this entails worsening the spatial resolution.

To determine the revisit period of a configuration, we are using the previously described tools to propagate the orbits. The revisit period will depend on the location of the observer, on the satellite trajectory, and on the FOV. Therefore, calculations were made at different locations on a gridded map of the whole globe for each satellite. To determine the locations on Earth of the observations we utilized an implementation of the method described in [Swinbank and Purser, 2006]. Their proposed approach involves drawing golden spirals (logarithmic spirals whose growth factor is the golden ratio) on perfect spheres and dispersing the points on those to evenly distribute the points on the globe. We define a period of time for which the revisit times are computed at each location. Given the order of magnitude of the computed revisit periods, it seemed adapted to choose 6 months for the study. The precise date and time of revisit are then combined for all of the satellites of the constellation. Finally, we determine the maximum elapsed duration between two observations. It gives an estimate of the revisit period depending on the location of the observer but it is crucial to select the indicator of revisit period over the whole globe as the objective is to cover the whole globe. The indicator can be to choose the maximum, the median, or other quantities to characterize the constellation and its ability to cover the whole globe. The first phase consists in defining the architecture of the satellite configuration. An example is the Walker constellation. Walker constellations appear to be best for global comprehensive coverage. If there aren't enough satellites to provide continuous coverage, the maximum revisit time is optimized to reduce the number of satellites [Casanova et al., 2012]. In our case, we will define a constellation of several satellites each located on a different orbital plane in a Sun-synchronous orbit. The configurations were described in Section 2.2.2. In those particular configurations, no satellite is able to monitor the North and South poles due to the inclination of the Sun-synchronous orbit. Indeed, Sun-synchronous satellites never pass directly over the poles. We chose to limit the study to latitudes between -80 and 80°. The revisit time is computed for each observable point chosen. Figure 2.17 is a map representing the revisit time for each location on the Globe plate carrée projection. The configuration corresponds to 128 satellites on 128 different equi-spaced planes.

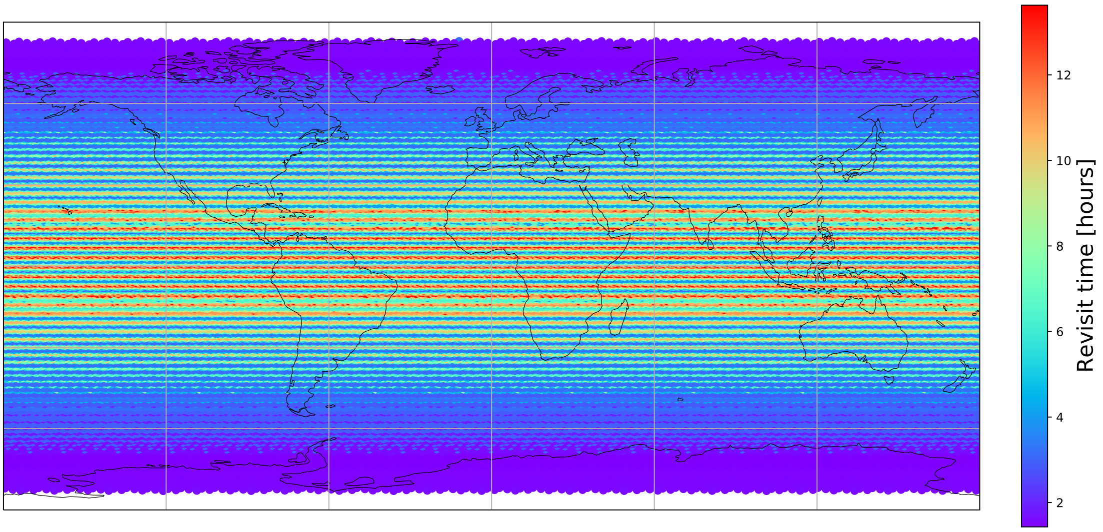

Figure 2.17: Revisit period map for 128 Sun-synchronous satellites.

The figure shows that the revisit times are clearly not homogeneous over the entire map. A specific North/South symmetry is noticeable. Also, the revisit time is more important in the tropics. This is justified by the choice of a configuration with several polar orbit planes.

Figure 2.18 shows the revisit period for different configurations. Each satellite has a 10° FOV and is facing nadir. Three variables are represented, the median of the revisit period, the first and third quartile of the revisit period.

The median is the value that separates the higher half from the lower half of a data, therefore it can be a simple and adequate indicator to characterize the revisit period of the constellation.

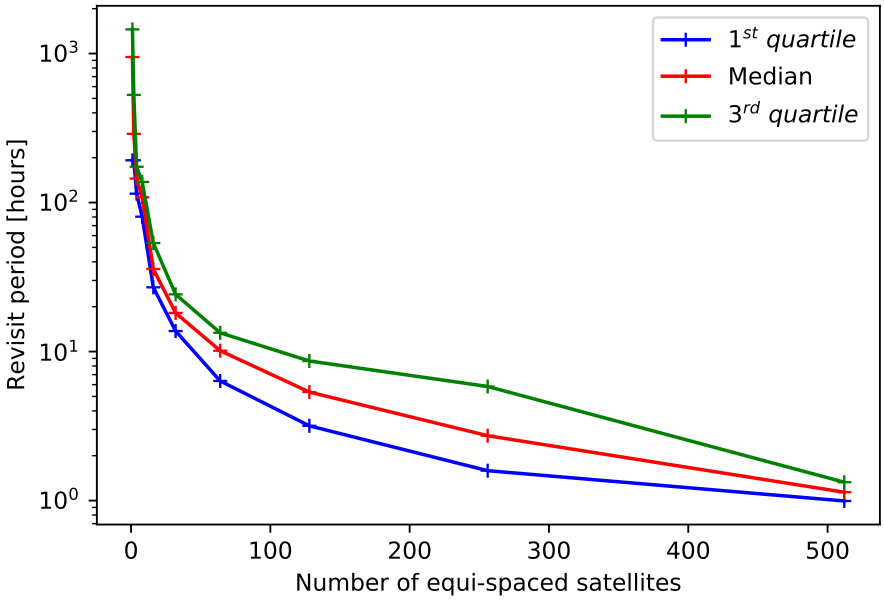

Figure 2.18: Revisit period for equi-spaced Sun-synchronous orbits.

According to this indicator, to reach a 3 h median revisit time over the whole globe, we estimate that between 256 and 512 satellites are necessary on different equi-spaced Sun-synchronous orbital planes. The median revisit time is 5 h and 21 min for the 128 satellites constellation, 2 h and 44 min for the 256 satellites constellation, and 1 h and 8 min for the 512 satellites constellation. Choosing the maximum as a reference will ensure that we stay below a certain revisit time, however, the maximum value can be singular and very far from the rest of the data set. Therefore, the third quartile is preferred here to compare the configurations.

2.2.5 Local Time Criterion

Local time is another important criterion for Earth observation to properly discuss the variations. An example is the monitoring of the diurnal cycle, having satellites monitoring different local times entails a better understanding of those variations. Diurnal changes in deep convective clouds affect incoming shortwave and OLR which are the components of the EEI [Hendon and Woodberry, 1993]. It is crucial as for example, stratospheric clouds follow a diurnal rhythm linked to convective activity [Dauhut et al., 2020]. This could not be monitored by CALIPSO because of its Sun-synchronous orbit and its fixed overpass local time. Those phenomena are nevertheless directly linked to the EEI components. The architecture of the constellation is based on the choice of equi-spaced orbits covering local times. This choice allows monitoring a particular local time with each satellite in order to avoid biases and to study the phenomena related to the true solar time. This makes it possible to monitor almost instantaneously the diurnal cycle with variations of the order of 3 hours, if not to observe the diurnal cycle on an annual average (in the long term). This is crucial to observe the impact of each phenomenon in the climate system.

2.2.6 An Optimal Configuration

Therefore we can establish a configuration that can meet our needs.

Few assumptions were made in the study. Considering the satellites are in Sun-synchronous orbits, about fifty satellites with a FOV of 10° would allow a MAE of the order of a few Wm^{-2} which would suit the accuracy specifications. But this is not the only key parameter. The overall local time coverage and spatio-temporal resolution are crucial.

According to the targeted specifications, the FOV of the instrument should actually be close to 1.06° to reach 10 km on-ground. Given this information, the need for an array of sensors to increase the instrument swath seems necessary to reach a much smaller temporal resolution. For a 10° swath, a constellation of 512 satellites is necessary to reach a revisit period below 3 h revisit period (the revisit period third quartile being 1 h 20 min), while the 256 satellites configuration has a median revisit time below 3 h this is not the case of its third quartile. For 512 satellites, 99% of the revisit period computed (at equispaced locations on Earth between -80° and 80° latitudes) are below 1 h 35 min. The assumptions on the configuration are that we consider only Sun-synchronous orbital planes with several satellites in-orbit on each of them to reach the specifications.

Constellation simulations for revisit period calculation are very computationally intensive (several weeks of calculation). It was therefore not possible to simulate for lots of different configurations and to simulate a map over 3 hours for 512 satellites with a narrow field of view. The satellites are assumed to be pointed toward the nadir. Such a constellation could be developed with the help of precise attitude control.

2.3 Conclusions and Perspectives

A constellation, as opposed to a single satellite, can provide permanent global or near-global coverage, ensuring that at any time, at least one satellite is visible everywhere on Earth. This would allow us to see the phenomena in certain high-impact areas such as the poles and the tropics. It can provide more continuous coverage and can be more resilient to individual satellite failures or other disruptions.

A constellation of satellites is necessary to reach the specifications for the measurement of the radiation balance and to improve the resolution of the measurements carried out for terrestrial flux. However, its architecture has a direct impact on the measurement whether it is specific or not to the radiation balance study.

A determination of the constellation architecture was realized to deduce the number of satellites needed along with the instruments' characteristics to respect the specifications. Important parameters such as the FOV of the satellite or the reconstruction methods are directly put at the center of the challenge. A small FOV directly entails a better spatial resolution but requires more satellites to reach the same temporal resolution as with a larger FOV. Therefore, a constellation of 512 satellites with 10° narrow FOV is necessary to fit the specification mentioned in Chapter 1 reaching 10 km spatial resolution, and 3 h revisit time. Because of the hostile environment in which the instruments are operated, they typically degrade. Radiometers are especially sensitive since their optical parts are unprotected from solar radiation. The degradation can result from a combination of solar irradiation and instrumental contamination, which can cause the polymerization of organic material and, as a result, irreversible deposition of this material on the instruments' optical surfaces [BenMoussa et al., 2013]. Therefore, although it was not part of this study, the aging of the instrument also plays a significant role in order to obtain optimal performance on the measurements. Instrument design could allow for in-orbit degradation tracking and calibration. The theoretical constellation has been defined. In case of development and deployment of such a constellation, further studies would be necessary. The technologies and methods implemented will be very different from those currently implemented. The number of satellites in the constellation must be designed to be insensitive to the risk of satellite failure. The instruments on board will have to be redundant and have been validated in orbit (TRL9). The communication chain with the satellites must be adapted, and a sufficient ground network for telecommunication must be implemented. Actually, the whole process should be adequately adapted to new challenges linked to the mega constellation. The constellation designed as it is, improves coverage of the short-term phenomena at high spatio-temporal dynamics. The choice of Sun-synchronous orbits for the constellation would entail equi-spaced measurements to monitor every local time. It aims to avoid biases and to study phenomena that are linked to true solar time such as convective clouds that have a direct impact on the Earth's radiation budget.

The spatial and temporal resolution of the measurements would be greatly improved by deploying a constellation such as the one described. Compared to the results presented in Chapter 1, this is a great step forward for the measurement of the radiation budget and potentially other variables intrinsically linked to the evolution of the climate. This constellation would make it possible to observe and quantify numerous radiative forcings at short-term dynamics such as radiative impacts of aerosols and clouds which are highly variable spatially and temporally.

The question of space debris is at the center of the current challenges, the constellation of satellites must be as optimized as possible. The number of satellites must be justified and ideal in order not to congest space.

The UVSQ-SAT satellite presented in Chapter 3 is a pathfinder that aims to validate scientific and technological hypotheses with a small satellite before industrializing the monitoring process with a constellation.

Chapter 3

The UVSQ-SAT Mission and Attitude Determination

3.1 The UVSQ-SAT Mission

Figure 3.1: UVSQ-SAT in the cleanroom (credits: LATMOS).

A constellation of satellites is crucial and would be a major improvement in measuring the ERB. This section presents the UVSQ-SAT satellite. Its objective is to validate scientific hypotheses for a future constellation to observe terrestrial radiation. It is the first phase of the future deployment of a constellation of satellites for the measurement of the radiation balance. The satellite is detailed and instrumental and behavior equations are developed.

3.1.1 Objectives and Current State

Scientific Objectives

As explained in [Meftah et al., 2021], UltraViolet & infrared Sensors at high Quantum efficiency on-board a small SATellite (UVSQ-SAT) (Figure 3.1) is a pioneering space-based mission to demonstrate technologies for broadband measurements of ERB [Meftah et al., 2020b]. The mission is part of the International Satellite Program in Research and Education (INSPIRE). The motivation of the UVSQ-SAT mission (INSPIRE-05) is to implement miniaturized disruptive technologies for remote sensing with compact sensors that could be used in the future for a multi-point satellite constellation for observing ECV, namely shortwave and long-wave radiative fluxes at the TOA and UV solar spectral irradiance [Meftah et al., 2018, 2020c]. Measuring the absolute value of the EEI and its variability over time appears to be a very difficult challenge. Ideally, EEI monitoring should be performed with a constellation of satellites in order to resolve as much as possible spatio-temporal fluctuations in EEI which are indicative of the underlying mechanisms driving climate change at global and regional scales. At the present stage, the UVSQ-SAT CubeSat is a demonstrator, expecting future developments and improvements that would then really allow for making use of CubeSat technology for these scientific purposes. The expected performances for UVSQ-SAT are to measure the EEI with a stability per year of $\pm 5\,\mathrm{Wm}^{-2}$ at 1σ [Meftah et al., 2020c]. The UVSQ-SAT EEI expected performances depend on the error budget of several parameters.

Proceedings

During the year 2020, UVSQ-SAT environmental testing and calibrations were carried out. Vibration testing, electromagnetic compatibility tests, calibration with a Xenon lamp and a black body, thermal vacuum, and thermal balance tests, magnetic cleanliness verification of the satellite, and end-to-end tests with the UHF/VHF LATMOS ground-based station were performed (telemetry at 437.020 MHz, telecommand at 145.905 MHz) [Meftah et al., 2021].
After delivery of the satellite to the Cape Canaveral launch pad in the United States, UVSQ-SAT was launched among 142 other spacecrafts (Figure 3.2). A world record at that time. The CubeSat was launched into a Sun-synchronous orbit by the LATMOS with the Falcon 9 rocket on the 24^{th} of January 2021. After a commissioning phase, the routine phase started on the 13^{th} of March 2021. The satellite is on a sun-synchronous orbit around the Earth at an altitude of about 533 km (515 km at perigee), an inclination of 97.5010°, an eccentricity of 0.0014455, a right ascension at the ascending node of 128.4244°, and an argument at the perigee of 94.1573°. The duration of an orbit is about 95.18 min.

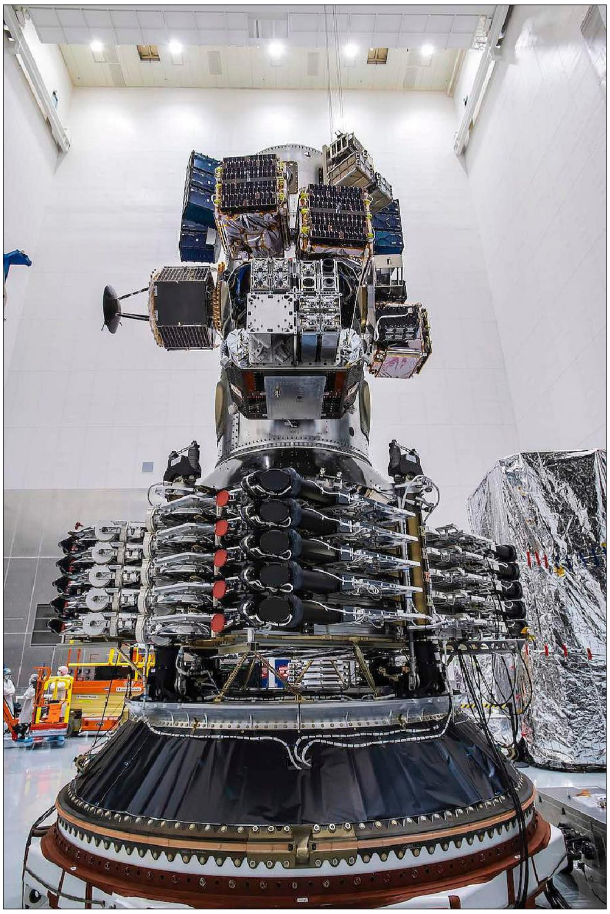

Figure 3.2: Transporter-1 mission with 143 spacecrafts on-board (credits: SpaceX).

3.1.2 Implementation

Spacecraft

UVSQ-SAT is a one-unit (1U) CubeSat with a usable volume of 11.10 cm × 11.10 cm × 11.35 cm (stowed configuration) based on the CubeSat standards from [Puig-Suari et al., 2000]. LATMOS is a prime contractor for the 1U CubeSat and is working with a manufacturer (Innovative Solutions In Space (ISIS)) to construct a specialized satellite platform. Despite its small size, the CubeSat features all of the important subsystems and operations found in bigger spacecraft. The nanosatellite platform is shown in Figure 3.3.

As explained in [Meftah et al., 2020a, 2021], UVSQ-SAT is made up of multiple subsystems, including the mechanical structure, the power subsystem, the thermal control subsystem, the magnetorquer board, the command and data handling subsystem (CDHS), the communication subsystem, and the payload subsystem (ERS, UVS, TSIS, and a 3-axis accelerometer/gyroscope/compass (TW sensor)). The UVSQ-SAT is a CubeSat that adheres to the CubeSat standard and is compatible with an ISIS Quadpack CubeSat deployer. The satellite structure includes two separation switches. This guarantees that the UVSQ-SAT CubeSat remains inactive during the launch and pre-launch phases. All UVSQ-SAT materials and coating selection, are compliant with requirements such as total mass loss (TML) less than 1% and collected volatile condensable material (CVCM) less than 0.1%, according to guidelines for spacecraft cleanliness control (ESA-PSS-51 from European Space Agency). The electric power supply (iEPS) is designed to support power conversion and store and distribute the energy to the UVSQ-SAT CubeSat subsystems.

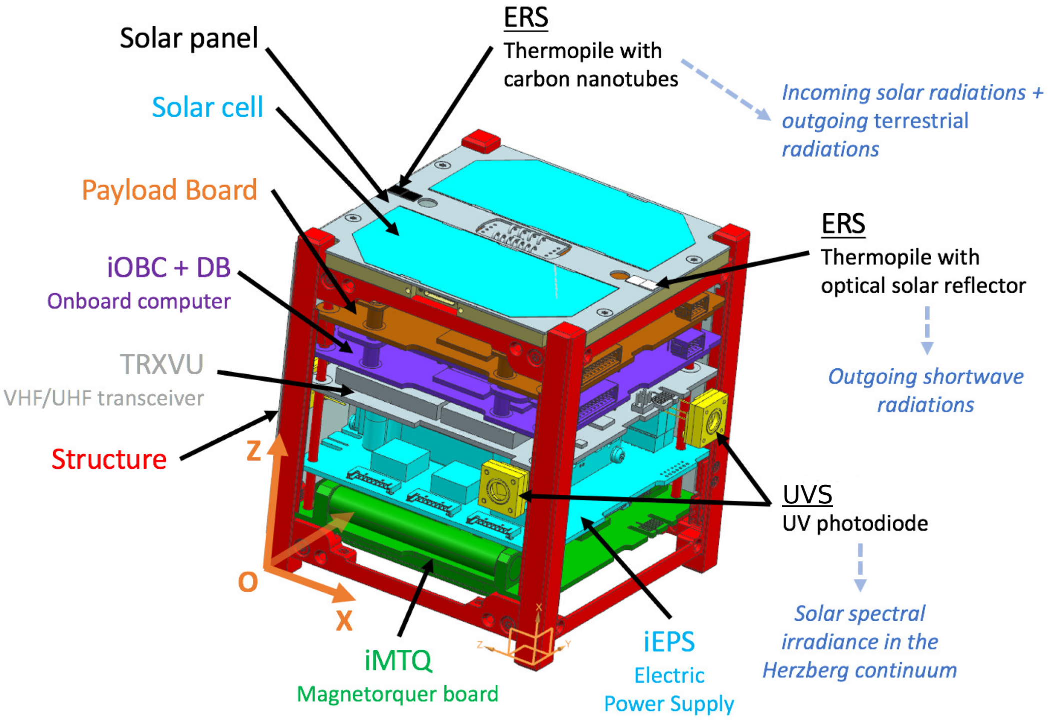

Figure 3.3: The UVSQ-SAT satellite and subsystems [Meftah et al., 2020a].

Power conversion up to 25 W is provided by the iEPS with 3 max power point tracking (MPPT). This would improve the amount of power delivered to the batteries of the CubeSat. By using MPPT, the solar panel cells are connected at the best voltage possible that maximizes solar power, as opposed to using fixed point voltage like other EPS.

Table 3.1: UVSQ-SAT CubeSat Properties from [Meftah et al., 2020a, 2021].

Properties	**Value**	**Comments**
Orbit	SSO	~534 km, LTAN of ~21:30
Design lifetime	1 year for LEO	3 years desired
Launch date	24 January 2021	Launch vehicle: Falcon 9
Size	1 U	11.10 (X) ×11.10 (Y) ×11.35 cm (Z)
Mass	1.2 kg	Nominal mass
Solar cells	12	3G30A solar (Azurspace)
Batteries	22.5 W h @ 8 V	2 batteries (NCR18650B)
Power generated	2.2 W	Orbit average power (OAP) in LEO
Power consumption	1.2 W	Orbit average
ADCS	3-axis magnetometer	Earth magnetic field measures
	3-axis magnetorquer	0.2 Am^2 magnetic dipole
	6 SLCD-61N8 photodiodes	Estimation of the Sun's direction
CDHS and OBC	400 MHz, 32-bit ARM9	Processor
	32 MB SDRAM	Dynamic Random Access Memory
	2×2 GB SD-cards	Non-volatile data storage
	1 MB NOR flash	Code storage
	$\mathrm{I}^2\mathrm{C}$, SPI, UARTs	UART used for debugging iOBC
Data downlink	1.2/9.6 kbps	UHF BPSK (437.020 MHz)
Data uplink	9.6 kbps	VHF FSK (145.905 MHz)
Ground contact station	Less than 1 h per day	LATMOS station
Redundancy stations	NCU, LASP	Satnogs network
Downlink UVSQ-SAT data	1.8 Mbyte per day	Maximum during a day
Uplink UVSQ-SAT data	0.3 Mbyte per day	Maximum during a day
Transponder	Link with amateur radio	Live retransmission of FM signals
Payload	12 ERS	EEI measurements
	1 UVS	UV SSI measurements
	3 TSIS	Part of TSI measurements
	1 TW sensor	Accelerometer, gyro and compass
Launch adapter	Quadpack	CubeSat deployer mass up to 2 kg

IEPS has two batteries (22.5 W h), which supply voltage to several outputs

(3.3 V, 5 V, and unregulated battery line (6-8 V)) over multiple switchable and permanent power lines. The depth of discharge (DoD) of a fully charged battery is 0%. In general, less than 30% DoD is recommended full-time. UVSQ-SAT is equipped with six solar panels made up of 12 Azurspace solar cells. These have a high conversion efficiency (30% for the beginning of life (BOL)), enabling solar power conversion of up to 2.2 W per 1 U area in low Earth orbit. The satellite properties in terms of hardware, payload, and orbit are detailed in Table 3.1.

Payload

The UVSQ-SAT satellite described by [Meftah et al., 2020a] is equipped with different subsystems and sensors. As mentioned in [Finance et al., 2021a], the instruments to measure terrestrial radiative flux are six photodiodes in the visible domains, six Earth radiative sensors (ERS) with an Optical Solar Reflector, and six ERS sensors with carbon nanotubes (CNT).

Ground segment (Antenna/MOC/SOC)

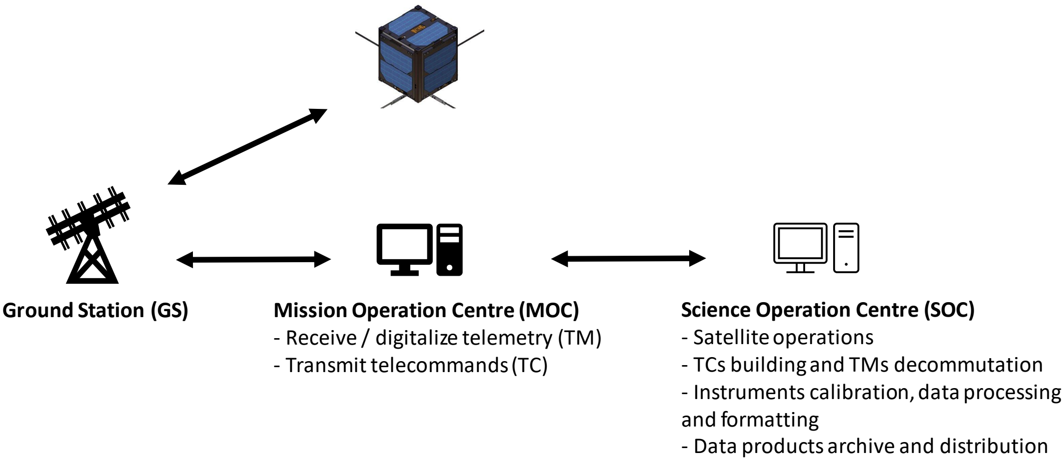

Figure 3.4: Ground segment architecture.

The ground segment of the UVSQ-SAT satellite (Figure 3.4) is based in the LATMOS. Its objective is to retrieve the data from the satellite to distribute it to scientists. It is composed of an antenna positioned on the roof of the laboratory and controlled by a computer to aim toward the satellite. The mission operation center (MOC) aims to communicate with the satellite through telecommand and telemetry reception. The scientific operation center (SOC) allows the planning of the different satellite operations including uplink and downlink. It prepares, calibrates, and formats the data before archiving and distributing the products.

3.2 UVSQ-SAT Instrumental Equations

The instruments on-board the satellite measure radiative fluxes. In order to explain, understand and calculate the fluxes it is important to apply the theory behind the measurement of each sensor and to determine the instrumental equations. Those parts are described in [Meftah et al., 2021].

3.2.1 Earth's Radiative Sensors

Each face of the UVSQ-SAT satellite has two ERS sensors, which have different optical coatings (carbon nanotubes or optical solar reflectors). The properties of the coatings were characterized in the lab (solar absorption, hemispherical emissivity, bidirectional reflectance distribution function (BRDF)). The principle of these ERS sensors with their associated coatings is to convert thermal energy into electrical energy. The output voltage (V) is passively induced from the thermopile proportional to the heat flux (Wm^{-2}) through the sensor or similarly the temperature gradient across the thin-film substrate and the number of thermocouple junction pairs. The output voltage is conditioned by an electronic unit and converted into analog-to-digital units (ADU) and is read by the UVSQ-SAT onboard computer (OBC) thanks to a serial peripheral interface (SPI) bus, and stored by the OBC. Once data are retrieved, the ADU signals S_{ADU} are converted into physical units to express the incident flux measurements Φ_{in} in on an ERS sensor using the transfer function (Equation 3.1):

$$\Phi_{in} = \left(\frac{S_{\mathrm{ADU}}(T_s, T_b) - V_{\mathrm{ADU}}^{\mathrm{ref}}(T_b)}{N_{\mathrm{samp}}} + C_1(T_s, T_b) \right) \times \frac{1}{G(T_b)} \times \frac{1}{\mathrm{Sens}(T_s)} + C_2(T_s) \quad (3.1)$$

where V_{ADU} is a reference voltage, N_{samp} is the number of samples for measurement, $G(T_b)$ is the gain of the electronic unit, Sens is the sensitivity of the sensor (calibration in the lab), C_1 and C_2 are corrective offsets, which depend on the temperature of the sensor. In the case of thermopiles, $C_2 = -\epsilon\sigma T_s^4$. ϵ is the hemispherical emissivity of the thermopile coating and T_s is the ERS sensor temperature. T_b represents the temperature of the sensor's electronic board. The total incident flux (Φ_{in}) on each ERS sensor is the sum of the solar incident flux, the planetary incident flux (Φp_{in}), and the albedo incident flux (Φa_{in}). The incident solar flux is considered to be known (TSI is measured precisely elsewhere). By combining information from two ERS sensors on the same face (sensor with carbon nanotubes (solar absorption close to 1) and sensor with optical solar reflector (solar absorption less than 0.1)), we get the albedo (α) of the planet and the OLR at a measurement point located in latitude and longitude on the world map (Equations 3.2 and 3.3 are given as example if a satellite face observes at the nadir):

$$\Phi p_{in} = \epsilon \times OLR \times \left(\frac{R_{\mathrm{Earth}}}{R_{\mathrm{Earth}} + z_{\mathrm{sat}}} \right)^2 \quad (3.2)$$

$$\Phi a_{in} = \alpha \times a \times \left(\frac{R_{\mathrm{Earth}}}{R_{\mathrm{Earth}} + z_{\mathrm{sat}}} \right)^2 \times \cos(\xi) \times TSI \times \left(\frac{1\ \mathrm{au}}{d_{\mathrm{Sun/Sat}}} \right)^2 \quad (3.3)$$

where R_{Earth} is Earth's radius, z_{sat} is the satellite altitude, a is the ERS (coating) solar absorption, ξ is the solar zenith angle, 1 au is one astronomical unit, and $d_{\mathrm{Sun/Sat}}$ is the distance UVSQ-SAT—Sun.

During satellite eclipse periods, two ERS sensors on the same face measure only OLR, which allow obtaining direct measurements and inter-calibration of the sensors.

3.2.2 Photodiodes

Each face of the satellite has at least one photodiode which observes external fluxes. A photodiode is a semiconductor p-n junction device that converts light into an electrical current. The resulting current is converted into ADU and stored by the UVSQ-SAT onboard computer. Once data are retrieved, the ADU signals Sp_{ADU} are converted into physical units to express the measurements Φ_{pho} using the transfer function (Equation 3.4):

$$\Phi_{\mathrm{pho}} = \left(\frac{Sp_{\mathrm{ADU}}(T_{\mathrm{pho}}, T_b) - V^{\mathrm{ref}}_{\mathrm{ADU}}(T_{\mathrm{pho}}, T_b)}{Np_{\mathrm{samp}}} + Cp_1(T_{\mathrm{pho}}, T_b) \right) \times \frac{1}{G_{\mathrm{pho}}(T_b)} \times \frac{1}{S_{\mathrm{pho}}(T_{\mathrm{pho}})} \tag{3.4}$$

where Np_{samp} is the number of samples for measurement, G_{pho} is the gain of the electronic unit, $S_{\mathrm{pho}}(T_{\mathrm{pho}})$ is the responsivity of the photodiode (calibration done by the manufacturer), Cp_1 is a corrective offset, which depends on the temperature of the photodiode. T_{pho} is the satellite structure temperature close to the photodiode.

For the six photodiodes that measure the TSI and the OSR, the albedo of the Earth can be obtained using an equation similar to that proposed in Equation 3.3.

3.2.3 Map Reconstruction Method from UVSQ-SAT Observation Time Series

Time series of the albedo and the OLR at the TOA are obtained from the observations made by the dedicated sensors on-board UVSQ-SAT.

Physically, each measurement of these time series represents the integral of the signal of interest (OLR, albedo) and depends in practice on a large number of parameters among which the bidirectional reflectance distribution function of the Earth's surface, the opacity of the atmosphere, the spectral and angular sensitivities of the sensors and their FOV. In particular, concerning opacity, it depends on factors such as aerosol composition, clouds, temperature, or pressure.

In the first approach, we consider that each measurement results from the contribution of a Gaussian distribution $G(\theta_{i,j})$ of points located at the surface of the Earth [Meftah et al., 2021]. Let the surface of the Earth be modeled by a regular grid whose coordinates are expressed with latitude and longitude. Each pixel (i, j) of the grid is defined by its longitude λ_i and latitude ϕ_j coordinates and by its area S_{ij} (Equation 3.5):

$$S_{ij} = R^2 \times \cos(\phi_j)\Delta\lambda_i\Delta\phi_j \tag{3.5}$$

where $\Delta\lambda_i$, $\Delta\phi_j$ are the sizes in radians of the pixel at longitude λ_i and latitude ϕ_j.

The observed flux by UVSQ-SAT $F_{sat}(\lambda_{\text{sat}}, \phi_{\text{sat}})$ is given by (Equation 3.6):

$$F_{sat}(\lambda_{\text{sat}}, \phi_{\text{sat}}) = \frac{\Sigma_{i,j}\Omega_{i,j}G_{i,j}F_{i,j}}{\Sigma_{i,j}\Omega_{i,j}G_{i,j}} \tag{3.6}$$

where $\Sigma_{i,j}$, $\Omega_{i,j}$, $G_{i,j}$ and $F_{i,j}$ are defined in Equations 2.1-2.5. Finally, to reconstruct the map of what was measured by UVSQ-SAT, i.e., $F_{\text{sat}}(\lambda_{\text{sat}}, \phi_{\text{sat}})$, we calculate the functions $\Omega_{i,j}$, $G_{i,j}$ for the satellite track to find the flux $F_{i,j}$ associated with each pixel.

3.2.4 Dissociation and Calculation of Terrestrial Flux

Due to redundancy in the measurements justified by the distribution of the sensors on each side of the spacecraft, it is possible to combine those sensors to compute the flux of interest. Therefore it entails multiple equations to dissociate the different flux based on the wavelength-band of the detector to determine the part of reflected solar flux or outgoing terrestrial thermal flux. The incident flux on the detector i is defined as ϕ_i in Equation 3.7 as mentioned in [Meftah et al., 2020a]:

$$\begin{aligned}\phi_i = A_i \cos(\theta_i)\frac{d^2_{\text{Sun/Earth}}}{d^2_{\text{Sun/Sat}}} \int_\lambda SI(\lambda)\alpha_i(\lambda)d\lambda \\ +A_i F_{\text{i/Earth}} \int_\lambda \varepsilon_i(\lambda)EI(\lambda)d\lambda \\ +A_i \frac{d^2_{\text{Sun/Earth}}}{d^2_{\text{Sun/Sat}}} F_{\text{i/Earth}} \int_\lambda \alpha SI(\lambda)a_i(\lambda)d\lambda \\ +\sum_{j=1}^{N} GL_{i-j}(T_j - T_i) + \sigma\sum_{j=1}^{N} GR_{i-j}(T_j^4 - T_i^4) + Qr_i\end{aligned} \tag{3.7}$$

where i is the index of the ERS thermopile detector, T_i is the temperature of thermopile i (K), A_i is the surface area of thermopile i (m^2), θ_i is the angle between the solar direction and the normal of the thermopile, $d_{\text{Sun/Earth}}$ is the Sun/Earth distance (km), $d_{\text{Sun/Sat}}$ is the distance between the satellite and the Sun (km), $SI(\lambda)$ is the spectral solar irradiance in $\mathrm{Wm^{-2}µmm^{-1}}$, λ is the wavelength in µm, $a_i(\lambda)$ is the solar absorption of thermopile i, $F_{\text{i/Earth}}$ is the Earth view factor, $\varepsilon_i(\lambda)$ is the normal emittance of thermopile i, $EI(\lambda)$ is the spectral Earth irradiance in $\mathrm{Wm^{-2}µmm^{-1}}$, α is the Earth's albedo, GL is the conductive couplings of thermopile i ($\mathrm{WK^{-1}}$), GR is the radiative couplings of thermopile i ($\mathrm{WK^{-1}}$) σ is the Stefan–Boltzmann constant ($5.6704 \times 10^{-8}\,\mathrm{Wm^{-2}K^{-4}}$), and Qr_i is the absorbed residual power (Moon, planets, etc.). This yields solving a set of N differential nonlinear equations to obtain OLR ($\int_\lambda EI(\lambda)d\lambda$) and OSR ($\int_\lambda aSI(\lambda)d\lambda$).

$$\phi_i/A_i - \left(\sum_{j=1}^{N} GL_{i-j}(T_j - T_i) + \sigma \sum_{j=1}^{N} GR_{i-j}(T_j^4 - T_i^4) + Qr_i\right)/A_i = \Phi_i \tag{3.8}$$

$$\begin{aligned}\Phi_i = \cos(\theta_i)\frac{d^2_{\text{Sun/Earth}}}{d^2_{\text{Sun/Sat}}}\int_\lambda SI(\lambda)a_i(\lambda)d\lambda + F_{\text{i/Earth}}\int_\lambda \varepsilon_i(\lambda)EI(\lambda)d\lambda \\ +\frac{d^2_{\text{Sun/Earth}}}{d^2_{\text{Sun/Sat}}}F_{\text{i/Earth}}\int_\lambda aSI(\lambda)a_i(\lambda)d\lambda\end{aligned} \tag{3.9}$$

We note Φ_i as the first part of the equation, we have then Equation 3.10 as follows:

$$\Phi_i = \cos(\theta_i)a_i TSI\frac{d^2_{\text{Sun/Earth}}}{d^2_{\text{Sun/Sat}}} + F_{\text{i/Earth}}\varepsilon_i OLR + F_{\text{i/Earth}}a_i\frac{d^2_{\text{Sun/Earth}}}{d^2_{\text{Sun/Sat}}}OSR \tag{3.10}$$

where, TSI is the total solar irradiance, OLR is the outgoing longwave radiation, OSR is the outgoing shortwave radiation.

The global equation combining the photodiodes and thermopiles is as follows (Equation 3.11):

$$\begin{bmatrix}\Gamma_{\text{cnt}}\\ \Gamma_{\text{photo}}\\ \Gamma_{\text{osr}}\end{bmatrix}\begin{bmatrix}OLR\\ OSR\end{bmatrix} = \begin{bmatrix}\Sigma_{\text{cnt}}\\ \Sigma_{\text{photo}}\\ \Sigma_{\text{osr}}\end{bmatrix} \tag{3.11}$$

For n_i being defined as the i element of the list $[+X_{\text{sat}}, -X_{\text{sat}}, +Y_{\text{sat}}, -Y_{\text{sat}}, +Z_{\text{sat}}, -Z_{\text{sat}}]$.

$$\Gamma_{cnt\ i,1} = F_{[n_i/\text{Earth}]}\varepsilon_{[cnt/n_i]} \text{ and, } \Gamma_{cnt\ i,2} = F_{[n_i/\text{Earth}]}a_{[cnt/n_i]} \tag{3.12}$$

$$\Gamma_{\text{photo i, 1}} = 0 \text{ and, } \Gamma_{\text{photo i, 1}} = F_{[n_i/\text{Earth}]}a_{[\text{photo}/n_i]}\rho_{photo[n_i/\text{Earth}]} \tag{3.13}$$

where $\rho_{\text{photo[i/Earth]}}$ is the angular function that represents the angular response of the photodiode. The angular response is defined for an angle β_{limit} for which the sensor stops sensing the flux, in Equation 3.14 as follows:

$$\rho_{photo}(\beta) = \begin{cases} 1 & \text{for} \quad |\beta| < \beta_{\text{limit}} \\ 0 & \text{for} \quad |\beta| \geq \beta_{\text{limit}} \end{cases} \tag{3.14}$$

$$\Gamma_{osr\ i,1} = F_{[n_i/\text{Earth}]}\varepsilon_{[osr/n_i]} \text{ and, } \Gamma_{osr\ i,2} = F_{[n_i/\text{Earth}]}a_{[osr/n_i]} \tag{3.15}$$

$$\Sigma_{cnt\ i} = \Phi_{cnt}(n_i) - \cos(\theta_{[n_i]})a_{[cnt/n_i]}TSI\frac{d^2_{\text{Sun/Earth}}}{d^2_{\text{Sun/Sat}}} \tag{3.16}$$

$$\Sigma_{\text{photo i}} = \Phi_{\text{photo}}(n_i) - \cos(\theta_{[n_i]})a_{[\text{photo}/n_i]}TSI\frac{d^2_{\text{Sun/Earth}}}{d^2_{\text{Sun/Sat}}} \tag{3.17}$$

$$\Sigma_{osr\ i} = \Phi_{osr}(n_i) - \cos(\theta_{[n_i]})a_{[osr/n_i]}TSI\frac{d^2_{\text{Sun/Earth}}}{d^2_{\text{Sun/Sat}}} \tag{3.18}$$

The system presented previously can be solved using the least square method with bounds on the variables. The difference between the first product and the right part of the equation is to be optimized for the value of OLR and OSR to be determined.

3.2.5 Attitude Determination is Directly Linked to Flux Computation uncertainty

The incident flux is ϕ_{ref} and can be incident solar flux or incident terrestrial flux on each of the detectors on the satellite. We will consider each sensor separately from the others to quantify the uncertainty. The true amount of flux received by a sensor will be defined as ϕ_{detect}. For example, defining the angle between the normal to the sensor and the direction of the Sun as θ_{Sun} we write as follows (Equation 3.19):

$$\phi_{\text{detect/Sun}} = \phi_{\text{ref/Sun}}.\cos(\theta_{\text{Sun}}) \tag{3.19}$$

This is done the same for terrestrial flux and we get Equation 3.20:

$$\phi_{\text{detect/Earth}} = \phi_{\text{ref/Earth}}.F(\beta) \tag{3.20}$$

where $F(\beta)$ is the view factor between the Earth and the sensor with β the angle between the normal to the sensors and the Earth's nadir. The view factor is defined as follows.
If $|\beta| \leq \arccos(1/h)$, $F(\beta)$ is defined in Equation 3.21:

$$F(\beta) = \frac{\cos(\beta)}{h^2} \tag{3.21}$$

If $|\beta| > \arccos(1/h)$, $F(\beta)$ is defined in Equation 3.22:

$$\begin{aligned} F(\beta) = \frac{1}{\pi h^2}&\left(\cos(\beta)\arccos(y) - x\sin(\beta)\sqrt{1-y^2}\right) \\ &+\frac{1}{\pi}\arctan\left(\frac{\sin(\beta)\sqrt{1-y^2}}{x}\right) \end{aligned} \tag{3.22}$$

with, $h \equiv d_{\text{Sat/Earth}}/R_{\text{Earth}}$, $d_{\text{Sat/Earth}}$ is the distance from the satellite to the center of the Earth and R_{Earth} is the Earth radius, $x \equiv \sqrt{h^2-1}$ and $y \equiv \cot(\beta)$.

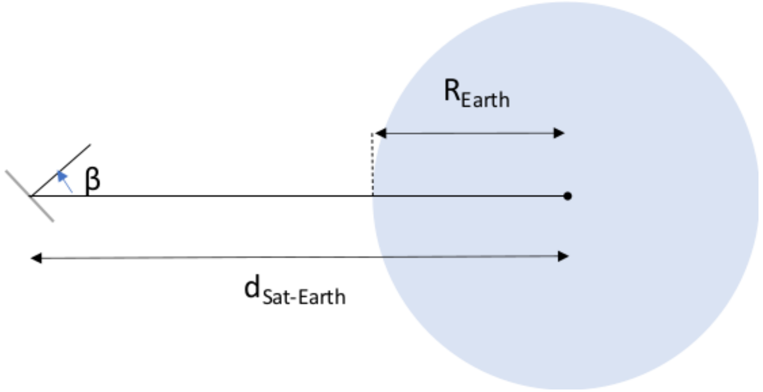

Figure 3.5: Diagram of the terrestrial view factor from a sensor on-board the satellite.

If we consider an error to be defined on the angle θ_{Sun} or β we have Equation 3.23:

$$\phi_{\text{detect/Sun}} = \phi_{\text{error/Sun}}.\cos\left(\theta_{\text{Sun}} + \Delta\theta_{\text{Sun}}\right) \text{ or, } \phi_{\text{detect/Earth}} = \phi_{\text{error/Earth}}.F(\beta + \Delta\beta) \tag{3.23}$$

We define γ_{Sun} as the ratio between the computed incident Solar flux and the true Solar flux. γ_{Earth} is the ratio in the case of terrestrial flux. They are defined in Equation 3.24 and 3.25.

$$\gamma_{\text{Sun}} = \frac{\phi_{\text{error/Sun}}}{\phi_{\text{ref/Sun}}} = \frac{\cos\left(\theta_{\text{Sun}}\right)}{\cos\left(\theta_{\text{Sun}} + \Delta\theta_{\text{Sun}}\right)} \tag{3.24}$$

$$\gamma_{\text{Earth}} = \frac{\phi_{\text{error/Earth}}}{\phi_{\text{ref/Earth}}} = \frac{F(\beta)}{F(\beta + \Delta\beta)} \tag{3.25}$$

Given an uncertainty on θ_{Sun} and β we can compute the uncertainty equivalent on the ratio presented. The uncertainty is increasing as the β angle increases. Therefore we choose to consider the worst-case scenario where the angle is equal to the magic angle of $\arccos\left(\frac{1}{\sqrt{3}}\right)$ as it is the angle where the nadir direction would be the furthest from each normal to the sensors. As the uncertainty of the attitude increases so does the one of the flux. The uncertainty of the solar flux is more important than the terrestrial radiation. For example, for an uncertainty on β of about 10° the uncertainty on the ratio is equal to 0.15°. Given an average terrestrial longwave radiation of about 240 Wm^{-2} the uncertainty is equivalent to 36 Wm^{-2}. This shows the importance of determining the attitude of the spacecraft with accuracy. Actually, the accuracy of the flux computation is better than the value mentioned here as for the UVSQ-SAT, the sensors are deployed on each side of the CubeSat. Therefore, the same measurement is done by several sensors. And in the calculation, it is really rare in fact to reach the highest uncertainty equivalent to an angle of 54.74°.

To conclude means were deployed to develop the process, from integration, calibration, to TM/TC communication and data processing. The instrumental equations were precisely described and directly used to calculate and dissociate the different flux observed by the instruments. The attitude determination of the satellite is crucial for those computations. This is closely related to the restitution of the flux

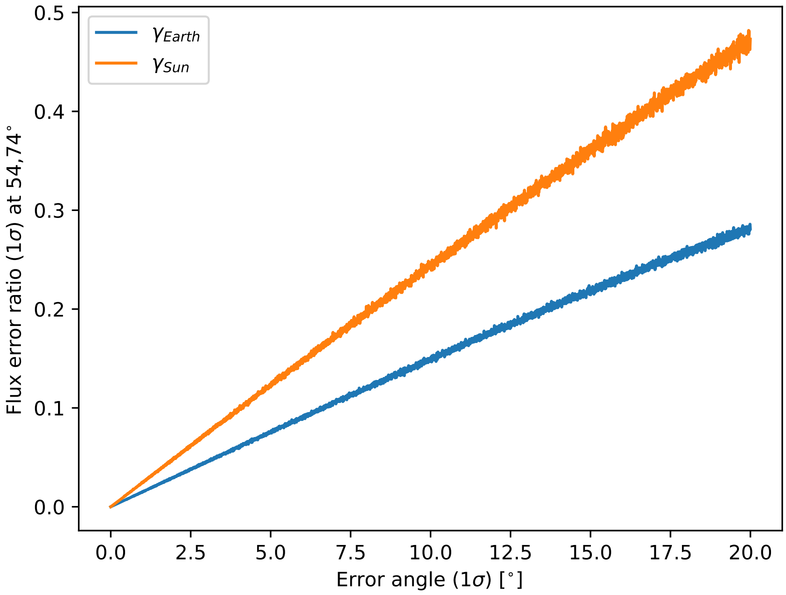

Figure 3.6: Uncertainty on the flux ratio defined in Equation 3.24 and 3.25 based on the uncertainty on the angle θ_{Sun} for Solar flux and β for terrestrial flux.

and therefore of the maps. These methods will be explained in the next section. The methods developed hereafter are for a part totally new and original and for another part very rarely described in articles. In the literature, the methods are usually presented using simulations and not real in-orbit data. Moreover, these methods are specific to the UVSQ-SAT satellite but can be adapted to other space missions by following the implementation logic. These applications are therefore to our knowledge unique and very little detailed in the application to real data.

3.3 Ground Testing and Validation of a Neural Network to Determine the CubeSat Attitude

3.3.1 Introduction

The UVSQ-SAT satellite presented in Section 3.1 does not have a dedicated active attitude determination and control system as can be found in larger satellites (star tracker, dedicated sun sensors, reaction wheels). Nevertheless, the knowledge of the attitude has a direct effect on the restitution of the terrestrial flux. The more precisely this is known, the more precise the flux calculation will be.

UVSQ-SAT being a CubeSat in the standard format, the methods used for this platform could be usable on other missions (depending on the interest of the payload embraced for the attitude restitution). Despite the fact that no dedicated system is onboard the satellite, a lot of information is recorded and transmitted by the satellite. This information ranges from radiative payloads to satellite health data. This data informs us about the evolution of the satellite in its environment and thus about its behavior and orientation. The idea is attributed to the fact that scientific sensors and housekeeping data can be of great importance to locate the Earth and the Sun from the satellite perspective.

Artificial intelligence and more particularly neural networks can allow us to extract the desired information which is the orientation of the satellite. This data allows us to dissociate and calculate the different terrestrial flows. In supervised learning, the machine is taught with well-labeled training data and then anticipates the output based on that data. The training data presented to the computers act as the supervisor. A supervised learning algorithm's goal is to discover a mapping function that will connect the input variables to the output variables even if the link is relatively complex and variables dependent. In the case of attitude determination, each sensor may have a different response and anticipation would be complicated. Moreover, noise anomalies should be detected and not have any repercussions on attitude determination.

Section 3.3.2 presents the stakes and the validation of a proof of concept on the ground realized with the flight model of the UVSQ-SAT satellite.

3.3.2 Paper: A New Method Based on a Multilayer Perceptron Network to Determine In-Orbit Satellite Attitude for Spacecrafts without Active ADCS Like UVSQ-SAT

As we have seen in Chapter 1, the EEI is considered an ECV that has to be monitored continuously from space to study climate change. However, accurate TOA radiation measurements remain very challenging. Ideally, as explained in Chapter 2 EEI monitoring should be performed with a constellation of satellites in order to resolve as much as possible spatio-temporal fluctuations in EEI which contain important information on the underlying mechanisms driving climate change. Chapter 3 presents that the monitoring of EEI and its components is the main objective of the UVSQ-SAT pathfinder nanosatellite, the first of its kind in the construction of a future constellation. UVSQ-SAT does not have an active attitude determination system that is necessary for the calculation of EEI from satellite radiation measurements. This paper presents a new effective method to determine the UVSQ-SAT's in-orbit attitude based on a deep learning algorithm. One of the objectives is to estimate the satellite attitude precisely enough to retrieve the radiative fluxes on each side of the satellite with an uncertainty of less than $\pm 5\,\mathrm{Wm}^{-2}$ (1σ). This innovative technology is applicable to any other satellite that lacks an active attitude determination or control mechanism thanks to its versatility. A ground-based calibration experiment with varying attitudes is done to assess the method's accuracy, with the Sun providing the radiative flux reference. According to the estimation of the satellite ground-based attitude, the uncertainty on the solar flux retrieval is about $\pm 16\,\mathrm{Wm}^{-2}$ (1σ). Limits of the test and perspectives are discussed as a very similar algorithm will be implemented and used in-orbit for UVSQ-SAT.

remote sensing

Article

A New Method Based on a Multilayer Perceptron Network to Determine In-Orbit Satellite Attitude for Spacecrafts without Active ADCS Like UVSQ-SAT

Adrien Finance [1,2], Mustapha Meftah [1,*], Christophe Dufour [1], Thomas Boutéraon [1], Slimane Bekki [1], Alain Hauchecorne [1], Philippe Keckhut [1], Alain Sarkissian [1], Luc Damé [1] and Antoine Mangin [2]

[1] Université de Versailles Saint-Quentin-en-Yvelines, Université Paris-Saclay, Sorbonne Université (SU), CNRS, LATMOS, 11 Boulevard d'Alembert, 78280 Guyancourt, France; Adrien.Finance@latmos.ipsl.fr (A.F.); Christophe.Dufour@latmos.ipsl.fr (C.D.); Thomas.Bouteraon@latmos.ipsl.fr (T.B.); Slimane.Bekki@latmos.ipsl.fr (S.B.); Alain.Hauchecorne@latmos.ipsl.fr (A.H.); Philippe.Keckhut@latmos.ipsl.fr (P.K.); Alain.Sarkissian@latmos.ipsl.fr (A.S.); Luc.Dame@latmos.ipsl.fr (L.D.)

[2] ACRI-ST—CERGA, 10 Avenue Nicolas Copernic, 06130 Grasse, France; Antoine.Mangin@acri-st.fr

* Correspondence: Mustapha.Meftah@latmos.ipsl.fr

Abstract: Climate change is largely determined by the radiation budget imbalance at the Top Of the Atmosphere (TOA), which is generated by the increasing concentrations of greenhouse gases (GHGs). As a result, the Earth Energy Imbalance (EEI) is considered as an Essential Climate Variable (ECV) that has to be monitored continuously from space. However, accurate TOA radiation measurements remain very challenging. Ideally, EEI monitoring should be performed with a constellation of satellites in order to resolve as much as possible spatio-temporal fluctuations in EEI which contain important information on the underlying mechanisms driving climate change. The monitoring of EEI and its components (incoming solar, reflected solar, and terrestrial infrared fluxes) is the main objective of the UVSQ-SAT pathfinder nanosatellite, the first of its kind in the construction of a future constellation. UVSQ-SAT does not have an active determination system of its orientation with respect to the Sun and the Earth (i.e., the so-called attitude), a prerequisite in the calculation of EEI from the satellite radiation measurements. We present a new effective method to determine the UVSQ-SAT's in-orbit attitude using its housekeeping and scientific sensors measurements and a well-established deep learning algorithm. One of the goals is to estimate the satellite attitude with a sufficient accuracy for retrieving the radiative fluxes (incoming solar, reflected solar, terrestrial infrared) on each face of the satellite with an uncertainty of less than ± 5 Wm^{-2} (1σ). This new method can be extended to any other satellites with no active attitude determination or control system. To test the accuracy of the method, a ground-based calibration experiment with different attitudes is performed using the Sun as the radiative flux reference. Based on the deep learning estimation of the satellite ground-based attitude, the uncertainty on the solar flux retrieval is about ± 16 Wm^{-2} (1σ). The quality of the retrieval is mainly limited by test conditions and the number of data samples used in training the deep learning system during the ground-based calibration. The expected increase in the number of training data samples will drastically decrease the uncertainty in the retrieved radiative fluxes. A very similar algorithm will be implemented and used in-orbit for UVSQ-SAT.

Keywords: climate; earth energy imbalance; satellite; remote sensors; deep learning method

check for updates

Citation: Finance, A.; Meftah, M.; Dufour, C.; Bouteraon, T.; Bekki, S.; Hauchecorne, A.; Keckhut, P.; Sarkissian, A.; Damé, L.; Mangin, A. A New Method Based on a Multilayer Perceptron Network to Determine In-Orbit Satellite Attitude for Spacecrafts without Active ADCS Like UVSQ-SAT. *Remote Sens.* **2021**, *13*, 1185. https://doi.org/10.3390/rs13061185

Academic Editors: Ka Lok Chan and Lefei Zhang

Received: 12 January 2021
Accepted: 14 March 2021
Published: 21 March 2021

1. Introduction

UltraViolet & infrared Sensors at high Quantum efficiency on-board a small SATellite (UVSQ-SAT) is a pioneering space-based mission to demonstrate technologies for broadband measurements of Earth Radiation Budget (ERB) [1]. The mission is part of the International Satellite Program in Research and Education (INSPIRE). The motivation of the UVSQ-SAT mission (INSPIRE-05) is to implement miniaturized disruptive technologies for remote sensing with compact sensors that could be used in the future for a multi-point satellite constellation for observing Essential Climate Variables (ECV), namely shortwave and longwave radiative fluxes at the Top Of the Atmosphere (TOA) and UV solar spectral irradiance [2,3]. As a result of the increasing levels of infrared (IR) radiation-trapping greenhouse gases (GHGs), the global energy budget is not balanced with the excess energy accumulating in the Earth system. As a response, global mean surface temperatures increase in order to enhance the outgoing terrestrial IR radiation and thus restore the Earth energy balance. Measuring the absolute value of the Earth's Energy Imbalance (EEI) and its variability over time appears to be a very difficult challenge. Indeed, EEI is a measure of the energy accumulation rate and hence of the warming trend of the Earth system. EEI is derived from the simultaneous measurements of its different components: incoming solar, reflected solar, and terrestrial infrared radiative fluxes. Ideally, EEI monitoring should be performed with a constellation of satellites in order to resolve as much as possible spatio-temporal fluctuations in EEI which are indicative of the underlying mechanisms driving climate change at global and regional scales. The relevant scientific goal is to be able to detect any EEI long-term trend with a target accuracy of 1/10 of the expected signal of 0.5–1.0 Wm^{-2} in the global mean during a decade [4–6]. These EEI scientific objectives are extremely relevant and have not been achieved so far. At the present stage, the UVSQ-SAT CubeSat is a demonstrator, expecting future developments and improvements that would then really allow for making use of CubeSat technology for these scientific purposes. The expected performances for UVSQ-SAT are to measure the EEI with a stability per year of ± 5 Wm^{-2} at 1σ [1]. The UVSQ-SAT EEI expected performances depend on the error budget of several parameters. The in-orbit attitude determination of the satellite is one of these parameters, which represents a random error. Thus, the accurate determination of the UVSQ-SAT CubeSat in-orbit attitude is essential and implies an EEI determination that should be less than $\pm 5\,Wm^{-2}$ at 1σ.

To measure the EEI at the TOA, the UVSQ-SAT satellite has Earth Radiative Sensors (ERS) on each face of the CubeSat. The main goal of the UVSQ-SAT mission is to measure with accuracy the incoming solar radiation (Total Solar Irradiance (TSI)) and the Earth outgoing radiation (EOR = TOA Outgoing Longwave Radiation (OLR) + Shortwave Radiation (OSR)). There are two different strategies to measure and recover all Earth radiative fluxes (solar, albedo, infrared) from UVSQ-SAT sensors. The first one is to compute an average flux on the six different faces of the CubeSat as explained in details by [1]. However, this method implies identical responsivity and the same bidirectional reflectance distribution function (BRDF) for all sensors of all faces of the CubeSat. The second strategy is to compute the radiative fluxes (solar, albedo, infrared) for each face of the spacecraft. This method implies a good knowledge of the UVSQ-SAT's in-orbit attitude. However, the UVSQ-SAT CubeSat does not have an attitude control system due to its compact design. Indeed, no instrument is integrated on-board the UVSQ-SAT CubeSat to determine its attitude (i.e., orientation in the reference frame) explicitly. For this reason, a new method based on a deep learning algorithm was developed to determine accurately the UVSQ-SAT in-orbit attitude using its on-board housekeeping and scientific sensors' measurements. The method is first tested here against ground-based calibration data. The method will also be tested further in orbit. Ultimately, this approach for attitude determination could be applicable to all future small satellites with radiative and optical scientific sensors on several faces on the spacecraft but without the need for specific active on-board attitude determination equipments.

Different approaches can be implemented to determine the in-orbit attitude of a satellite. Satellite attitude determination and control system (ADCS) include sensors used to determine attitude and attitude rate, such as Sun sensors, horizon sensors, magnetometers, gyros and star trackers while actuators (magnetorquers, reaction wheels, thrusters) are designed to change the spacecraft's attitude. All of these sensors are more or less accurate and all are different, as described in [7]. Sun sensors are used to provide an estimate of the solar location in the spacecraft body frame, which can be used to estimate satellite attitude (accuracy less than 1°). Horizon sensors can be simple infrared horizon crossing indicators or more advanced thermopile sensors to detect the temperature differences between the poles and the equator (accuracy less than 1°). Magnetometers provide a measurement of the local magnetic field used to provide both estimates of attitude and also orbital position. Star tracker can provide an accurate, standalone estimate of the spacecraft's attitude by comparing a digital image captured with a CCD or CMOS sensor to an onboard star catalog. For three-axis-stabilized spacecraft missions using star trackers, the pointing accuracy can vary from 0.001° to approximately 0.7° at 1σ. For spin-stabilized spacecraft missions, the pointing accuracy vary from 0.2° to 1° at 1σ. These values correspond to the optimum conditions of use. In practice, many factors affect this accuracy, such as stray light and magnetic interference. Other spacecrafts use photocells or camera to detect stars or Earth [8] for attitude determination. Earth detection using real time image recognition in deep learning has been described to determine the attitude of a satellite in [9]. On the UVSQ-SAT satellite, no devices are present to perform image recognition to detect the Earth's location. To determine the UVSQ-SAT's in-orbit attitude, we will use housekeeping (temperatures sensors and solar photodiodes (400–1100 nm)) and scientific sensors (Earth Radiative sensors—thermopiles) measurements.

The main goal of this manuscript is to develop a new concept based on deep learning method to obtain the UVSQ-SAT in-orbit attitude to retrieve the different components of the EEI for each face of the spacecraft. To validate the method before launch, a ground-based calibration was carried out in Guyancourt (France) in October 2020. The Sun was used as radiative flux reference. The amount of calibration data acquired was limited due to the tight schedule and associated constraints (such as delay in integrations, bad weather conditions during the test period, delivery date to the launcher). One of the initial objectives was to validate new miniaturized technologies in orbit at technology readiness level of 9 (system proven in operational environment) in a short time frame program. An objective of UVSQ-SAT is to be able to learn from this first mission about the development of a future satellites constellation.

Section 2 gives a description of the deep learning method to retrieve the attitude of the UVSQ-SAT satellite and presents the ground-based validation process. This method allows for retrieving the attitude of a small spacecraft without any dedicated instrument to do so. This technique does not require to add a specific instrument. This is favorable as a small satellite tends to reduce the space needed along with the complexity of integrating one more instrument. Moreover, it will lower the data rate to provide. Deep learning algorithms are often used for remote sensing applications [10]. Neural networks are implemented using satellite data for detect farms or to classify lands as in [11–14]. This technique appears to be really convenient in the remote sensing field.

Section 3 presents the results and performance of the algorithm for the validation process. Finally, Section 4 provides discussion and perspectives for in-orbit applications.

2. Method to Retrieve Terrestrial Net Radiation for Satellite That Does Not Have Active ADCS

The main goal of the UVSQ-SAT pathfinder mission is to determine the Terrestrial Net Radiation using remote sensors. The UVSQ-SAT CubeSat described in [1] has several sensors on its six different faces:

- 12 ERS sensors are part of the UVSQ-SAT satellite (2 per face). Six ERS sensors aims to measure radiation between 0.2 and 100 µm using Carbon NanoTubes coatings (absorptivity close to 1). Six other ERS sensors aim to measure radiation wavelength between 0.2 and 3 µm with 0.06 absorptivity and between 3 and 100 µm with 0.84 absorptivity using optical solar reflector coatings. ERS measurements represent indicators to detect Earth and the Sun positions.
- Three ultraviolet sensors (UVS) are part of the UVSQ-SAT scientific payload. They focus on the 200–1100 nm wavelength range.

- Six photodiodes (LED) are located on the spacecraft and measure solar and outgoing shortwave radiations in the 400–1100 nm wavelength range.
- Temperature sensors (solar cells) are also located on each satellite panel.
- Teach' Wear (TW) is a new three axis accelerometer/gyroscope/compass. The TW module on-board UVSQ-SAT has an instrumentation that will be very helpful to determine the reference position during the training phase such as: a three-axis accelerometer, a three-axis gyrometer, and a three-axis magnetometer.

In the case of a satellite such as UVSQ-SAT that does not have an active attitude determination and control system, it is necessary to develop a typical method to retrieve terrestrial net radiation.

2.1. General Method Description to Determine the Terrestrial Net Radiation

Figure 1 presents the general method to determine the terrestrial net radiation from the UVSQ-SAT satellite. The main goal is to obtain the incoming solar radiation (TSI), the Outgoing Longwave Radiation (OLR), and the Outgoing Shortwave Radiation (OSR) from the satellite measurements.

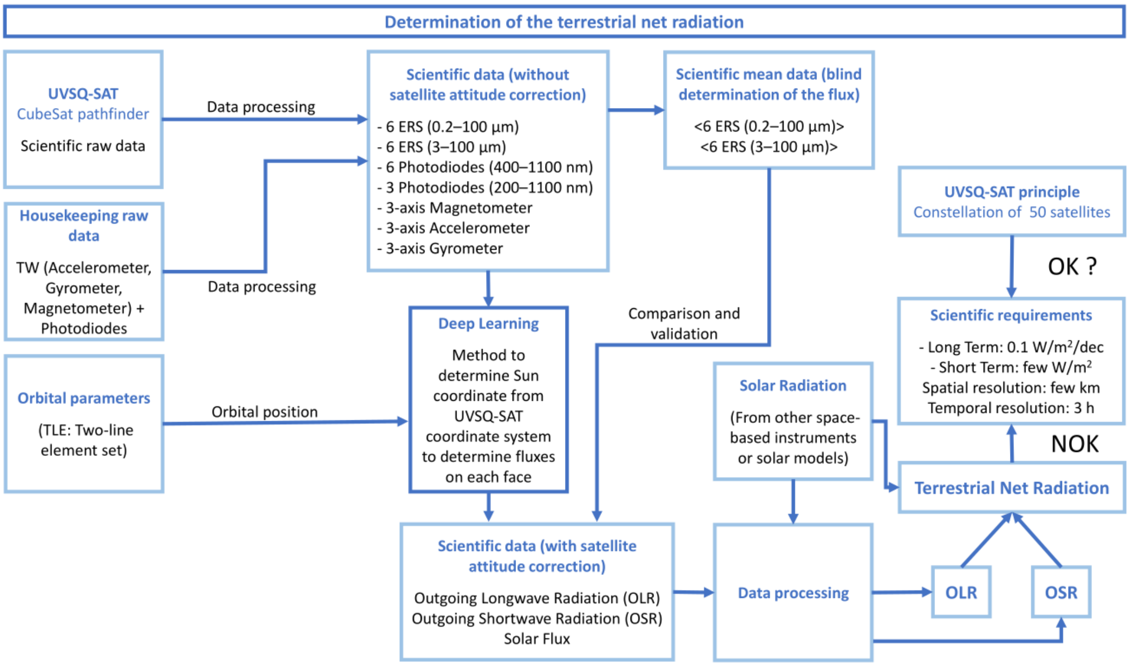

Figure 1. General method to determine the terrestrial net radiation from UVSQ-SAT remote sensors.

First of all, UVSQ-SAT scientific and housekeeping raw data are processed relatively to their transfer function to obtain scientific values without satellite attitude correction. In parallel, orbital parameters are retrieved to get the satellite's orbital position. The latter provides reference locations of the Sun and the Earth according to the satellite's frame of reference using an algorithm developed by the National Renewable Energy Laboratory (NREL) in [15]. Thereby, scientific data and orbital parameters are used as inputs for our deep learning algorithm. The deep learning method helps us to compute the satellite's attitude to then recover the different fluxes. The retrieved flux such as the outgoing longwave radiation, the outgoing shortwave radiation and the solar radiation are processed relatively to known solar radiation from other space-based instruments or solar models. Finally, thanks to the three previous quantities, it is possible to compute the terrestrial net radiation and to check whether we verify the scientific requirements presented in [1].

2.2. Method Based on a Deep Learning Approach to Determine Satellite Attitude

The method involves the development of a new deep learning approach to determine the UVSQ-SAT's in-orbit attitude using its housekeeping and scientific sensors' measurements [16]. This method is based on a multilayer perceptron (MLP), a class of feedforward artificial neural network (ANN) that is commonly used in simple regression problems. A multilayer perceptron strives to remember patterns in sequential data. It requires a large number of parameters to process multidimensional data.

The UVSQ-SAT satellite does not have an active attitude determination and control system. It does not have the ability to point toward the nadir or the Sun with an on-board automatic process using actuators. Section 1 shows that the computation of the radiative fluxes (solar, albedo, infrared) for each face of the spacecraft implies a good knowledge of the UVSQ-SAT's in-orbit attitude. Therefore, an attitude determination algorithm is required for that purpose and will be detailed below as well as its ground-based validation. The deep learning algorithm regroups a five hidden fully connected layers neural network detailed in Section 2.2.2. In this following method, we will exploit the symmetrical aspect of the CubeSat and the sensors distribution on the six different faces.

This approach is based on an empirical method to determine the satellite's attitude as the algorithm will be trained using experimental observations retrieved by the different sensors.

2.2.1. Training of the Deep Learning Neural Network

The first step to validate the deep learning method is to train the neural network. The training has to be done with ground-based calibration and in-flight calibration (once in orbit). Regarding the ground-based calibration, it can be done using the Physikalisch-Technische Bundesanstalt (PTB, Braunschweig in Germany) standard blackbody (BB 3200 pg) developed for temperatures up to 3200 K. This solution has the advantage of having a stable and known source, and allows easy positioning of the satellite. Due to the COVID-19 sanitary crisis and the associated travel restrictions, we were unable to use this facility. Therefore, we have used the Sun as a reference source for this purpose.

Figure 2 presents the different phases of the ground-based validation using the Sun as a reference source. First of all, to be able to run the way described in Section 2.1, the deep learning algorithm needs training. It will be implemented via supervised learning. To train the algorithm, it is important to exhaustively specify the experimental model as well as the inputs and outputs.

For this phase, the objective of the algorithm is to determine the azimuth of the Sun according to the satellite's frame of reference at any time thanks to the measurements made by the satellite. We must train the algorithm as close as possible to in-orbit conditions. Therefore, managing to expose the satellite straight to the Sun with different orientations seemed to be the best option. The satellite was placed under a protection glass, on a mobile support, in an open area (Guyancourt, France). The support allowed us to modify the orientation of the satellite according to the position of the Sun. Since the final goal of the attitude determination is to measure the flux, we benefited from a reference instrument that performed flux measurement in parallel. This instrument was an SMP 6 model pyranometer from Kipp and Zonen, and was placed on another support which remained stationary throughout the experiment. The idea being to be able to compare the flux of the pyranometer to the flux measured by the satellite sensors corrected by its attitude.

The Satellite Inertial Measurements Unit (IMU) in the Teach' Wear module contains a magnetometer, an accelerometer and a gyrometer. Therefore, knowing the Sun's location at each time along with the information retrieved from the Satellite IMU, it is relatively practical to obtain the Sun's position in the satellite's frame of reference determining the rotational components as follows:

The satellite's acceleration vector is defined as $\vec{a_{Sat}}$, B_{Sat} represents the basis related to the satellite's frame of reference, and B_{TW} is the basis related to the Teach' Wear, inertial unit's frame of reference, defined in Equations (1) and (2):

$$\forall(x,y,z) \text{ as, } \quad \begin{bmatrix} x \\ y \\ z \end{bmatrix}_{Sat} = \begin{bmatrix} -x \\ y \\ -z \end{bmatrix}_{TW} \quad \text{therefore,} \quad \vec{a_{sat}} = \begin{bmatrix} a_x \\ a_y \\ a_z \end{bmatrix}_{Sat} = \begin{bmatrix} -a_x \\ a_y \\ -a_z \end{bmatrix}_{TW} \tag{1}$$

$$\vec{k} = \begin{bmatrix} a_x \\ a_y \\ a_z \end{bmatrix}_{Sat} \times \frac{1}{\|\vec{a_{sat}}\|} \qquad \vec{i} = \begin{bmatrix} m_x \\ m_y \\ m_z \end{bmatrix}_{Sat} \times \frac{1}{\|\vec{m}\|} \wedge \vec{k} \qquad \vec{j} = \vec{k} \wedge \vec{i} \tag{2}$$

where B_{Sat} represents the basis related to the satellite's frame of reference, B_{TW} is the basis related to the Teach' Wear, $\vec{a_{Sat}}$ is the satellite's acceleration vector, a_x, a_y, and a_z are the three components of $\vec{a_{Sat}}$ in B_{Sat} and are measured by the accelerometer, m_x, m_y, and m_z are the three components of the magnetic North $\vec{m}$ in B_{Sat} and are measured by the magnetometer, and $\vec{i}$, $\vec{j}$, $\vec{k}$ forms the new basis.

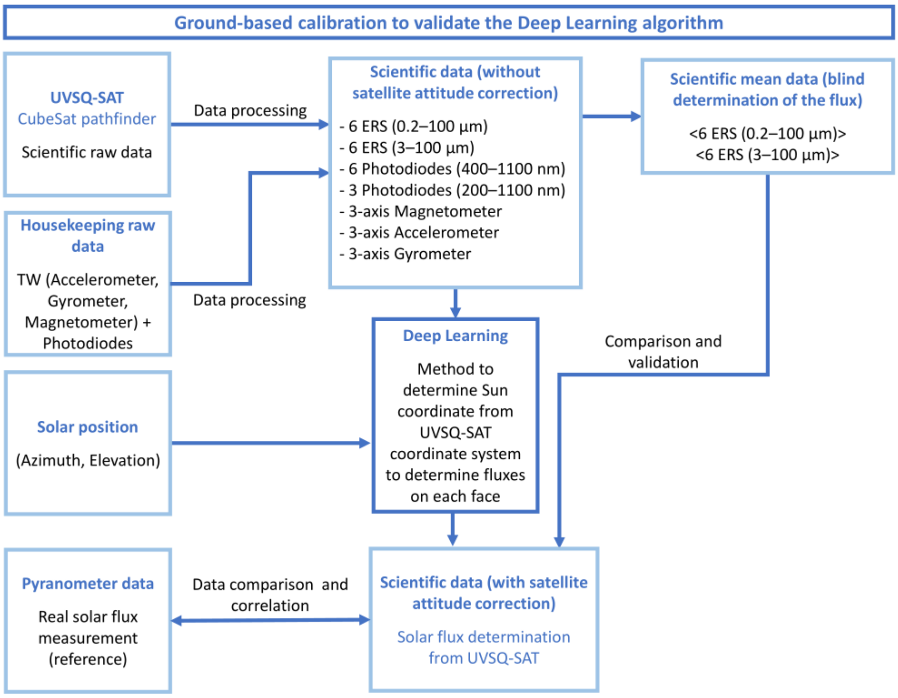

Figure 2. Ground-based calibration implemented to train and validate the satellite attitude determination algorithm.

The satellite's reference frame is moving in the terrestrial reference frame, but the latter can be recovered using the Inertial Unit (IU) reference frame in Figure 3. The accelerometer recovers the gravity vector which defines one direction. The magnetometer retrieves the magnetic North, which, projected on the plane for which the normal is the gravity vector, defines another direction. The last direction is directly computed to create an orthonormal basis. This new basis is created from the intrinsic satellite basis and described in Equation (3):

$$\vec{i} = \begin{bmatrix} I_x \\ I_y \\ I_z \end{bmatrix}_{Sat} \qquad \vec{j} = \begin{bmatrix} J_x \\ J_y \\ J_z \end{bmatrix}_{Sat} \qquad \vec{k} = \begin{bmatrix} K_x \\ K_y \\ K_z \end{bmatrix}_{Sat} \tag{3}$$

where I_x, I_y, and I_z are the three components of $\vec{i}$ in B_{Sat}, J_x, J_y, and J_z are the three components of $\vec{j}$ in B_{Sat}, and K_x, K_y, and K_z are the three components of $\vec{k}$ in B_{Sat}.

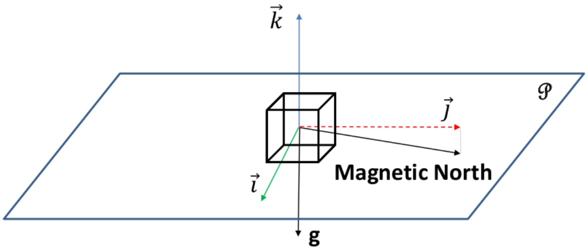

Figure 3. Representation of the reference basis in the satellite frame of reference.

Therefore, it is straightforward to draw the rotation matrix related to each of those basis and consequently to find the angular position of the CubeSat during training in Equation (4):

$$R_{B_{sat} \to B_{reference}} = \begin{bmatrix} I_x & I_y & I_z \\ J_x & J_y & J_z \\ K_x & K_y & K_z \end{bmatrix} \tag{4}$$

The solar position is given thanks to reference data or algorithms and its azimuth and elevation can then be converted thanks to the previous rotation matrix so that they appear in the satellite frame of reference.

The output of the trained algorithm should be the relative azimuth previously computed; it corresponds to the azimuth of the Sun in the satellite's frame of reference. In the training phase, the error between this output and the computed reference position will be quantified using a loss function. This function is detailed in Section 2.2.3. The output is then used to retrieve the solar flux and quantitatively validated thanks to the reference pyranometer.

As a summary, training/test/validation datasets are all the inputs (solar elevation in the satellite reference frame along with the normalized signals from the ERS sensors and the photodiodes) and reference outputs (cosine and sine of the solar azimuth in the satellite reference frame) of the UVSQ-SAT MLP neural network. We have chosen to randomly distribute these previous samples in the three different datasets so that about 70% of the samples will be in the training set, 15% in the validation set, and 15% in the test set.

The inputs are generated from the sensors. Outputs are generated from calculations. The azimuth was first generated in the terrestrial reference frame thanks to a NREL algorithm and was then transformed to the satellite reference frame, previously defined thanks to the on-board accelerometer and magnetometer.

2.2.2. Neural Network Architecture of the Deep Learning Method

The diagram in Figure 4 describes the neural network architecture implemented and how it is trained and validated during the experiments. The architecture is an MLP neural network, which is a computational model with 587 neurons. Multilayer Perceptrons are the classical type of neural network. They are suitable for regression prediction problems where a real-valued quantity is predicted given a set of inputs. The hyper-parameters (number of layers, learning rate, layer width, activation function, . . .) of the UVSQ-SAT MLP neural network were empirically determined based on output accuracies and rates of convergence of the loss function.

The inputs are detailed in the following explanation. It is here the ideal case, and for an optimum the output predicted should be the solar position that is computed following the procedure mentioned in Section 2.2.1.

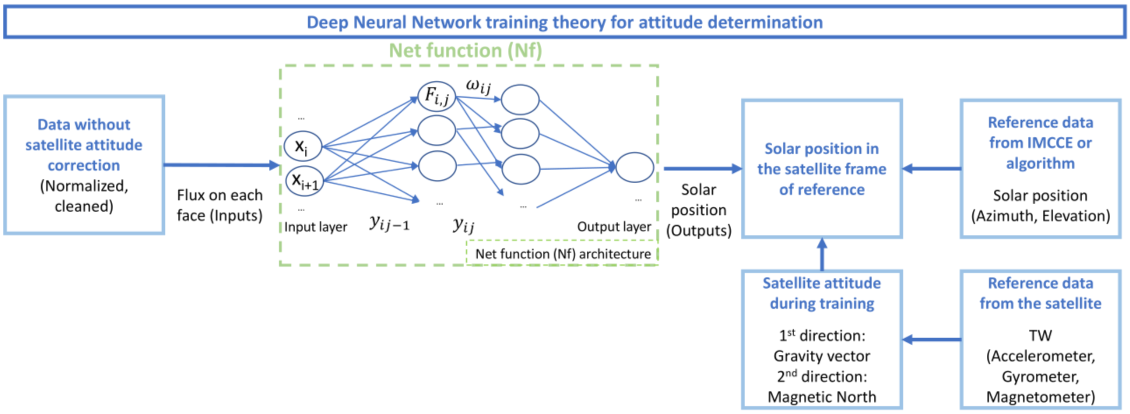

Figure 4. Neural Network architecture with fully connected layers, as well as the inputs and outputs.

For each layer represented in Figure 4, the functions that are applied to the inputs of the related layers structure the Net Function and are defined in Equations (5) and (6):

$$y_{i,j} = g(\sigma_{i,j}) = g\left(\sum_{i=1}^{n^{j-1}} \omega_{i,j-1} y_{i,j-1} + \omega_{0,j-1}\right) \tag{5}$$

$$y_{i,j} = F_{i,j}(y_{1,j-1} \ldots, y_{n^{j-1},j-1}) \tag{6}$$

where $y_{i,j}$ are the outputs and $y_{i,0} = x_i$ are the inputs of the node (*i*,*j*), $\forall i \in [1, n^0]$ and $\forall j \in [1, l]$, l is the total number of layers, $\sigma_{i,j}$ is the cache output before going through the activation function, n^j is the number of neurons at layer j, g is the activation function, $\omega_{i,j}$ are the weights, and $\omega_{0,j}$ are called the biases.

For the UVSQ-SAT's training, due to its efficiency and the ability to get more accurate outputs in Table 1, we choose to use the rectified linear unit (ReLU) activation function defined in Equation (7):

$$g(z) = \begin{cases} 0 & \text{for} \quad z < 0 \\ z & \text{for} \quad z \geq 0 \end{cases} \tag{7}$$

For a reference case, we switch to different activation functions in order to empirically determine the best one in terms of mean-squared-error on the results desired. The other parameters were constants. The number of iterations of reference was fixed to be 300 maximum. A comparison is represented in Table 1 for two trainings (different Kaiming uniform initialization of the weights). The Sigmoid activation function allows for computing the relative azimuth with the worst accuracy as the convergence of the neural network is much slower and would entail a much higher computation time (approximately 10,000 iterations).

Table 1. Averaged results obtained for each activation function comparing their mean squared error between the predicted and desired azimuth as well as the number of iterations to reach the optimum.

Activation Function	Mean Squared Error	Iteration
RELU	55.6	282
ELU	61.8	284
Tanh	61.1	288
Sigmoid	6259.5	240
Leaky RELU	59.2	260

The exact architecture of the MLP neural network used for the determination of attitude is such that the algorithm combines:

- 5 Hidden fully connected layers
- 25 Inputs

- 2 Outputs
- Learning rate of 10^{-5}, determined empirically
- Layers dimensions (width): 25/48/128/256/128/2

We compared the alternative structures in terms of accuracy and convergence rate. Other activation functions (ELU, Tanh, Sigmoid, Leaky RELU) or value of the learning rate (optimal for 10^{-5}) would worsen the performance of the MLP neural network. Reducing the number of layers in the MLP neural network would decrease the accuracy of the system but increasing the number of layers would leave the accuracy unchanged with a longer computation time.

The instruments of interest to locate the Sun in the satellite's frame of reference are the six panel photodiodes focusing in the 400–1100 nm wavelength range and the six ERS sensors focusing on the 0.2–100 µm wavelength range.

The function takes signals from the ERS sensors (thermopiles) and photodiodes (LED) as inputs and the orientation angle as output (Figure 4). The 25 inputs for the neural network are four ERS sensors with Carbon NanoTubes signals from the four lateral sides of the CubeSat, at three different following times, making 12 inputs, along with the four photodiodes' signals from the four lateral sides at the same three different times. The last input is the elevation of the Sun at the spacecraft coordinates. The idea was not to consider the upper and lower faces of the CubeSat as to be able to generalize the trained function to new conditions. Specifically, we assumed that the bottom not considered for training would respond very differently in orbit. It is also known that this side never sees the Sun during the training phase, so its detection seems impossible. As the desired output is an angle, a straightforward way to avoid discontinuities is to use two trigonometric functions cosine and sine of the output angle as two desired outputs to then easily compute the related angle using *atan2* function. Then, the orientation of the satellite in terms of cosine and sine in time will not have discontinuities and will be continuous. During the experiment, no abrupt change of orientation has taken place, as no abrupt changes will occur in orbit according to the sampling frequency chosen for the satellite's measurements. The orientation at different following times is correlated. Therefore, taking different values of the signals before and, after the instant we consider, seems logical. It is the equivalent of a second-order central in finite differences' components. One more input is the elevation of the Sun, even though the dynamics of this parameter during the experiment is very small compared to that of the other inputs, the elevation that will be known at this stage as an input can influence the output in this three-dimensional problem.

2.2.3. Loss Function for Training the Deep Learning Neural Network

The loss function, also called cost function, characterizes the error between the predicted output and the targeted value of reference. In our case, as the deviation increases, we will have continuously worse results derived from the output. Therefore, as the predicted output is getting further from the reference value, the quantified error should be higher. In particular, we would rather have a small but regular error rather than very large errors a little less frequently since this would completely affect the precision of the flux measurement. Common loss functions are being investigated in [17].

Therefore, two bilateral loss functions that can be clearly defined are: Mean Squared Error (MSE) and Mean Absolute Error (MAE), which are defined in Equations (8) and (9):

$$\mathrm{MSE}(y, y^p) = \frac{\sum_{i=1}^{n} (y_i - y_i^p)^2}{n} \tag{8}$$

$$\mathrm{MAE}(y, y^p) = \frac{\sum_{i=1}^{n} |y_i - y_i^p|}{n} \tag{9}$$

where $y = [y_1, ..y_n]$ are the targeted values, $y^p = [y_1^p, ..y_n^p]$ are the predicted values, and n is the total number of data points.

The MSE function will give more weight to the outliers than the MAE function that will be more robust to those. If anomalies should be detected and taken into account, MSE is the function to use, but, if outliers are present in the training set and not in the test set, MAE should be chosen. Therefore, the most suitable function in our case is the MSE.

2.2.4. Performance and Uncertainties

Learning is based on optimization of the net function as mentioned above to obtain the most accurate output, close to the reference data. The samples are split into three sets. It is important that those sets are totally decorrelated. The first one is the train set that is used to optimize the net function. Another one is the validation set that is used to check the performance of the algorithm at each iteration over the train set. This is important as it is a great indication to whether the function is able to generalize to other samples of data in the validation set. It is critical as the net function's parameters chosen are based on the iteration that minimizes the loss for the validation set. The last dataset is the test set for which the performance of the net function is evaluated. Figure 5 shows the loss evaluated at each iteration during the training for both of the train and validation set. It is clear that, at first, both of the computed losses decrease with the number of iterations. However, at some point, the loss value for the validation set starts increasing. We have reached a point where the neural network is over-fitting the data from the train set and is unable to generalize to a new dataset. The net function retained is chosen at the iteration, where the validation set loss reaches a minimum to avoid this over-fitting situation.

Here, the optimum for the validation set loss is reached at epoch 126 as the loss will increase after that epoch; this means that the algorithm is getting worse at generalizing to new samples. The performance of the function based on the last set is detailed in the following section.

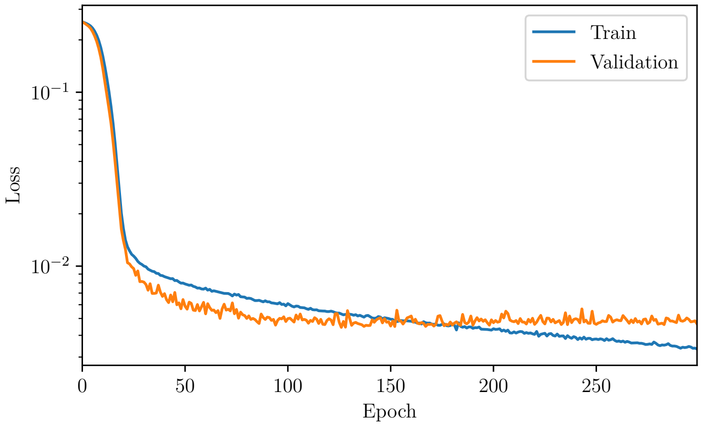

Figure 5. Loss functions for the validation set and the train set at each iteration (Epoch) during training.

3. Results

This section presents the results of the method to determine the UVSQ-SAT's attitude using its housekeeping and scientific sensors' measurements.

Section 2.2.2 presents the architecture chosen along with the hyper-parameters selected. The number of hidden layers, the learning rate, the activation function, the inputs, and the format of the outputs were meticulously studied and set for this issue. Those choices were made to optimize the deep learning algorithm for the training phase and the test phase. This architecture has been validated and constitutes a first result of our application to be replicated. To evaluate the ability of the algorithm to generalize to another set of samples, the net function optimized previously is applied to the test set with unseen data to compute the relative azimuth.

To validate the new method based on a deep learning approach to determine UVSQ-SAT in-orbit satellite attitude, a ground-based calibration experiment was carried out in

October 2020 in Guyancourt (France), using the Sun as the radiative flux reference. In Figure 6, we compare the predicted azimuth of the Sun and the real ones that are used as a reference to assess the ability of this method to determine the on-ground orientation of the satellite. The root-mean-square deviation (RMSD) quantifies the error between the prediction and the real value. The first bisector is plotted as the ideal result from a perfect algorithm for which predicted azimuth would be equal to real azimuth characterizing the orientation of the CubeSat.

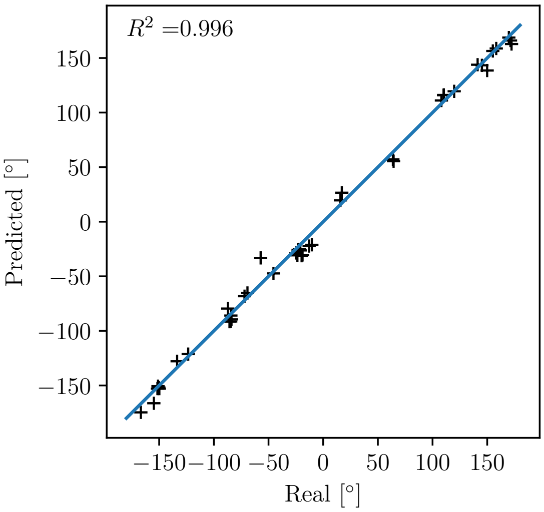

Figure 6. Predicted azimuth of the Sun versus real azimuth of reference in degrees based on the test set done in October 2020 and the optimized neural network. The continuous blue curve represents the ideal case when the observed values perfectly fit the predicted values.

The correlation coefficient indicates a strong linear relationship between those angles which confirm the ability of the algorithm to learn and generalize. The root-mean-square deviation is evaluated at 7.1° at 1σ using the previous function. It characterizes the error we would find on the precession angle of the satellite. Overall, the orientation itself is useful in that case to determine the nature of the flux observed at a given time and reconstruct the observed flux. In this case, we precisely know the actual configuration and we focus on the solar flux. In Figure 7, we evaluate the error induced on the calculation of the flux that is evaluated as a function of the recovered orientation. To do so, we present a comparison of the flux with correction of the attitude with the predicted azimuth, the real azimuth and the reference flux retrieved by the pyranometer. Then, to validate the method (MLP network to determine the attitude of orbiting satellites for spacecraft without active ADCS), measurements made by UVSQ-SAT instruments and corrected by the attitude of the satellite are compared with those measured by a pyranometer (independent measurements taken on the ground).

We want to measure the solar flux; this computation can only be applied here as conditions will differ in-orbit, but the main idea stays similar. As we retrieved the predicted attitude from the deep learning method with the accuracy mentioned above, we are able to determine which sides of the CubeSat are facing the Sun and which ones are not. In order to remove noise and reflections from the environment, we removed at each time the average ambient flux that is detected by the sides that are not directly facing the Sun. Then, we select the measurements from the sensors that are facing the Sun with a minimal angle of about 60 degrees (in a 120 degrees field of view). The measurements are then corrected using the dot product between the Sun's direction and the normal vector relatively to each of the faces of the CubeSat facing the Sun (see Equations (10) and (11)). This parameter is directly linked to the attitude of the satellite recovered previously. By doing this, we discriminated the faces that were hidden from the Sun similarly to in-orbit conditions when sensors will face the Earth and would measure the albedo while others will directly measure incoming solar flux.

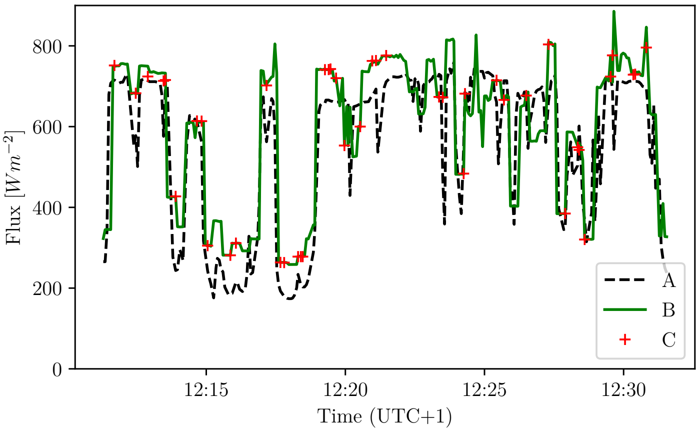

Figure 7. Comparison of the different solar flux computations for the test conducted on 26 October 2020. (**A**) pyranometer flux corrected of the Sun's elevation; (**B**) photodiodes's flux corrected of the reference attitude; (**C**) photodiodes's normalized flux corrected of the predicted attitude.

At each time of the experiment, we have:

$$F_{Sun} = \frac{f_k}{\vec{s} \cdot \vec{n_k}} = \frac{f_k}{\omega_k} \tag{10}$$

where F_{Sun} is the incoming solar flux, f_k is the flux on face k of the satellite for the selected field of view, 0, otherwise, k is the index of the faces, $\vec{s}$ is the the Sun position vector, $\vec{n_k}$ is the normal vector to the face $k \in [1, 6]$, ω_k is the dot product between $\vec{s}$ and $\vec{n_k}$. The idea is to compute the average using the dot products as weights for the flux computed on each face facing the Sun such as:

$$F_{Sun} = \frac{1}{\sum_1^6 \frac{1}{\omega_k}} \sum_1^6 \frac{f_k}{\omega_k} \tag{11}$$

The results obtained to compute the solar flux using the predicted attitude of the satellite are closer to the flux measured by the pyranometer than to blindly compute an average from the six different faces of the CubeSat. The configuration of the experiment requires good weather conditions. The ideal case is to have a sunny day without cloud. During the UVSQ-SAT ground-based calibration using the Sun as reference, the solar irradiance had to be at least 200 Wm^{-2}. The solar irradiance measurement was carried out by a dedicated pyranometer (SMP 6 model from Kipp & Zonen) calibrated according to international standards. The SMP 6 measures solar irradiance on a planar surface, and it is designed to measure the solar radiation flux density (Wm^{-2}) from the hemisphere in the 280 to 3000 nm spectral range. The directional response of the pyranometer has a deviation of less than 10 Wm^{-2} from a direct beam of 1000 Wm^{-2} up to a zenith angle of 80°. Observing at the zenith, the deviation is negligible. For the UVSQ-SAT measurements, the flux of each sensor on each face of the satellite has been corrected of the attitude (direction of the line of sight of the Sun). The angular flux correction of each face of the satellite is based on Equation (10).

In Figures 7 and 8, we compare the flux computed with predicted and reference orientation as well as the flux retrieved from the pyranometer. To quantify the error of our prediction, we compute the RMSD between the flux computed with the azimuth of reference and the flux computed thanks to the predicted azimuth. The RMSD of the residue of the ratio of the compared flux quantifies the normalized error between those fluxes. We find 0.1261 between the pyranometer flux and the predicted flux from the photodiodes. However, it appears that most of that error already exists between the reference flux and the pyranometer flux as the RMSD between those two fluxes, which is equal to 0.1255. First of all, we compute what we call the reference flux. It is defined by the solar flux that we would compute from the satellite's photodiodes with Equation (11), if we would know the real orientation of the satellite at each time. This would happen if the algorithm would perfectly predict the satellite attitude at each time. For the pyranometer flux, we retrieve the data from the SMP 6 calibrated pyranometer. The instrument was located next to the satellite in order to get as close as possible to the observation conditions of the satellite. The pyranometer data are interpolated to suit the satellite time scale. We can then compare the different values found with the two different methods applying the root mean square deviation. For the photodiodes, we retrieve an RMSD of 0.0219 between the reference and predicted attitude corrected flux from the photodiodes. Here, we compared the previously computed reference flux and the flux obtained with the same computation method but considering predicted orientation instead of the real one. In the context of the experiment, one cannot claim to compare the two instruments in absolute terms, since the measurements are made under different conditions and having different instrument specifications. However, we can compare the flux obtained using the reference/targeted orientation of the CubeSat and the flux retrieved determining the attitude using the deep learning algorithm. The root-mean-square deviation between the flux corrected with the predicted attitude and the flux corrected with the known attitude is equal to 16 Wm^{-2} or about 2 % in terms of RMSD of the residue.

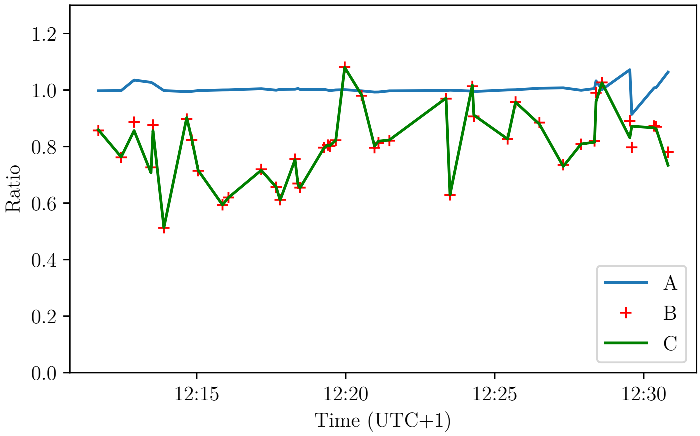

Figure 8. Ratio of the flux for the pyranometer and the corrected flux thanks to the reference and predicted attitude. (**A**) ratio between the reference flux and the predicted flux; (**B**) ratio between pyranometer flux and the predicted flux; (**C**) ratio between the pyranometer flux and the reference flux.

4. Discussion and Perspectives

UVSQ-SAT is the first in a future satellite constellation, as a demonstrator to measure incoming and outgoing radiation at the TOA using miniaturized sensors on its six faces. To retrieve the required flux to compute the terrestrial net radiation, it is necessary to discriminate the flux measured from some of the sensors to select only solar flux or terrestrial radiation in the longwave or in the shortwave. It is also relevant to correct the different flux knowing the angle between the source of the flux and the instrument. To do so, the orientation of the satellite must be known at each time. However, small satellites such as UVSQ-SAT do not have an active ADCS, mainly due to limitations of mass, volume, and power. Therefore, another method using available sensors can be adopted to have a good knowledge of the satellite attitude. The UVSQ-SAT attitude determination algorithm using deep learning methods allowed for retrieving the orientation of the satellite on-ground thanks to its sensors on its sides. The algorithm was accurate at $\pm 7.1°$ at 1σ. It helped select and measure the desired flux with an accuracy of 16 Wm^{-2}.

However, there are several limitations that need to be taken into account for the next step and to apply the method to in-orbit attitude determination. As the amount of samples available to train the algorithm was not optimal during the ground test, the accuracy of the algorithm was limited due to over-fitting issues. Thousands of different samples including different orientations on the three-axis would have been better to train the neural network. During the experiment that aimed to retrieve signals to train the algorithm, the satellite was initially enclosed in a transparent box at ambient temperature and pressure. Therefore, temperature measurements on each side of the CubeSat could not be relevant for the study. Indeed, the convective heat transfer effects taking place during the experiment will be non-existent in-orbit. The responses of the temperature sensors will therefore be different in-orbit. The average temperature kept increasing with time as the enclosure got warmer and warmer. Thus, these are unusable for training on the ground. In orbit, using the temperature sensors will be really relevant and helpful for the determination of the attitude. It will improve the accuracy of the algorithm. Moreover, the UVSQ-SAT is equipped with three narrow field of view (NFOV) UVS sensors that will be pertinent for the Sun's detection.

To take the differences between in-orbit and on-ground conditions into consideration, in-orbit training will be required to retrieve accurate predictions from the algorithm. The idea is to implement adaptation domains to benefit from the on-ground training and to adapt to targeted in-orbit responses. To retrieve the complete attitude of the satellite, we showed a way to compute the precession angle knowing the nutation and spin angles that define the plane characterized by its nadir normal vector. This plane was considered as a reference as the algorithm was trained on-ground but in-orbit; this will need to be implemented. Therefore, the first step of that method will be to train the neural network using an Attitude and Heading Reference System (AHRS) to determine the Earth's position and therefore the previous plane.

Other main limitations of the ground calibration were the inefficiency of the ERS sensors (between 3 and 100 μm) due to diffuse ambient temperature, and the fact that we could only search the Sun on a small excursion. This means that we were unable to rotate the satellite in the plane normal to Earth and slightly tilted it, but we could not flip the satellite upside down, and we therefore only trained it in one hemisphere. Furthermore, even if this ground study allowed for verifying the feasibility of our method, we only had one very bright source to find in the sky, while in flight we also have the Earth reflecting the Sun. This is why we are going to do a flight training in accordance with the method presented in Section 2 (and now demonstrated) and with the following solution, where one of the first steps will be to calibrate the magnetometer in-orbit.

Thanks to the Teach' Wear magnetometer data, we know the three components of the magnetic field for each measurement, whose positions are calculated with the orbital parameters. Then, the International Geomagnetic Reference Field (IGRF-13) model gives the expected magnetic field, which allows for calibrating the UVSQ-SAT TW magnetometer. Then, a resulting map will be obtained and will illustrate the correct calibration of the system. While the mean of the field will be good, the instantaneous signal on each component will be noisy. This is why we will use a Kalman filter to reduce the noise such as explained in [18]. Since we will have the magnetic field vector in two reference frames, we will calculate the change of reference matrix in order to roughly orientate the satellite. We will then manually improve the accuracy of the attitude of the satellite by using the other sensors (photodiodes (LED), temperatures (solar cells), ERS sensors), in order to get data for learning steps. Some methods that will be implemented in-orbit can be described here. The objective to improve the algorithm is to determine the Earth's location in the satellite's frame of reference thanks to the ERS sensors (second type described in Section 2) measuring the radiation in the 3–100 μm wavelengths range. We will compute the barycenter of the coordinates of the center of the faces assigned with the coefficients corresponding to those fluxes. The recovered vector will indicate the direction where the infrared flux is the highest, which means the Earth's direction. A method that will be used in some orientations of the satellite to refine the detection of the Sun will be based on the use of the UVS sensors. They have a very narrow field of view allowing for having a better accuracy on the location of the Sun in the satellite's reference frame. The orbital parameters and the National Renewable Energy Laboratory method described in [15] allow for retrieving the azimuth and the elevation of the Sun at each time based on the satellite's location. Therefore, we will obtain the orientation of the satellite. This method will only be used to train the algorithm but cannot be always relevant in the case of eclipses. We will perform in-orbit training thanks to the previous computed output and the signals from the different sensors. First, measurements were recovered from the satellite since 24 January 2021. UVSQ-SAT solar cells temperature, photodiodes flux (LED), and the magnetic in-orbit variations are shown in Figures 9–11. This temperature and flux are proof of the satellite's good health and will be used as inputs for the neural network. The magnetic field will help us with the training phase as described previously. These inputs will be used to estimate the UVSQ-SAT attitude in orbit. This analysis will be the subject of another manuscript.

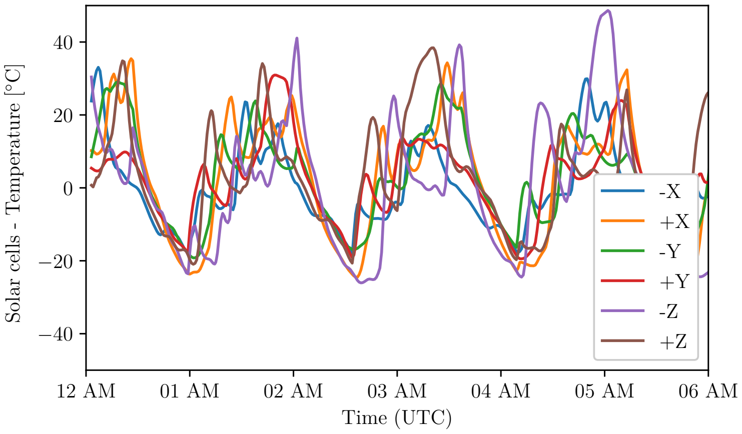

Figure 9. Solar cells temperature for all UVSQ-SAT faces. Measurements start from 7 February 2021 at 12:00 AM (UTC). The orbital period is about 95.18 mn. UVSQ-SAT spins during the orbit.

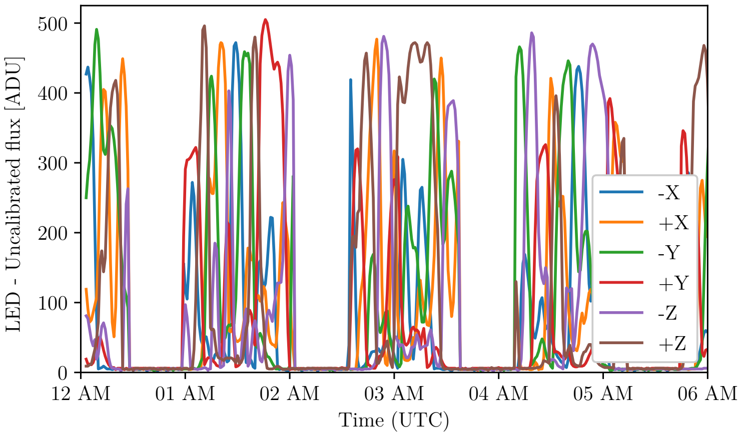

Figure 10. Uncalibrated LED flux (photodiodes in the 400–1100 nm wavelength range) for all faces of the UVSQ-SAT CubeSat. Measurements (TSI + OSR) start from 7 February 2021 at 12:00 AM (UTC).

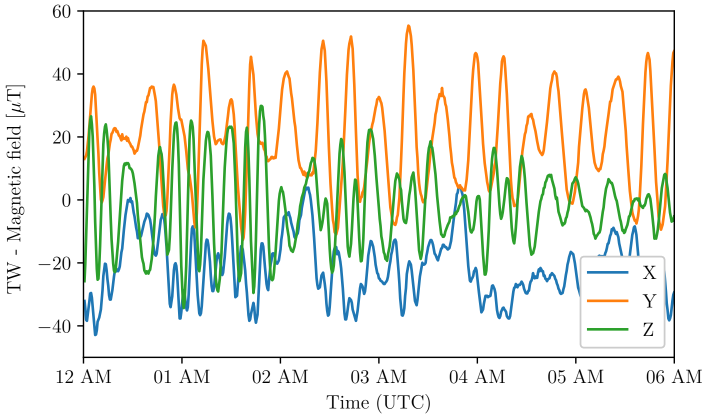

Figure 11. Magnetic field components on the x-axis, y-axis, and z-axis.

5. Conclusions

The UVSQ-SAT space-based mission (technological demonstrator) aims to implement miniaturized and disruptive technologies for remote sensing with compact sensors. It is a first step towards a future satellite constellation mainly to measure the terrestrial net radiation. Terrestrial net radiation can be obtained with radiometers on all faces of the satellites that measure solar flux and fluxes of short-wave and long-wave radiation.
In this manuscript, we presented a new method based on a deep learning approach to retrieve terrestrial net radiation from satellites without attitude and orbital control system. Knowledge of the satellite attitude allows for applying the appropriate corrections to the incident flux measurements (solar (TSI), albedo (OSR), infrared (OLR)) on all faces of the spacecraft. Thus, the attitude determination is crucial for the computation of the fluxes. Therefore, we performed a ground-based calibration to validate and check the performance of the developed method that seems to be efficient. It was able to provide convenient results on the satellite attitude determination and its resulting fluxes.

We plan to improve its accuracy by increasing the number of training samples as well as by performing training under in-orbit conditions. More specific training will allow compliance with the mission specifications for measuring the EEI. This method represents a new way to determine the attitude of satellites and the terrestrial net radiation retrieval for the case of a constellation of small satellites.

UVSQ-SAT was successfully launched on 24 January 2021 into a Sun-synchronous orbit (at 535 km) thanks to a Falcon 9 rocket (Space X). During the commissioning phase, an in-orbit calibration will be done to consolidate the method described in this manuscript. The main goal will be to minimize the uncertainty on the knowledge of the UVSQ-SAT CubeSat attitude.

Based on the deep learning method applied to space-based attitude determination of the satellite with a great number of data samples, the uncertainty on the outgoing longwave radiation and shortwave radiation determination should be less than $\pm 5\,\mathrm{W m^{-2}}$ (1σ).

Author Contributions: Conceptualization, A.F., M.M., C.D., T.B., S.B., A.H., P.K., A.S. and L.D.; methodology, A.F., C.D., M.M. and T.B.; software, A.F.; validation, A.F.; formal analysis, A.F.; investigation, M.M.; resources, M.M.; data curation, A.F.; writing—original draft preparation, A.F.; writing—review and editing, A.F., C.D., M.M., T.B. and A.M.; visualization, C.D.; supervision, M.M.; project administration, M.M.; funding acquisition, M.M. All authors have read and agreed to the published version of the manuscript.

Funding: The UVSQ-SAT research was mainly funded by Centre National de la Recherche Scientifique (CNRS, France), Centre National d'Études Spatiales (CNES, France), UVSQ (Université de Versailles Saint-Quentin-en-Yvelines, France), and Agence Nationale de La Recherche (ANR, France). This work was supported by the Programme National Soleil Terre (PNST) of CNRS/INSU (France) co-funded by CNES and Commissariat à l'énergie atomique (CEA, France).

Acknowledgments: The authors acknowledge support from the Centre National de la Recherche Scientifique (CNRS, France), the Centre National d'Études Spatiales (CNES, France), and Office National d'Études et de Recherches Aérospatiales (ONERA, France). The authors would like to thank the reviewers for their assistance in evaluating this manuscript.

Conflicts of Interest: The authors declare no conflict of interest.

References

1. Meftah, M.; Damé, L.; Keckhut, P.; Bekki, S.; Sarkissian, A.; Hauchecorne, A.; Bertran, E.; Carta, J.P.; Rogers, D.; Abbaki, S.; et al. UVSQ-SAT, a pathfinder cubesat mission for observing essential climate variables. *Remote Sens.* **2020**, *12*, 92. [CrossRef]
2. Meftah, M.; Damé, L.; Bolsée, D.; Hauchecorne, A.; Pereira, N.; Sluse, D.; Cessateur, G.; Irbah, A.; Bureau, J.; Weber, M.; et al. SOLAR-ISS: A new reference spectrum based on SOLAR/SOLSPEC observations. *Astron. Astrophys.* **2018**, *611*, A1. [CrossRef]
3. Meftah, M.; Snow, M.; Damé, L.; Bolseé, D.; Pereira, N.; Cessateur, G.; Bekki, S.; Keckhut, P.; Sarkissian, A.; Hauchecorne, A. SOLAR-v: A new solar spectral irradiance dataset based on SOLAR/SOLSPEC observations during solar cycle 24. *Astron. Astrophys.* **2021**, *2*, 1–9. [CrossRef]
4. Stephens, G.L.; Li, J.; Wild, M.; Clayson, C.A.; Loeb, N.; Kato, S.; L'Ecuyer, T.; Stackhouse, P.W.; Lebsock, M.; Andrews, T. An update on Earth's energy balance in light of the latest global observations. *Nat. Geosci.* **2012**, *5*, 691–696. [CrossRef]
5. Allan, R.P.; Liu, C.; Loeb, N.G.; Palmer, M.D.; Roberts, M.; Smith, D.; Vidale, P.L. Changes in global net radiative imbalance 1985–2012. *Geophys. Res. Lett.* **2014**, *41*, 5588–5597. [CrossRef] [PubMed]
6. Wild, M.; Ohmura, A.; Schär, C.; Müller, G.; Folini, D.; Schwarz, M.; Hakuba, M.Z.; Sanchez-Lorenzo, A. The Global Energy Balance Archive (GEBA) version 2017: A database for worldwide measured surface energy fluxes. *Earth Syst. Sci. Data* **2017**, *9*, 601–613. [CrossRef]
7. Brasoveanu, D.; Hashmall, J.; Baker, D. Spacecraft Attitude Determination Accuracy from Mission Experience. *NASA GSFC Tech. Rep.* **1994**, *95*, 12858.
8. Markley, F.L.; Crassidis, J.L. Static Attitude Determination Methods. In *Fundamentals of Spacecraft Attitude Determination and Control*; Springer: New York, NY, USA, 2014; pp. 183–233. [CrossRef]
9. Iwasaki, Y.; Kikuya, Y.; Sasaki, K.; Ozawa, T.; Shintani, Y.; Masuda, Y.; Watanabe, K.; Mamiya, H.; Ando, H.; Nakashima, T.; et al. Development and Initial On-orbit Performance of Multi-Functional Attitude Sensor using Image Recognition. In Proceedings of the AIAA/USU Conference on Small Satellites, Logan, UT, USA, 3–8 August 2019.
10. Zhu, X.X.; Tuia, D.; Mou, L.; Xia, G.; Zhang, L.; Xu, F.; Fraundorfer, F. Deep Learning in Remote Sensing: A Comprehensive Review and List of Resources. *IEEE Geosci. Remote Sens. Mag.* **2017**, *5*, 8–36. [CrossRef]
11. Malerba, M.E.; Wright, N.; Macreadie, P.I. A continental-scale assessment of density, size, distribution and historical trends of farm dams using deep learning convolutional neural networks. *Remote Sens.* **2021**, *13*, 319. [CrossRef]
12. Debella-Gilo, M.; Gjertsen, A.K. Mapping Seasonal Agricultural Land Use Types Using Deep Learning on Sentinel-2 Image Time Series. *Remote Sens.* **2021**, *13*, 289. [CrossRef]
13. Rostami, M.; Kolouri, S.; Eaton, E.; Kim, K. Deep transfer learning for few-shot SAR image classification. *Remote Sens.* **2019**, *11*, 1374. [CrossRef]
14. Shao, Z.; Zhou, Z.; Huang, X.; Zhang, Y. Mrenet: Simultaneous extraction of road surface and road centerline in complex urban scenes from very high-resolution images. *Remote Sens.* **2021**, *13*, 239. [CrossRef]
15. Reda, I.; Nrel, A.A. *Solar Position Algorithm for Solar Radiation Applications (Revised)*; National Renewable Energy Laboratory Nrel/Tp-560-34302; National Renewable Energy Laboratory: Golden, CO, USA, 2005; pp. 1–56.
16. Finance, A.; Meftah, M.; Mangin, A.; Keckhut, P. *UVSQ-SAT a New Way to Obtain Spatio-Temporal Variations of the Radiation Budget with a Satellite Constellation*; Earth and Space Science Open Archive; American Geophysical Union: Washington, DC, USA, 2021; p. 21. [CrossRef]
17. Nie, F.; Hu, Z.; Li, X. An investigation for loss functions widely used in machine learning. *Commun. Inf. Syst.* **2018**, *18*, 37–52. [CrossRef]
18. Martel, F.; Pal, P.K.; Psiaki, M.L. Three-axis attitude determination via Kalman filtering of magnetometer data. *J. Guid. Control. Dyn.* **1990**, *13*, 344–367.

3.4 In-orbit Attitude Determination using Deterministic Methods

3.4.1 Introduction

The UVSQ-SAT satellite after being tested on the ground, was launched as detailed in Section 3.1.1. The neural network presented earlier cannot be directly applied since the test environment is extremely different as presented in Section 3.3.2. More classical methods must therefore be developed and adapted to the satellite and the distribution of sensors on it. Two methods are explained and the associated performances are evaluated in Section 3.4.2. The Tri-Axial Attitude Determination (TRIAD) method is a direct instantaneous method. The Multiplicative Extended Kalman Filter (MEKF) algorithm is a method using a Kalman filter to correct the errors related to the instruments and improve the accuracy of the attitude determination. These methods can be used as they are to determine the attitude of the satellite or serve as a database to train a deep learning algorithm to improve the methods used (computation time and step-by-step usage).

This is an excellent opportunity to apply these methods to data from a functional satellite in orbit. This allows us to have direct feedback on experience and to validate one or several methods adapted to the instruments on board and to the architecture of the spacecraft. Section 3.4.2 describes the processes of development of the methods and their performances.

3.4.2 Paper: In-Orbit Attitude Determination of the UVSQ-SAT CubeSat Using TRIAD and MEKF Methods

As explained in the previous section, the attitude determination of small satellites remains a challenge. UVSQ-SAT is a real and unique case to date for testing and evaluating several approaches for CubeSat's in-orbit attitude determination. This paper presents the in-orbit results of the UVSQ-SAT's attitude determination. The TRIAD method is presented as one of the simplest solutions to the spacecraft attitude determination problem. Another method based on the MEKF was used to improve the results obtained with the TRIAD method. This paper quantifies the accuracy of the implemented methods with real in-orbit data from the mission. In sunlight, the CubeSat attitude is determined at an accuracy better than 3° (at one σ) for both methods. During eclipses, the accuracy of the TRIAD method is 14°, while it reaches 10° (at one σ) for the recursive MEKF method. Feedback and lessons learned are presented as many future satellites could benefit from these studies in order to validate methods and configurations before launch.

sensors

MDPI

Article

In-Orbit Attitude Determination of the UVSQ-SAT CubeSat Using TRIAD and MEKF Methods

Adrien Finance [1,2], Christophe Dufour [1], Thomas Boutéraon [1], Alain Sarkissian [1], Antoine Mangin [2], Philippe Keckhut [1] and Mustapha Meftah [1,*]

[1] Université de Versailles Saint-Quentin-en-Yvelines, Université Paris-Saclay, Sorbonne Université (SU), CNRS, LATMOS, 11 Boulevard d'Alembert, 78280 Guyancourt, France; Adrien.Finance@latmos.ipsl.fr (A.F.); Christophe.Dufour@latmos.ipsl.fr (C.D.); Thomas.Bouteraon@latmos.ipsl.fr (T.B.); Alain.Sarkissian@latmos.ipsl.fr (A.S.); Philippe.Keckhut@latmos.ipsl.fr (P.K.)
[2] ACRI-ST CERGA, 10 Avenue Nicolas Copernic, 06130 Grasse, France; Antoine.Mangin@acri-st.fr
* Correspondence: Mustapha.Meftah@latmos.ipsl.fr

Abstract: Ultraviolet and infrared sensors at high quantum efficiency on-board a small satellite (UVSQ-SAT) is a CubeSat dedicated to the observation of the Earth and the Sun. This satellite has been in orbit since January 2021. It measures the Earth's outgoing shortwave and longwave radiations. The satellite does not have an active pointing system. To improve the accuracy of the Earth's radiative measurements and to resolve spatio-temporal fluctuations as much as possible, it is necessary to have a good knowledge of the attitude of the UVSQ-SAT CubeSat. The attitude determination of small satellites remains a challenge, and UVSQ-SAT represents a real and unique example to date for testing and validating different methods to improve the in-orbit attitude determination of a CubeSat. This paper presents the flight results of the UVSQ-SAT's attitude determination. The Tri-Axial Attitude Determination (TRIAD) method was used, which represents one of the simplest solutions to the spacecraft attitude determination problem. Another method based on the Multiplicative Extended Kalman Filter (MEKF) was used to improve the results obtained with the TRIAD method. In sunlight, the CubeSat attitude is determined at an accuracy better than 3° (at one σ) for both methods. During eclipses, the accuracy of the TRIAD method is 14°, while it reaches 10° (at one σ) for the recursive MEKF method. Many future satellites could benefit from these studies in order to validate methods and configurations before launch.

Keywords: CubeSat attitude determination; TRIAD; Kalman filter; climate

Citation: Finance, A.; Dufour, C.; Boutéraon, T.; Sarkissian, A.; Mangin, A.; Keckhut, P.; Meftah, M. In-Orbit Attitude Determination of the UVSQ-SAT CubeSat Using TRIAD and MEKF Methods. *Sensors* **2021**, *21*, 7361. https://doi.org/10.3390/s21217361

Academic Editor: Daniele Mortari

Received: 7 October 2021
Accepted: 4 November 2021
Published: 5 November 2021

1. Introduction

Ultraviolet and infrared sensors at high quantum efficiency on-board a small satellite (UVSQ-SAT) is a scientific and technological demonstrator dedicated to the observation of essential climate variables [1]. UVSQ-SAT was launched into a Sun-synchronous orbit by the LATMOS with the Falcon 9 rocket on 24 January 2021. After a commissioning phase, the routine phase started on 13 March 2021. Since then, the CubeSat has been fully functional, and first results have been published [2]. The methods used by [1] to obtain these results (maps of the solar radiation reflected by the Earth and of the outgoing longwave radiation at the top of the atmosphere) do not take into account the attitude of the UVSQ-SAT CubeSat. To improve the accuracy of the results, it is highly recommended to have an excellent knowledge of the attitude of the UVSQ-SAT CubeSat. This would allow researchers to obtain the Earth's incident flux on each UVSQ-SAT face, given that the CubeSat has Earth radiative sensors and photodiodes on all its faces [1].

To determine the attitude of the UVSQ-SAT CubeSat, two methods are used: the Tri-Axial Attitude Determination (TRIAD) method and the Multiplicative Extended Kalman Filter (MEKF) method. TRIAD is a basic method, which is implemented by considering that the instruments' measurements can be easily related to the information from models in an inertial frame of reference at the satellite's location. Then, it is necessary to find the perfect rotation matrix to move from one reference frame to another. The MEKF method improves the results obtained with the TRIAD method. It aims to calibrate and correct the data from noise and inaccuracies.

The most commonly used methods in the literature are TRIAD and MEKF. Indeed, there are very few examples of results associated with CubeSat attitude determination in orbit. Table 1 presents a detailed background of the recent studies related to the problem of satellite attitude determination (AD). Simulations show that the restitution of the attitude can be better than 1°. Moreover, the Radio Aurora Explorer satellites 3U CubeSat [3] demonstrated that it was possible to obtain knowledge of a satellite's attitude with an accuracy better than 1° (sunlight) in orbit. Despite the small size of the CubeSats, it seems possible to accurately determine their attitude in orbit. This is mainly valid when the satellite is aimed at the Sun because several sensors (solar photodiodes, magnetometers, and gyroscopes) are used to perform this task successfully. During eclipses, this determination is more complex. CubeSat attitude determination is still a challenge as they are small, and they still do not have active attitude determination and control systems (ADCS). Furthermore, new miniaturized space-based payloads are becoming increasingly complex and require accurate knowledge of the satellite attitude. One of the objectives of the UVSQ-SAT mission is to obtain knowledge of the CubeSat attitude with an accuracy better than a few degrees in sunlight.

Table 1. Studies related to attitude determination (simulation and in-orbit observations).

Reference	Method (Instruments)	Goal	Results/Remarks
[4]	Simulation	Attitude determination (AD) based solely on magnetometer	Converges from initial attitude errors of maximum 60° and with an attitude accuracy of 1° (1σ) or better
[5]	Observation (Rossi X-ray Timing Explorer satellite calibration maneuvers, Terra and Wide-Field Infrared Explorer mission, Upper Atmosphere Research Satellite (UARS))	On-orbit calibration of satellite gyroscopes	Methods comparison (attitude accuracy below 1°). The Delta-bias algorithm gives slightly less accurate results than the Davenport and BICal algorithms
[6]	Simulation	Absolute alignment calibration of a system comprising two star trackers, an inertial sensor assembly (ISA) of three fiber-optic gyros, and an imaging instrument based on Alignment Kalman Filter (AKF)	AKF is effective to estimate absolute misalignments and gyro calibration parameters
[7]	Simulation	AD using an Extended Kalman Filter (EKF), which applies the albedo model with a magnetometer and sun sensor	Attitude accuracy below 1°
[8]	Simulation and Observation (Total Ozone Mapping Spectrometer (TOMS))	Modeling the albedo for Sun/Earth sensor used in attitude determination	Albedo compensation in attitude estimation, improves the maximum error from 9.9° to 1.9°
[9]	Simulation	AD using Unscented Kalman Filter (UKF) based only on magnetometer	The attitude estimation accuracies are below 0.5° after convergence
[10]	Simulation (PROBA-2 Spacecraft scenarios)	Navigation system for magnetic-only orbit and attitude estimation using the square-root Unscented filter (MAGSURF)	RSS attitude error of less than 1.4° and a time of convergence of less than 2 orbits
[11]	Simulation	Attitude and rate estimation algorithm using EKF based only on geomagnetic field data	Filter converges within the $+/-8°$ range for any initial attitude error

Table 1. *Cont.*

Reference	Method (Instruments)	Goal	Results/Remarks
[12]	Simulation (Radio Aurora Explorer satellites (3U CubeSat))	AD based on gyros, magnetometers, coarse sun sensors, and an EKF	In the sun, the angular uncertainty is between 2° and 3°, and in eclipse, the uncertainty increases to between 7° and 8°
[13]	Simulation	AD using two-step EKF based on a magnetometer only	Attitude accuracies of less than 1°
[3]	Observation (Radio Aurora Explorer satellites (3U CubeSat))	Photodiodes calibration and AD from EKF/UKF with albedo model based on the calibrated photodiodes, three-axis magnetometer and gyrometer	Angular improvement of 10° in sun vector from the photodiodes, and below 1° accuracy on the attitude determination
[14]	Simulation	AD via a robust Adaptive Kalman Filter based on magnetometer and gyro measurement	Precision of traditional EKF is about 0.2°, and the maximum estimate error of the robust adaptive filter is 0.1°
[15]	Simulation and Observation (experimental data with on-ground nano-satellite)	Gain-scheduled EKF (GSEKF) to reduce the computational requirement in the nanosatellite attitude determination process	Attitude accuracy below 0.2° during the entire orbital period. Computation time could be reduced by 86.29% and 89.45%
[16]	Simulation	Magnetometer calibration with Hyper least square (HyperLS) estimator for ellipsoid fitting, then utilized for attitude determination via non-linear colored noise filters of EKF, simplex UKF and cubature Kalman filter	Attitude accuracy below 1° for simplex UKF
[17]	Observation (images taken from International Space Station (ISS))	AD utilizing color earth images taken with visible light camera	Attitude accuracy is about few degrees or less
[18]	Simulation	Heat attitude model for satellite attitude determination	Attitude accuracy between 0.2 ° to 5°
[19]	Simulation	AD method based on an UKF, using a gyrometer, a magnetometer and solar panels as a sun sensor	The UKF has shown precision in Euler angles of about 1.1°, which is better than for EKF. UKF has a considerably longer processing time compared to EKF
[20]	Simulation and Observation (experimentation on-ground set up)	Thermal imaging sensors to determine attitude of the Sun and the horizon by employing a homogeneous array of such detectors	Angular accuracy below 1°

This manuscript presents two methods to determine the attitude of the UVSQ-SAT CubeSat. This is an important step in the implementation process of the scientific results of the UVSQ-SAT space-based mission. Section 2 describes the inputs from the satellite along with the models and geometrical considerations of the two methods. Section 3 presents the implementation of the two different methods and how they differ. Section 4 shows the results obtained from the different methods and how the MEKF method has improved the accuracy of the determination of the UVSQ-SAT CubeSat attitude of the TRIAD method. Finally, Section 5 is dedicated to the presentation of conclusions and perspectives.

2. UVSQ-SAT Attitude Determination Considerations

This section presents a description of the sensors of the UVSQ-SAT CubeSat, reference frames and attitude representation, and the theoretical approach of the method.

2.1. Sensors Description

The UVSQ-SAT satellite described by [1] is equipped with different subsystems and sensors, among which some are used to determine its attitude. Those instruments are defined in the spacecraft body frame (B). The different faces of the spacecraft are named after this reference frame. Two opposite faces correspond to one axis. This is shown in Figure 1. The instrumental reference frame is fixed with respect to the satellite. It undergoes only one constant rotation with respect to the satellite reference frame. To simplify this, we apply this rotation and consider the measurements in the spacecraft body frame. We do not mention the instrument frame in the following explanations.

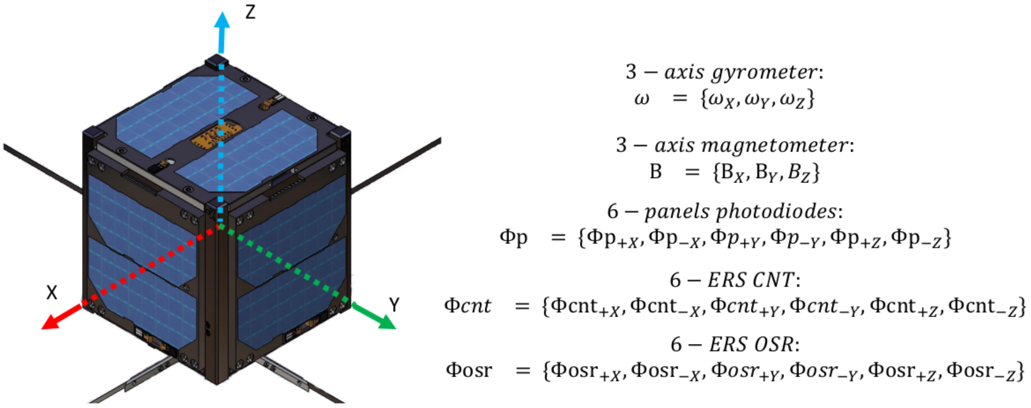

Figure 1. Spacecraft body frame of the UVSQ-SAT satellite.

The different inputs available to the algorithms are as follows:

- Three-axis angular velocities. The gyrometer measures the three-axis angular velocities in the sensor frame to the inertial reference frame (I), defined by $\omega_g = \{\omega_X,\ \omega_Y,\ \omega_z\}_{B/I}$, as the calibrated measurement.
- Three-axis magnetic field. The magnetometer measures the magnetic field along its three axes in the instrument's reference frame defined by $B = \{B_X,\ B_Y,\ B_Z\}_B$, as the calibrated measurement.
- Six photodiodes in the visible domain. They measure solar and outgoing shortwave radiations in the 400–1100 nm wavelength range. They are defined as the calibrated fluxes $\Phi p = \{\Phi p_{+X},\ \Phi p_{-X},\ \Phi p_{+Y},\ \Phi p_{-Y},\ \Phi p_{+Z},\ \Phi p_{-Z}\}$. They are used as a Sun sensor.
- Six Earth radiative sensors (ERS) sensors with an Optical Solar Reflector (OSR). They aim to measure radiation between 0.2 and 3 µm. They are defined as $\Phi osr = \{\Phi osr_{+X},\ \Phi osr_{-X},\ \Phi osr_{+Y},\ \Phi osr_{-Y},\ \Phi osr_{+Z},\ \Phi osr_{-Z}\}$. Those sensors are used as an Earth sensor and aimed toward the nadir.
- Six ERS sensors with carbon nanotubes (CNT). Six sensors aim to measure total radiation between 0.2 and 100 µm. They are defined as $\Phi cnt = \{\Phi cnt_{+X},\ \Phi cnt_{-X},\ \Phi cnt_{+Y},\ \Phi cnt_{-Y},\ \Phi cnt_{+Z},\ \Phi cnt_{-Z}\}$. They are used as Earth sensors.

An example of the time series of the UVSQ-SAT inputs is given in Figure 2. Oscillations are present in the magnetometer and gyrometer measurements as the satellite rotates. For the photodiode measurements, sunlight and eclipses periods appear clearly. ERS sensors measure all Earth and solar radiative fluxes. Eclipses periods appear also clearly.

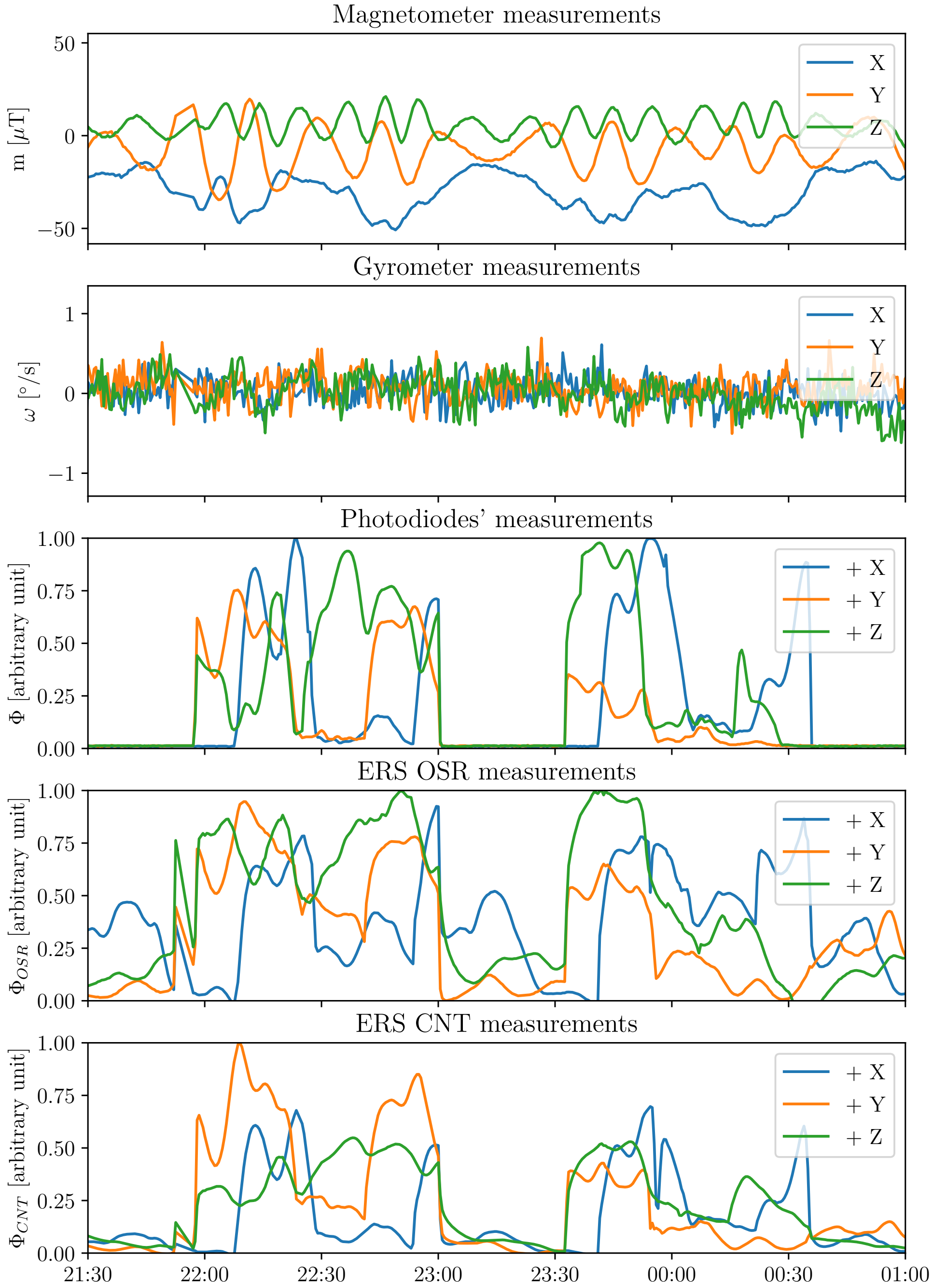

Figure 2. Time series of the measurements for two orbits on 26 March 2021 from the three-axis magnetometer, the three-axis gyrometer, the photodiodes, and the ERS sensors.

2.2. Orbital Reference Frames and Attitude Representation

2.2.1. Orbital Reference Frames

The following reference frames are required for the in-orbit attitude determination of the UVSQ-SAT CubeSat. They allow us to compute the satellite's attitude with respect to one of those frames. The reference frames are shown in Figures 3–5. We recall that the gyrometer measures an angular velocity in the body frame with respect to an inertial reference frame. Therefore, an essential reference frame defined here is the Earth-centered inertial (ECI) along with the Earth-centered orbit reference frame (OC). The reference frames are described as follows:

- Earth-centered inertial (ECI). The reference frame is defined in blue in Figure 3 with an origin at the Earth's center of mass. The X-axis is defined as the vernal equinox axis at J2000, the intersection between the equatorial and the ecliptic planes. The Z-axis is defined as the Earth rotation axis at epoch J2000. Finally, the Y-axis is defined according to the previous directions to create an orthogonal basis.

- Earth-centered Earth-fixed (ECEF). The reference frame is defined in red in Figure 3 with its origin at the Earth's center of mass. Its X-axis is defined at the intersection of the Greenwich prime meridian and the equator. Its Y-axis is the intersection of the equatorial plane and the 90° longitude. The Z-axis extends through the true north and south poles and coincides with the Earth's rotation axis.
- North East Down (NED). Assuming a WGS84 ellipsoid model of the Earth, the NED, defined in purple in Figure 3, is a local reference frame that moves the body frame's position in the ECEF. It is defined so that the X–Y plane is tangential to the surface of the ellipsoid at the given location in the ECEF. Given those conditions, the X-axis should point toward true North, the Z-axis toward the interior of the Earth, and the Y-axis will finalize the orthogonal basis.
- Earth-centered orbit reference frame (OC). The reference frame is defined in blue in Figures 4 and 5 and centered at the Earth's center, with the X-axis towards the perigee, the Y-axis along the semi-minor axis, and the Z-axis perpendicular to the orbital plane to complete the right-hand system. From the previous reference frame, it is thus necessary to define a local reference frame that will follow the satellite in its center. This reference frame is chosen for its logic with respect to the satellite motion as well as the possibility of taking into account the orbital velocity in order to correct the gyrometer of this frame.
- Orbit reference frame (O). The reference frame is defined such that its origin is located at the center of the spacecraft. The origin rotates relative to the ECI with an angular velocity of ω_0. Its Z-axis points towards the center of the Earth. The X-axis is perpendicular to the previous axis in the spacecraft's direction of motion. The Y-axis completes the right-hand system.

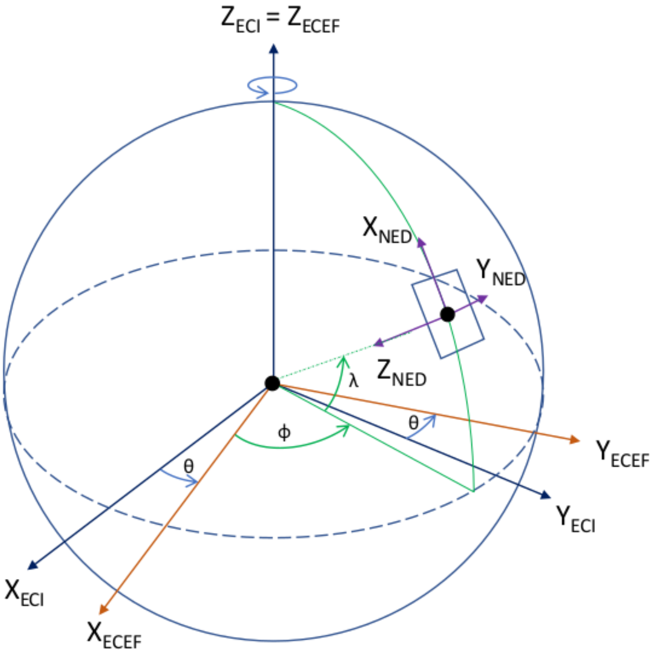

Figure 3. Earth-centered inertial (ECI), Earth-centered Earth-fixed (ECEF), and North East Down (NED) reference frames.

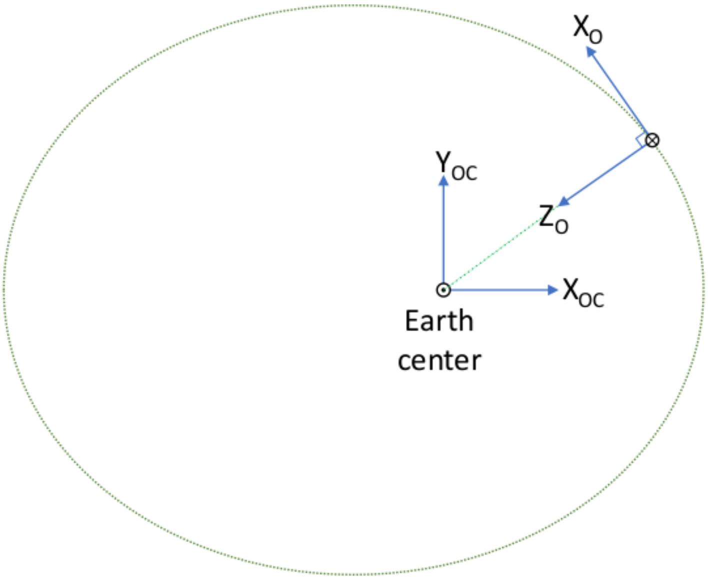

Figure 4. Earth centered orbit reference frame (OC) and orbit (O) reference frames.

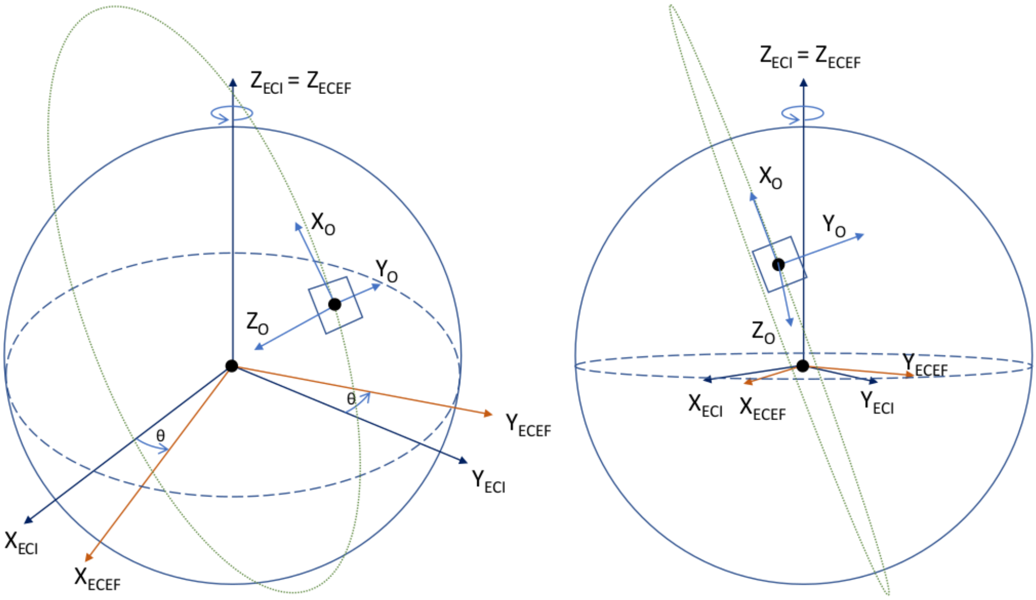

Figure 5. Earth-centered inertial (ECI), Earth-centered Earth-fixed (ECEF), and orbit (O) reference frames.

2.2.2. Attitude Representation

There are different ways to express the satellite attitude in its reference frame. The first basic representations are known as the Euler angles. The orientation of the body with respect to a reference frame is given by three Euler angles. Those angles define three successive rotations around different axes. Roll, pitch, and yaw angles are defined in Figure 6 and are called ϕ, θ, and ψ, respectively.

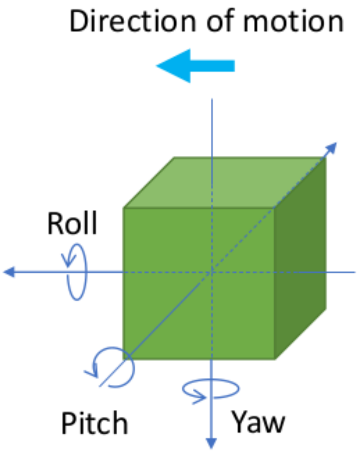

Figure 6. Euler angles defined for the satellite.

In order to avoid singularities that come with the choice of using Euler angles for attitude representation, we define the quaternion representation where a quaternion $\mathbf{q}$ is defined as

$$\mathbf{q} = q_1 + q_2\mathbf{i} + q_3\mathbf{j} + q_4\mathbf{k} = \begin{bmatrix} q_1 \\ q_2 \\ q_3 \\ q_4 \end{bmatrix} \tag{1}$$

where q_1, q_2, q_3, and q_4 are real numbers with $\{1, \mathbf{i}, \mathbf{j},$ and $\mathbf{k}\}$ as a basis for a 4-dimensional vector space. $i^2 = j^2 = k^2 = ijk = -1$ and as $\mathbf{q} \neq \mathbf{0}$. The rotation resulting from the previous quaternion is characterized by its rotation angle α around its axis of coordinates (r_x, r_y, r_z) defined in Equation (2a,b):

$$\alpha = 2\,\mathrm{atan2}\left(\sqrt{q_2^2 + q_3^2 + q_4^2}, q_1\right) \tag{2a}$$

$$(r_x, r_y, r_z) = \frac{(q_2, q_3, q_4)}{\sqrt{q_2^2 + q_3^2 + q_4^2}} \tag{2b}$$

Then, we obtain Equation (3) as follows:

$$\begin{bmatrix} q_1 \\ q_2 \\ q_3 \\ q_4 \end{bmatrix} = \begin{bmatrix} \cos\frac{\alpha}{2} \\ r_x \sin\frac{\alpha}{2} \\ r_y \sin\frac{\alpha}{2} \\ r_y \sin\frac{\alpha}{2} \end{bmatrix} \tag{3}$$

The quaternions and the Euler angles can be associated as (Equation (4))

$$\begin{aligned} q_1 &= \cos\left(\tfrac{\alpha}{2}\right) \\ q_2 &= \sin\left(\tfrac{\alpha}{2}\right)\cos(\alpha_x) \\ q_3 &= \sin\left(\tfrac{\alpha}{2}\right)\cos(\alpha_y) \\ q_4 &= \sin\left(\tfrac{\alpha}{2}\right)\cos(\alpha_z) \end{aligned} \tag{4}$$

where α_x, α_y, and α_z are the angles between the axis of rotation and the axes X, Y, and Z, respectively. From those two representations, we can create a third tool—the Direction Cosine Matrix (DCM)—that is used in the algorithm. We define the rotation matrix, also called the attitude matrix, which represents the rotation of the body in the body frame

(B) with respect to a specified frame—for example, the orbital frame (O)—as follows in Equation (5a,b):

$$DCM_{O\to B}(\phi,\theta,\psi) = \begin{bmatrix} 1 & 0 & 0 \\ 0 & \cos\phi & \sin\phi \\ 0 & -\sin\phi & \cos\phi \end{bmatrix} \begin{bmatrix} \cos\theta & 0 & -\sin\theta \\ 0 & 1 & 0 \\ \sin\theta & 0 & \cos\theta \end{bmatrix} \begin{bmatrix} \cos\psi & \sin\psi & 0 \\ -\sin\psi & \cos\psi & 0 \\ 0 & 0 & 1 \end{bmatrix} \tag{5a}$$

$$DCM_{O\to B}(q) = \begin{bmatrix} 1-2s(q_3^2+q_4^2) & 2s(q_2q_3-q_4q_1) & 2s(q_2q_4+q_3q_1) \\ 2s(q_2q_3+q_4q_1) & 1-2s(q_2^2+q_4^2) & 2s(q_3q_4-q_2q_1) \\ 2s(q_2q_4-q_3q_1) & 2s(q_3q_4+q_2q_1) & 1-2s(q_2^2+q_3^2) \end{bmatrix} \tag{5b}$$

where s is the quaternion's norm.

2.3. Theoretical Approach of the Method

The instruments and the reference frames are described in the previous section. It is now possible to present the different inputs required for attitude determination. Those inputs are the nadir direction, the Sun line-of-sight (LOS), the magnetic field vectors, and the gyrometer data. We suppose that those vectors are defined as follows (Equation (6a–c)):

$$\hat{\mathbf{S}}(\mathbf{t}) = \mathbf{S}(\mathbf{t}) + \boldsymbol{\eta_S(t)} \tag{6a}$$

$$\hat{\mathbf{N}}(\mathbf{t}) = \mathbf{N}(\mathbf{t}) + \boldsymbol{\eta_N(t)} \tag{6b}$$

$$\hat{\mathbf{B}}(\mathbf{t}) = \mathbf{B}(\mathbf{t}) + \boldsymbol{\eta_B(t)} \tag{6c}$$

where $\hat{\mathbf{S}}(\mathbf{t})$, $\hat{\mathbf{N}}(\mathbf{t})$, and $\hat{\mathbf{B}}(\mathbf{t})$ are the Sun LOS, the nadir direction, and the magnetic field vectors retrieved from the instruments on-board the satellite, respectively. $\mathbf{S}(\mathbf{t})$, $\mathbf{N}(\mathbf{t})$ and $\mathbf{B}(\mathbf{t})$ are the true Sun LOS, the true nadir direction, and the true magnetic field vectors, respectively. $\boldsymbol{\eta_S(t)}$, $\boldsymbol{\eta_N(t)}$, and $\boldsymbol{\eta_B(t)}$ are the three zero-mean Gaussian noises that we assume for the three vectors. According to Table 1, the use of a nadir direction in an eclipse to determine the satellite attitude is not common. In an eclipse, Table 1 shows that the most common idea is to rely only on magnetometer and gyrometer measurements. Indeed, we know that the gyrometer can be very noisy and inaccurate [21]. However, the UVSQ-SAT is equipped with the infrared sensors presented in Section 2. Thus, those infrared sensors will help to determine the nadir direction from the terrestrial infrared radiations.

The three-axis rate from the gyrometer is defined with $\boldsymbol{\hat{\omega}(t)}$ as follows (Equation (7a,b)):

$$\boldsymbol{\hat{\omega}(t)} = \boldsymbol{\omega(t)} + \boldsymbol{\beta(t)} + \boldsymbol{\eta_\omega(t)} \tag{7a}$$

$$\dot{\boldsymbol{\beta}}(t) = \boldsymbol{\eta_\beta(t)} \tag{7b}$$

where $\boldsymbol{\omega(t)}$ is the true rate, $\boldsymbol{\beta(t)}$ is the drift, and $\boldsymbol{\eta_\omega(t)}$ and $\boldsymbol{\eta_\beta(t)}$ are the zero-mean Gaussian noises.

As the measurements from the gyrometer are conducted with respect to an inertial reference frame, this is defined as (Equation (8))

$$\boldsymbol{\omega_{B/I}} = \boldsymbol{\omega_{B/OC}} + \boldsymbol{\omega_{OC/I}} \tag{8}$$

where $\boldsymbol{\omega_{OC/I}}$ is the rate from the body frame with respect to the inertial frame that is equal to $\boldsymbol{\omega_0}$ the orbital angular velocity along the axis orthogonal to the orbital plane. $\boldsymbol{\omega_0}$ is computed from the mean motion given at each time. This information is contained in a list of orbital elements for a given point in time called a two-line element set (retrieved by the NORAD). The angular velocity with respect to the orbital frame is computed at each time given the attitude matrix at that time with respect to the orbital frame in Equation (9).

$$\boldsymbol{\omega_{B/O}} = \boldsymbol{\omega_{B/I}} - A_{O\to B}\boldsymbol{\omega_{O/I}} = \boldsymbol{\omega_{B/I}} - A_{O\to B}\boldsymbol{\omega_0} \tag{9}$$

where $A_{O \rightarrow B}$ is the rotation matrix from the local orbital frame to the body reference frame. The changes in the reference frame presented are directly related to the description of the reference frames in Section 2.2.1. The choice of the inertial reference frame to use has been meticulously made to facilitate the calculations in Equation (9).

3. Attitude Determination Methods

3.1. Tri-Axial Attitude Determination Method (TRIAD)

3.1.1. Formulation of the Method

The TRIAD algorithm aims to determine the attitude of the CubeSat. The output of the algorithm is the rotation matrix from the orbit reference frame (O) to the body reference frame (B). This matrix is also called the attitude matrix. The calculations are done instantaneously using two known vectors in both of the reference frames. The inputs required to compute the attitude matrix are the Sun LOS and the magnetic field in the two reference frames. In the body reference frame, the vectors are determined from the UVSQ-SAT measurements. In the orbit reference frame, the inputs are computed from the International Geomagnetic Reference Field [22] and orbital models at the satellite's location and time. We note that in an eclipse, we use nadir vectors instead of Sun LOS vectors. The nadir vector is defined as $\boldsymbol{N}$ in the body frame and $\boldsymbol{N_o}$ in the local orbital frame. The method is described in sunlight in the Equations (10) and (11). For the eclipse periods, $\boldsymbol{N}$ and $\boldsymbol{S}$ would commute. Nevertheless, less accurate results are expected in an eclipse since it is more complicated to determine the nadir from the infrared sensors rather than the Sun LOS.

To compute the attitude from the TRIAD algorithm, we introduce a new reference frame based on the body and orbital reference frames. This new reference frame is called the TRIAD frame and was described in [23,24]. The TRIAD frame is meant to be an intermediary between the orbital and the body frame; therefore, it should be easily defined in each of those reference frames. This reference frame is based on the magnetic field and the Sun LOS vectors. Let us start by expressing the TRIAD frame in the body reference frame, which is described as $\{\mathbf{t_{1b}},\ \mathbf{t_{2b}},\ \mathbf{t_{3b}}\}$ in Figure 7. Ideally, the most accurate vector should be used as the first axis. Usually, Sun sensors are more accurate than magnetometers. The Sun LOS is therefore chosen as the first direction. This axis is often called the anchor as it remains unchanged. Thus, the frame can be described in the body reference frame as (Equation (10))

$$\mathbf{t_{1b}} = \frac{\mathbf{S}}{\|\mathbf{S}\|},\ \mathbf{t_{2b}} = \frac{\mathbf{S} \times \mathbf{B}}{\|\mathbf{S} \times \mathbf{B}\|},\ \mathbf{t_{3b}} = \mathbf{t_{1b}} \times \mathbf{t_{2b}} \tag{10}$$

where $\mathbf{S}$ and $\mathbf{B}$ are the Sun LOS and magnetic field vector in the body frame retrieved from the instruments on-board the spacecraft, and the TRIAD's basis can be expressed as $\{\mathbf{t_{1o}},\ \mathbf{t_{2o}},\ \mathbf{t_{3o}}\}$ in the orbital frame, in Equation (11):

$$\mathbf{t_{1o}} = \frac{\mathbf{S_o}}{\|\mathbf{S_o}\|},\ \mathbf{t_{2o}} = \frac{\mathbf{S_o} \times \mathbf{B_o}}{\|\mathbf{S_o} \times \mathbf{B_o}\|},\ \mathbf{t_{3o}} = \mathbf{t_{1o}} \times \mathbf{t_{2o}} \tag{11}$$

where $\mathbf{S_o}$ and $\mathbf{B_o}$ are the Sun LOS and magnetic field vectors in the orbital frame computed from models. Therefore, it is rather simple to recover the transfer matrix from the orbital to body frame via the TRIAD frame. The rotation matrix can be written as in Equation (12):

$$R_{TRIAD,O \rightarrow B} = [\mathbf{t_{1o}},\ \mathbf{t_{2o}},\ \mathbf{t_{3o}}][\mathbf{t_{1b}},\ \mathbf{t_{2b}},\ \mathbf{t_{3b}}]^T \tag{12}$$

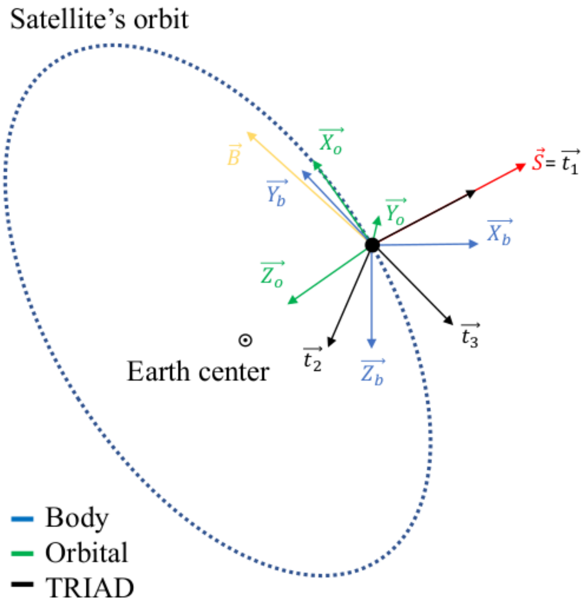

Figure 7. Reference frames for TRIAD method.

3.1.2. Optimized TRIAD

One of the limitations of the TRIAD method presented in Section 3.1.1 is the dependence on the choice of the first direction. This direction, called the anchor, remains untouched through the TRIAD process. However, in reality, neither of the two vectors used are perfectly aligned with the model. Therefore, in [25], the authors proposed to improve the method by taking the relative accuracy of the two measurements into account. The idea is to weight the two attitude matrices corresponding to the choice of using either of the two vectors as the first direction. This algorithm is called the optimized TRIAD algorithm. We define σ_S and σ_B as the standard deviations of the error of the LOS vector and the magnetic field vector, respectively. The attitude matrices A_S and A_B computed via the TRIAD method are for using the Sun LOS vector and magnetic field vector, respectively, as the first direction of the TRIAD frame. The weighting process is done as follows (Equation (13)).

$$A^* = \frac{\sigma_S^2}{\sigma_S^2 + \sigma_B^2} A_S + \frac{\sigma_B^2}{\sigma_S^2 + \sigma_B^2} A_B \tag{13}$$

In order to obtain an attitude matrix, the resulting matrix must be orthogonal; therefore, the final attitude matrix is obtained in Equation (14). According to [26], one orthogonalization cycle is needed as A^* is close to being orthogonal.

$$A = \frac{1}{2}[A^* + (A^{*-1})^T] \tag{14}$$

Coarse Sun sensors are obviously not as accurate as Sun sensors. Therefore, it is quite legitimate to take the relative uncertainties of the two components into account via the presented method.

As for the simple TRIAD algorithm, no noise correction is applied. In case of large noise or, for example, high variability of the magnetic field, the computed attitude would not be accurate.

3.2. Multiplicative Extended Kalman Method

The MEKF method aims to improve the attitude determination accuracy by correcting instrument noise and calibrating the gyrometer in real-time. The Kalman filter was described by Swerling in 1958 or Kalman [27] and Kalman and Bucy [28]. The principle is based on a two-step method that aims to correct noises and instrument uncertainties.

The state variables describe the system at each time. These variables provide information on the corrections to be made to the instruments as well as the orientation of the satellite. They are first estimated and then corrected based on the observation from the instruments. Although standard Kalman filters are truly efficient for linear systems, they cannot be accurate for non-linear systems. Therefore, in our case, we use an Extended Kalman Filter (EKF). This algorithm is a linearized Kalman filter at the point of reference using the Taylor series expansions principle.

3.2.1. Formulation

At each iteration, MEKF [29] uses the quaternion as the attitude representation and the state vector $\delta\vartheta$ for the representation of the attitude errors. The true quaternion can then be defined as follows (Equation (15)):

$$\mathbf{q}^{\mathbf{true}} = \delta \boldsymbol{q}(\delta\boldsymbol{\vartheta}) \otimes \hat{\mathbf{q}} \tag{15}$$

where $\mathbf{q}^{\mathbf{true}}$ is the true quaternion that represents the real orientation of the object that is defined from a product. $\hat{\mathbf{q}}$ is the estimate quaternion giving an estimate of the object orientation. $\delta\boldsymbol{q}(\delta\boldsymbol{\vartheta})$ is the error quaternion defined by $\delta\boldsymbol{\vartheta}$, with the three components representing the attitude error. $\otimes$ is the quaternion product symbol first used in [30] and defined in [29] as follows (Equation (16)):

$$\bar{\mathbf{q}} \otimes \mathbf{q} = \begin{bmatrix} q_4 \bar{\mathbf{q}}_{\mathbf{1:3}} + \bar{q}_4 \mathbf{q}_{\mathbf{1:3}} + \bar{\mathbf{q}}_{\mathbf{1:3}} \times \mathbf{q}_{\mathbf{1:3}} \\ \bar{q}_4 q_4 - \bar{\mathbf{q}}_{\mathbf{1:3}} \cdot \mathbf{q}_{\mathbf{1:3}} \end{bmatrix} \tag{16}$$

where $\hat{x}$ represents the estimate of the quantity x (for example, the state vector). $\hat{x}^+$ represents the updated quantity of $\hat{x}^-$, before being updated. The local attitude error is the true linearized variable of interest to compute the attitude at each iteration. However, the gyrometer which is required to predict the motion of the satellite has several calibration parameters that need to be computed, such as the misalignments, scale factors, and time-dependent drift biases. Therefore, those quantities must be computed at each iteration. So, they must be considered as state variables.

3.2.2. Initialization

The state vector as mentioned previously is computed as (Equation (17))

$$\hat{\mathbf{x}}_{\mathbf{0}} = \left[\delta\hat{\boldsymbol{\vartheta}}_{\mathbf{0}}{}^{T} \hat{\boldsymbol{\beta}}_{\mathbf{0}}{}^{T} \hat{\mathbf{s}}_{\mathbf{0}}^{T} \hat{\mathbf{k}}_{\mathbf{U0}}^{T} \hat{\mathbf{k}}_{\mathbf{L0}}^{T} \right] \tag{17}$$

where $\hat{\boldsymbol{\beta}}_{\mathbf{0}}$ is the initial gyro drift biases. $\hat{\mathbf{s}}_{\mathbf{0}}$ is the initial gyrometer scale factor. $\hat{\mathbf{k}}_{\mathbf{U0}}$ and $\hat{\mathbf{k}}_{\mathbf{L0}}$ are the initial misalignments. P_0 is the initial covariance matrix defined from the predicted instrument uncertainties. $\delta\hat{\boldsymbol{\vartheta}}_{\mathbf{0}} = 0_3$ is the initial attitude error for $\hat{\mathbf{q}}_{\mathbf{0}}$ (initial quaternion).

3.2.3. Gain

The Kalman gain is used to give different weights to the measurements and the current estimate of the state. This is the weight assigned to the prediction or the observation and is defined by K_k as (Equation (18))

$$K_k = P_k^- H_k^T(\hat{\boldsymbol{x}}_{\boldsymbol{k}}^-)[H_k(\hat{\boldsymbol{x}}_{\boldsymbol{k}}^-)P_k^- H_k^T(\hat{\boldsymbol{x}}_{\boldsymbol{k}}^-) + R_k]^{-1} \tag{18}$$

where $H_k(\boldsymbol{x}_{\boldsymbol{k}}^-)$ is the observation model at time t_k. R_k is the measurement-error covariance matrix at t_k. P_k is the state error covariance at t_k. $H_k(\boldsymbol{x}_{\boldsymbol{k}}^-)$ is the observation matrix and is defined by (Equation 19):

$$H_k(\boldsymbol{x}_{\boldsymbol{k}}^-) = \begin{bmatrix} A(\hat{\boldsymbol{q}}^-)\boldsymbol{B_o} \times & | & 0_{3\times12} \\ A(\hat{\boldsymbol{q}}^-)\boldsymbol{S_o} \times & | & 0_{3\times12} \\ A(\hat{\boldsymbol{q}}^-)\boldsymbol{N_o} \times & | & 0_{3\times12} \end{bmatrix} \tag{19}$$

The operator $\times$ is such that (Equation (20))

$$\mathbf{x_{1:3}} \times = \begin{bmatrix} 0 & -x_3 & x_2 \\ x_3 & 0 & -x_1 \\ -x_2 & x_1 & 0 \end{bmatrix} \tag{20}$$

where $A(\boldsymbol{q})$ is the attitude matrix in Equation (21):

$$A(\boldsymbol{q}) = \|\boldsymbol{q}\|^{-2}((q_4^2 - \|\boldsymbol{q_{1:3}}\|^2)I + 2\boldsymbol{q_{1:3}}\boldsymbol{q_{1:3}}^T - 2q_4[\boldsymbol{q_{1:3}}\times])) \tag{21}$$

3.2.4. Update

This subsection aims to compute the post-update of the different variables at time t_k. The covariance matrix P can then be post-updated in Equation (22):

$$P_k^+ = [I - K_k H_k(\hat{\boldsymbol{x}}_k^-)]P_k^- \tag{22}$$

At this phase, a reset is applied to the pre-estimate of the error angle in Equation (23):

$$\delta\hat{\boldsymbol{\vartheta}}_k^- = \mathbf{0_3} \tag{23}$$

It is then possible to update the state vector in Equation (24):

$$\hat{\boldsymbol{x}}_k^+ = \hat{\boldsymbol{x}}_k^- + K_k[\boldsymbol{y}_k - \boldsymbol{h}_k(\hat{\boldsymbol{x}}_k^-)] \tag{24}$$

where $\mathbf{\hat{x}_k} = [\delta\hat{\boldsymbol{\vartheta}}_k{}^T \ \hat{\boldsymbol{\beta}}_k{}^T \ \mathbf{\hat{s}_k^T} \ \mathbf{\hat{k}_{U_k}^T} \ \mathbf{\hat{k}_{L_k}^T}]$. $\boldsymbol{h}_k(\hat{\boldsymbol{x}}_k^-)$ is the estimated observation that is given in Equation (25). The measurements are given in Equation (26).

$$\boldsymbol{h}_k(\hat{\boldsymbol{x}}_k^-) = \begin{bmatrix} A(\mathbf{\hat{q}}^-)\boldsymbol{B_o} \\ A(\mathbf{\hat{q}}^-)\boldsymbol{S_o} \\ A(\mathbf{\hat{q}}^-)\boldsymbol{N_o} \end{bmatrix}_{t_k} \tag{25}$$

$$\boldsymbol{y}_k = \begin{bmatrix} \boldsymbol{B} \\ \boldsymbol{S} \\ \boldsymbol{N} \end{bmatrix}_{t_k} \tag{26}$$

The quaternion's update is performed through two steps that aim to compute the quaternion corresponding to the error estimate in Equation (27a) and to preserve the unit quaternion norm in Equation (27b).

$$\mathbf{\hat{q}}^* = \mathbf{\hat{q}_k^-} + \frac{1}{2}\Xi(\mathbf{\hat{q}_k^-})\delta\hat{\boldsymbol{\vartheta}}_k{}^+ \tag{27a}$$

$$\mathbf{\hat{q}_k^+} = \frac{\mathbf{q}^*}{\|\mathbf{q}^*\|} \tag{27b}$$

where $\delta\hat{\boldsymbol{\vartheta}}_k{}^+$ corresponds to the first three components of the state vector $\hat{\boldsymbol{x}}_k^+$ and the $\Xi(q)$ matrix is defined in Equation (28):

$$\Xi(q) = \begin{bmatrix} q_4 I_3 + [\mathbf{q_{1:3}}\times] \\ -\mathbf{q_{1:3}}^T \end{bmatrix} \tag{28}$$

3.2.5. Propagation

The propagation part aims to propagate the expected values and covariance at time t_{k+1}. First of all, we compute the estimate of the gyrometer components corrected based on the factors, drifts, and misalignments obtained from the previous step as (Equation (29))

$$\hat{\omega}^+(\boldsymbol{t}) = [I_3 - \hat{S}(t)][\hat{\omega}^-(t) - \hat{\boldsymbol{\beta}}(\boldsymbol{t})] \tag{29}$$

where S characterizes the gyrometer biases and misalignments and is defined as (Equation (30)):

$$S = \begin{bmatrix} s_1 & k_{U1} & k_{U2} \\ k_{L1} & s_2 & k_{U3} \\ k_{L2} & k_{L3} & s_3 \end{bmatrix} \tag{30}$$

Based on the knowledge of the updated angular rate and quaternion at time t_k, the quaternion's estimate at time t_{k+1} is defined in Equation (31) as

$$\hat{\mathbf{q}}^{-}_{\mathbf{k+1}} = \bar{\Theta}(\hat{\boldsymbol{\omega}}^{+}_{\boldsymbol{k}})\hat{\mathbf{q}}^{+}_{\mathbf{k}} \tag{31}$$

where $\bar{\Theta}(\hat{\boldsymbol{\omega}}^{+}_{\boldsymbol{k}})$ is defined as (Equation (32))

$$\bar{\Theta}(\hat{\boldsymbol{\omega}}^{+}_{\boldsymbol{k}}) = \begin{bmatrix} \cos\left(\frac{1}{2}\left\|\hat{\boldsymbol{\omega}}^{+}_{\boldsymbol{k}}\right\|\Delta t\right) I_3 - [\hat{\Psi}^{+}_{k}\times] & \hat{\Psi}^{+}_{k} \\ -\hat{\Psi}^{+}_{k} & \cos\left(\frac{1}{2}\left\|\hat{\boldsymbol{\omega}}^{+}_{\boldsymbol{k}}\right\|\Delta t\right) \end{bmatrix} \tag{32}$$

where Δt is the duration between the two considered epochs. $\hat{\Psi}^{+}_{k}$ is computed in Equation (33) as

$$\hat{\Psi}^{+}_{k} = \frac{\sin\left(\frac{1}{2}\left\|\hat{\boldsymbol{\omega}}^{+}_{\boldsymbol{k}}\right\|\Delta t\right)\hat{\boldsymbol{\omega}}^{+}_{\boldsymbol{k}}}{\left\|\hat{\boldsymbol{\omega}}^{+}_{\boldsymbol{k}}\right\|} \tag{33}$$

The covariance matrix P estimate at t_{k+1} is such that (Equation (34))

$$P^{-}_{k+1} = \Phi_k P^{+}_{k} \Phi^{T}_{k} + \Gamma_k Q_k \Gamma^{T}_{k} \tag{34}$$

where Q_k is defined as in Equations (35)–(37) at the initialization and during the iterations as

$$Q(t) = block\ \ diagonal([\sigma^2_v I_3\ \ \sigma^2_u I_3\ \ \sigma^2_s I_3\ \ \sigma^2_U I_3\ \ \sigma^2_L I_3]) \tag{35}$$

$$Q_k = \Delta t\ G\ Q\ G^T \tag{36}$$

$$G(t) = \begin{bmatrix} -(I_3 - \hat{S}) & 0_{3\times 12} \\ 0_{12\times 3} & I_{12} \end{bmatrix} \tag{37}$$

where Φ_k is the state transition matrix that is computed as follows (Equations (38)–(40b)) for a simple first-order approximation:

$$\Phi_k = I_{15} + \Delta t F(t_k) \tag{38}$$

$$F(t) = \begin{bmatrix} -[\hat{\boldsymbol{\omega}}\boldsymbol{(t)}\times] & -(I_3 - \hat{S}) & diag(\boldsymbol{\omega} - \hat{\boldsymbol{\beta}}) & -\hat{U} & -\hat{L} \\ 0_{12\times 3} & 0_{12\times 3} & 0_{12\times 3} & 0_{12\times 3} & 0_{12\times 3} \end{bmatrix} \tag{39}$$

$$\hat{U} = \begin{bmatrix} \omega_2 - \hat{\beta}_2 & \omega_3 - \hat{\beta}_3 & 0 \\ 0 & 0 & \omega_3 - \hat{\beta}_3 \\ 0 & 0 & 0 \end{bmatrix} \tag{40a}$$

$$\hat{L} = \begin{bmatrix} 0 & 0 & 0 \\ \omega_1 - \hat{\beta}_1 & 0 & 0 \\ 0 & \omega_1 - \hat{\beta}_1 & \omega_2 - \hat{\beta}_2 \end{bmatrix} \tag{40b}$$

These calculation steps are applied to the inputs for each time step. In the case where the uncertainties related to the dynamics model are not very important, the corrections related to the gyro will converge at least in the short term. Nevertheless, they could evolve with the aging of the instrument and the flight conditions; thus, real-time calibration is legitimate.

4. Results

Once the algorithm is implemented, it is possible to calculate the satellite attitude for each measurement acquisition. The objective of calculating this attitude is required to compute the incident flux for each face of the CubeSat, as presented in Section 1. This means that the measured fluxes are corrected from their angle to the observed source. Therefore, the flux corrections are directly related to the Sun LOS and nadir vectors in the spacecraft body frame.

This section presents the two unit vectors in the satellite's body reference frame for both TRIAD and MEKF methods. The vectors are represented as a function of time according to each of their components in the satellite reference frame.

For example, if the X component of the Sun LOS is equal to 1, the satellite's +X face is facing the Sun, the normal to the face coincides with the Sun LOS vector, and this would be the case for the −X face if the Sun LOS X component was −1. In the following studies, only data from the UVSQ-SAT satellite in orbit are used to test the TRIAD and MEKF methods.

4.1. Results with TRIAD Method

The TRIAD method (Section 3.1) provides the CubeSat attitude matrix. The Sun LOS in the body frame is computed from the model and the attitude matrix. The nadir direction in the body frame is obtained from the transformation of the nadir vector in the orbital frame (defined as the third axis of the reference frame basis). Those two vectors are represented in Figure 8.

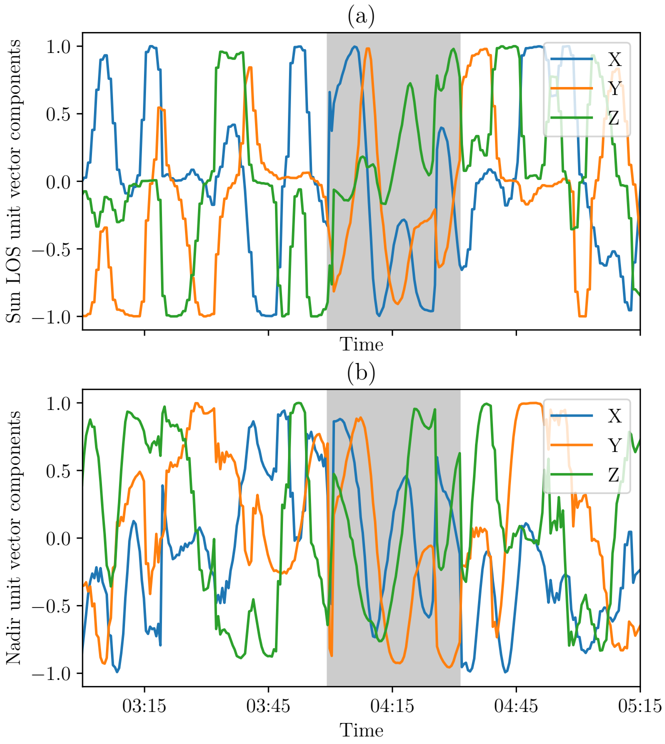

Figure 8. First lights of the Sun LOS (**a**) and nadir (**b**) components in the satellite body frame based on TRIAD method on 2 March 2021 (representative period in the case of measurements at 30 s intervals almost continuously, with eclipse phase in gray).

4.2. Results with MEKF Method

The second method, described in Section 3.2, should correct the signals from noise and gyrometer biases. The Sun LOS and nadir directions are computed in the body reference frame from the attitude matrix. Their components in this frame are shown in Figure 9.

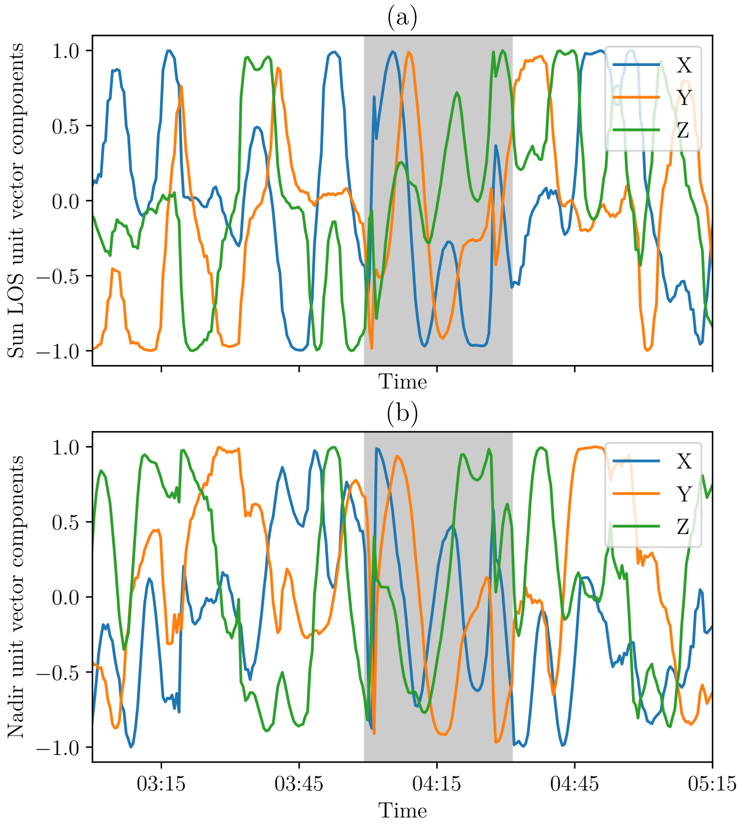

Figure 9. First lights of the Sun LOS (**a**) and nadir (**b**) components in the satellite body frame based on MEKF on 2 March 2021 (representative period in the case of measurements at 30 s intervals almost continuously with eclipse phase in gray).

4.3. Discussion and Perspectives

The TRIAD and MEKF methods were applied to in-orbit data. The objective is to compare the two methods. To visualize the improvement expected from the MEKF method, it can be wise to superpose the results from the different methods in Figure 10. Three indicators to compare the methods are described in this part. The first indicator is based on the variations of the attitude itself while the second one is derived from the measurements of a sensor that was not used as an input by the two methods. The last indicator is the uncertainty of each method. The satellite attitude computed with the Kalman filter is continuous, which corresponds to a realistic case in orbit. Discontinuities mostly come from noise in the measurement process. It is therefore relevant to quantify the fast changes in attitude. This can be done studying the gradient of the Sun LOS or nadir components. Studying the standard deviation of the gradient is representative of the short variations that could be due to the attitude determination error. The average of the standard deviations of the Sun LOS gradients is equal to 5.17×10^{-3} s^{-1} for the TRIAD method compared to 4.1×10^{-3} s^{-1} for the MEKF method (UVSQ-SAT data on the 2 and 3 February 2021). Therefore, the MEKF method seems to represent the satellite attitude variations better based on the previous indicator as it reduces discontinuities thanks to its smoothing asset.

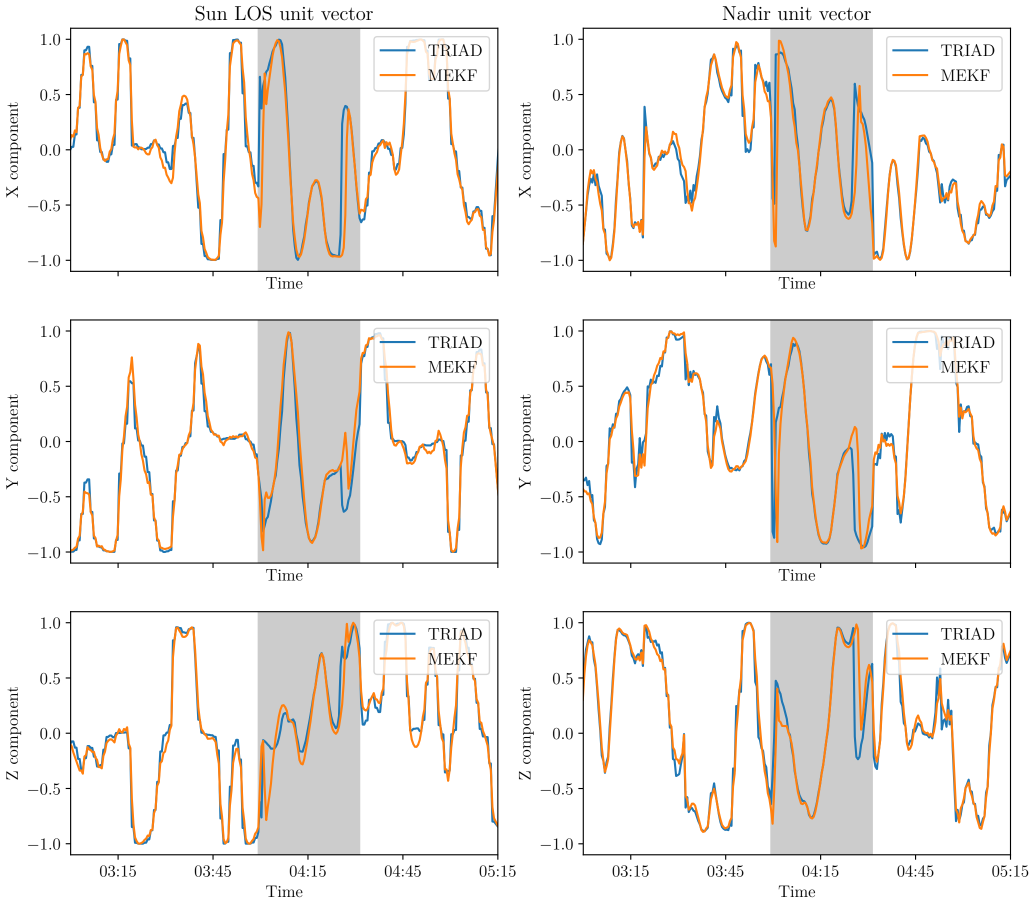

Figure 10. First lights of the Sun LOS and nadir coordinates in the satellite body frame based on MEKF and TRIAD on 2 March 2021 (representative period in the case of measurements at 30 s intervals almost continuously with eclipse phase in gray).

A more accurate analysis can be established based on the measurements of a sensor not used in the attitude determination process. UV sensors (UVSs) with a narrow field of view (FOV) are used to compare the results based on the two methods. Those sensors are primarily sensitive to solar radiation. Therefore, the sensors should detect when the Sun appears in the FOV. It is therefore a great indicator to evaluate the precision and accuracy of both methods. This allows us to determine which method is the most adequate to find the orientation of the satellite (in the majority of cases). It is important to note that this study has limitations as it is realized only in the phases of sunlight and in some configurations. The reference cases are related to direct solar observations.

The accuracy and precision values are computed for each method. The accuracy value is defined in Equation (41a) as the proximity of a measured value to a real value. The value of precision in Equation (41b) refers to the proximity of two or more measurements to each other. This allows us to monitor the presence of a bias in the attitude determination.

$$Accuracy = \frac{TP + TN}{TP + FP + FN + TN} \tag{41a}$$

$$Precision = \frac{TP}{TP + FP} \tag{41b}$$

where TP, FN, FP, and TN are defined in Table 2.

Table 2. Definition of the true positive, false negative, false positive, and true negative.

Definition		**Attitude Determination**	
		Facing the Sun	**Not Facing the Sun**
UVS	Facing the Sun	*True Positive (TP)*	*False Negative (FN)*
	Not facing the Sun	*False Positive (FP)*	*True Negative (TN)*

These values are calculated in the case of the TRIAD method in Figure 11 and then for MEKF in Figure 12.

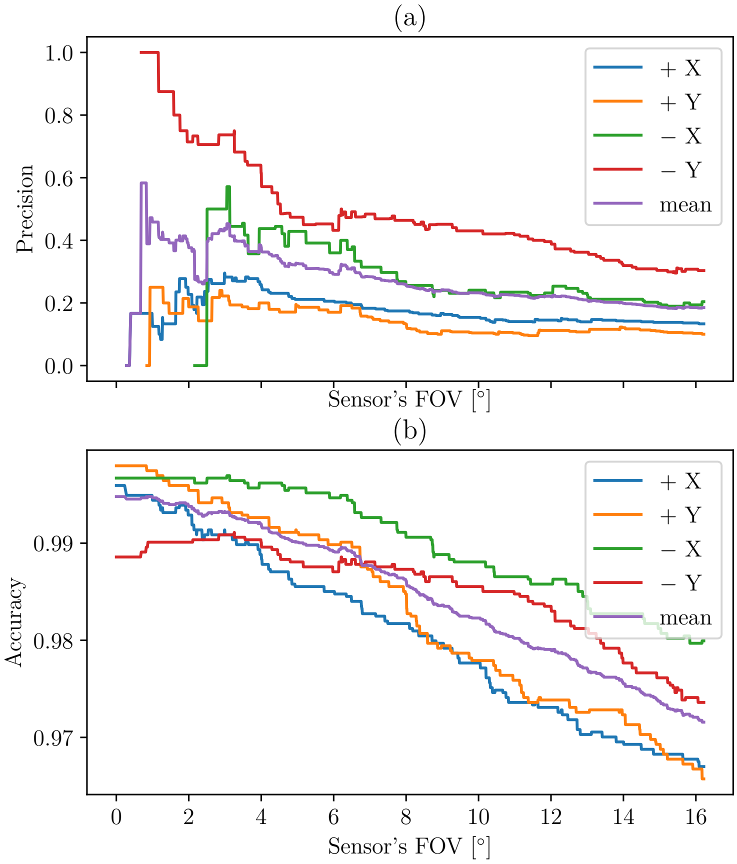

Figure 11. Precision (**a**) and accuracy (**b**) of the TRIAD method based on the UVS indicator.

The indicators are plotted according to different FOV. Indeed, the FOV of the instrument can be different from the theoretical FOV due to uncertainties of measurements and misalignments. This is the reason why we choose to calculate the accuracy and precision for different values of angle threshold (theoretical FOV). When the angle between the normal to the sensor and the Sun LOS determined by each method is below a certain threshold (FOV), it is verified that the UVS sensor receives a signal corresponding to the incident solar flux. This is an indicator that the considered face is facing the Sun. Using large numbers of values corresponding to large numbers of different configurations helps us to quantify the ability of the methods to recover the Sun LOS in the body frame.

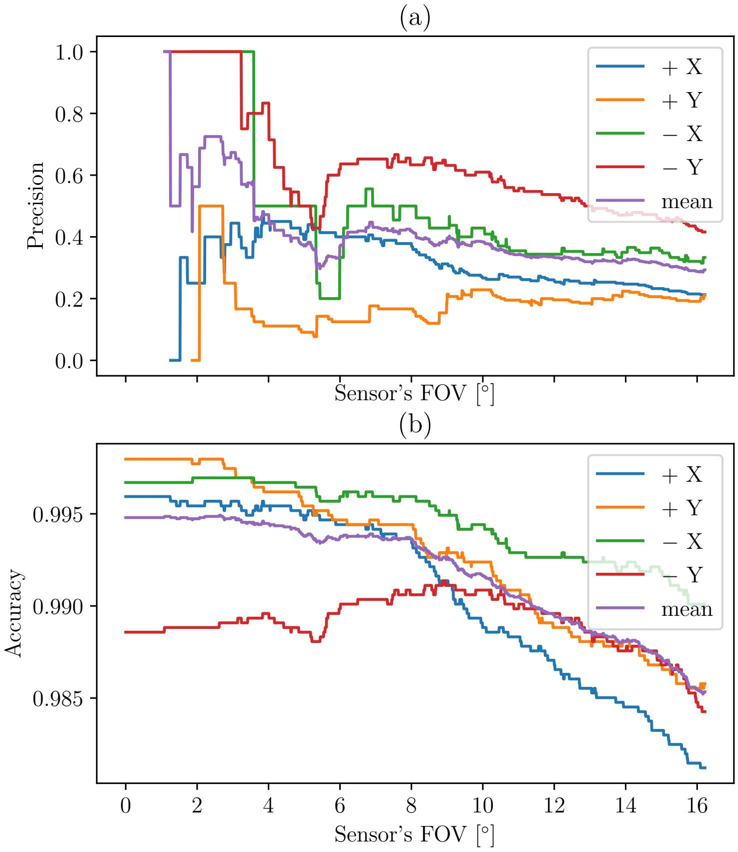

Figure 12. Precision (**a**) and accuracy (**b**) of the MEKF method based on the UVS indicator.

The methods can be compared by computing the difference between the indicators for MEKF and TRIAD. The results are presented in Figure 13. The MEKF method allows us to increase the precision by about 20% and the accuracy by a few percent.

The last indicator used to compare the methods is the absolute uncertainty of the two methods developed above. To do this, we choose to use the Monte Carlo method to perform the propagation of uncertainties. The uncertainties of the instruments are quantified from the specifications and empirically. They are represented as a Gaussian probability density function. We then seek to quantify the uncertainty propagated on the angle to the Sun and the angle to the nadir as the flux computation depends on those parameters. The uncertainty is estimated in two different cases. The plot at the top of Figure 14 shows the evolution of the uncertainty for TRIAD and MEKF methods in the case of the data received almost continuously over the whole selected period. The sampling rate is thus almost constant and regular. This represents the ideal case where all the data are retrieved, and the only limitation is the sampling rate. The plot at the bottom of Figure 14 represents the same evolution for a longer period equivalent to more than 22 orbits including phases with missing data. It is thus possible to obtain the restitution of attitude with a 3° uncertainty (at 1 σ) in sunlight for both methods. In eclipse, for long periods of time (including missing data), the uncertainty reaches 14° for TRIAD while it converges to about 10° for the MEKF method. In general, we see an improvement of about 4°. Eclipse phases appear in gray and sunlight in white. The determination of the uncertainty in time is pertinent as the attitude will be time-dependent for the MEKF method. This is apparent in Figure 14 as the uncertainty for the MEKF method converges with time. We also see that sunlight and eclipse phases have totally different results in terms of uncertainty as the data provided come from different instruments.

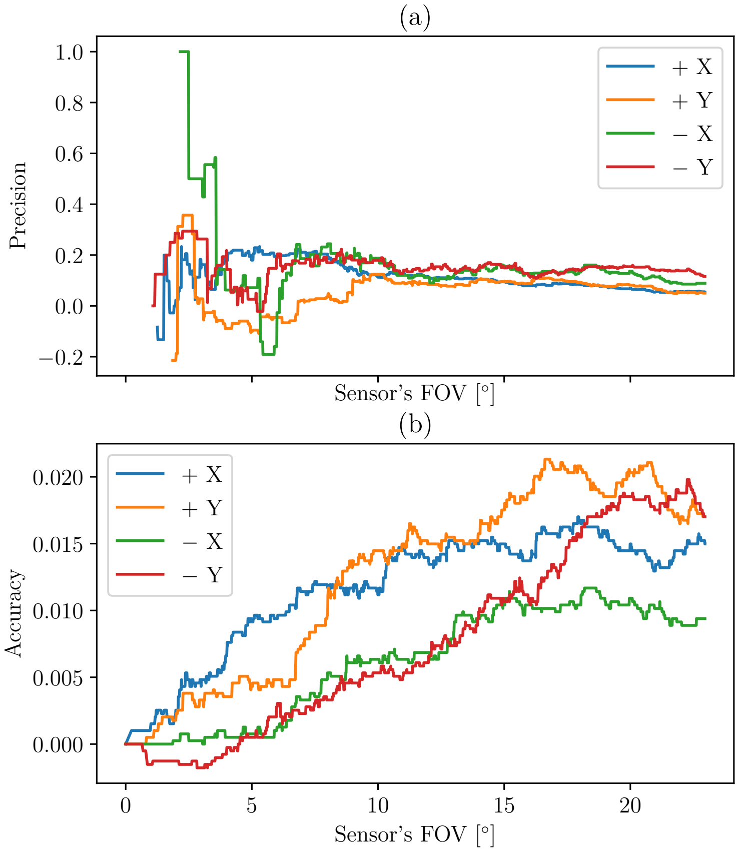

Figure 13. Difference between the precision (**a**) and accuracy (**b**) of the MEKF and the TRIAD methods based on the UVS indicator (positive means that MEKF has better performance compared to TRIAD).

The accuracy of the MEKF method can be compared to validation with in-orbit data from [3]. It appears that the uncertainty is much lower for the Radio Aurora Explorer satellites with a 1 Hz sampling rate (below 1°). A 1 Hz sampling rate was not enough to capture the spacecraft motion, and a slowing down of the satellite rotation was therefore undertaken and allowed to improve the results. In our case, the sampling period of 30 s does not allow us to reach such accuracy. This is nevertheless important to note as feedback.

It is possible to estimate the uncertainties on the incident flux from the uncertainties on the angles to the source. Indeed, fluxes are corrected using the cosine of the angle for the Sun and the view factor in the case of terrestrial flux. Those uncertainties are based only on the attitude determination uncertainties. Therefore, for the solar flux, the uncertainty is estimated at 4% (1σ) for both methods. For the eclipse phase and terrestrial flux, the TRIAD method allows us to compute the flux with around 19% uncertainty, although MEKF allows for around 13% accuracy (1σ). The MEKF method brings improvements. but it also presents limitations. The algorithm loads the data on-ground from in-orbit data to compute the CubeSat attitude. However, the method relies on the need to predict the state vector at the next iteration from the previous measurements.

Therefore, it is important that those two steps are not too far in time given the chosen sampling rate. Rarely, but not impossibly, the inputs data can be missing due to a single-event upset (SEU) or missing values in the communication process. An example of this appears in Figure 15.

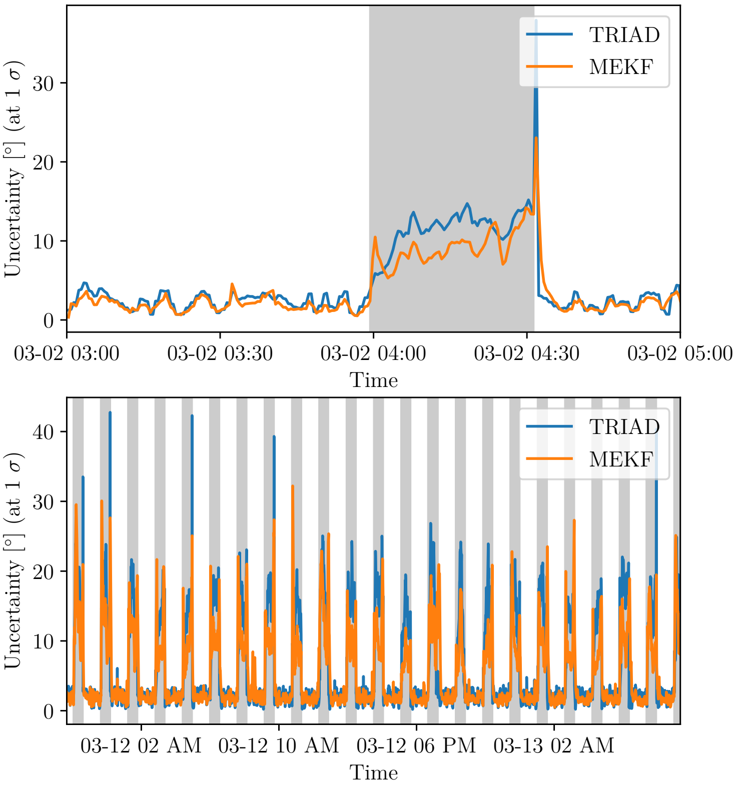

Figure 14. Uncertainties estimated from the Monte Carlo method for TRIAD and MEKF methods for continuous sampling on 2 March 2021 (**top**) and from 11–13 March 2021 (**bottom**) with eclipse phases in gray.

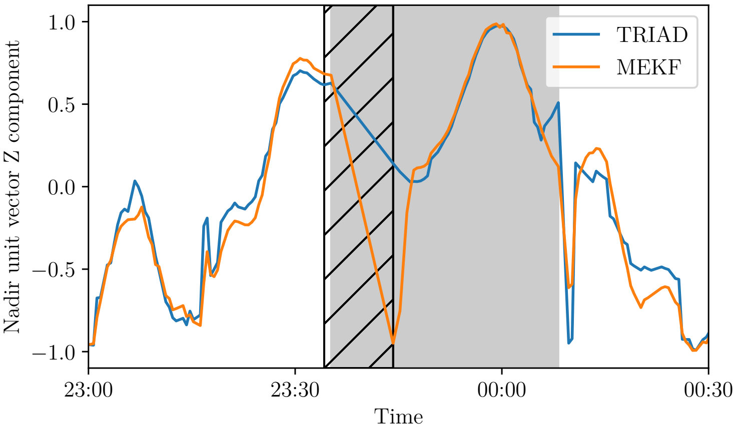

Figure 15. Nadir Z component in the satellite frame based on the TRIAD and MEKF methods—missing values are delimited with hatches for a 10 min duration on 3 February 2021.

After the missing values, the first estimations of the nadir component from the MEKF method seem to be very different from the TRIAD estimations. Data gaps cause the poor prediction of the next iteration. This issue can be solved by implementing the algorithm on-board the satellite to avoid missing values due to communication issues. To do so, the computations should be executed on the on-board computer. Computational resources can be limited in-orbit. Therefore, an optimized algorithm was developed to reduce the required computations and is described in [15].

This section has presented the results of the methods. The advantages and limitations can be summarized as follows. The use of infrared sensors instead of photodiodes in an eclipse allows us to greatly reduce the measurement uncertainty. This is still recent and rarely developed in the literature (Table 1, such as in [12] or [19]), but its use could be validated in orbit. Moreover, the use of the Kalman filter allowed us to increase the accuracy of the attitude restitution and is relatively computationally efficient compared to the Unscented Kalman Filter presented in [19]. However, certain limitations are present due to difficulties of a making predictions due to a lack of data.

5. Conclusions

UVSQ-SAT CubeSat aims to validate innovative technologies in-orbit for a future constellation to study the Earth's energy imbalance. UVSQ-SAT has been in orbit since 24 January 2021. To improve the UVSQ-SAT's reflected solar radiation and outgoing long-wave radiation measurements at the top of the atmosphere, the UVSQ-SAT's attitude must be accurately known. Two different methods were implemented to determine the UVSQ-SAT CubeSat's attitude, and they are based on real data from space observations.

The first method developed is based on the TRIAD algorithm. The accuracy of the UVSQ-SAT attitude knowledge obtained with the TRIAD method is close to $\pm 3^\circ$ (at one σ) in sunlight. During eclipse periods, the accuracy of the UVSQ-SAT attitude knowledge is $\pm 14^\circ$ (at one σ). In this observation phase, accurate knowledge of the CubeSat attitude is more difficult to obtain. This mode of operation with other sensors (Earth radiative sensors instead of solar visible photodiodes) brings limits. Moreover, the TRIAD method does not correct all measurement noises.

The MEKF method allows us to estimate and correct instrument noise. It performs the real-time calibration of the UVSQ-SAT gyrometer. The MEKF method computes the UVSQ-SAT attitude knowledge with an accuracy similar to TRIAD in sunlight, but with an accuracy of $\pm 10^\circ$ during eclipse periods (at one σ). There are limitations to the MEKF method, such as the lack of continuous data. This is a limiting factor since it leads to large divergence errors. The prediction becomes better when the time between two measurements is short. Then, the linearization becomes more realistic. Reducing the time-step could be beneficial for future CubeSats, and ground-based tests in near-space conditions would be recommended to optimize the various parameters.

The methods presented on this manuscript are based on direct measurements (TRIAD) or Kalman filters (MEKF). Another approach would be to use neural networks to determine the UVSQ-SAT satellite's attitude as described in [31]. The neural network will be implemented and trained in-orbit in sunlight to improve the attitude determination accuracy during eclipse periods. The training will be based on the previously described methods, and the performance of the new method will be evaluated to assess the ability of the method to be implemented for the future satellites of the constellation.

Author Contributions: Conceptualization, A.F., C.D., T.B., M.M.; methodology, A.F., C.D., T.B. and M.M.; software, A.F., C.D.; validation, C.D.; resources, M.M.; writing—original draft preparation, A.F., C.D., T.B., M.M.; writing—review and editing, A.F., C.D., M.M., A.M., A.S., P.K. and T.B.; visualization, A.F., C.D., M.M.; supervision, M.M.; project administration, M.M.; funding acquisition, M.M. All authors have read and agreed to the published version of the manuscript.

Funding: This research was mainly funded by Centre National de la Recherche Scientifique (CNRS, France), UVSQ (Université de Versailles Saint-Quentin-en-Yvelines, France), and Agence Nationale de La Recherche (ANR, France). This work was supported by the Programme National Soleil Terre (PNST) of CNRS/INSU (France) co-funded by CNES and Commissariat à l'énergie atomique (CEA, France).

Institutional Review Board Statement: Not applicable.

Informed Consent Statement: Not applicable.

Data Availability Statement: Not applicable.

Acknowledgments: The authors acknowledge support from the Centre National de la Recherche Scientifique (CNRS, France), the Centre National d'Études Spatiales (CNES, France), and Office National d'Études et de Recherches Aérospatiales (ONERA, France).

Conflicts of Interest: The authors declare no conflict of interest.

References

1. Meftah, M.; Damé, L.; Keckhut, P.; Bekki, S.; Sarkissian, A.; Hauchecorne, A.; Bertran, E.; Carta, J.P.; Rogers, D.; Abbaki, S.; et al. UVSQ-SAT, a pathfinder cubesat mission for observing essential climate variables. *Remote Sens.* **2020**, *12*, 92. [CrossRef]
2. Meftah, M.; Boutéraon, T.; Dufour, C.; Hauchecorne, A.; Keckhut, P.; Finance, A.; Bekki, S.; Abbaki, S.; Bertran, E.; Damé, L.; et al. The UVSQ-SAT/INSPIRESat-5 CubeSat Mission: First In-Orbit Measurements of the Earth's Outgoing Radiation. *Remote Sens.* **2021**, *13*, 1449. [CrossRef]
3. Springmann, J.C.; Cutler, J.W. On-orbit Calibration of Photodiodes for Attitude Determination. *J. Guid. Control. Dyn.* **2014**, *37*, 1808–1823. [CrossRef]
4. Psiaki, M.L.; Martel, F.; Pal, P.K. Three-axis attitude determination via Kalman filtering of magnetometer data. *J. Guid. Control. Dyn.* **1990**, *13*, 506–514. [CrossRef]
5. Hashmall, J.A.; Radomski, M.; Sedlak, J. On-orbit calibration of satellite gyroscopes. In Proceedings of the Astrodynamics Specialist Conference, Minneapolis, MN, USA, 13–16 August 2000; pp. 339–349. [CrossRef]
6. Pittelkau, M.E. Kalman Filtering for Spacecraft System Alignment Calibration. *J. Guid. Control. Dyn.* **2001**, *24*, 1187–1195. [CrossRef]
7. Theil, S.; Appel, P.; Schleicher, A. Low Cost, Good Accuracy—Attitude Determination Using Magnetometer and Simple Sun Sensor. 2003. Available online: https://digitalcommons.usu.edu/smallsat/2003/All2003/81/ (accessed on 20 July 2021).
8. Bhanderi, D.; Bak, T. Modeling Earth Albedo for Satellites in Earth Orbit. In Proceedings of the AIAA Guidance, Navigation, and Control Conference and Exhibit, San Francisco, CA, USA, 15–18 August 2005; Volume 8. [CrossRef]
9. Ma, G.-F.; Jiang, X.-Y. Unscented Kalman Filter for Spacecraft Attitude Estimation and Calibration Using Magnetometer Measurements. In Proceedings of the 2005 International Conference on Machine Learning and Cybernetics, Guangzhou, China, 18–21 August 2005; Volume 1, pp. 506–511. [CrossRef]
10. Côté, J.; De Lafontaine, J. Magnetic-only orbit and attitude estimation using the Square-Root Unscented Kalman Filter: Application to the PROBA-2 spacecraft. In *AIAA Guidance, Navigation and Control Conference and Exhibit*; AIAA: Reston, VA, USA, 2008; pp. 1–24. [CrossRef]
11. Filipski, M.N.; Varatharajoo, R. Evaluation of a spacecraft attitude and rate estimation algorithm. *Aircr. Eng. Aerosp. Technol.* **2010**, *82*, 184–193. [CrossRef]
12. Springmann, J.C.; Sloboda, A.J.; Klesh, A.T.; Bennett, M.W.; Cutler, J.W. The attitude determination system of the RAX satellite. *Acta Astronaut.* **2012**, *75*, 120–135. [CrossRef]
13. Searcy, J.D.; Pernicka, H.J. Magnetometer-Only Attitude Determination Using Novel Two-Step Kalman Filter Approach. *J. Guid. Control. Dyn.* **2012**, *35*, 1693–1701. [CrossRef]
14. Zeng, Z.; Zhang, S.; Xing, Y.; Cao, X. Robust Adaptive Filter for Small Satellite Attitude Estimation Based on Magnetometer and Gyro. *Abstr. Appl. Anal.* **2014**, *2014*, 159149. [CrossRef]
15. Pham, M.D.; Low, K.S.; Goh, S.T.; Chen, S. Gain-scheduled extended Kalman filter for nanosatellite attitude determination system. *IEEE Trans. Aerosp. Electron. Syst.* **2015**, *51*, 1017–1028. [CrossRef]
16. Kiani, M.; Pourtakdoust, S.H.; Sheikhy, A.A. Consistent calibration of magnetometers for nonlinear attitude determination. *Meas. J. Int. Meas. Confed.* **2015**, *73*, 180–190. [CrossRef]
17. Koizumi, S.; Kikuya, Y.; Sasaki, K.; Masuda, Y.; Iwasaki, Y.; Watanabe, K. Development of Attitude Sensor using Deep Learning. In *AIAA/USU Conference on Small Satellites*; AIAA: Reston, VA, USA, 2018; pp. 1–8.
18. Labibian, A.; Pourtakdoust, S.H.; Alikhani, A.; Fourati, H. Development of a radiation based heat model for satellite attitude determination. *Aerosp. Sci. Technol.* **2018**, *82–83*, 479–486. [CrossRef]
19. Baroni, L. Attitude determination by unscented Kalman filter and solar panels as sun sensor. *Eur. Phys. J. Spec. Top.* **2020**, *229*, 1501–1506. [CrossRef]
20. Kapás, K.; Bozóki, T.; Dálya, G.; Takátsy, J.; Mészáros, L.; Pál, A. Attitude Determination for Nano-Satellites—I. Spherical Projections for Large Field of View Infrasensors. *Exp. Astron.* **2021**, *51*, 1–13. [CrossRef]
21. Mimasu, Y.; Narumi, T.; Van der Ha, J. *Attitude Determination by Magnetometer and Gyros During Eclipse*; AIAA: Reston, VA, USA, 2008. [CrossRef]
22. Alken, P.; Thébault, E.; Beggan, C.D.; Amit, H.; Aubert, J.; Baerenzung, J.; Bondar, T.N.; Brown, W.J.; Califf, S.; Chambodut, A.; et al. International Geomagnetic Reference Field: The thirteenth generation. *Earth Planets Space* **2021**, *73*, 49. [CrossRef]
23. Black, H.D. A passive system for determining the attitude of a satellite. *AIAA J.* **1964**, *2*, 1350–1351. [CrossRef]
24. Markley, F.L.; Mortari, D. How to estimate attitude from vector observations. *Adv. Astronaut. Sci.* **2000**, *103*, 1979–1996.
25. Bar-Itzhack, I.Y.; Harman, R.R. Optimized TRIAD Algorithm for Attitude Determination. *J. Guid. Control. Dyn.* **1997**, *20*, 208–211. [CrossRef]
26. Bar-itzhack, I.Y.; Meyer, J. On the Convergence of Iterative Orthogonalization Processes. *IEEE Trans. Aerosp. Electron. Syst.* **1976**, *AES-12*, 146–151. [CrossRef]
27. Kalman, R.E. A New Approach to Linear Filtering and Prediction Problems. *Trans. ASME-Basic Eng.* **1960**, *82*, 35–45. [CrossRef]
28. Kalman, R.E.; Bucy, R.S. New Results in Linear Filtering and Prediction Theory. *J. Basic Eng.* **1961**, *83*, 95–108. [CrossRef]

29. Markley, F.L.; Crassidis, J.L. Static Attitude Determination Methods. In *Fundamentals of Spacecraft Attitude Determination and Control*; Springer: New York, NY, USA, 2014; pp. 183–233. [CrossRef]
30. Lefferts, E.J.; Markley, F.L.; Shuster, M.D. Kalman Filtering for Spacecraft Attitude Estimation. *J. Guid. Control. Dyn.* **1982**, *5*, 417–429. [CrossRef]
31. Finance, A.; Meftah, M.; Dufour, C.; Boutéraon, T.; Bekki, S.; Hauchecorne, A.; Keckhut, P.; Sarkissian, A.; Damé, L.; Mangin, A. A New Method Based on a Multilayer Perceptron Network to Determine In-Orbit Satellite Attitude for Spacecrafts without active ADCS like UVSQ-SAT. *Remote Sens.* **2021**, *13*, 1185. [CrossRef]

3.5 Application of the Neural Network to Determine the Satellite Attitude

3.5.1 In-orbit Attitude Determination with the Multi-layer Perceptron

The results were presented at AGU 2021 in [Finance et al., 2021c]. The section presents the outcome of the application of the neural network to in-orbit data.

General Method

This section describes a method that aims to compute the satellite attitude with the best accuracy possible at each time. The algorithm uses neural networks to predict the UVSQ-SAT attitude based on the instruments on-board and models. The general method is the same as the one presented in Section 3.3.2. The neural network is a MLP that is trained based on the attitude determination realized with TRIAD and MEKF methods described in Section 3.4.2. Training the neural network allows the optimization of the characteristic parameters of each layer in order to get closer to the expected result. This step should allow the use of the neural network to compute the satellite attitude without intermediate calculations.

Data Processing

Data are received at the mission center. The data processing is realized on-ground. Raw values are converted to scientific units. Instruments that can be calibrated are calibrated. Once the inputs are available, additional values are indicated or calculated which allow characterizing the satellite orbit for example, the surrounding magnetic field or the direction of the Sun in relation to the satellite. Then, different methods can be implemented to determine the UVSQ-SAT attitude. The methods are TRIAD and MEKF.

Main Objectives

The main goal of the algorithm is to determine the satellite's attitude at each time. As mentioned earlier, attitude knowledge is crucial to dissociate and compute the terrestrial flux. The main advantage of using the MLP based on the other methods is to obtain the best possible accuracy, avoiding the Kalman filter's drawbacks. The purpose is to compute instantaneously avoiding the recursive loop of the Kalman filter. The use of the neural network favors the use of all the instruments and sensors on board the satellite for attitude determination. In addition to adding the gyrometer values as in the case of the MEKF method, we integrate all the information known on board.

Inputs and Outputs

The inputs are measurements from the satellite (counting for 136 features) along with data from models at the location and time of the satellite (counting for 6 features).
The outputs are nadir and Sun coordinates (counting for 2×3), they are the vectors of reference that are used to dissociate and compute incident flux.

Feature Selection is a technique for limiting the input variable to the model by utilizing only relevant features. It is the technique of selecting suitable characteristics for the neural network model automatically based on the sort of problem being solved. We implement feature selection to improve the understanding of the neural network trained and more particularly to estimate the significance of the different features in the attitude determination process. Feature selection allows us to remove useless features in the process. It can also be used to improve attitude determination by clearly determining what measurements should be used in sunlight, and eclipse and removing the inappropriate ones.
Therefore, features selection is implemented from different techniques:

- Linear regression
- Random Forest regression
- SHapley Additive exPlanations (SHAP) [Shapley, 1951]

The objective of the techniques is to weigh the parameters that will have great importance in the determination of the satellite attitude. In the example of linear regression, we consider a layer of neurons. In this very basic case, the multiplier

becomes the weighting factor for the features. The more important it is the more the feature will have an impact on the output.
In sunlight:

- the Sun's direction is computed mostly thanks to the photodiodes.
- the nadir direction appears to be determined mostly from the magnetic field data, photodiodes, and infrared sensors.

Architecture

This architecture was presented by [Finance et al., 2021b] as tests were realized on-ground before launch. It has been slightly modified since, to allow for a different number of inputs and outputs and to adapt to different data. The inputs used in orbit are much more numerous since many features such as the temperature of the panels, and data on all sides are usable and can help deduce the orientation of the satellite.

- 5 Hidden fully connected layers
- 142 (max) inputs
- 6 (3 per direction) outputs
- Learning rate of 10^5, determined empirically
- Layers dimensions (width): 142/48/128/256/128/6

Training

The training of the neural network is done based on results from the TRIAD method for random samples from the first 9 months of data (around 500 000 samples). The ideal would have been to be able to train the neural network with a large number of samples from the MEKF method. However, due to the lack of data (mostly related to communication with the satellite), we use the TRIAD method to validate the training in orbit. We expect to have a performance altered by the noise present with TRIAD.

Performance of the UVSQ-SAT Multi-layer Perceptron in Sunlight

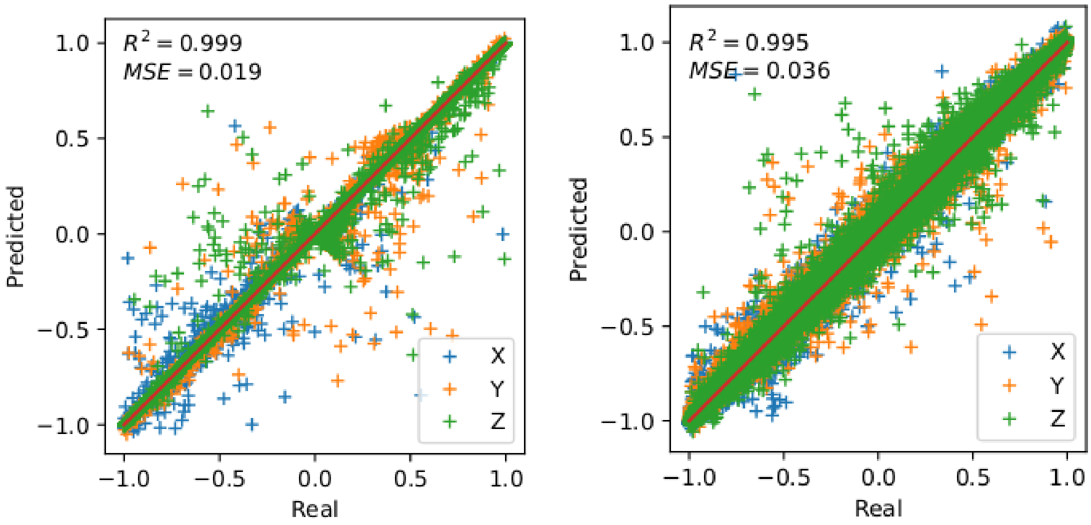

(a) Sun LOS coordinates

(b) Nadir direction coordinates

Figure 3.7: Predicted and real coordinates of the Sun LOS and nadir vector in daylight.

Figure 3.7 represents the predicted coordinates of the Sun LOS versus coordinates of reference (TRIAD) based on the optimized neural network. It is important to mention that the accuracy is estimated based on the TRIAD results and is not absolute accuracy. The continuous red curve illustrates the ideal case where the observed values exactly match the predicted values. We can compute an error for the Sun vector of 7° (at 1σ) compared to the test set. The error for the nadir vector is 10° (at 1σ) compared to the test set. We observe important errors for small coordinates, it corresponds to a low Sun meaning the Sun rays are far from the incident. Signals observed on the sensors of the related side are lower and less precise. The MEKF-based training is not represented as it could not allow training the algorithm as it is. Indeed, as the MEKF method needs iterations to converge it is an issue as the data provided from the mission can be discontinuous. The model used in the algorithm to predict the next state has issues when the time elapsed between two measurements is too long (e.g. more than 60 s). We chose here to evaluate the MLP performance using TRIAD as the method is instantaneous and does not need precise datarate. The performance is evaluated based on TRIAD algorithm results. No instruments on-board gives the true orientation. Those results are estimations. We quantify the ability of the MLP algorithm to learn from TRIAD.

Results

It uses the TRIAD training set based on random samples in the data from the launch and the optimized neural network. We have tested the ability of the neural network to predict the sun and nadir direction based on the available sensors. Those results are preliminary and allow quantifying the accuracy of the algorithm compared to the values computes from the TRIAD method in sunlight.

Perspectives

Method	Uncertainty		Advantage
	Sunlight	Eclipse	
TRIAD	3°	14°	Instantaneous
MEKF	3°	10°	Correct noise and calibrate instruments
MLP	3°*	3-10°*	Instantaneous and more accurate in eclipse

Table 3.2: Accuracy and advantages of each method (*desired).

The MLP method can be adapted to the architecture of the UVSQ-SAT and based on the reference dataset we have shown that it could be trained. This method could be implemented using more precise information from the MEKF algorithm. The sample rate and continuity of the measurement would improve the convergence and the accuracy of the algorithm. Future work is in progress to improve the MEKF method in the next satellite which will be described in the following. However, Table 3.2 recaps the accuracy in each condition for each method and expected accuracy based on the MLP. Subsequently, the neural network methods could be improved by using correlation related to the opposite faces which will have signals strongly influenced by the solar flux. Moreover, in terms of neural network architecture, the use of long short-term memory (LSTM) could be beneficial. An LSTM cell is a specific recurrent neural network (RNN). Recurrent neural networks work with sequences of arbitrary length rather than with fixed size inputs. They retain the memory of past data to predict sequences of data in the near future.

3.5.2 Outcomes

The accuracy of this method can be quantified. We have observed that the learning by neural network allowed once functional to reduce the execution time of calculations to find the attitude of the satellite. Such an algorithm must allow ignoring the errors which can appear following a solar eruption and thus a real magnetic field not corresponding at all to the modeled magnetic field. Moreover, the attitude determination can be done instantaneously at each sample of measurement received on the ground.

3.6 Lessons Learned

We have studied and applied different methods to retrieve the satellite attitude. We have noted several aspects that should be verified to ensure better attitude determination. An important geometric consideration is the fact that the frame of reference of each instrument used for deterministic attitude determination should be properly defined in the main frame of reference (example of the inertial measurement unit). The information provided to determine reference vectors such as nadir, magnetic field or Sun LOS should be correctly recovered in a 3-dimensional space. At each time, meaning in each configuration, the satellite should have enough information to locate itself. This can be extrapolated using Kalman filter but it lowers the accuracy as the algorithm has to be based on predictions. For example, the photodiode and IR sensors signals should be available in every 6 directions (+X, -X, +Y, -Y, +Z, -Z).

We have examined the fact that missing values due to a problem of communication or other issues during the recovery of the data cause a loss in accuracy using the Kalman filter. It takes several iterations for the filter to recover its stability. Moreover, a higher sample rate could improve attitude accuracy by making better predictions. Ground-based calibration of the instruments and algorithms is recommended to evaluate the performance and adjust the parameters of the algorithms. Uncertainties of the sensors should be determined precisely to ensure a better first estimation of the hyperparameters (covariance matrix). We manage to quantify the deviation on the flux according to the uncertainty that we have on the attitude of the satellite in the Figure 3.6. This quantification is done for the worst case scenario, that is to say in the case where the configuration is most likely to reach a large uncertainty (depending on the angle to the source). A perspective would be to create an adequate model in order to propagate the uncertainties related to the lack of data directly on the recalculated flux at each time. It is assumed that the noise is Gaussian, but we could study the impact of other types of noise such as pink noise, which is more difficult to measure.

3.7 Conclusions

The UVSQ-SAT mission has been described in this chapter as it represents a way of measuring the EEI components at the TOA. Those measurements aim to validate scientific hypotheses along with the whole process of data processing and communication. The UVSQ-SAT satellite was launched in January 2021 and has been fully functional since. Instrumental equations for each sensor and reconstruction methods have been developed in this chapter. As the satellite is rotating and no precise control is available on-board, attitude determination is crucial to compute the terrestrial flux.

We could benefit from data during on-ground calibration and in-orbit. Although the satellite attitude needs to be known as accurately as possible to compute the terrestrial flux, the methods are not straightforward. Given its size and compactness, novel methods were implemented to process the data from the on-board sensors such as the attitude determination algorithms.

We have tested an MLP to recover the satellite's attitude on-ground to validate the proof of concept. An uncertainty of 7.1° at 1σ was estimated on the attitude determination. This makes it possible to consider the use of this type of method in orbit in order to combine a multitude of sensors with more complex links without making the calculation too complex.

Once the satellite was in orbit we could retrieve data from the sensors. Those sensors were used to estimate the UVSQ-SAT attitude at each measurement. To achieve this objective two methods were selected, and adapted to the satellite's architecture and the data retrieved. One method is a direct and instantaneous method called TRIAD and one is an indirect and iterative method called MEKF based on a Kalman filter. The two were used to reach 3° accuracy in Sunlight and 10° accuracy in eclipse (1σ). The first method was then applied to in-orbit data thanks to the two deterministic methods implemented. The MLP method can be adapted to the UVSQ-SAT architecture and, based on the reference dataset, we have shown that it can be trained. This method could be implemented using more accurate information from the MEKF algorithm. This was not successful in our case because of the discontinuities present in the data. We have targeted some points that could be improved in order to enhance the use of the MEKF method as a training source for the neural network.

The information on the attitude allows us to determine that the satellite rotates on itself with an average speed of one revolution about every 20 min since the beginning of the mission. The attitude of the satellite relative to the Earth and the Sun is utilized to dissociate and compute the different flux observed by the satellite through the instrumental equations presented. This allows us to draw monthly maps of the terrestrial flux. Those results are shown and analyzed in the next chapter. These results are unique and allow many external feedbacks that can be transposed to other space missions for the measurement of the radiation balance. The issues raised by this mission are common and not well documented.

Chapter 4

UVSQ-SAT Observations and First Results

4.1 UVSQ-SAT Outcomes

The UVSQ-SAT mission was presented in Chapter 3 with the objective to measure the EEI components. The attitude determination work presented previously in the same chapter is fundamental for the calculation of the fluxes at the top of the atmosphere. Indeed, it allows the resolution of the instrumental equations. Once determined it is possible to reconstruct flux maps according to the method defined in Chapter 2. Chapter 4 presents the process sequence and the results of the mission and the analysis that can be done compared to other missions.
The UVSQ-SAT data is organized into different layers called levels. Each level is adapted to the amount of processing that has taken place. The different processes aim to transform this data into data that can be understood by the UVSQ-SAT team and scientists who seek to study ECV. The data processing levels are an indicator of how far the archived version of data has been processed since it was created. Typically, they reflect the progressive transformation of raw data to processed data and data products. For this project, the distribution of levels is done as follows.

At Level 0, the data is recovered and the duplicates and communication artifacts from the telemetry are removed. The data is time referenced.
At Level 1A the data are converted to scientific units. To do so, conversions are based on ground and in-orbit calibrations. For this, we base ourselves on the calibration parameters carried out on the ground. Indeed, several calibrations took place on-ground. A Xenon lamp allowed for calibrating the photodiodes during tests at different intensities. The ERS could be calibrated using reference black bodies on the ground for different body temperatures. The instrument's reference temperatures were determined during tests in a thermal vacuum tank. The inertial units and in particular the magnetometer, pre-calibrations were carried out on the ground and consolidated in orbit. We note that on the ground the calibration is very complex given the completely different conditions found in space. Indeed, the instruments of measurement are subjected to conditions of vacuum and temperatures very different from the conditions during the assemblies and tests on the ground.

Level 1B data are reached given the satellite attitude. As explained in Chapter 3, the attitude determination gives information on the relative orientation of each sensor relative to the source. This information is crucial to resolve the instrumental equations presented in Chapter 3. Equations are solved to dissociate and compute the terrestrial flux.

Level 2 data are obtained given the location of the satellite at each time, the flux can be plotted to map the radiation over the whole globe. The equations presented in Chapters 2 and 3 describe how the map reconstruction is performed. Indeed, we consider a certain FOV which is in this case a wide 135° FOV, due to the distribution of sensors on each side of the satellite. The reconstruction is done by considering a Gaussian distribution function. At each time and position of the satellite's measurements, we obtain a spot corresponding to a value and an observed area. By combining all these instants we can then cover almost the entire surface of the globe and thus draw monthly maps of terrestrial flux from UVSQ-SAT data.

4.2 UVSQ-SAT Instantaneous Terrestrial Flux

The UVSQ-SAT has been in-orbit since the 24^{th} of January 2021. The satellite is still fully operational. Almost two years of data retrieved can be presented and compared to reference datasets such as ERA5 reanalysis, CERES, and HIRS measurements.

Figure 4.1 represents the ground track of the satellite on the 8^{th} of February 2022 for 2 orbits. The data recovered from the instruments were processed according to the method described in Section 4.1 to compute the OSR presented in Figure 4.2. Figure 4.2 shows the comparison between UVSQ-SAT and ERA5 data for two orbits measurements of the OSR. The ERA5 data represented in the figure needs explanations as it is based on a model of the UVSQ-SAT instrument. Global hourly ERA5 data are used to model UVSQ-SAT observations. As detailed in Section 2.2, the UVSQ-SAT platform was modeled based on its ground track and instruments' characteristics. The FOV of the instrument is computed to be 135° and the trajectory is given and updated by the NORAD as TLE. Observations can be modeled for each measurement of the UVSQ-SAT instruments based on ERA5 data.

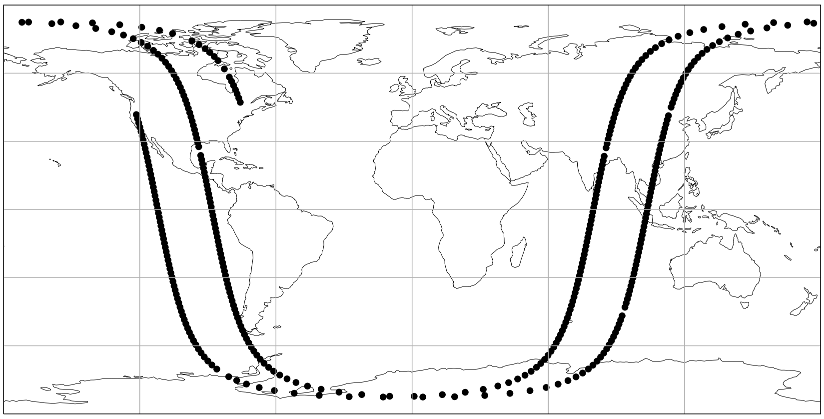

Figure 4.1: Ground track of the UVSQ-SAT satellite at each measurement for two orbits on 8 February 2022.

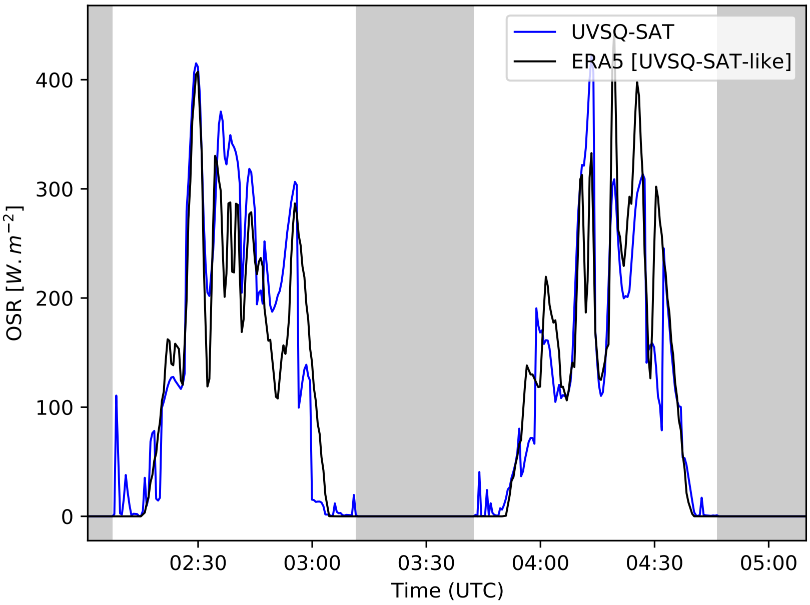

Figure 4.2: OSR component measured along two orbits from the UVSQ-SAT satellite compared to ERA5 transformed data on 8 February 2022 (eclipse phase in gray).

The differences between the time series can be explained because we are dealing here with two data sets from totally different sources. On the one hand, they are the reanalyses, and on the other hand a single satellite. The instruments that served as a basis for the reanalyses have characteristics significantly different from those of the sensors on board the UVSQ-SAT satellite (for example resolution and FOV). In addition, for ERA5 it is reanalysis and therefore extrapolation of information through models, the satellite makes a measurement at a location and at a given time which is not necessarily the case for an instrument used by ERA5 reanalysis. We observe that the flux observed on the sensors is zero in eclipse because it is the flux reflected by the Earth. It is therefore logical that in the case of an eclipse the incident solar flux is absent when the satellite observes the hidden side in the umbra of the Sun. The elevation of the Sun with respect to the satellite for which we consider that the satellite is in the umbra is calculated in Equation 4.1.

$$\text{elevation}_{\text{limit}} = \arcsin\left(\frac{R_{\text{Earth}}}{R_{\text{Earth}} + z_{\text{sat}}}\right) - \frac{\pi}{2} \tag{4.1}$$

where, R_{Earth} is still the Earth radius and z_{sat} the satellite altitude. We consider a perfectly spherical Earth and for the example, at an altitude of 540 km the limit elevation is 22.8°.

After 2 orbits, the satellite will not have covered the entire globe. The tools presented in Section 2.2 give us an estimate of the number of days or hours needed to map the globe. Parameters from the UVSQ-SAT mission are selected and simulations are launched to simulate maps at regular intervals. Examples are shown for OSR maps in Figure 4.3. It is estimated that it takes about 15 days to cover the entire surface of the globe and eliminate as much as possible biases related to the orbit tracks.

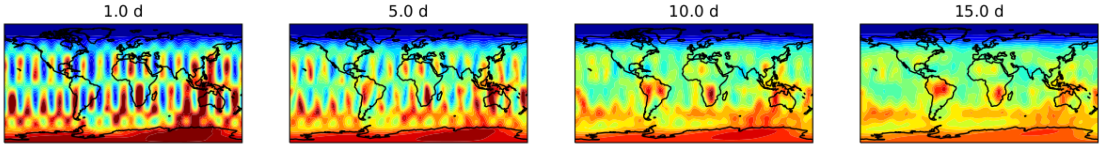

Figure 4.3: Example of an OSR map made after several days of data accumulation.

Actually, given a 135° FOV, for the UVSQ-SAT mission, it will be necessary to wait for 30 days to have global maps of the flows. Indeed, this duration takes into account the loss of data. This is explained by multiple reasons such as the loss of data during an unwanted reset due to a single event upset or during communication with the satellite.

4.2.1 Monthly Averaged Outgoing Terrestrial Radiation

Monthly Accumulation of UVSQ-SAT Data

Radiation flux maps can therefore be plotted by accumulating satellite data over a period of 1 month.

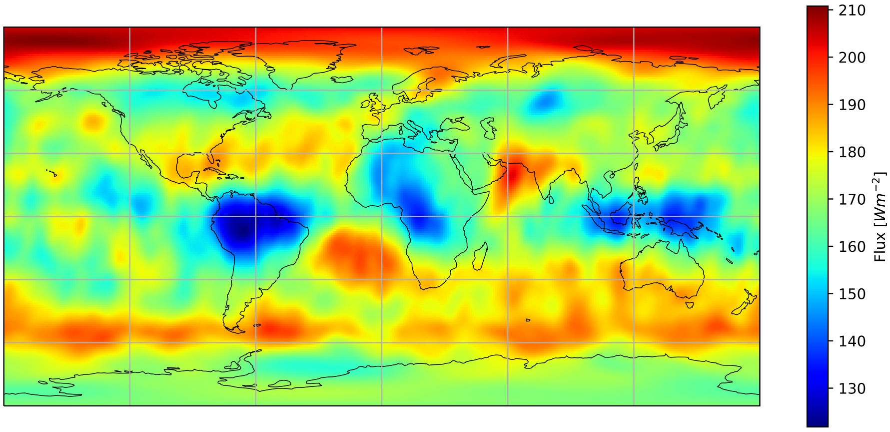

Figure 4.4: OLR in Wm^{-2} from UVSQ-SAT observations averaged for the month of March 2022.

Figure 4.4 shows the OLR observed by the UVSQ-SAT satellite in March 2022. OLR values vary with latitude and are primarily related to near-surface and atmospheric temperatures, clouds, skin surface emissivity, and water vapor profile. Those parameters are related to the intensity of convective activity as well as the variability's latitude and altitude dependence. High latitudes are colder and produce less infrared radiation. The humid tropical regions can be seen clearly. The presence of clouds at high altitudes causes weak radiation to emerge at the TOA at long wavelengths in tropical and equatorial regions. The radiation emitted by the Earth's surface is absorbed by these clouds. As a result, they emit weak outgoing radiation into space. Deep atmospheric convection is directly linked to a low value of OLR. Clouds gain energy by absorbing a small fraction of solar radiation, by absorbing terrestrial radiation, and during condensation of water vapor. They lose energy in turn by emitting as black bodies at their temperature between 10 and 13 µm. An increase in the OLR above the Sahara can be explained by the dust of the Sahara that can lead to a 50 $\mathrm{Wm^{-2}}$ [Haywood et al., 2005, Chedin et al., 2018].

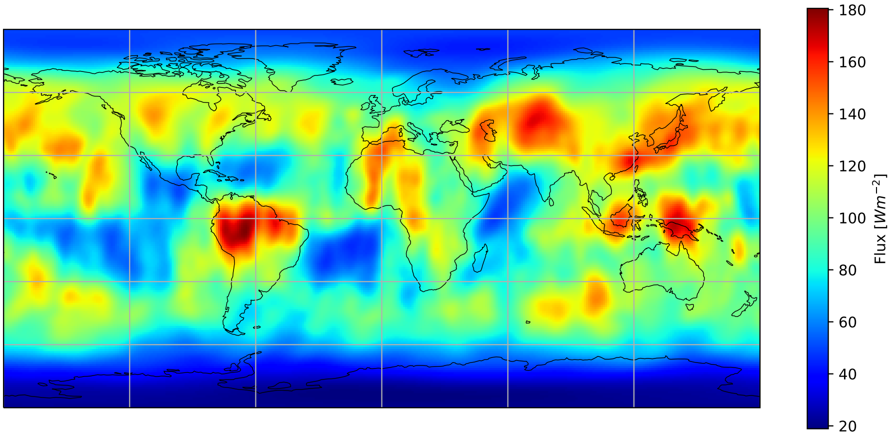

Figure 4.5: OSR in $\mathrm{Wm^{-2}}$ from UVSQ-SAT observations averaged for the month of March 2022.

Figure 4.5 shows the OSR observed by the UVSQ-SAT satellite in March 2022. The OSR is directly linked to the albedo as the albedo is computed as the ratio between the incoming and the outgoing shortwave radiation. It characterizes the relicity. For example, the albedo at the poles can be above 0.7. In the tropics, the albedo is between 0.1 and 0.4. High OSR could be explained by structures with highly reflective clouds. Oceans appear as absorbing radiation and this is explained by the albedo of the ocean close to 0.05 to 0.10 [Seitz, 2011].

4.2.2 Comparison with Instruments and Reanalysis

We can compare the mission data with different datasets that offer advantages for studying different aspects of the Earth's terrestrial radiation. ERA5 provides a high spatio-temporal resolution of atmospheric data at the TOA, but it is affected by biases related to data assimilation. CERES, on the other hand, offers 20 years of real data at the TOA, widely used by the scientific community. HIRS has a lower spatial resolution, and its data are affected by various sources of noise. Finally, OHC covers only the oceans and provides a historical record of several years, enabling the study of long-term trends in OHC. Combining these datasets could provide a more comprehensive comparison. The idea is to compare data at the TOA for monthly average flux. The comparison is shown in Figure 4.6. Monthly averages are displayed in the figure.

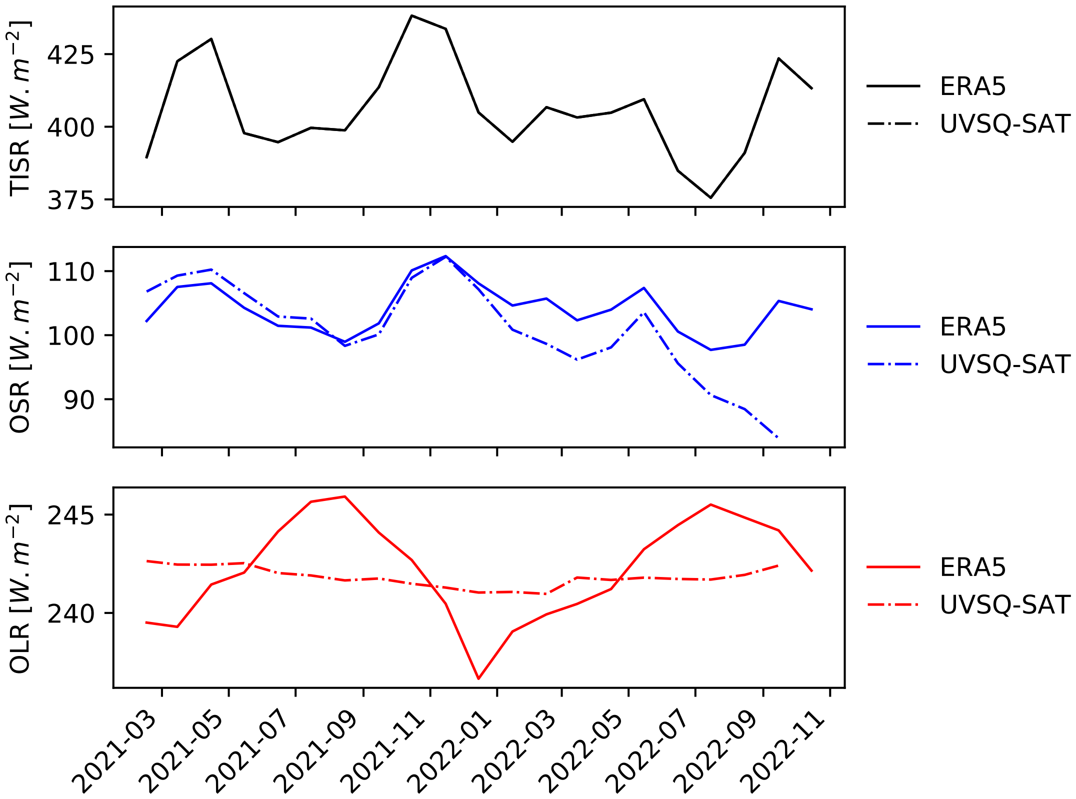

Figure 4.6: Monthly averaged flux.

As we know the OLR evolves at about 240 $\mathrm{Wm^{-2}}$ whereas the OSR is equal to about 100 $\mathrm{Wm^{-2}}$. The OSR is higher as it corresponds to the UVSQ-SAT local time and not global monitoring of the OSR. We observe a cycle in both variables. The gap between the ERA5 OSR and UVSQ-SAT OSR for the last measurements is due to an issue with the magnetometer and therefore high uncertainty in the attitude determination. UVSQ-SAT OLR data has been normalized to focus on

relative variations.
Figure 4.7 shows the evolution of monthly averages over the entire surface of the globe for CERES, ERA5, and HIRS compared to the modeling done with ERA5 data.

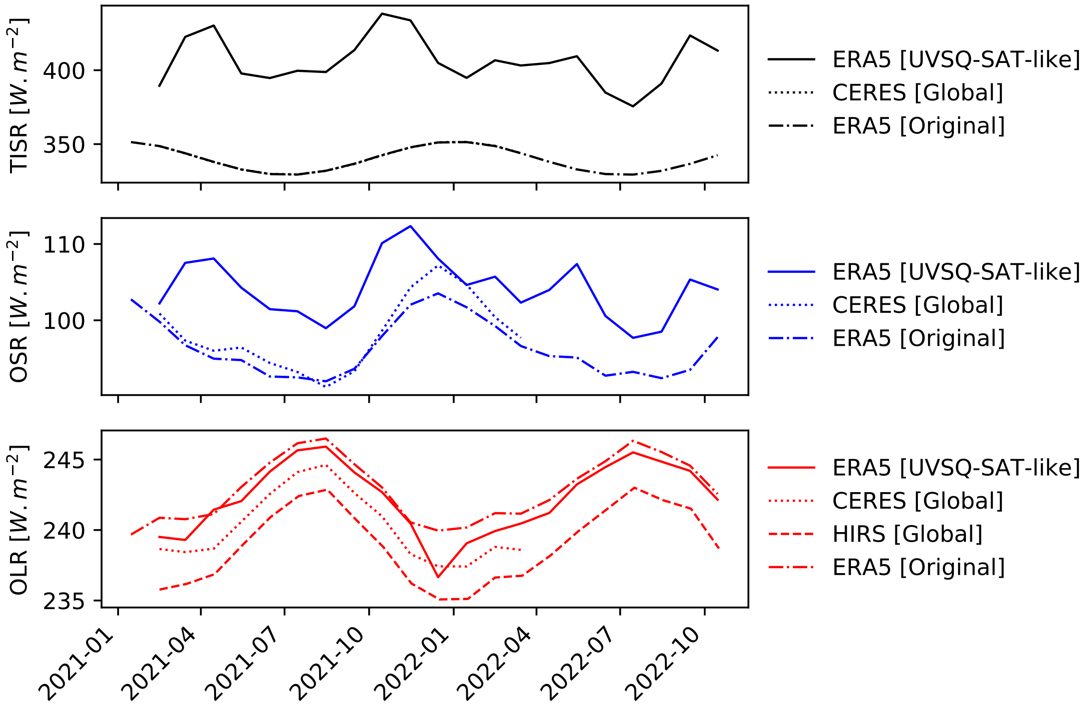

Figure 4.7: Monthly averaged flux.

This allows a direct comparison of what is observed from a satellite compared to the total coverage of the entire surface of the globe. The trends are comparable nevertheless the results are different, indeed measuring from a single satellite does not allow us to have a global view of the phenomena at each moment on the whole globe. As explained in chapter 2, a satellite constellation is necessary to reach the specifications sought for the measurement of the components of the radiation imbalance. This shows the importance of a constellation for the observation of these variables.

Combining ERA5 and UVSQ-SAT Data for Enhanced OLR and OSR Analysis

Combining low-frequency dynamics from ERA5 data with high-frequency data from UVSQ-SAT entails merging the two data sets to improve understanding of OLR and OSR.

The first step in the approach is to compute a daily average of the ERA5 dataset. The ERA5 must be adapted to the UVSQ-SAT observations. The method has been explained in Section 4.2 for which we calculate the variable supposed to be observed by the satellite from the ERA5 data (given its location and time). We then take the average of the OLR and OSR values for each day throughout the time period of interest. This gives a daily average of the low-frequency dynamics of OLR and OSR, which we can then integrate with the high-frequency UVSQ-SAT data.

The next step is to select the high-frequency dynamics from the UVSQ-SAT data. This may be accomplished by subtracting the daily average of the UVSQ-SAT data from the original observations, resulting in a residue that represents the high-frequency changes in OLR and OSR.

The final step is to combine the daily average of the ERA5 data with the high-frequency UVSQ-SAT residue, creating a composite dataset that combines the low-frequency dynamics of ERA5 with the high-frequency variations of UVSQ-SAT. This composite dataset can then be analyzed to study the dynamics of OLR and OSR.

The timeseries are represented in Figures 4.8 and 4.9. Indeed, the long-term trends between ERA5 and the composite are very similar given the construction method used. There is a discrepancy with the CERES data since, as the observations are different, with the use of a single satellite at one local time for UVSQ-SAT versus multiple observations for CERES at different local times. The bias is therefore apparently understandable. Nevertheless, improving the information from UVSQ-SAT measurements takes place in the short term with enhanced high-frequency dynamics.

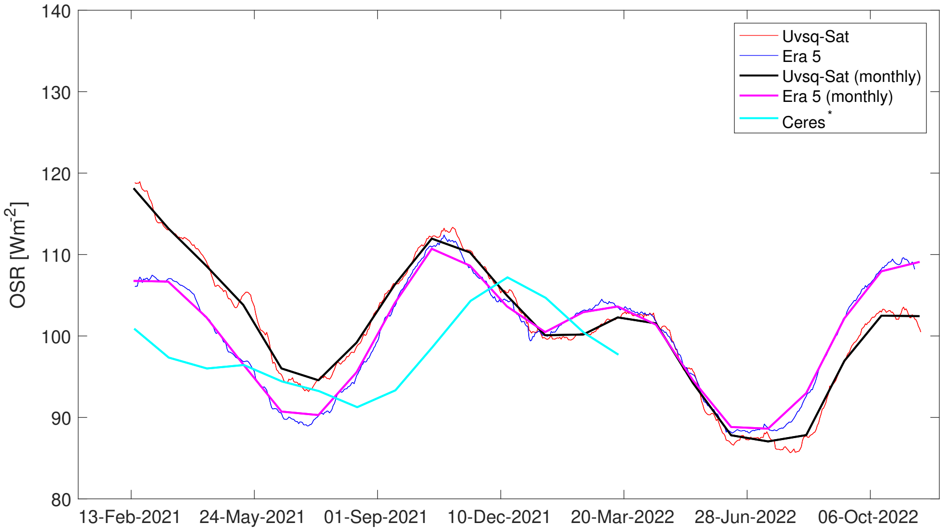

Figure 4.8: OSR timeseries during daylight in Wm^{-2} from UVSQ-SAT/ERA5 composite dataset and monthly averages since the beginning of the UVSQ-SAT mission.

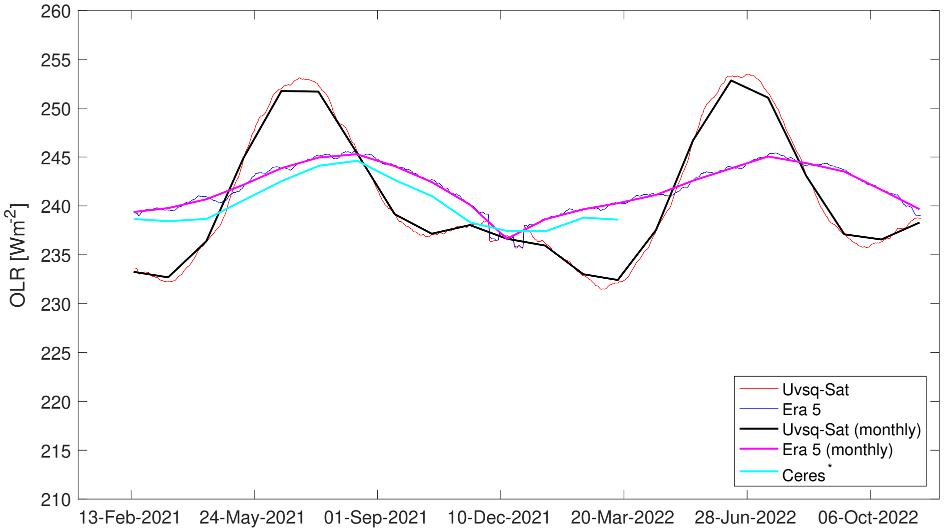

Figure 4.9: OLR timeseries during eclipse in Wm^{-2} from UVSQ-SAT/ERA5 composite dataset and monthly averages since the beginning of the UVSQ-SAT mission.

OSR is plotted in Figure 4.8 and shows the cycles observed due to the inclination of the Earth correlated to seasonal changes. OLR (relative evolution) is represented in Figure 4.9 and shows high dynamics in the evolution of the variable. Highs reach almost 255 $\mathrm{Wm^{-2}}$ and lows 230 $\mathrm{Wm^{-2}}$. One way to justify the difference between the ERA5 dataset and the composite is that the composite gives instantaneous data and the ERA5 dataset comes from reanalysis that is not based on similar information (e.g. sensors and spatio-temporal resolution).
Figure 4.10 shows the accumulation of the OSR in sunlight since the beginning of the mission. We can note different zones where the OSR is the highest. For example, in some parts of Africa, such as the Sahara Desert, the albedo may be relatively high due to the presence of sand. This can explain the high level of OSR.

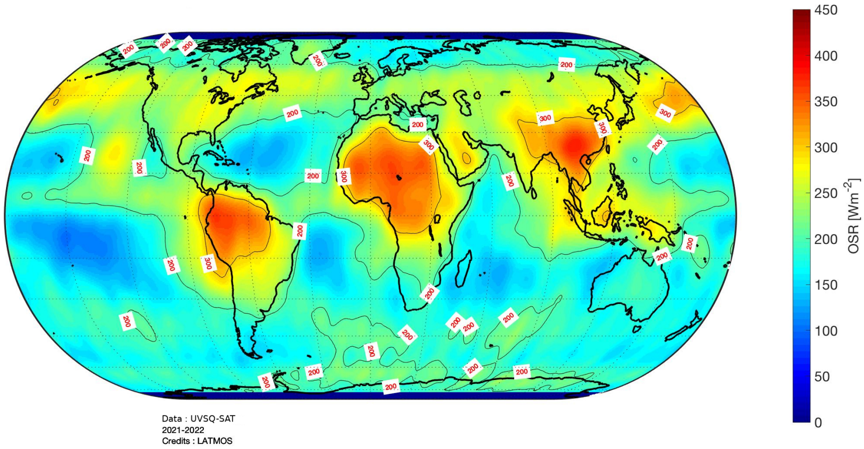

Figure 4.10: OSR at the TOA from the composite dataset in $\mathrm{Wm^{-2}}$ since the beginning of the UVSQ-SAT mission.

There is a zone of high OSR above the American rainforest which we can try to explain as rainforests tend to have high levels of cloud cover, which can reflect shortwave radiation back into space. Low OSR is observed in oceans which is justified by a lower albedo.

4.3 Conclusion

Since February 2021, the UVSQ-SAT satellite observes the Earth and the Sun. A whole process is implemented to transform the data from its raw aspect to the scientific quantities of interest. We have developed the implemented methods and the level of data processing to achieve the determination of the radiative components. Thanks to the attitude determination of the satellite, we could solve the instrumental equations for each sensor on-board the CubeSat to compute the EEI components. Flux can be calculated and presented as a time series. Flux maps could be achieved based on the presented reconstruction methods. It allows us to observe structures and phenomena such as pollution areas, soil transformation, and clouds. These data are then compared to ERA5 reanalyses or data sets from CERES or HIRS instruments. The whole approach could be validated in terms of design and methods.

These findings are highly promising, demonstrating that small satellites may provide quick answers to important scientific issues. It shows the possibility of making essential measurements with nanosatellites. The feedbacks are very important to take into account for the development of future missions. The opportunity to approach the mission as a whole, from design to data collection, is a real plus and allows a direct and efficient improvement of the technologies and methods implemented.

We notice the need for a constellation in order to monitor at higher spatiotemporal resolution. This mission clearly demonstrates that a constellation of Cubesats devoted to the measurement of the EEI is viable in the NewSpace period benefiting from technological advances in miniaturization and reasonable costs to access space. It provides a versatile platform for collecting data on the Earth's climate. CubeSats have the potential to advance our understanding of climate change causes and consequences, as well as to help efforts to solve this global concern.

Conclusions and Perspectives

Nowadays, the challenges have changed compared to the mid 20^{th} century. The priorities are no longer the same. Global warming is a phenomenon that speaks directly to us. The consequences of this phenomenon are numerous and increasingly prevalent, including rising sea levels, more frequent heatwaves, devastating wildfires, and a growing frequency of extreme weather events. Solutions of attenuation and adaptation are thus necessary. This requires the ability to accurately predict and quantify the evolving climate, which in turn depends on the availability of high-quality data with both high spatial and temporal resolution.

This thesis describes an initial approach for the validation of measurement and processing techniques for terrestrial fluxes, with a focus on quantifying key parameters that are crucial for understanding and observing the effects of global warming. This thesis mainly focuses on the attitude determination of a satellite for Earth observation. The aim of this research is to establish a solid foundation for the assessment of the accuracy and reliability of these techniques and to identify any potential areas for improvement. Through this process, the mission aims to contribute to a deeper understanding of the dynamics of global warming. Additionally, the research aims to make recommendations for further missions and studies in order to improve the monitoring and understanding of the ERB.

The first chapter of this thesis provides an overview of the current state of the art in measuring the ERB. The study investigates various techniques for observing both high and low-frequency dynamics of the climate, in order to gain a more comprehensive understanding of how the climate is changing in real-time. The use of satellite measurements is of particular importance in this research, as they provide the ability to quickly acquire and process large amounts of data on climate evolution, providing valuable insights into the dynamics of climate change.

Additionally, the analysis of multiple data sources and measurements can further increase the robustness and validity of the results. By combining these techniques, we are able to create a comprehensive and detailed picture of the current state of the climate and to identify key areas that require further study. Indeed, a constellation of satellites is necessary to reach high spatio-temporal resolution with 10-100 km at 3 h and monitor high-frequency dynamics at a local scale. We have highlighted measurement specifications to monitor the different long and short-term phenomena. The instruments should determine the TSI with an absolute accuracy of less than $0.54\,\mathrm{Wm}^{-2}$ and a per decade stability of $0.14\,\mathrm{Wm}^{-2}$. The OSR and OLR must be known with an absolute accuracy of $1\,\mathrm{Wm}^{-2}$ and a stability of $0.1\,\mathrm{Wm}^{-2}$ per decade. Therefore, the EEI should be measured with $1\,\mathrm{Wm}^{-2}$ absolute accuracy and $0.1\,\mathrm{Wm}^{-2}$ per decade.

The second chapter detailed the necessity to develop a constellation of satellites to reach the expected scientific requirements. The configuration of the satellite constellation and instruments is important as it constrains the coverage, the revisit time, and the resolution. We have seen that a narrow FOV directly entails a better spatial resolution but requires more satellites to reach the same temporal resolution as with a larger FOV. A constellation of 512 satellites with 10° narrow FOV is necessary to fit the specifications reaching 10 km spatial resolution with 1.06° sensors, and 3 h revisit time. The constellation covers the short-term phenomena at high spatio-temporal dynamics. The choice of Sun-synchronous orbits for the constellation would entail equi-spaced measurements to monitor every local time. Such constellations would provide frequent revisits to monitor the Earth, enabling high temporal resolution and more accurate modeling of dynamic processes. We can better identify the drivers of climate variability, such as greenhouse gas emissions, aerosols, and land modifications. It would improve climate models by providing more accurate and precise data on essential climate variables. This can lead to more accurate predictions of future climate change using deterministic methods or neural networks. A constellation of satellites could be particularly beneficial for using neural networks to predict future climate conditions because it would provide a large amount of high spatio-temporal resolution data. Given the complexity and dynamic of the Earth's radiation budget, lots of data are necessary to train neural networks to provide reliable predictions. By offering additional information and complete coverage of the Earth's radiation budget, a constellation of satellites may be able to improve our knowledge of these feedback mechanisms. The UVSQ-SAT satellite was presented and detailed in the third chapter. It represents a pathfinder to test the ability to measure with high accuracy the EEI using a future constellation of small satellites (Gaïa Y78). The mission was presented in a book in order to discuss the different issues [Francesco et al., 2023]. The UVSQ-SAT aims to measure terrestrial radiation on board a small satellite. We have detailed the instrumental equations and how attitude determination plays a significant role in terrestrial flux computation. We have developed a method that was tested on-ground and validated using neural network. Two methods were implemented in orbit, one method is a direct and instantaneous method called TRIAD and one is an indirect and iterative method called MEKF based on a Kalman filter. The two were used to reach 3° accuracy in Sunlight and 10° accuracy in eclipse (1σ). We have proved that the neural network could be adapted to the TRIAD method to validate the feasibility of the MLP in-orbit making use of the numerous sensors on board. The attitude determination was a challenge and we have validated methods with unique in-orbit data. This is a significant accomplishment, as accurate attitude determination is essential for solving the instrumental equation and accurately measuring terrestrial flux. We manage to quantify the deviation in the flux according to the uncertainty that we have on the attitude of the satellite. In the future, an adequate model could be developed in order to propagate the uncertainties related to the lack of data directly on the recalculated flux at each time. A global model would provide comprehensive information on the total uncertainty associated with the measurement by this satellite. It would consider the error balance of the sampling, the error balance of the instruments, errors in averaging on the planet as a function of the angle, and the measurement of radiance against flux. These studies have highlighted the need for an adequate model that combines the tool developed for observing climate variables through a constellation with thermal and thermo-mechanical models. Such integration would facilitate the creation of a "digital twin" of the satellite, serving to validate the signals perceived by the satellite and improve the restitution of the flows along with the associated uncertainty.

The data processing methods and outcomes from the UVSQ-SAT mission are presented in the fourth chapter. It successfully demonstrated the feasibility of measuring terrestrial radiation at the TOA, the low orbit being an asset. The mission's measurements have provided valuable data and the UVSQ-SAT pathfinder mission is presented as a success. We have reached scientific results and validated the whole process from raw signals in orbit to scientific results. The UVSQ-SAT mission allows for data accessibility almost in real-time compared to longer delay for other datasets such as EBAF or ERA5. The success of the UVSQ-SAT pathfinder mission paves the way for future missions that will use these innovative observation techniques to gather even more data on climate change. These new observation methods will allow feeding models with multitudes of data at high spatial and temporal resolution in order to predict climate evolution.

The benefits of such a future constellation of CubeSats are discussed in this thesis, and they allow for better revisit time and spatial resolution, particularly for monitoring the EEI. A constellation of satellites is required to estimate the global daily mean top of atmospheric outgoing longwave and shortwave radiation. The choice for CubeSats is also adapted. Indeed, CubeSats are far less expensive to manufacture and launch than regular satellites because they are smaller and less expensive. They can be built and launched more quickly, allowing for faster deployment of new satellite systems. CubeSats are also modular and adapted for a wide range of purposes. This enables greater flexibility in the design and deployment of satellite systems for specialized objectives. Finally, CubeSats are built to last, with several types capable of withstanding severe space settings for lengthy periods of time. The methods developed in this study allow us to revisit and improve upon technologies that are important to us. These approaches can be applied to miniaturization, optimization, and artificial intelligence techniques to achieve specific goals. By adopting these methods, we can increase efficiency and effectiveness in various applications. These new technologies are developed being a great asset as it is critical to note that climate change is a long-term process. To understand and anticipate the effects of climate change on the Earth's weather and climate, it is important to continuously monitor and gather data on a wide range of variables. There is a need for ongoing monitoring and data collection on a regular basis. The industrialization of radiation balance measurement appears to be fundamental. Although temperature and CO2 are good indicators for quantifying global warming, the ERB makes it possible to better quantify the evolution of what will happen in the long term.

Moreover, the UVSQ-SAT mission has helped validate and prepare other future missions such as the INSPIRE-SAT 7 mission. As described in Meftah et al. [2022], the first objective of INSPIRE-SAT 7 is to improve the UVSQ-SAT technologies that are used to measure the ERB components and compute the EEI, which is the difference between global mean solar radiation absorbed by the Earth system and thermal infrared radiation emitted to space by it. EEI results primarily from the increase in greenhouse gas levels and drives global change. It is a crucial quantity for testing climate models and for the prediction of the future course of global warming. INSPIRE-SAT 7 will measure the ISR and the OSR and OLR using 12 miniaturized Earth's radiative sensors (thermopiles with carbon nanotubes and optical solar reflectors).

The second objective is to validate new technologies that help to characterize the state of the ionosphere for space weather studies and test an innovative approach based on the combined use of a ground-based HF transmitter and of an HF receiver onboard the INSPIRE-SAT 7 CubeSat. The attenuation of HF waves by the ionosphere crossing will be measured during the entire CubeSat trajectory when it is visible from the ground transmitter. This kind of technology is important for monitoring the state of the ionosphere and, in particular, for wave propagation predictions. Indeed, multiple phenomena can strongly disturb the ionosphere and wave propagation, even posing a threat to orbiting satellites in the case of powerful solar storms.

The third objective of the INSPIRE-SAT 7 mission is to validate new technologies for other purposes. For instance, 14 photodiodes will be used to measure the TSI but also solar radiation in the UV range, whose variability directly impacts the ozone layer and the temperatures in the middle atmosphere.

The last objective of the INSPIRE-SAT 7 mission is educational. It is to provide hands-on experience and training to students with a NewSpace approach (science objectives, mission analysis, design, construction, CubeSat integration and test, mission operations, management, cost and risks, and mission and product assurance). This training of the new generation in the field of the NewSpace is important for a variety of future space missions for the Earth constellation and for

Astronomy and Astrophysics.

Improvement measures are considered in order to take into account the feedback from the UVSQ-SAT mission. We have shown limitations of the mission and margin of improvement that are essential for future developments. For example, one of the important issues is data recovery, and the lack of data impacting attitude determination and flux determination is important to find solutions. One of the reasons is the inability to perform measurements during a download due to the over-consumption of the platform. The use of an antenna at another location would combine the need for a single location for the downloads with the need to decongest the area for more measurements. Tests are conducted on this satellite to validate the neural network and ground attitude control methods. Analyses will then be carried out in order to quantify the possibilities that there can be with this platform and for the next missions. Moreover, the neural network is validated with the INSPIRE-SAT 7 on-ground in-order to improve the satellite attitude.

CubeSats could be used in the future to study planetary atmospheres (radiation balance, atmospheric constituents). UVSQ-SAT opens up new possibilities since this space mission has demonstrated that it was possible to do science with small satellite platforms. In addition, it allows considering the use of small satellite constellations to address major scientific issues in which certain questions require high spatial resolution and revisit time.

The research presented in the thesis can be used as foundations for further studies on measuring and processing techniques for terrestrial fluxes from small satellites and a constellation. Lessons learned and recommendations presented in the thesis can be beneficial to develop new and improved methods for observing and understanding the dynamics of global warming (from hardware, integration to attitude determination and reconstruction). Technology advancements continue to progress, and as a result, there is a growing potential for greater availability of high-quality data. These advancements can offer data with enhanced spatial and temporal resolution, thereby providing valuable insights. Acquiring information on the EEI is crucial for enhancing models and constraining measurements at the TOA. This information would contribute to the refinement of quantification methods and a better understanding of the impacts caused by greenhouse gases and aerosols. This thesis has been completed under exceptional circumstances, as we were able to work with authentic remote sensing data from a mission developed in the lab. This allowed an unparalleled level of insight into the entire process of developing and implementing methods and technologies for remote sensing.

Résumé français

Chapitre 1 : L'Importance de la Mesure du Bilan Énergétique Terrestre

Depuis 1880, la température annuelle globale a augmenté à un rythme moyen de 0,08°C par décennie, et de plus du double de ce rythme (+0,18°C par décennie) depuis 1981 tel qu'il apparaît dans le rapport [for Environmental Information, 2021]. Selon le rapport 2022 du Groupe d'experts intergouvernemental sur l'évolution du climat (GIEC) [Rama et al., 2022], le globe est en passe de dépasser la barrière des 1,5°C au cours des deux prochaines décennies, et seules les réductions les plus extrêmes des émissions de carbone permettront d'éviter une catastrophe environnementale. Il est important de savoir que la Terre n'a pas connu d'augmentation de température de plus de 2,5°C sur une période aussi courte depuis plus de 3 millions d'années. Ce phénomène est donc totalement nouveau et de grande ampleur. Le GIEC a créé cinq scénarios, appelés "trajectoires socio-économiques de référence", dans lesquels il souligne les répercussions d'une action drastique menée maintenant par rapport à ce qui se passerait si aucune mesure n'était prise. Le scénario le plus pessimiste, à forte teneur en carbone, entraînerait une augmentation de la température mondiale de plus de 4°C d'ici la fin du siècle. Ce changement serait dangereux en raison de l'augmentation des sécheresses, des incendies de forêt, des tempêtes tropicales et d'autres phénomènes météorologiques extrêmes. Le changement climatique apparaît comme une menace pour l'humanité. Pour comprendre l'évolution des températures de la Terre et la variabilité du climat, il est nécessaire de calculer un indicateur pour quantifier cette évolution. Cet indicateur devrait être la meilleure statistique unique dont nous disposons pour évaluer l'effet des actions d'atténuation du changement climatique [von Schuckmann et al., 2020].

La quantification de ce réchauffement à travers de nombreuses variables semble indispensable pour comprendre les phénomènes et agir à l'échelle locale et mondiale. Une variable qui permet de rendre compte du phénomène est le bilan radiatif terrestre. Celui-ci quantifie les échanges énergétiques au sommet de l'atmosphère et est directement lié à la température sur Terre. Cette variable est évidemment nécessaire au comité scientifique pour fournir aux décideurs politiques des informations sur le changement climatique, ses implications, ses risques, et pour proposer des options d'adaptation et d'atténuation comme avec le GIEC. Une façon de la mesurer est l'observation par satellite.

Il est donc intéressant d'étudier le déséquilibre énergétique de la Terre (EEI) et de quantifier chacun des flux d'entrée/sortie du système terrestre que nous devons connaître pour le calculer. Une résolution spatio-temporelle plus élevée permet par exemple d'explorer les cycles diurnes qui peuvent être déterminants pour l'observation des nuages et des aérosols formés par photochimie à une échelle locale de quelques kilomètres. Une meilleure résolution implique un meilleur suivi de variables telles que l'albédo ou les flux géomorphologiques. Cela permettrait d'améliorer les modèles atmosphériques, en mesurant les flux radiatifs pour de nombreux cas différents, en termes de surfaces et de conditions permettant de les observer et de les relier à l'impact qu'ils ont sur les flux au sommet de l'atmosphère.

Plusieurs missions ont été développées pour mesurer les composantes du déséquilibre énergétique de la Terre.

Dans le cas du bilan radiatif de la Terre, il comporte trois composantes principales : le rayonnement solaire entrant, le rayonnement solaire réfléchi et le rayonnement terrestre sortant.

L'irradiance solaire totale (TSI) est une mesure de la puissance solaire par unité de surface incidente au sommet de l'atmosphère de la Terre sur toutes les longueurs d'onde. Elle est calculée en prenant des mesures perpendiculaires aux rayons du Soleil. La constante solaire est une mesure standard de la TSI moyenne à une unité astronomique de distance.

Le rayonnement solaire réfléchi est le rayonnement à ondes courtes du Soleil qui est réfléchi sur l'atmosphère et sur la surface de la Terre. Le pourcentage d'énergie solaire réfléchie vers l'espace est l'albédo du système Terre-atmosphère. Sa valeur varie de 0 à 1. Plus l'albédo d'une surface est élevé, plus elle est réfléchissante. Les nuages, les surfaces de neige et de glace, et les aérosols sont les principaux contributeurs de l'albédo de la Terre.

Le rayonnement sortant infrarouge, également appelé rayonnement thermique, est émis par la Terre et son atmosphère. La loi de Stefan ou de Stefan-Boltzmann (du nom des physiciens Jožef Stefan et Ludwig Boltzmann) définit la relation entre le rayonnement thermique et la température d'un objet considéré comme un corps noir. Elle établit que l'émittance énergétique d'un corps en watts par mètre carré (puissance totale rayonnée par unité de surface dans le demi-espace libre d'un corps noir) est liée à sa température T exprimée en Kelvin. Le spectre du rayonnement solaire représenté est proche de celui d'un corps noir dont la température est d'environ 5 800 K. La température du corps noir de la Terre est de 250°K.

Dines a fourni la première estimation du bilan énergétique de ce type en 1917. Kiehl and Trenberth a fourni le premier bilan modérément complet des échanges énergétiques et de l'atmosphère de la Terre en 1997. Stephens et al. a amélioré le chiffre du bilan énergétique de la Terre en 2012. Entre 2000 et 2010, le bilan radiatif a été calculé au sommet de l'atmosphère comme étant de $+0{,}60 \pm 0{,}40$ Wm^{-2} [Stephens et al., 2012]. Selon Von Schuckmann et al., l'EEI devrait désormais être de $+0{,}87 \pm 0{,}12$ Wm^{-2} pour la période 2010-2018, contre $+0{,}47 \pm 0{,}10$ Wm^{-2} pour la période 1971-2018.

L'accumulation d'énergie dans les océans apparaissant comme un bon proxy de l'accumulation dans le système Terre atmosphère océan, peut être mesurée de différentes manières. La première approche consiste à calculer l'accumulation d'énergie à partir des profils de température et de salinité in-situ grâce aux flotteurs Argo. Une autre approche serait de combiner avec un modèle l'approche précédente avec des mesures du niveau de la mer issues de l'observation spatiale [Stammer et al., 2016]. De plus, les mesures des satellites de radiation peuvent être utiles pour calculer le flux net de surface [L'Ecuyer et al., 2015]. Enfin, [Marti et al., 2022] a décrit une nouvelle approche de géodésie spatiale pour estimer les changements de l'accumulation d'énergie à partir des changements de niveau stérique, en se basant sur les mesures altimétriques et gravimétriques des satellites. Elle est basée sur le principe physique pour lequel la variation totale du niveau de la mer résulte d'une augmentation de la masse de l'océan et de la variation stérique de la mer. La variation stérique du niveau de la mer est égale à la somme de l'expansion thermique de l'océan et de la variation halostérique de l'océan. Le changement halostérique se réfère à un changement de la salinité tandis que l'expansion thermique est due aux variations de température de l'océan. Par conséquent, si l'on considère que l'effet halostérique est ici négligeable [Gregory and Lowe, 2000], la variation thermostérique du niveau de la mer est égale à la différence entre la variation moyenne globale du niveau de la mer et la masse moyenne globale de l'océan. La proportion d'énergie entrant dans l'océan est d'environ 0,9. Le bilan radiatif terrestre peut alors être calculé en divisant l'absorption de chaleur globale de l'océan, qui est la dérivée temporelle du contenu thermique global de l'océan, par la proportion d'énergie entrant dans l'océan [von Schuckmann et al., 2020]. La résolution spatio-temporelle des observations des composantes du bilan énergétique de la Terre semble être la clé. Elle est limitative et ne permettra une bonne quantification du bilan radiatif que si elle est appropriée au phénomène climatique que l'on observe. Ainsi, de nouvelles méthodes doivent être mises en place et combinées afin d'atteindre les objectifs en question. Pour ce faire, différentes solutions sont proposées à bord de différentes plateformes.

Chapitre 2 : Vers une constellation de satellites pour le bilan radiatif Terrestre

L'observation Terrestre à l'aide d'une multitude de satellites semble être la seule manière de répondre aux spécifications scientifiques qui permettent de comprendre les phénomènes climatiques qui nous entourent. Le temps de revisite jouant un rôle important dans l'observation, l'instrument doit également permettre d'atteindre une résolution spatiale adaptée. Des méthodes de balayage sont réalisées sur de gros satellites afin de réduire la résolution spatiale. Ces techniques d'observation sont utilisables dans divers domaines notamment dans l'agriculture en améliorant la visualisation et caractérisation des sols, structures au sol. Afin de déterminer la constellation optimale qui répondrait à nos besoins dans le cas du bilan radiatif, l'une des premières étapes est de disposer d'un outil de simulation permettant de simuler la reconstruction des cartes à partir d'observations de plusieurs satellites. Cet outil permet de quantifier les performances des différentes architectures afin de choisir celle qui répondra aux spécifications. Une multitude de simulations sont donc lancées afin de comprendre les paramètres qui ont un rôle décisif dans cette détermination. L'un des premiers paramètres est le nombre de satellites qui constituent la constellation. Plus celui-ci augmente, meilleurs seront les résultats. Néanmoins, un second paramètre qui devient alors limitant est le champ de vue du satellite. En effet, plus celui-ci sera étroit meilleurs seront les résultats néanmoins la durée pour couvrir toute la surface du globe sera importante. À partir d'un certain point on a beau augmenter le nombre satellites, les résultats ne sont pas meilleurs, le champ de vue doit être diminué. Certains critères importants à respecter sont les résolutions spatio-temporelles afin d'observer les phénomènes avec une résolution assez fine, tels que les nuages et les cycles diurnes. Ainsi pour une résolution de 10 km un champ de vue de 1.06° est nécessaire. Pour obtenir une résolution temporelle de 3 h on suppose un balayage de largeur de 10° de champ de vue. On développe un outil qui nous permet de déterminer le temps de revisite par localisation sur toute la surface du globe. On choisit alors une multitude de points equi-répartis pour réaliser notre étude et obtenir un temps de revisite de moins de 3 h. La constellation optimale est définie comme une configuration à 512 satellites afin d'atteindre un temps de revisite médian d'environ 1 h. Les satellites étant considérés en orbites héliosynchrones on balaie ainsi toutes les heures locales ce qui permet d'étudier les phénomènes diurnes et liés à des heures locales spécifiques. La résolution spatiale et temporelle des mesures serait grandement améliorée par le déploiement d'une constellation telle que celle décrite. Cela serait un grand pas en avant pour la mesure du bilan radiatif et potentiellement d'autres variables intrinsèquement liées à l'évolution du climat. Cette constellation permettrait d'observer et de quantifier de nombreux forçages radiatifs à court terme tels que les impacts radiatifs des aérosols et des nuages qui sont très variables dans l'espace et dans le temps. La question des débris spatiaux étant au centre des enjeux actuels, la constellation de satellites doit être optimisée au maximum. Le nombre de satellites doit être justifié et idéal afin de ne pas congestionner l'espace.

Chapitre 3 : La mission UVSQ-SAT et la détermination d'attitude

Le satellite UVSQ-SAT est un Cubesat 1 U développé par le LATMOS et lancé le 24 janvier 2020 en orbite héliosynchrone. L'objectif de ce satellite est de valider des hypothèses pour la mesure du bilan radiatif. Nombreux capteurs sont disposés sur toutes les surfaces du satellite. L'objectif étant de mesurer les flux terrestres sortant pour retracer des cartes. UVSQ-SAT est composé de plusieurs sous-systèmes, notamment la structure mécanique, le sous-système d'alimentation, le sous-système de contrôle thermique, la carte magnéto, le sous-système de commande et de traitement des données, le sous-système de communication et le sous-système de charge utile (ERS, UVS, TSIS et un accéléromètre/gyroscope/magnétomètre à 3 axes (capteur TW)). UVSQ-SAT est un CubeSat qui adhère à la norme CubeSat et est compatible avec un déployeur de CubeSat ISIS Quadpack. Le gyromètre mesure les vitesses angulaires sur trois axes dans le cadre du capteur par rapport au cadre de référence inertiel. Le magnétomètre mesure le champ magnétique selon ses trois axes dans le cadre de référence de l'instrument. Six photodiodes dans le domaine visible. Elles mesurent le rayonnement solaire et le rayonnement OSR dans la gamme de longueurs d'onde 400–1100 nm. Six capteurs de rayonnement terrestre (ERS) avec un réflecteur solaire optique. Ils visent à mesurer le rayonnement entre 0,2 et 3 µm. Six capteurs ERS avec des nanotubes de carbone (CNT). Six capteurs ont pour objectif de mesurer le rayonnement total entre 0,2 et 100 µm. Ce satellite très compact ne possède néanmoins pas de système de pointage actif. Afin de résoudre les équations instrumentales correspondant à chacun des capteurs du satellite, il est essentiel de connaître le plus précisément possible l'orientation du satellite à chaque instant. On détermine ainsi les flux observés. Il est crucial d'utiliser les données à bord du satellite afin de retrouver cette orientation. Une première méthode présentée a été développer au sol. Les tests réalisés ont pour objectif de valider le concept de la méthode. Celle-ci repose sur l'utilisation d'un apprentissage pour retrouver la position du Soleil par rapport au satellite en utilisant uniquement les données à bord du satellite. La méthode fut validée au sol. Une fois en orbite, les données sont différentes et n'ayant pas la possibilité d'entraîner un réseau de neurones en se basant sur une vérité terrain comme c'est le cas au sol, il faut développer des méthodes dites déterministes. Ces méthodes sont TRIAD et MEKF, la méthode TRIAD est instantanée et directe néanmoins elle ne prend pas en compte les erreurs liées au bruit de mesure. La méthode MEKF utilise un filtre de Kalman linéarisé afin de corriger le bruit sur les données en se basant sur l'utilisation d'un gyromètre. Les précisions des deux méthodes ont été estimées avec une méthode de Monte Carlo. On estime à 3° à 1σ face au Soleil et 10° en éclipse. De plus nous avons démontré que la méthode MLP peut être appliquée à l'architecture UVSQ-SAT en utilisant un jeu de données issu de la méthode TRIAD. Cette méthode pourrait être mise en œuvre en utilisant des informations plus précises avec la méthode MEKF. Cela n'a pas été probant dans notre cas en raison des discontinuités de données. Nous avons identifié certains points à améliorer afin de mettre en évidence l'utilisation de la méthode MEKF comme source d'entraînement pour les réseaux de neurones.

Chapitre 4 : Les Observations et Premiers Résultats du Satellite UVSQ-SAT

Les données UVSQ-SAT sont traitées de la manière suivante. Au niveau 0, les données sont récupérées et les doublons et artefacts de communication de la télémétrie sont supprimés. Les données sont ensuite référencées dans le temps. Au niveau 1A, les données sont converties en unités scientifiques, pour cela on se réfère aux étalonnages réalisés au sol et en orbite. Une fois l'attitude du satellite connue, les flux terrestres peuvent être estimés pour obtenir les données de niveau 1B. Les données de niveau 2 sont obtenues étant donnée la position du satellite à chaque instant, le flux peut être tracé pour cartographier le rayonnement sur l'ensemble du globe. On peut ainsi observer des cartes mensuelles établies uniquement à partir des données UVSQ-SAT. Les résultats de la mission UVSQ-SAT sont cartographiés et permettent de quantifier les flux radiatifs sortants au sommet de l'atmosphère.
Il est possible d'utiliser les données telles quelles ou bien de créer un composite composé de l'évolution basse fréquence ERA5 et de l'évolution haute fréquence UVSQ-SAT. Des comparaisons sont alors réalisées avec des données ERA5, EBAF ou bien HIRS. La viabilité de la mission est prouvée, on relève néanmoins l'intérêt de la constellation en terme de résolution spatio-temporelle et couverture globale de la Terre.

Conclusions et Perspectives

Les priorités ne sont plus les mêmes aujourd'hui. Les conséquences du réchauffement climatique sont diverses et actuelles. Le réchauffement climatique représente un des enjeux majeurs du XXI^{e} siècle. Des solutions d'atténuation et d'adaptation sont donc nécessaires. Pour ce faire, il est important de pouvoir prédire et quantifier l'évolution du climat, et il est donc nécessaire d'alimenter les modèles avec une multitude de données. Une haute résolution spatiale et temporelle est nécessaire pour suivre les événements terrestres. Cette thèse décrit une première approche pour valider les principes de mesure et d'analyse des flux terrestres et la quantification des paramètres essentiels à l'observation et à la compréhension du réchauffement climatique. Dans cette thèse nous avons vu l'importance de la mesure du bilan radiatif au sommet de l'atmosphère. Nous avons étudié l'intérêt de la constellation de satellites pour réaliser cette mesure et proposé une configuration possible répondant aux spécifications. Dans le cas de la mission UVSQ-SAT, une plateforme instrumentale a été proposée et de nombreuses méthodes ont été décrites et validées pour la restitution de l'attitude et des flux que l'on cherche à mesurer. Ces résultats ont pu être décrits et analysés. Plusieurs retours d'expériences ont pu être relevés préparant ainsi la prochaine mission INSPIRE-SAT 7. Le premier objectif d'INSPIRE-SAT 7 est d'améliorer les technologies issues d'UVSQ-SAT qui sont utilisées pour mesurer les composantes de l'ERB et dériver le déséquilibre énergétique de la Terre. INSPIRE-SAT 7 mesurera le rayonnement solaire entrant (irradiance solaire totale) et le rayonnement terrestre sortant à l'aide de 12 capteurs radiatifs terrestres miniaturisés (thermopiles avec nanotubes de carbone et réflecteurs solaires optiques). Le deuxième objectif est de valider les nouvelles technologies qui aident à caractériser l'état de l'ionosphère pour les études de météorologie spatiale et de tester une approche innovante basée sur l'utilisation combinée d'un émetteur haute fréquence (HF) au sol et d'un récepteur HF à bord du CubeSat INSPIRE-SAT 7. Ce type de technologie est important pour la surveillance de l'état de l'ionosphère. Le troisième objectif de la mission est de valider de nouvelles technologies à d'autres fins. Par exemple, 14 photodiodes seront utilisées pour mesurer l'irradiance solaire totale mais aussi le rayonnement solaire dans le domaine de l'ultraviolet, dont la variabilité a un impact direct sur la couche d'ozone et les températures de la moyenne atmosphère. INSPIRE-SAT 7 exploitera également le premier module Li-Fi (ou Light Fidelity) en orbite à bord d'un CubeSat. Enfin, une charge utile de radio amateur sera testée à bord d'INSPIRE-SAT 7. Le dernier objectif de la mission INSPIRE-SAT 7 est éducatif. Il s'agit de fournir une expérience pratique et une formation aux étudiants. Ces nouvelles technologies permettent un pas en avant puisque les CubeSats permettent des mesures à coût moins important et des missions plus courtes avec une grand flexibilité et une marge d'action. La mission UVSQ-SAT a montré qu'il était possible de réaliser des mesures cruciales pour les enjeux actuels au sommet de l'atmosphère.

Publications, Conferences and Trainings

Publications

Finance, A.; Meftah, M.; Dufour, C.; Boutéraon, T.; Bekki, S.; Hauchecorne, A.; Keckhut, P.; Sarkissian, A.; Damé, L.; Mangin, A. A New Method Based on a Multilayer Perceptron Network to Determine In-Orbit Satellite Attitude for Spacecrafts without Active ADCS Like UVSQ-SAT. Remote Sens. 2021, 13, 1185. doi:10.3390/rs13061185

Finance, A.; Dufour, C.; Boutéraon, T.; Sarkissian, A.; Mangin, A.; Keckhut, P.; Meftah, M. In-Orbit Attitude Determination of the UVSQ-SAT CubeSat Using TRIAD and MEKF Methods. Sensors 2021, 21, 7361. https://doi.org/10.3390/s21217361

Meftah, M.; Boutéraon, T.; 2 3 Dufour, C.; Hauchecorne, A.; Keckhut, P.; Finance, A.; Bekki, S.; Abbaki, S.; Bertran, E.; Damé, L.; et al. The UVSQ-SAT/INSPIRESat-5 CubeSat Mission: First In-Orbit Measurements of the Earth's Outgoing Radiation. Remote Sens. 2021, 13, 1449. https://doi.org/ 10.3390/rs13081449

Meftah, M.; Boutéraon, T.; Dufour, C.; Hauchecorne, A.; Keckhut, P.; Finance, A.; Bekki, S.; Abbaki, S.; Bertran, E.; Damé, L.; Engler, J.-L.; Galopeau, P.; Gilbert, P.; Lapauw, L.; Sarkissian, A.; Vieau, A.-J.; Lacroix, P.; Caignard, N.; Arrateig, X.; Hembise Fanton d'Andon, O.; Mangin, A.; Carta, J.-P.; Boust, F.; Mahé, M.; Mercier, C. The UVSQ-SAT/INSPIRESat-5 CubeSat Mission: First

In-Orbit Measurements of the Earth's Outgoing Radiation. Remote Sens. 2021, 13, 1449. https://doi.org/10.3390/rs13081449

Conferences

Finance, A.; Meftah, M.; Mangin, A.; Keckhut, P. UVSQ-SAT a New Way to Obtain Spatio-Temporal Variations of the Radiation Budget with a Satellite Constellation; Earth and Space Science Open Archive; AGU 2020: Washington, DC, USA, 2021; p. 21.

Finance, A.; Meftah, M.; Dufour, C.; Boutéraon, T.; Mangin, A.; UVSQ-SAT Team. Remote Sensing Based Methods to Retrieve UVSQ-SAT Cubesat Attitude to Map the Earth's Radiation Budget, AGU 2021

Boutéraon, T.; Meftah, M.; Dufour, C.; Finance, A.; Keckhut, P.; UVSQ-SAT Team. What Characteristics for a Constellation of UVSQ-SAT-like CubeSats to Monitor the Earth's Radiation Budget at the Top Of the Atmosphere, AGU 2021

Meftah, M.; Finance, A.; Damé, L.; Bekki, S.; Galopeau, P.; Sarkissian, A.; Dufour, C.; Boutéraon, T.; Hauchecorne, A.; Boust, F.; Grossel, K.; Mangin, A.; Chang, L. C.; Chandran, A.; Keckhut, P.; INSPIRE-SAT team. Earth's Energy Imbalance measured from Space with a CubeSat constellation, AGU 2021

Finance, A., Meftah, M.; Dufour, C.; Boutéraon, T.; the UVSQ-SAT / INSPIRE-SAT 7 team. The UVSQ-SAT mission dedicated to the observation of the Earth and the Sun, Elbereth Conference 2022

Finance, A., Meftah, M.; Dufour, C.; Boutéraon, T.; Mangin, A.; the UVSQ-SAT / INSPIRE-SAT 7 team. La mission UVSQ- SAT dédiée à l'observation de la Terre et du Soleil, PNST 2022

Trainings

- An introduction to Machine Learning with Python: Classification of satellite thermal infrared images with Cécile Ferrari (Professor, University of Paris).
- Online Earth Observation Satellite System Design Training Course 2021, ESA/ESA Academy/ARES.
- Scientific Integrity: Principles and Practice.

List of Figures

List of Tables

List of Abbreviations and Acronyms

A

ADU Analog-to-Digital Units
AHRS Attitude and Heading Reference System
ANN Artificial Neural Network
API Application Program Interface
AU Astronomical Unit

B

BOL Beginning Of Life
BOS Bolometric Oscillation Sensor
BRDF Bidirectional Reflectance Distribution Function

C

C3S Copernicus Climate Change Service
CDHS Command and Data Handling Subsystem
CDS Climate Data Store
CERES Clouds and the Earth's Radiant Energy System
CMIP Coupled Model Intercomparison Project
COP Conference Of the Parties
CTD Conductivity-Temperature-Depth
CVCM Collected Volatile Condensable Material

D

DoD Depth of Discharge
DSCO Deep Space Climate Observatory

E

EBAF Energy Balanced and Filled
ECMWF European Centre for Medium Range Weather Forecast
ECT Equatorial Crossing Time
ECV Essential Climate Variable
EEI Earth Energy Imbalance
ELU Exponential Linear Unit
ENSO El Nino Southern Oscillation
EPS Electric Power Supply
ERB Earth Radiation Budget
ERBE Earth Radiation Budget Experiment
ERBS Earth Radiation Budget Satellite
ERS Earth Radiation Sensor
ESA European Space Agency
EUMETSAT European Organisation for the Exploitation of Meteorological Satellites

F

FORUM Far-infrared Outgoing Radiation Understanding and Monitoring
FOV Field Of View
FWHM Full Width at Half Maximum

G

GCOS Global Climate Observing System
GERB Geostationary Earth Radiation Budget
GOOS Global Ocean Observing System

H

HIRS High Resolution Infrared Radiation Sounder

I

IAP Institute of Atmospheric Physics
IMU Inertial Measurement Unit
INSPIRE International Satellite Program in Research and Education
IOC-UNESCO Intergovernmental Oceanographic Commission of the United Nations Educational, Scientific and Cultural Organization
IPCC Intergovernmental Panel on Climate Change
ISC International Science Council
ISIS Innovative Solutions In Space
ISR Incoming Solar Radiation

J

JAXA Japan Aerospace Exploration Agency

L

LASP Laboratory for Atmospheric and Space Physics
LATMOS Laboratoire Atmosphères, Milieux, Observations Spatiales
LEO Low Earth Orbit
LW Longwave

M

MAE Mean Absolute Error
MLP MultiLayer Perceptron
MOC Mission Operation Center
MPPT Max Power Point Tracking
MSE Mean Squared Error

N

NASA National Aeronautics and Space Administration
NFOV Narrow Field Of View
NISTAR National Institute of Standards and Technology Advanced Radiometer
NOAA National Oceanic and Atmospheric Administration

O

OBC OnBoard Computer
OHC Ocean Heat Content
OLR Outgoing Longwave Radiation
OSR Outgoing Shortwave Radiation

R

RELU Rectified Linear Unit
RMSD Root-Mean-Square Deviation

S

ScaRaB Scanner for Radiation Budget
SGP Simplified General Perturbations
SNPP Suomi National Polar-Orbiting Partnership
SOC Scientific Operation Center
SW Shortwave

T

TLE Two-Line Element
TML Total Mass Loss
TOA Top Of Atmosphere
TOT Total
TSI Total Solar Irradiance
TW TeachWear

U

UHF Ultra High Frequency
UNFCCC United Nations Framework Convention on Climate Change
UV Ultra-Violet
UVS Ultra-Violet Sensor
UVSQ-SAT UltraViolet and infrared Sensors at high Quantum efficiency onboard a small SATellite

V

VACNTS Vertically Aligned Carbon Nanotubes
VHF Very High Frequency

W

WFOV Wide Field Of View
WMO World Meteorological Organization

Nomenclature

α	Albedo
α	Reciprocal of the semimajor axis
α	Rotation angle
$\alpha_{i,j}$	Angle between the nadir of the satellite and the pixel (i, j)
α_{TOA}	Planetary albedo
$\alpha_{x/y/z}$	Angle of rotation around x/y/z-axis
$\bar{\Theta}(\hat{\boldsymbol{\omega}}_{\boldsymbol{k}}^{+})$	Representation of the quaternion's propagation
$\beta_{i,j}$	The satellite elevation (complement of zenith angle) seen by the pixel (i, j)
$\boldsymbol{\beta(t)}$	Drift
$\boldsymbol{\delta q(\delta\vartheta)}$	Error quaternion defined by $\boldsymbol{\delta\vartheta}$, with the three components representing the attitude error
$\boldsymbol{\delta\hat{\vartheta}_0}$	Initial attitude error for $\hat{\mathbf{q}}_{\mathbf{0}}$ (initial quaternion)
$\boldsymbol{\delta\hat{\vartheta}}_k^-$	Pre-estimate of the error angle
$\boldsymbol{\eta_B(t)}$	Zero-mean Gaussian noise for the Magnetic field vector
$\boldsymbol{\eta_N(t)}$	Zero-mean Gaussian noise for the Nadir direction vector
$\boldsymbol{\eta_S(t)}$	Zero-mean Gaussian noise for the Sun LOS vector
$\boldsymbol{\eta_\beta(t)}$	Zero-mean Gaussian noise for the drift
$\boldsymbol{\eta_\omega(t)}$	Zero-mean Gaussian noise for the three-axis rate
$\boldsymbol{\hat{\beta}(t)}$	Gyrometer biases

$\hat{\boldsymbol{\beta}}_{\mathbf{0}}$	Initial gyro drift biases
$\hat{\boldsymbol{\omega}}(\boldsymbol{t})$	Three-axis rate from the gyrometer
$\hat{\boldsymbol{\omega}}^{-}(t)$	Gyrometer components corrected based on the factors, drifts, and misalignments obtained from the previous step
$\hat{\boldsymbol{x}}_k^{+}$	Updated state vector
$\boldsymbol{\omega}(\boldsymbol{t})$	True rate
$\boldsymbol{\omega}_{\boldsymbol{B/I}}$	Measurements from the gyrometer with respect to an inertial reference frame
$\boldsymbol{\omega}_{\boldsymbol{B/OC}}$	Measurements from the gyrometer with respect to the body-fixed reference frame
$\boldsymbol{\omega}_{\boldsymbol{OC/I}}$	Angular velocity vector from the body-fixed reference frame to the inertial reference frame
$\boldsymbol{h}_{\boldsymbol{k}}(\hat{\boldsymbol{x}}_{\boldsymbol{k}}^{-})$	Estimated observation
$\Delta\lambda_i$	Element size along the longitude axis
$\Delta\phi_j$	Element size along the latitude axis
Δt	Duration between the two considered epochs
Δ_X	Spatial resolution
ϵ	Hemispherical emissivity of the thermopile coating
γ_{Earth}	Ratio between the computed terrestrial flux and the true terrestrial flux
γ_{Sun}	Ratio between the computed incident Solar flux and the true Solar flux
$\hat{S}(t)$	Gyrometer misalignments
λ	Wavelength
λ_{sat}	Satellite's longitude
$\hat{\mathbf{B}}(\mathbf{t})$	Magnetic field vector retrieved from the instruments on-board the satellite
$\hat{\mathbf{k}}\mathbf{L}_{\mathbf{0}}$	Initial misalignments
$\hat{\mathbf{k}}\mathbf{U}_{\mathbf{0}}$	Initial misalignments

$\hat{\mathbf{N}}(\mathbf{t})$	Nadir direction vector retrieved from the instruments on-board the satellite
$\hat{\mathbf{q}}^{-}_{\mathbf{k+1}}$	Estimate of the quaternion at time t_{k+1}
$\hat{\mathbf{q}}$	Estimate quaternion giving an estimate of the object orientation
$\hat{\mathbf{S}}(\mathbf{t})$	Sun LOS vector retrieved from the instruments on-board the satellite
$\hat{\mathbf{s}}_{\mathbf{0}}$	Initial gyrometer scale factor
$\hat{\mathbf{x}}_{\mathbf{0}}$	State vector
$\mathbf{a}_{\mathbf{cc}}$	Satellite acceleration vector
$\mathbf{B}(\mathbf{t})$	True Magnetic field vector
$\mathbf{N}(\mathbf{t})$	True Nadir direction vector
$\mathbf{q}^{\mathbf{true}}$	True quaternion representing the real orientation of the object
$\mathbf{q}$	Quaternion
$\mathbf{r}$	Satellite position vector
$\mathbf{S}(\mathbf{t})$	True Sun LOS vector
$\mathbf{v}$	Satellite velocity vector
μ	Standard gravitational parameter
Ω	Longitude of Ascending Node
ω	Argument of Periapsis
ω_k	Dot product between $\vec{s}$ and $\vec{n_k}$
$\omega_{0,j}$	Biases
$\Omega_{i,j}$	The view angle under which the pixel (i, j) is seen by the satellite
$\omega_{i,j}$	Weights
Ω_{J_2}	Rate of change of Ω due to J_2 (Non-spherical Earth)
ω_{J_2}	Rate of change of ω due to J_2 (Non-spherical Earth)
$\otimes$	Quaternion product symbol

Φa_{in}	Albedo incident flux
Φp_{in}	Planetary incident flux
ϕ	Roll angle
ϕ_{detect}	True amount of flux received by a sensor
ϕ_{ref}	Incident flux on each of the detectors
ϕ_j	Element latitude
Φ_k	Process noise matrix
Φ_{in}	Incoming flux
$\Phi_{\text{out/LW}}$	Outgoing Longwave flux
$\Phi_{\text{out/SW}}$	Outgoing Shortwave flux
Φ_{out}	Outgoing flux
ϕ_{sat}	Satellite's latitude
ψ	Yaw angle
$\rho_{\text{photo[i/Earth]}}$	Angular function that represents the angular response of the photodiode
σ	Stefan-Boltzmann's constant
σ_v^2, σ_u^2, σ_s^2	Gyrometer measurement noise variances
$\sigma_{i,j}$	Cache output before going through the activation function
θ	Pitch angle
θ	Right ascension
θ_i	Angle between the solar direction and the normal of the thermopile
θ_{Sun}	Angle between the normal to the sensor and the direction of the Sun
$\theta_{i,j}$	Angle at the center of the Earth (nadir) between the satellite and the pixel (i, j)
$\varepsilon_i(\lambda)$	Normal emittance of thermopile i

$\vec{a_{Sat}}$	Satellite's acceleration vector
$\vec{m}$	Magnetic North
$\vec{n_k}$	Normal vector to the face k
$\vec{s}$	Sun vector
ξ	Solar zenith angle
a	ERS (coating) solar absorption
a	Semi-major axis (km)
$A(\boldsymbol{q})$	Attitude matrix
A_i	Surface area of thermopile i
$a_i(\lambda)$	Solar absorption of thermopile i
B_{Sat}	Satellite's reference frame
B_{TW}	Teach' Wear's reference frame
C_1, C_2	Corrective offsets
Cp_1	Corrective offset
$d_{\text{Sun/Earth}}$	Sun-Earth distance in AU
$d_{\text{Sat/Earth}}$	Distance from the satellite to the center of the Earth
$d_{\text{Sun/Sat}}$	Sun-Satellite distance in AU
E	Eccentric anomaly
$EI(\lambda)$	Spectral Earth irradiance
$F(\beta)$	View factor between the Earth and the sensor with β the angle between the normal to the sensors and the Earth nadir
$F_{\text{i/Earth}}$	Earth view factor
f_k	Flux on face k of the satellite for the selected field of view
$F_{i,j}$	Function of inputs $y_{1,j-1}..., y_{n^{j-1},j-1}$
$F_{sat}(\lambda_{\text{sat}}, \phi_{\text{sat}})$	Observed flux by UVSQ-SAT

F_{Sun}	Incoming solar flux
g	Activation function
$G(T_b)$	Gain of the electronic unit
G_{pho}	Gain of the electronic unit
GL	Conductive couplings of thermopile i
GR	Radiative couplings of thermopile i
h	Specific angular momentum
$H_k(\boldsymbol{x}_{\boldsymbol{k}}^{-})$	Observation model at time t_k
i	Inclination
i	Index of neurons in the range of $[1,\ n^0]$
j	Index of layers in the range of $[1,\ l]$
J_2	Zonal coefficient, describing the perturbation effect due to the oblateness of Earth
k	Index of the faces
K_k	Kalman gain at time t_k
k_{U1}, k_{U2}, k_{U3}, k_{L1}, k_{L2}, k_{L3}	Gyrometer cross-coupling errors
l	Total number of layers
M	Energetic emittance of a body
M_0	Initial mean anomaly, azimuth position (rad) at t_0
M_e	Mean anomaly, azimuth position (rad)
n^j	Number of neurons at layer j
N_{samp}	Number of samples for measurement
Np_{samp}	Number of samples for measurement
P_0	Initial covariance matrix defined from the predicted instrument uncertainties

P_k	State error covariance at time t_k
P_{k+1}^-	Covariance matrix estimate at t_{k+1}
Q_k	Measurement noise matrix
$q_{1...4}$	Real numbers
Qr_i	Absorbed residual power from the Moon, planets, etc
R_{Earth}	Earth Radius (km)
R_k	Measurement-error covariance matrix at time t_k
$r_{x/y/z}$	X/Y/Z-coordinate of the rotation axis
s_1, s_2, s_3	Gyrometer scale factors
$S_{\text{pho}}(T_{\text{pho}})$	Responsivity of the photodiode (calibration done by the manufacturer)
$SI(\lambda)$	Spectral solar irradiance
T	Temperature
T	Time of Periapsis Passage
T_{pho}	Temperature of the satellite's structure
T_b	Temperature of the sensors electronic board
T_i	The temperature of thermopile i
T_s	ERS sensor temperature
V_{ADU}	Reference voltage
$y_{i,0} = x_i$	Inputs of the node (i,j)
$y_{i,j}$	Outputs of the node (i,j)
z_{sat}	Satellite's altitude
Sens	Sensitivity of the sensor

Bibliography

Copernicus. `https://www.copernicus.eu/fr/propos-de-copernicus/copernicus-en-bref`, 2022. Accessed: 2022-11-02.

Airbus. Pléiades imagery user guide. Technical report, Airbus Defence and Space Intelligence, France, 2012.

R. P. Allan, C. Liu, N. G. Loeb, M. D. Palmer, M. Roberts, D. Smith, and P. L. Vidale. Changes in global net radiative imbalance 1985-2012. Geophysical Research Letters, 41:5588–5597, 2014. ISSN 19448007. doi: 10.1002/2014GL060962.

V. E. Amaro, L. R. S. Gomes, F. G. F. de Lima, A. C. Scudelari, C. F. Neves, D. V. Busman, and A. L. S. Santos. Multitemporal analysis of coastal erosion based on multisource satellite images, ponta negra beach, natal city, northeastern brazil. Marine Geodesy, 38(1):1–25, 2015. doi: 10.1080/01490419.2014.904257. URL `https://doi.org/10.1080/01490419.2014.904257`.

T. Andrews and M. J. Webb. The dependence of global cloud and lapse rate feedbacks on the spatial structure of tropical pacific warming. Journal of Climate, 31: 641–654, 2018. doi: https://doi.org/10.1175/JCLI-D-17-0087.1. URL `https://journals.ametsoc.org/view/journals/clim/31/2/jcli-d-17-0087.1.xml`.

A. Bagnell and T. DeVries. 20th century cooling of the deep ocean contributed to delayed acceleration of earth's energy imbalance. Nature Communications, 12, 12 2021. ISSN 20411723. doi: 10.1038/s41467-021-24472-3.

B. Barkstrom. Earth radiation budget experiment (erbe) archival and april 1985 results. Bulletin - American Meteorological Society, 70:1254–1262, 1989. ISSN 0003-0007. doi: 10.1175/1520-0477(1989)070<1254:ERBEAA>2.0.CO;2.

P. Barmpoutis, P. Papaioannou, K. Dimitropoulos, and N. Grammalidis. A review on early forest fire detection systems using optical remote sensing. Sensors (Switzerland), 20:1–26, 11 2020. ISSN 14248220. doi: 10.3390/s20226442.

A. BenMoussa, S. Gissot, U. Schühle, G. Del Zanna, F. Auchère, S. Mekaoui, A. Jones, D. Walton, C. Eyles, G. Thuillier, et al. On-orbit degradation of solar instruments. Solar Physics, 288(1):389–434, 2013.

P. G. Buzzi, D. Selva, N. Hitomi, and W. J. Blackwell. Assessment of constellation designs for earth observation: Application to the tropics mission. Acta Astronautica, 161:166–182, 2019. ISSN 0094-5765. doi: https://doi.org/10.1016/j.actaastro.2019.05.007. URL `https://www.sciencedirect.com/science/article/pii/S0094576518317338`.

R. Caballero and M. Huber. State-dependent climate sensitivity in past warm climates and its implications for future climate projections. Proceedings of the National Academy of Sciences, 110:14162–14167, 8 2013. doi: 10.1073/pnas.1303365110. URL `https://doi.org/10.1073/pnas.1303365110`. doi: 10.1073/pnas.1303365110.

D. Casanova, M. Avendano, and D. Mortari. Optimizing flower constellations for global coverage. AIAA/AAS Astrodynamics Specialist Conference, 8 2012. doi: doi:10.2514/6.2012-4805. URL `https://doi.org/10.2514/6.2012-4805`. doi:10.2514/6.2012-4805.

CEOS and C. member agencies. Ecv inventory, Nov 2022. URL `https://climatemonitoring.info/ecvinventory/`.

A. Chedin, V. Capelle, and N. A. Scott. Detection of iasi dust aod trends over sahara: How many years of data required? Atmospheric Research, 212:120–129, 11 2018. ISSN 01698095. doi: 10.1016/j.atmosres.2018.05.004.

H. Y. Cheng, C. C. Yu, K. C. Hsu, C. C. Chan, M. H. Tseng, and C. L. Lin. Estimating solar irradiance on tilted surface with arbitrary orientations and tilt angles. Energies, 12(8):1–14, 2019a. ISSN 19961073. doi: 10.3390/en12081427.

L. Cheng, J. Abraham, Z. Hausfather, and K. E. Trenberth. How fast are the oceans warming? Science, 363(6423):128–129, 2019b. doi: 10.1126/science.aav7619. URL `https://www.science.org/doi/abs/10.1126/science.aav7619`.

L. Cheng, J. Abraham, K. E. Trenberth, J. Fasullo, T. Boyer, M. E. Mann, J. Zhu, F. Wang, R. Locarnini, Y. Li, B. Zhang, Z. Tan, F. Yu, L. Wan, X. Chen, X. Song, Y. Liu, F. Reseghetti, S. Simoncelli, V. Gouretski, G. Chen, A. Mishonov, and J. Reagan. Another record: Ocean warming continues through 2021 despite la niña conditions. Advances in Atmospheric Sciences, 39:373–385, 3 2022. ISSN 18619533. doi: 10.1007/s00376-022-1461-3.

J. Cook, N. Oreskes, P. T. Doran, W. R. Anderegg, B. Verheggen, E. W. Maibach, J. S. Carlton, S. Lewandowsky, A. G. Skuce, S. A. Green, D. Nuccitelli, P. Jacobs, M. Richardson, B. Winkler, R. Painting, and K. Rice. Consensus on consensus: A synthesis of consensus estimates on human-caused global warming. Environmental Research Letters, 11, 4 2016. ISSN 17489326. doi: 10.1088/1748-9326/11/4/048002.

T. Dauhut, V. Noel, and I.-A. Dion. The diurnal cycle of the clouds extending above the tropical tropopause observed by spaceborne lidar. Atmospheric Chemistry and Physics, 20:3921–3929, 4 2020. ISSN 1680-7324. doi: 10.5194/acp-20-3921-2020. URL `https://acp.copernicus.org/articles/20/3921/2020/`.

M. Debella-Gilo and A. K. Gjertsen. Mapping seasonal agricultural land use types using deep learning on sentinel-2 image time series. Remote Sensing, page 289, 2021. URL `https://doi.org/10.3390/rs13020289`.

S. Dewitte and N. Clerbaux. Measurement of the earth radiation budget at the top of the atmosphere-a review. Remote Sensing, 9, 2017. ISSN 20724292. doi: 10.3390/rs9111143.

S. Dewitte, Ö. Karatekin, A. Chevalier, N. Clerbaux, M. Meftah, A. Irbah, and T. Delabie. The Sun-earth Imbalance radiometer for a direct measurement of the net heating of the earth. EGU General Assembly 2015, pages EGU2015–15259, Apr. 2015. URL `https://hal-insu.archives-ouvertes.fr/insu-01145599`. Poster.

W. H. Dines. The heat balance of the atmosphere. Quarterly Journal of the Royal Meteorological Society, 43:151–158, 1917. doi: https://doi.org/10.1002/qj.49704318203. URL `https://rmets.onlinelibrary.wiley.com/doi/abs/10.1002/qj.49704318203`.

W. Duan, J. Liu, Q. Yan, H. Ruan, and S. Jin. The effect of spatial resolution and temporal sampling schemes on the measurement error for a moon-based earth radiation observatory. Remote Sensing, 13, 11 2021. ISSN 20724292. doi: 10.3390/rs13214432.

A. Finance, C. Dufour, T. Boutéraon, A. Sarkissian, A. Mangin, P. Keckhut, and M. Meftah. In-orbit attitude determination of the uvsq-sat cubesat using triad and mekf methods. Sensors, 21:7361, 11 2021a. ISSN 1424-8220. doi: 10.3390/s21217361. URL `https://www.mdpi.com/1424-8220/21/21/7361`.

A. Finance, M. Meftah, C. Dufour, T. Boutéraon, S. Bekki, A. Hauchecorne, P. Keckhut, A. Sarkissian, L. Damé, and A. Mangin. A New Method Based on a Multilayer Perceptron Network to Determine In-Orbit Satellite Attitude for Spacecrafts without active ADCS like UVSQ-SAT. Remote Sensing, pages 1–17, 2021b. URL `https://www.mdpi.com/2072-4292/13/6/1185{#}metrics`.

A. Finance, M. Meftah, A. Mangin, and P. Keckhut. Uvsq-sat a new way to obtain spatio-temporal variations of the radiation budget with a satellite constellation. Earth and Space Science Open Archive, page 21, 2021c. doi: 10.1002/essoar.10505801.1. URL `https://doi.org/10.1002/essoar.10505801.1`.

N. N. C. for Environmental Information. State of the climate: Global climate report for annual 2020, 1 2021. URL `https://www.ncei.noaa.gov/access/monitoring/monthly-report/global/202013`.

B. Francesco, C. Chantal, R. Antonio, H. J. M. Mustapha, and F. Adrien), editors. Next Generation CubeSats and SmallSats: Enabling Technologies, Missions and Markets, volume in press. Elsevier, 2023. ISBN 978-0-12-824541-5.

E. Friis-Christensen, H. Lühr, D. Knudsen, and R. Haagmans. Swarm – an earth observation mission investigating geospace. Advances in Space Research, 41:210–216, 2008. ISSN 0273-1177. doi: https://doi.org/10.1016/j.asr.2006.10.008. URL `https://www.sciencedirect.com/science/article/pii/S0273117706005497`.

J. M. Gregory and J. A. Lowe. Predictions of global and regional sea-level rise using aogcms with and without flux adjustment. Geophysical Research Letters, 27:3069–3072, 2000. ISSN 00948276. doi: 10.1029/1999GL011228.

J. J. Gristey, J. C. Chiu, R. J. Gurney, S. C. Han, and C. J. Morcrette. Determination of global earth outgoing radiation at high temporal resolution using a theoretical constellation of satellites. Journal of Geophysical Research, 122:1114–1131, 2017. ISSN 21562202. doi: 10.1002/2016JD025514. URL `https://agupubs.onlinelibrary.wiley.com/doi/pdfdirect/10.1002/2016JD025514`.

H. Guo, G. Liu, and Y. Ding. Moon-based earth observation: scientific concept and potential applications. International Journal of Digital Earth, 11:546–557, 6 2018. ISSN 17538955. doi: 10.1080/17538947.2017.1356879.

M. Z. Hakuba, G. L. Stephens, B. Christophe, A. E. Nash, B. Foulon, S. V. Bettadpur, B. D. Tapley, and F. H. Webb. Earth's energy imbalance measured from space. IEEE Transactions on Geoscience and Remote Sensing, 57:32–45, 1 2019. ISSN 01962892. doi: 10.1109/TGRS.2018.2851976.

J. Hansen, D. Johnson, A. Lacis, S. Lebedeff, P. Lee, D. Rind, and G. Russell. Climate impact of increasing atmospheric carbon dioxide. Science, 213:957–966, 8 1981. doi: 10.1126/science.213.4511.957. URL `https://doi.org/10.1126/science.213.4511.957`. doi: 10.1126/science.213.4511.957.

J. Hansen, M. Sato, and R. Ruedy. Radiative forcing and climate response. Journal of Geophysical Research: Atmospheres, 102:6831–6864, 3 1997. ISSN 0148-0227. doi: https://doi.org/10.1029/96JD03436. URL `https://doi.org/10.1029/96JD03436`. https://doi.org/10.1029/96JD03436.

J. Hansen, L. Nazarenko, R. Ruedy, M. Sato, J. Willis, A. D. Genio, D. Koch, A. Lacis, K. Lo, S. Menon, T. Novakov, J. Perlwitz, G. Russell, G. A. Schmidt, and N. Tausnev. Earth's energy imbalance: Confirmation and implications. Science, pages 1431–1435, 2005. URL `www.sciencemag.org`.

J. Hansen, M. Sato, P. Kharecha, and K. von Schuckmann. Earth's energy imbalance and implications. Atmospheric Chemistry and Physics, 11:13421–13449, 12 2011. ISSN 1680-7324. doi: 10.5194/acp-11-13421-2011. URL `https://acp.copernicus.org/articles/11/13421/2011/`.

J. E. Harries, J. E. Russell, J. A. Hanafin, H. Brindley, J. Futyan, J. Rufus, S. Kellock, G. Matthews, R. Wrigley, A. Last, J. Mueller, R. Mossavati, J. Ashmall, E. Sawyer, D. Parker, M. Caldwell, P. M. Allan, A. Smith, M. J. Bates, B. Coan, B. C. Stewart, D. R. Lepine, L. A. Cornwall, D. R. Corney, M. J. Ricketts, D. Drummond, D. Smart, R. Cutler, S. Dewitte, N. Clerbaux, L. Gonzalez, A. Ipe, C. Bertrand, A. Joukoff, D. Crommelynck, N. Nelms, D. T. Llewellyn-Jones, G. Butcher, G. L. Smith, Z. P. Szewczyk, P. E. Mlynczak, A. Slingo, R. P. Allan, and M. A. Ringer. The geostationary earth radiation budget project. Bulletin of the American Meteorological Society, 86:945–960, 7 2005. ISSN 00030007. doi: 10.1175/BAMS-86-7-945.

D. Hartmann, A. Klein Tank, M. Rusticucci, L. Alexander, S. Brönnimann, Y. Charabi, F. Dentener, E. Dlugokencky, D. Easterling, A. Kaplan, B. Soden, P. Thorne, M. Wild, and P. Zhai. Observations: Atmosphere and surface, volume 9781107057999, pages 159–254. Cambridge University Press, Jan. 2013. ISBN 9781107057999. doi: 10.1017/CBO9781107415324.008. Publisher Copyright: © Intergovernmental Panel on Climate Change 2014.

J. M. Haywood, R. P. Allan, I. Culverwell, T. Slingo, S. Milton, J. Edwards, and N. Clerbaux. Can desert dust explain the outgoing longwave radiation anomaly over the sahara during july 2003? J. Geophys. Res, 110:5105, 2005. doi: 10.1029/2004JD005232.

C. Hedemann, T. Mauritsen, J. Jungclaus, and J. Marotzke. The subtle origins of surface-warming hiatuses. Nature Climate Change, 7:336–339, 5 2017. ISSN 17586798. doi: 10.1038/nclimate3274.

H. H. Hendon and K. Woodberry. The diurnal cycle of tropical convection. Journal of Geophysical Research, 98, 1993. ISSN 01480227. doi: 10.1029/93jd00525.

H. Hersbach, B. Bell, P. Berrisford, S. Hirahara, A. Horányi, J. Muñoz-Sabater, J. Nicolas, C. Peubey, R. Radu, D. Schepers, A. Simmons, C. Soci, S. Abdalla, X. Abellan, G. Balsamo, P. Bechtold, G. Biavati, J. Bidlot, M. Bonavita, G. D. Chiara, P. Dahlgren, D. Dee, M. Diamantakis, R. Dragani, J. Flemming, R. Forbes, M. Fuentes, A. Geer, L. Haimberger, S. Healy, R. J. Hogan, E. Hólm, M. Janisková, S. Keeley, P. Laloyaux, P. Lopez, C. Lupu, G. Radnoti, P. de Rosnay, I. Rozum, F. Vamborg, S. Villaume, and J.-N. Thépaut. The era5 global reanalysis. Quarterly Journal of the Royal Meteorological Society, n/a, 5 2020. ISSN 0035-9009. doi: 10.1002/qj.3803. URL `https://doi.org/10.1002/qj.3803`. doi: 10.1002/qj.3803.

A. J. Illingworth, H. W. Barker, A. Beljaars, M. Ceccaldi, H. Chepfer, N. Clerbaux, J. Cole, J. Delanoë, C. Domenech, D. P. Donovan, S. Fukuda, M. Hirakata, R. J. Hogan, A. Huenerbein, P. Kollias, T. Kubota, T. Nakajima, T. Y. Nakajima, T. Nishizawa, Y. Ohno, H. Okamoto, R. Oki, K. Sato, M. Satoh, M. W. Shephard, A. Velázquez-Blázquez, U. Wandinger, T. Wehr, and G. J. V. Zadelhoff. The earthcare satellite : The next step forward in global measurements of clouds, aerosols, precipitation, and radiation. Bulletin of the American Meteorological Society, 96:1311–1332, 8 2015. ISSN 15200477. doi: 10.1175/BAMS-D-12-00227.1.

M. Ishii, Y. Fukuda, S. Hirahara, S. Yasui, T. Suzuki, and K. Sato. Accuracy of global upper ocean heat content estimation expected from present observational data sets. SOLA, 13:163–167, 2017. ISSN 1349-6476. doi: 10.2151/sola.2017-030.

M. J. Jeon, S. R. Lee, E. Kim, S. B. Lim, and S. W. Choi. Launch and early operation results of kompsat-3a. 14th International Conference on Space Operations, 2016, 2016. doi: 10.2514/6.2016-2394.

G. C. Johnson, J. M. Lyman, and N. G. Loeb. Improving estimates of earth's energy imbalance. Nature Climate Change, 6:639–640, 7 2016. ISSN 17586798. doi: 10.1038/nclimate3043.

M. Kameche, H. Benzeniar, A. B. Benbouzid, R. Amri, and N. Bouanani. Disaster monitoring constellation using nanosatellites. Journal of Aerospace Technology and Management, 6:93–100, 2014. ISSN 21759146. doi: 10.5028/jatm.v6i1.281.

R. K. Kaufmann, H. Kauppi, M. L. Mann, and J. H. Stock. Reconciling anthropogenic climate change with observed temperature 1998–2008. Proceedings of the National Academy of Sciences, 108:11790–11793, 2011. doi: 10.1073/pnas.1102467108. URL `https://www.pnas.org/doi/abs/10.1073/pnas.1102467108`.

J. T. Kiehl and K. E. Trenberth. Earth's annual global mean energy budget. Bulletin of the American Meteorological Society, 78(2):197–208, 1997.

Y. Kotak, M. Gul, T. Muneer, and S. Ivanova. Investigating the impact of ground albedo on the performance of pv systems. CIBSE Technical Symposium 2015, 4 2015.

T. S. L'Ecuyer, H. K. Beaudoing, M. Rodell, W. Olson, B. Lin, S. Kato, C. A. Clayson, E. Wood, J. Sheffield, R. Adler, G. Huffman, M. Bosilovich, G. Gu, F. Robertson, P. R. Houser, D. Chambers, J. S. Famiglietti, E. Fetzer, W. T. Liu, X. Gao, C. A. Schlosser, E. Clark, D. P. Lettenmaier, and K. Hilburn. The observed state of the energy budget in the early twenty-first century. Journal of Climate, 28:8319–8346, 2015. ISSN 08948755. doi: 10.1175/JCLI-D-14-00556.1.

T. S. Ledley, E. T. Sundquist, S. E. Schwartz, D. K. Hall, J. D. Fellows, and T. L. Killeen. Climate change and greenhouse gases. Eos, Transactions American Geophysical Union, 80:453–458, 1999. doi: https://doi.org/10.1029/99EO00325. URL `https://agupubs.onlinelibrary.wiley.com/doi/abs/10.1029/99EO00325`.

S. Liang, D. Wang, T. He, and Y. Yu. Remote sensing of earth's energy budget: synthesis and review. International Journal of Digital Earth, 12:737–780, 7 2019. ISSN 1753-8947. doi: 10.1080/17538947.2019.1597189. URL `https://doi.org/10.1080/17538947.2019.1597189`. doi: 10.1080/17538947.2019.1597189.

X. Liang, C. Liu, R. M. Ponte, and D. P. Chambers. A comparison of the variability and changes in global ocean heat content from multiple objective analysis products during the argo period. Journal of Climate, 34:7875 – 7895, 2021. doi: 10.1175/JCLI-D-20-0794.1. URL `https://journals.ametsoc.org/view/journals/clim/34/19/JCLI-D-20-0794.1.xml`.

R. S. Lindzen. Climate dynamics and global change. Annual Review of Fluid Mechanics, 26:353–378, 1994. doi: 10.1146/annurev.fl.26.010194.002033. URL `https://doi.org/10.1146/annurev.fl.26.010194.002033`.

R. S. Lindzen and C. Giannitsis. On the climatic implications of volcanic cooling. Journal of Geophysical Research: Atmospheres, 103:5929–5941, 1998. doi:

https://doi.org/10.1029/98JD00125. URL `https://agupubs.onlinelibrary.wiley.com/doi/abs/10.1029/98JD00125`.

M. Liu, B. J. Soden, G. A. Vecchi, and C. Wang. The spread of ocean heat uptake efficiency traced to ocean salinity. Geophysical Research Letters, 50:e2022GL100171, 2 2023. ISSN 0094-8276. doi: https://doi.org/10.1029/2022GL100171. URL `https://doi.org/10.1029/2022GL100171`. https://doi.org/10.1029/2022GL100171.

N. G. Loeb, B. A. Wielicki, F. G. Rose, and D. R. Doelling. Variability in global top-of-atmosphere shortwave radiation between 2000 and 2005. Geophysical Research Letters, 34, 2 2007. ISSN 00948276. doi: 10.1029/2006GL028196. URL `https://doi.org/10.1029/2006GL028196`. doi: 10.1029/2006GL028196.

N. G. Loeb, B. A. Wielicki, D. R. Doelling, G. L. Smith, D. F. Keyes, S. Kato, N. Manalo-Smith, and T. Wong. Toward optimal closure of the earth's top-of-atmosphere radiation budget. J. Climate, 22:748–766, 2009.

N. G. Loeb, J. M. Lyman, G. C. Johnson, R. P. Allan, D. R. Doelling, T. Wong, B. J. Soden, and G. L. Stephens. Observed changes in top-of-the-atmosphere radiation and upper-ocean heating consistent within uncertainty. Nature Geoscience, 5:110–113, 2012. ISSN 1752-0908. doi: 10.1038/ngeo1375. URL `https://doi.org/10.1038/ngeo1375`.

N. G. Loeb, D. R. Doelling, H. Wang, W. Su, C. Nguyen, J. G. Corbett, L. Liang, C. Mitrescu, F. G. Rose, and S. Kato. Clouds and the earth's radiant energy system (ceres) energy balanced and filled (ebaf) top-of-atmosphere (toa) edition-4.0 data product. Journal of Climate, 31:895–918, 1 2018a. ISSN 0894-8755. doi: 10.1175/JCLI-D-17-0208.1. URL `https://doi.org/10.1175/JCLI-D-17-0208.1`.

N. G. Loeb, T. J. Thorsen, J. R. Norris, H. Wang, and W. Su. Changes in earth's energy budget during and after the "pause" in global warming: An observational perspective. Climate, 6, 9 2018b. ISSN 22251154. doi: 10.3390/cli6030062.

N. G. Loeb, P. Yang, F. G. Rose, G. Hong, S. Sun-Mack, P. Minnis, S. Kato, S.-H. Ham, W. L. Smith, S. Hioki, and G. Tang. Impact of ice cloud microphysics on satellite cloud retrievals and broadband flux radiative transfer model calculations. Journal of Climate, 31:1851–1864, 2018c. doi: https://doi.org/10.1175/JCLI-D-17-0426.1. URL `https://journals.ametsoc.org/view/journals/clim/31/5/jcli-d-17-0426.1.xml`.

N. G. Loeb, G. C. Johnson, T. J. Thorsen, J. M. Lyman, F. G. Rose, and S. Kato. Satellite and ocean data reveal marked increase in earth's heating rate. Geophysical Research Letters, 48, 7 2021. ISSN 19448007. doi: 10.1029/2021GL093047.

M. E. Malerba, N. Wright, and P. I. Macreadie. A continental-scale assessment of density, size, distribution and historical trends of farm dams using deep learning convolutional neural networks. Remote Sensing, 13(2):1–17, 2021. ISSN 20724292. doi: 10.3390/rs13020319.

F. Marti, A. Blazquez, B. Meyssignac, M. Ablain, A. Barnoud, R. Fraudeau, R. Jugier, J. Chenal, G. Larnicol, J. Pfeffer, M. Restano, and J. Benveniste. Monitoring the ocean heat content change and the earth energy imbalance from space altimetry and space gravimetry. Earth System Science Data, 14:229–249, 1 2022. ISSN 1866-3516. doi: 10.5194/essd-14-229-2022. URL `https://essd.copernicus.org/articles/14/229/2022/`.

V. Masson-Delmotte, P. Zhai, A. Pirani, S. L. Connors, C. Pean, S. Berger, N. Caud, Y. Chen, L. Goldfarb, M. I. Gomis, M. Huang, K. Leitzell, E. Lonnoy, J. B. R. Matthews, T. K. Maycock, T. Waterfield, O. Yelekci, R. Yu, and B. Zhou, editors. IPCC, 2021: Climate Change 2021: The Physical Science Basis. Contribution of Working Group I to the Sixth Assessment Report of the Intergovernmental Panel on Climate Change. ARRAY(0x559e4d826f78), 2021. URL `https://www.ipcc.ch/report/ar6/wg1/`.

J. Maximillian, M. L. Brusseau, E. P. Glenn, and A. D. Matthias. Chapter 25 - Pollution and Environmental Perturbations in the Global System, pages 457–476. Academic Press, third edition edition, 2019. ISBN 978-0-12-814719-1. doi: https://doi.org/10.1016/B978-0-12-814719-1.00025-2. URL `https://www.sciencedirect.com/science/article/pii/B9780128147191000252`.

M. Meftah. L'espace et le NewSpace au service du climat. Books On Demand, 2023. URL `https://hal-insu.archives-ouvertes.fr/insu-04053151`.

M. Meftah, L. Damé, D. Bolsée, A. Hauchecorne, N. Pereira, D. Sluse, G. Cessateur, A. Irbah, J. Bureau, M. Weber, K. Bramstedt, T. Hilbig, R. Thiéblemont, M. Marchand, F. Lefèvre, A. Sarkissian, and S. Bekki. Solar-iss: A new reference spectrum based on solar/solspec observations. Astronomy and Astrophysics, 611:1–14, 2018. ISSN 14320746. doi: 10.1051/0004-6361/201731316.

M. Meftah, L. Damé, P. Keckhut, S. Bekki, A. Sarkissian, A. Hauchecorne, E. Bertran, J. P. Carta, D. Rogers, S. Abbaki, C. Dufour, P. Gilbert, L. Lapauw, A. J. Vieau, X. Arrateig, N. Muscat, P. Bove, É. Sandana, F. Teherani, T. Li, G. Pradel, M. Mahé, C. Mercier, A. Paskeviciute, K. Segura, A. B. Alba,

A. Aboulila, L. Chang, A. Chandran, P. R. Dahoo, and A. Bui. UVSQ-SAT, a pathfinder cubesat mission for observing essential climate variables. Remote Sensing, 12, 1 2020a. ISSN 20724292. doi: 10.3390/RS12010092.

M. Meftah, L. Damé, D. Bolsée, N. Pereira, M. Snow, M. Weber, K. Bramstedt, T. Hilbig, G. Cessateur, M. Y. Boudjella, M. Marchand, F. Lefèvre, R. Thiéblemont, A. Sarkissian, A. Hauchecorne, P. Keckhut, and S. Bekki. A new version of the solar-iss spectrum covering the 165 – 3000 nm spectral region. Solar Physics, 295:1–16, 2020b. ISSN 1573093X. doi: 10.1007/s11207-019-1571-y. URL `http://dx.doi.org/10.1007/s11207-019-1571-y`.

M. Meftah, M. Snow, L. Damé, D. Bolseé, N. Pereira, G. Cessateur, S. Bekki, P. Keckhut, A. Sarkissian, and A. Hauchecorne. Solar-v: A new solar spectral irradiance dataset based on solar/solspec observations during solar cycle 24. Astronomy and Astrophysics, 2:1–9, 2020c. ISSN 0004-6361. doi: 10.1051/0004-6361/202038422.

M. Meftah, T. Boutéraon, C. Dufour, A. Hauchecorne, P. Keckhut, A. Finance, S. Bekki, S. Abbaki, E. Bertran, L. Damé, J.-L. Engler, P. Galopeau, P. Gilbert, L. Lapauw, A. Sarkissian, A.-J. Vieau, P. Lacroix, N. Caignard, X. Arrateig, O. H. F. H. F. D'Andon, A. Mangin, J.-P. Carta, F. Boust, M. Mahé, and C. Mercier. The UVSQ-SAT/INSPIRESat-5 CubeSat Mission: First In-Orbit Measurements of the Earth's Outgoing Radiation. Remote Sensing, 13(8):1449, 2021. ISSN 2072-4292. doi: 10.3390/rs13081449. URL `https://www.mdpi.com/2072-4292/13/8/1449`.

M. Meftah, F. Boust, P. Keckhut, A. Sarkissian, T. Boutéraon, S. Bekki, L. Damé, P. Galopeau, A. Hauchecorne, C. Dufour, A. Finance, A.-J. Vieau, E. Bertran, P. Gilbert, N. Caignard, C. Dias, J.-L. Engler, P. Lacroix, K. Grossel, V. Rannou, S. Saillant, Y. Avelino, B. Azoulay, C. Brand, C. Dominguez, A. Haasz, A. Paskeviciute, K. Segura, P. Maso, S. Ancelin, C. Mercier, V. Stee, A. Mangin, D. Bolsée, and C. Billard. Inspire-sat 7, a second cubesat to measure the earth's energy budget and to probe the ionosphere. Remote Sensing, 14:186, 2022. doi: 10.3390/rs14010186.

B. Meyssignac. Les observations spatiales historiques permettent elles d'évaluer le bilan énergétique du climat et d'estimer la sensibilité climatique ? Une tentative avec les observations de géodésie spatiale. Habilitation à diriger des recherches, Université Toulouse-III-Paul-Sabatier, Dec. 2021. URL `https://hal.science/tel-03700636`.

B. Meyssignac, T. Boyer, Z. Zhao, M. Z. Hakuba, F. W. Landerer, D. Stammer, A. Köhl, S. Kato, T. L'Ecuyer, M. Ablain, J. P. Abraham, A. Blazquez,

A. Cazenave, J. A. Church, R. Cowley, L. Cheng, C. Domingues, D. Giglio, V. Gouretski, M. Ishii, G. C. Johnson, R. E. Killick, D. Legler, W. Llovel, J. Lyman, M. D. Palmer, S. Piotrowicz, S. Purkey, D. Roemmich, R. Roca, A. Savita, K. von Schuckmann, S. Speich, G. Stephens, G. G. Wang, S. E. Wijffels, and N. Zilberman. Measuring global ocean heat content to estimate the earth energy imbalance. Frontiers in Marine Science, 6, 2019. ISSN 22967745. doi: 10.3389/fmars.2019.00432.

F. Miskolczi and M. Mlynczak. The greenhouse effect and the spectral decomposition of the clear-sky terrestrial radiation. IDŐJÁRÁS Quarterly Journal of the Hungarian Meteorological Service, 108:209–251, 11 2022.

D. J. Mulla. Twenty five years of remote sensing in precision agriculture: Key advances and remaining knowledge gaps. Biosystems Engineering, 114(4):358–371, 2013. ISSN 1537-5110. doi: https://doi.org/10.1016/j.biosystemseng.2012.08.009. URL `https://www.sciencedirect.com/science/article/pii/S1537511012001419`. Special Issue: Sensing Technologies for Sustainable Agriculture.

M. M. Nezhad, B. Nastasi, D. Groppi, M. Lamagna, G. Piras, and D. A. Garcia. Green energy sources assessment using sentinel-1 satellite remote sensing. Frontiers in Energy Research, 9, 12 2021. ISSN 2296598X. doi: 10.3389/fenrg.2021.649305.

T. Nguyen, K. Cahoy, and A. Marinan. Attitude determination for small satellites with infrared earth horizon sensors. Journal of Spacecraft and Rockets, 55: 1466–1475, 11 2018. ISSN 15336794. doi: 10.2514/1.A34010.

I. P. on Climate Change. Climate Change 2007 - Mitigation of Climate Change: Working Group III contribution to the Fourth Assessment Report of the IPCC. Cambridge University Press, 2007. doi: DOI:10.1017/CBO9780511546013. URL `https://www.cambridge.org/core/books/climate-change-2007-mitigation-of-climate-change/5D933BDDA2CFE3ECEFE477EA3F9D7948`.

L. Palchetti, H. Brindley, R. Bantges, S. A. Buehler, C. Camy-Peyret, B. Carli, U. Cortesi, S. D. Bianco, G. D. Natale, B. M. Dinelli, D. Feldman, X. L. Huang, L. C.-Labonnote, Q. Libois, T. Maestri, M. G. Mlynczak, J. E. Murray, H. Oetjen, M. Ridolfi, M. Riese, J. Russell, R. Saunders, and C. Serio. Forum: unique far-infrared satellite observations to better understand how earth radiates energy to space. Bulletin of the American Meteorological Society, pages 1–52, 8 2020. ISSN 0003-0007. doi: 10.1175/bams-d-19-0322.1.

M. D. Palmer, C. D. Roberts, M. Balmaseda, Y. S. Chang, G. Chepurin, N. Ferry, Y. Fujii, S. A. Good, S. Guinehut, K. Haines, F. Hernandez, A. Köhl, T. Lee, M. J. Martin, S. Masina, S. Masuda, K. A. Peterson, A. Storto, T. Toyoda, M. Valdivieso, G. Vernieres, O. Wang, and Y. Xue. Ocean heat content variability and change in an ensemble of ocean reanalyses. Climate Dynamics, 49: 909–930, 8 2017. ISSN 14320894. doi: 10.1007/s00382-015-2801-0.

R. Parfitt, J. E. Russell, R. Bantges, N. Clerbaux, and H. Brindley. A study of the time evolution of gerb shortwave calibration by comparison with ceres edition-3a data. Remote Sensing of Environment, 186:416–427, 12 2016. ISSN 00344257. doi: 10.1016/j.rse.2016.09.005.

P. Pilewskie and M. Z. Hakuba. Libera and Continuity of the ERB Climate Data Record. In AGU Fall Meeting Abstracts, volume 2020, pages GC133–01, Dec. 2020.

K. J. Priestley, S. Thomas, and G. L. Smith. Validation of point spread functions of ceres radiometers by the use of lunar observations. Journal of Atmospheric and Oceanic Technology, 27:1005–1011, 6 2010. ISSN 07390572. doi: 10.1175/2010JTECHA1322.1.

J. Puig-Suari, J. Schoos, C. Turner, T. Wagner, R. Connolly, and R. P. Block. Cubesat developments at cal poly: the standard deployer and polysat. SPIE, 4136:72 – 78, 2000. doi: 10.1117/12.406645. URL `https://doi.org/10.1117/12.406645`.

H.-O. Rama, D. Roberts, M. Tignor, E. Poloczanska, K. Mintenbeck, A. Alegría, M. Craig, S. Langsdorf, S. Löschke, V. Möller, A. Okem, B. Rama, and S. Ayanlade. IPCC, 2022: Climate Change 2022 Impacts, Adaptation and Vulnerability Working Group II Contribution to the Sixth Assessment Report of the Intergovernmental Panel on Climate Change. Cambridge University Press. Cambridge University Press, Cambridge, UK and New York, NY, USA, 2022. ISBN 9789291691593. doi: 10.1017/9781009325844. URL `www.ipcc.ch`.

L. Resplandy, R. F. Keeling, Y. Eddebbar, M. K. Brooks, R. Wang, L. Bopp, M. C. Long, J. P. Dunne, W. Koeve, and A. Oschlies. Quantification of ocean heat uptake from changes in atmospheric o2 and co2 composition. Nature, 563:105–108, 2018. ISSN 1476-4687. doi: 10.1038/s41586-018-0651-8. URL `https://doi.org/10.1038/s41586-018-0651-8`.

M. Robic, R. Fraisse, E. Marchand, and F. Chaumette. Vision-based rotational control of an agile observation satellite. IEEE/RSJ Int. Conf. on Intelligent Robots and Systems, IROS'22, 2022.

R. Roca, H. Brogniez, P. Chambon, O. Chomette, S. Cloché, M. E. Gosset, J.-F. Mahfouf, P. Raberanto, and N. Viltard. The megha-tropiques mission: a review after three years in orbit. Frontiers in Earth Science, 3:17, 2015. ISSN 2296-6463. URL `https://www.frontiersin.org/article/10.3389/feart.2015.00017`.

D. Roemmich, J. Church, J. Gilson, D. Monselesan, P. Sutton, and S. Wijffels. Unabated planetary warming and its ocean structure since 2006. Nature Climate Change, 5:240–245, 2 2015. ISSN 17586798. doi: 10.1038/nclimate2513.

R. Sandau. Status and trends of small satellite missions for earth observation. Acta Astronautica, 66(1):1–12, 2010. ISSN 0094-5765. doi: https://doi.org/10.1016/j.actaastro.2009.06.008. URL `https://www.sciencedirect.com/science/article/pii/S0094576509003488`.

C. J. Schreck, H. T. Lee, and K. R. Knapp. Hirs outgoing longwave radiation-daily climate data record: Application toward identifying tropical subseasonal variability. Remote Sensing, 10:1–13, 2018. ISSN 20724292. doi: 10.3390/rs10091325.

K. V. Schuckmann, M. D. Palmer, K. E. Trenberth, A. Cazenave, D. Chambers, N. Champollion, J. Hansen, S. A. Josey, N. Loeb, P. P. Mathieu, B. Meyssignac, and M. Wild. An imperative to monitor earth's energy imbalance. Nature Climate Change, 6:138–144, 1 2016. ISSN 17586798. doi: 10.1038/nclimate2876.

G. J. Schumann, G. R. Brakenridge, A. J. Kettner, R. Kashif, and E. Niebuhr. Assisting flood disaster response with earth observation data and products: A critical assessment. Remote Sensing, 10, 8 2018. ISSN 20724292. doi: 10.3390/rs10081230.

R. Seitz. Bright water: hydrosols, water conservation and climate change. Climatic Change, 105:365–381, 2011. ISSN 1573-1480. doi: 10.1007/s10584-010-9965-8. URL `https://doi.org/10.1007/s10584-010-9965-8`.

H. Shang, Y. Ding, H. Guo, G. Liu, X. Liu, J. Wu, L. Liang, H. Jiang, and G. Chen. Simulation of earth's outward radiative flux and its radiance in moon-based view. Remote Sensing, 13:2535, 6 2021. ISSN 2072-4292. doi: 10.3390/rs13132535. URL `https://www.mdpi.com/2072-4292/13/13/2535`.

L. S. Shapley. Notes on the n-person game – ii: The value of an n-person game. Santa Monica, Calif.: RAND Corporation., 1951.

D. M. Smith, R. P. Allan, A. C. Coward, R. Eade, P. Hyder, C. Liu, N. G. Loeb, M. D. Palmer, C. D. Roberts, and A. A. Scaife. Earth's energy imbalance since

1960 in observations and cmip5 models. Geophysical Research Letters, 42:1205–1213, 2 2015. ISSN 19448007. doi: 10.1002/2014GL062669.

S. Solomon, J. S. Daniel, R. R. Neely, J.-P. Vernier, E. G. Dutton, and L. W. Thomason. The persistently variable “background” stratospheric aerosol layer and global climate change. Science, 333:866–870, 2011. doi: 10.1126/science.1206027. URL `https://www.science.org/doi/abs/10.1126/science.1206027`.

D. Stammer, M. Balmaseda, P. Heimbach, A. Köhl, and A. Weaver. Ocean data assimilation in support of climate applications: Status and perspectives. Annual Review of Marine Science, 8:491–518, 1 2016. ISSN 19410611. doi: 10.1146/annurev-marine-122414-034113.

G. L. Stephens, J. Li, M. Wild, C. A. Clayson, N. Loeb, S. Kato, T. L’Ecuyer, P. W. Stackhouse, M. Lebsock, and T. Andrews. An update on Earth’s energy balance in light of the latest global observations. Nature Geoscience, 5:691–696, Oct. 2012. doi: 10.1038/ngeo1580.

W. Swartz, S. Lorentz, S. Papadakis, P. Huang, A. Smith, D. Deglau, Y. Yu, S. Reilly, N. Reilly, and D. Anderson. Ravan: Cubesat demonstration for multi-point earth radiation budget measurements. Remote Sensing, 11:796, 4 2019. doi: 10.3390/rs11070796.

R. Swinbank and R. J. Purser. Fibonacci grids: A novel approach to global modelling. Quarterly Journal of the Royal Meteorological Society, 132:1769–1793, 7 2006. ISSN 00359009. doi: 10.1256/qj.05.227.

L. D. Talley, G. L. Pickard, W. J. Emery, and J. H. Swift. Chapter S16 - Instruments and Methods. Academic Press, 2011. ISBN 978-0-7506-4552-2. doi: https://doi.org/10.1016/B978-0-7506-4552-2.10028-9. URL `http://www.sciencedirect.com/science/article/pii/B9780750645522100289`.

Q. Tian, Q. Liu, J. Guang, L. Yang, H. Zhang, C. Fan, Y. Che, and Z. Li. The estimation of surface albedo from dscovr epic. Remote Sensing, 12, 6 2020. ISSN 20724292. doi: 10.3390/rs12111897.

R. Torres, P. Snoeij, D. Geudtner, D. Bibby, M. Davidson, E. Attema, P. Potin, B. Rommen, N. Floury, M. Brown, I. N. Traver, P. Deghaye, B. Duesmann, B. Rosich, N. Miranda, C. Bruno, M. L’Abbate, R. Croci, A. Pietropaolo, M. Huchler, and F. Rostan. Gmes sentinel-1 mission. Remote Sensing of Environment, 120:9–24, 2012. ISSN 0034-4257. doi: https://doi.org/10.1016/j.rse.2011.05.028. URL `https://www.sciencedirect.com/science/article/pii/S0034425712000600`. The Sentinel Missions - New Opportunities for Science.

K. E. Trenberth. ENSO in the Global Climate System, pages 21–37. American Geophysical Union (AGU), 2020. ISBN 9781119548164. doi: https://doi.org/10.1002/9781119548164.ch2. URL `https://agupubs.onlinelibrary.wiley.com/doi/abs/10.1002/9781119548164.ch2`.

K. E. Trenberth and J. T. Fasullo. Tracking earth's energy. Science, 328:316–317, 2010. ISSN 00368075. doi: 10.1126/science.1187272.

K. E. Trenberth and J. T. Fasullo. Tracking earth's energy: From el niño to global warming. Surveys in Geophysics, 33:413–426, 2012. ISSN 01693298. doi: 10.1007/s10712-011-9150-2.

K. E. Trenberth and J. T. Fasullo. An apparent hiatus in global warming? Earth's Future, 1:19–32, 2013. doi: https://doi.org/10.1002/2013EF000165. URL `https://agupubs.onlinelibrary.wiley.com/doi/abs/10.1002/2013EF000165`.

K. E. Trenberth, J. T. Fasullo, and M. A. Balmaseda. Earth's energy imbalance. Journal of Climate, 27:3129–3144, 2014. ISSN 08948755. doi: 10.1175/JCLI-D-13-00294.1.

K. E. Trenberth, J. T. Fasullo, K. von Schuckmann, and L. Cheng. Insights into earth's energy imbalance from multiple sources. Journal of Climate, 29:7495–7505, 2016. ISSN 08948755. doi: 10.1175/JCLI-D-16-0339.1.

P. Tysiąc, T. Strelets, and W. Tuszyńska. The application of satellite image analysis in oil spill detection. Applied Sciences, 12(8), 2022. ISSN 2076-3417. doi: 10.3390/app12084016. URL `https://www.mdpi.com/2076-3417/12/8/4016`.

M. Viollier, C. Standfuss, O. Chomette, and A. Quesney. Top-of-atmosphere radiance-to-flux conversion in the sw domain for the scarab-3 instrument on megha-tropiques. Journal of Atmospheric and Oceanic Technology, 26:2161–2171, 2009. ISSN 07390572. doi: 10.1175/2009JTECHA1264.1.

K. von Schuckmann, L. Cheng, M. D. Palmer, J. Hansen, C. Tassone, V. Aich, S. Adusumilli, H. Beltrami, T. Boyer, F. J. Cuesta-Valero, D. Desbruyères, C. Domingues, A. Garciá-Garciá, P. Gentine, J. Gilson, M. Gorfer, L. Haimberger, M. Ishii, G. C. Johnson, R. Killick, B. A. King, G. Kirchengast, N. Kolodziejczyk, J. Lyman, B. Marzeion, M. Mayer, M. Monier, D. P. Monselesan, S. Purkey, D. Roemmich, A. Schweiger, S. I. Seneviratne, A. Shepherd, D. A. Slater, A. K. Steiner, F. Straneo, M. L. Timmermans, and S. E. Wijffels. Heat stored in the earth system: Where does the energy go? Earth System Science Data, 12:2013–2041, 9 2020. ISSN 18663516. doi: 10.5194/essd-12-2013-2020.

K. Von Schuckmann, L. Cheng, M. D. Palmer, J. Hansen, C. Tassone, V. Aich, S. Adusumilli, H. Beltrami, T. Boyer, F. J. Cuesta-Valero, et al. Heat stored in the earth system: where does the energy go? Earth System Science Data, 12 (3):2013–2041, 2020.

B. A. Wielicki, B. R. Barkstrom, E. F. Harrison, R. B. Lee, G. L. Smith, and J. E. Cooper. Clouds and the earth's radiant energy system (ceres): An earth observing system experiment. Bulletin of the American Meteorological Society, 77:853–868, 1996. ISSN 00030007. doi: 10.1175/1520-0477(1996)077<0853:CATERE>2.0.CO;2.

S. Wu, W. Chen, C. Cao, C. Zhang, and Z. Mu. A multiple-cubesat constellation for integrated earth observation and marine/air traffic monitoring. Advances in Space Research, 67(11):3712–3724, 2021. ISSN 0273-1177. doi: https://doi.org/10.1016/j.asr.2020.04.025. URL `https://www.sciencedirect.com/science/article/pii/S0273117720302635`. Satellite Constellations and Formation Flying.

W. Yang, A. Marshak, T. Várnai, and Y. Knyazikhin. Epic spectral observations of variability in earth's global reflectance. Remote Sensing, 10, 2 2018. ISSN 20724292. doi: 10.3390/rs10020254.

Y. Yang. Spacecraft Modeling, Attitude Determination, and Control Quaternion-based Approach. CRC Press, 2 2019. ISBN 978-1138331501. doi: 10.1201/9780429446580.

H. Ye, H. Guo, G. Liu, J. Ping, L. Zhang, and Y. Zhang. Estimating the earth's outgoing longwave radiation measured from a moon-based platform. Remote Sensing, 13, 6 2021. ISSN 20724292. doi: 10.3390/rs13112201.

K. O. Yoro and M. O. Daramola. Chapter 1 - CO2 emission sources, greenhouse gases, and the global warming effect, pages 3–28. Woodhead Publishing, 2020. ISBN 978-0-12-819657-1. doi: https://doi.org/10.1016/B978-0-12-819657-1.00001-3. URL `https://www.sciencedirect.com/science/article/pii/B9780128196571000013`.

P. Zhu, M. V. Ruymbeke, Karatekin, J. P. Noël, G. Thuillier, S. Dewitte, A. Chevalier, C. Conscience, E. Janssen, M. Meftah, and A. Irbah. A high dynamic radiation measurement instrument: The bolometric oscillation sensor (bos). Geoscientific Instrumentation, Methods and Data Systems, 4:89–98, 5 2015. ISSN 21930864. doi: 10.5194/gi-4-89-2015.